Aeroacoustic testing in acoustically disturbed environments

Improvements to closed test section wind tunnel experiments

Mourão Bento, H.F.

DOI
10.4233/uuid:469dc840-b62a-4a75-a52e-b02cbb230f6a

Publication date
2025

Document Version
Final published version

Citation (APA)
Mourão Bento, H. F. (2025). *Aeroacoustic testing in acoustically disturbed environments: Improvements to closed test section wind tunnel experiments*. [Dissertation (TU Delft), Delft University of Technology]. https://doi.org/10.4233/uuid:469dc840-b62a-4a75-a52e-b02cbb230f6a

Important note
To cite this publication, please use the final published version (if applicable).
Please check the document version above.

Aeroacoustic testing in acoustically disturbed environments

Improvements to closed test section wind tunnel experiments

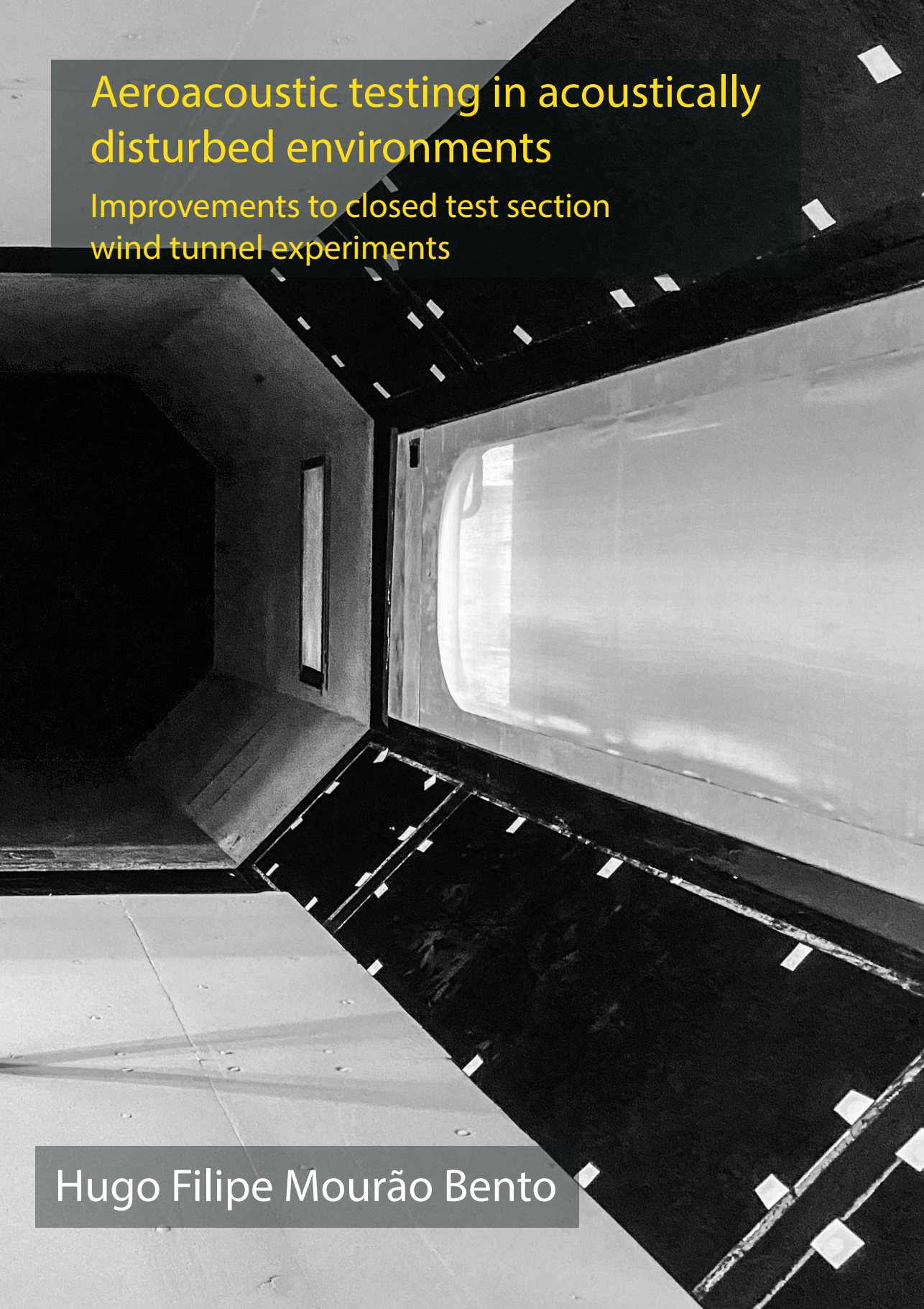

Hugo Filipe Mourão Bento

Propositions

accompanying the dissertation

Aeroacoustic testing in acoustically disturbed environments

Improvements to closed test section wind tunnel experiments

by

Hugo Filipe MOURÃO BENTO

1. The best wind tunnel wall microphone placement is in a cavity with maximum volume, and as far from the wall as possible (Chapter 4).
2. Flat Melamine foam liners (and other liners with similar roughness and inertial resistivity) do not cause any significant disturbance to the aerodynamic or noise generation characteristics of a wind tunnel. Thus, it is better to place them at the wind tunnel walls without any Kevlar or wire-mesh covers (Chapters 5, 6 and 7).
3. A well characterized wind tunnel wall liner is better than a liner with superior acoustic absorption (Chapter 7).
4. Sound reflections are beneficial for wind tunnel acoustic measurements (Chapter 7).
5. A research problem cannot be solved at the office.
6. The goal of an aeroacoustics researcher/engineer is not to make things silent, but to find more noise sources that need noise reduction.
7. Europe (and not only) should fight climate change caused by aviation by making trains and train rails instead of greener aircraft.
8. The biggest threat to science is that society sees it as religion.
9. PhD candidates in the Netherlands should receive extra salary for doing sports outside working hours.
10. Thanks to their nutritional value, oranges and chicken skin are a huge help for doing a PhD.

These propositions are regarded as opposable and defendable, and have been approved as such by the promotors Prof.dr.ir. M. Snellen, Dr. D. Ragni and Prof.dr. F. Avallone.

Stellingen

bij het proefschrift

Aeroacoustic testing in acoustically disturbed environments

Improvements to closed test section wind tunnel experiments

door

Hugo Filipe MOURÃO BENTO

1. De beste plaatsing van een microfoon op de wand van een windtunnel is in een holte met het maximale volume, en zo ver mogelijk van de wand (Hoofdstuk 4).
2. Platte melamine schuim liners (en andere liners met vergelijkbare ruwheid en inertiële resistiviteit) veroorzaken geen significante verstoring van de aerodynamische of geluidsgenererende kenmerken van een windtunnel. Het is dus beter om ze op de wanden van de windtunnel te plaatsen zonder Kevlar- of gaasbedekking (Hoofdstukken 5, 6 en 7).
3. Een goed gekarakteriseerde wandbekleding voor een windtunnel is beter dan een bekleding met superieure akoestische absorptie (Hoofdstuk 7).
4. Geluidreflecties zijn voordelig voor akoestische metingen in een windtunnel (Hoofdstuk 7).
5. Een onderzoeksprobleem kan niet op kantoor worden opgelost.
6. Het doel van een aeroakoestisch onderzoeker/ingenieur is niet om dingen stil te maken, maar om meer geluidsbronnen te vinden die geluidsreductie nodig hebben.
7. Europa (en niet alleen) zou de klimaatverandering veroorzaakt door de luchtvaart moeten bestrijden door treinen en treinrails te maken in plaats van groenere vliegtuigen.
8. De grootste bedreiging voor de wetenschap is dat de samenleving het als religie ziet.
9. Promovendikandidaten in Nederland zouden extra salaris moeten ontvangen voor het doen van sport buiten werktijd.
10. Dankzij hun voedingswaarde zijn sinaasappels en kippenvel een enorme hulp bij het doen van een PhD.

Deze stellingen worden opponeerbaar en verdedigbaar geacht en zijn als zodaniggoedgekeurd door de promotoren Prof.dr.ir. M. Snellen, Dr. D. Ragni and Prof.dr. F. Avallone.

Aeroacoustic testing in acoustically disturbed environments

Improvements to closed test section wind tunnel experiments

Aeroacoustic testing in acoustically disturbed environments

Improvements to closed test section wind tunnel experiments

Dissertation

for the purpose of obtaining the degree of doctor
at Delft University of Technology
by the authority of the Rector Magnificus, prof. dr. ir. T.H.J.J. van der Hagen,
chair of the Board for Doctorates
to be defended publicly on
Tuesday 9 December 2025 at 15:00 o'clock

by

Hugo Filipe MOURÃO BENTO

Master of Science in Aerospace Engineering,
Delft University of Technology, The Netherlands
born in Lisbon, Portugal

This dissertation has been approved by the promotors.

Composition of the doctoral committee:

Rector Magnificus,	chairperson
Prof.dr.ir. M. Snellen,	Delft University of Technology, *promotor*
Dr. D. Ragni,	Delft University of Technology, *promotor*
Prof.dr. F. Avallone,	Politecnico di Torino, Italy, *promotor*

Independent members:

Prof.dr.ir. L.L.M. Veldhuis,	Delft University of Technology
Prof.dr.ir. C.H. Venner,	University of Twente
Dr. A. Fischer	Technical University of Denmark, Denmark
Prof.Dr.-Ing. E. Sarradj	Technical University of Berlin, Germany
Prof.dr. F. Scarano,	Delft University of Technology, reserve member

Keywords: acoustic measurements, closed test section wind tunnel, microphone cavity design, acoustic reflections, wall liner, acoustic modelling, Beamforming, Green's function correction, experimental aeroacoustics, aeroacoustics

Printed by: ProefschriftMaken

Cover (front): Picture of a lined wind tunnel test section.
Cover (back): Illustration of a lined wind tunnel test section discretised by a numerical solver.

ISBN 978-94-6534-085-2

An electronic copy of this dissertation is available at
https://repository.tudelft.nl/.

CONTENTS

SUMMARY

The widespread implementation of new technologies from the aviation, automotive and renewable energy sectors, among others, is often slowed down by noise emission concerns. Excessive noise emissions lead to human discomfort and even health issues. Populations are protected by strict noise regulations. Reducing noise emissions from new engineering products is therefore a must for their success in the market. Many industries are now invested in research and development in the acoustic field. Aeroacoustics is the field which studies the noise impact from aerodynamically generated sound. Aerodynamic noise sources are always present, e.g., in new aircraft, wind turbines or home appliances such as vacuum cleaners. The process of understanding and mitigating the aerodynamic noise sources from these engineering products is ideally done with state—of—the—art prediction methods, including experiments and numerical simulations.

Most commonly, aerodynamic experiments are done in wind tunnel facilities. The highest aerodynamic fidelity can be achieved with closed test section wind tunnels. As consequence, these are also ideal testing facilities for aeroacoustic investigations. However, performing reliable acoustic measurements in closed section wind tunnels is challenging. Unlike acoustically treated open—jet test sections, closed (or even hybrid) test sections suffer from strong acoustic disturbances. Very noticeable are the disturbances resulting from the acoustic reflections on the walls of the wind tunnel. These lead to acoustic interference at the points of acoustic measurement, which in turn leads to over or under predicting noise emissions. Acoustic measurements are most often recorded with microphones. For these measurements, the signal to noise ratio is a critical parameter. The signal to noise ratio represents the strength of the acoustic signal from the test object, with respect to the strength of the remaining pressure fluctuations at a measurement point. The signal to noise ratio is reduced in closed test section wind tunnels by spurious acoustic noise sources, e.g., aerodynamic noise sources in the facility such as the wind tunnel fan, and by potentially strong reverberation. Additionally, wall mounted microphones suffer from the recording of hydrodynamic pressure fluctuations present in the turbulent boundary layer of the wind tunnel walls.

This research aims at improving aeroacoustic testing in acoustically disturbed environments, with particular focus on closed test section wind tunnels. Ideally, it should become possible to perform fully reliable

aeroacoustic experimental campaigns without the need of anechoic open—jet facilities.

The improvement of microphone placement is tackled by studying wall cavity designs. The improvement of the testing facility is investigated by analyzing the impact of lining the wind tunnel walls on the aerodynamic performance of the tunnel, on reverberation and on acoustic interference in the test section. Additionally, the step of post—processing acoustic wind tunnel data is improved by using data from a Finite Element Method (FEM) numerical acoustic solver.

The investigation of wall cavities for microphone placement was done with Computational Fluid Dynamics simulations, which in turn were validated experimentally. Cavities covered with a mesh cover were investigated, since previous literature shows that these reduce hydrodynamic noise while allowing for the transmission of waves to the microphones. The numerical simulations show that covering microphone cavities with a mesh cover results in a stagnant flow inside the cavities. This avoids the convection of hydrodynamic noise to the microphone position at the cavity bottoms. As consequence, the only source of pressure fluctuations at the cavity bottoms are acoustic waves. The hydrodynamic pressure fluctuations from the wall's boundary layer still propagate acoustically to the cavity bottoms. The findings show that increasing cavity size, in particular increasing the cavity opening diameter with respect to the length of the eddies in the turbulent boundary layer, leads to a lower propagation of spurious pressure fluctuations to the cavity bottoms. This in turn leads to an increased signal to noise ratio of acoustic measurements recorded at closed test section wind tunnels.

Wind tunnel wall liners have been characterized based on their viscous resistivity, inertial resistivity and roughness. Several porous liners have been tested experimentally. The aim was to analyze their impact on the aerodynamic properties of the wind tunnel boundary layer, on the generation of spurious noise, and on the absorption of acoustic reflections. The results show that the ideal choice of liner consists of a liner: with high viscous resistivity, which leads to high acoustic absorption; with low roughness, to reduce the impact on the wind tunnel wall's boundary layer; and with low inertial resistivity, to reduce the generation of spurious noise. The best lining material tested was melamine foam.

The improvement caused by lining a closed section wind tunnel was analyzed by lining a singular section of the tunnel circuit, the test section, with melamine foam. It was possible to verify a clear reduction of reverberation time by lining exclusively this section of the circuit. More importantly, acoustic interference at the microphones reduces drastically by lining the test section. On the other hand, the reverberation caused by the remaining sections of the wind tunnel circuit

was found to have a negligible influence on acoustic interference at the microphone locations, at the frequencies of interest. Further reducing reverberation in the wind tunnel circuit is expected to be beneficial for lowering background noise during the measurements.

The acoustic propagation and acoustic interference in a closed wind tunnel test section were predicted with a FEM acoustic solver. The propagation was modelled on a baseline test section and on test sections with lined walls. The baseline section walls are considered fully reflective. The numerical results were found to give a very accurate prediction of the acoustic experimental tests. It was possible to use the numerical results to improve the post—processing of experimental data. The Green's function used to process experimental microphone data with beamforming was corrected, using the numerical results. Beamforming with the Green's function corrected for the acoustically disturbed environment led to a higher beamforming spatial resolution. In addition, the estimated noise levels are more accurate when the correction is used. This improved approach was shown to work for post—processing experimental measurements of a monopole sound source placed at the center of the test section, with and without free—stream flow. For the flow—on cases, improving beamforming spatial resolution with the corrected Green's function also helps to increase the signal to noise ratio.

The research in this thesis presents an important step towards achieving optimum acoustic testing conditions in acoustically disturbed environments, such as closed section or hybrid test section wind tunnels. The understanding of the physics of the state—of—the—art cavities for microphone placement was extended, the understanding of the benefits of lining a wind tunnel circuit was explored, and the post-processing of acoustic data recorded in a disturbed environment was improved. However, there are still many improvements to be made within the field of aeroacoustics experimental testing. The findings of this thesis suggest that further exploring the best design for wind tunnel covered microphone cavities should be done with purely acoustic numerical studies, as pressure fluctuations propagate acoustically towards the microphones. The benefits of lining further sections of the wind tunnel circuit (besides the test section) should be investigated by analyzing its impact on reverberation and, consequently, on background noise. Finally, the FEM acoustic predictions presented in this thesis should be extended to different acoustic sources, such as line sources, rotating bodies, and sources with a different directivity, e.g. dipolar. This will enable the accurate estimation of noise levels from wind turbine blades, wind turbines and propellers from closed or hybrid test section wind tunnel data, by using the post—processing methodology proposed in this thesis.

SAMENVATTING

De brede implementatie van nieuwe technologieën uit onder andere de luchtvaart-, auto- en hernieuwbare energiesectoren wordt vaak vertraagd door zorgen over geluidsemissies. Overmatige geluidsemissies leiden tot menselijk ongemak en zelfs gezondheidsproblemen. Bevolkingen worden beschermd door strikte geluidsregulaties. Het verminderen van geluidsemissies van nieuwe technische producten is daarom een vereiste voor hun succes op de markt. Veel industrieën investeren tegenwoordig in onderzoek en ontwikkeling op het gebied van akoestiek. Aeroakoestiek is het vakgebied dat de geluidshinder bestudeert die ontstaat door aerodynamisch gegenereerd geluid. Aerodynamische geluidsbronnen zijn altijd aanwezig, bijvoorbeeld in nieuwe vliegtuigen, windturbines of huishoudelijke apparaten zoals stofzuigers. Het proces van het begrijpen en beperken van de aerodynamische geluidsbronnen van deze technische producten wordt idealiter uitgevoerd met state-of-the-art voorspellingsmethoden, inclusief experimenten en numerieke simulaties.

Meestal worden aerodynamische experimenten uitgevoerd in windtunnelvoorzieningen. De hoogste aerodynamische nauwkeurigheid kan worden bereikt met windtunnels met een gesloten testsectie. Als gevolg hiervan zijn dit ook ideale testfaciliteiten voor aeroakoestische onderzoeken. Het uitvoeren van betrouwbare akoestische metingen in windtunnels met gesloten testsecties is echter uitdagend. In tegenstelling tot akoestisch behandelde openjettestsecties, lijden gesloten (of zelfs hybride) testsecties onder sterke akoestische verstoringen. Zeer opvallend zijn de verstoringen die ontstaan door akoestische reflecties op de wanden van de windtunnel. Deze leiden tot akoestische interferentie op de meetpunten, wat op zijn beurt leidt tot over- of ondervoorspelling van de geluidsemissies. Akoestische metingen worden meestal geregistreerd met microfoons. Voor deze metingen is de signaal-ruisverhouding een kritieke parameter. De signaal-ruisverhouding geeft de sterkte van het akoestische signaal van het testobject weer ten opzichte van de sterkte van de resterende drukfluctuaties op een meetpunt. De signaal-ruisverhouding wordt verminderd in windtunnels met gesloten testsecties door spuriëuze akoestische geluidsbronnen, bijvoorbeeld aerodynamische geluidsbronnen in de faciliteit, zoals de ventilator van de windtunnel, en door mogelijk sterke nagalming. Bovendien lijden muurbevestigde microfoons onder de registratie van hydrodynamische drukfluctuaties die aanwezig zijn in de turbulente

grenslaag van de windtunnelwanden.

Dit onderzoek heeft als doel de verbetering van aeroakoestische tests in akoestisch verstoorde omgevingen, met bijzondere focus op windtunnels met gesloten testsecties. Idealiter zou het mogelijk moeten zijn om volledig betrouwbare aeroakoestische experimenten uit te voeren zonder de noodzaak van anechoïsche open-jetfaciliteiten.

De verbetering van de microfoonplaatsing wordt aangepakt door wandholte-ontwerpen te bestuderen. De verbetering van de testfaciliteit wordt onderzocht door de impact van het bekleden van de windtunnelwanden te analyseren op de aerodynamische prestaties van de tunnel, de nagalming en de akoestische interferentie in de testsectie. Bovendien wordt de stap van post-processing van akoestische windtunnelgegevens verbeterd door gebruik te maken van gegevens van een Finite Element Method (FEM) numerieke akoestische solver.

De studie van wandholtes voor microfoonplaatsing werd uitgevoerd met Computational Fluid Dynamics-simulaties, die op hun beurt experimenteel werden gevalideerd. Holtes bedekt met een gaasbedekking werden onderzocht, aangezien eerdere literatuur aantoont dat deze hydrodynamisch geluid verminderen terwijl ze de doorgang van golven naar de microfoons mogelijk maken. De numerieke simulaties tonen aan dat het bedekken van microfoonholtes met een gaasbedekking resulteert in een stilstaande stroming binnen de holtes. Dit voorkomt de convectie van hydrodynamisch geluid naar de microfoonpositie op de bodem van de holtes. Als gevolg hiervan is de enige bron van drukfluctuaties op de bodems van de holtes akoestische golven. De hydrodynamische drukfluctuaties van de grenslaag van de wand blijven akoestisch door de holtes naar de bodem van de holtes propagateren. De bevindingen tonen aan dat het vergroten van de holtegrootte, met name het vergroten van de diameter van de holteopening ten opzichte van de lengte van de wervelingen in de turbulente grenslaag, leidt tot een lagere propagatie van spuriëuze drukfluctuaties naar de bodem van de holtes. Dit leidt op zijn beurt tot een hogere signaal-ruisverhouding van akoestische metingen die in windtunnels met gesloten testsecties worden geregistreerd.

Windtunnelwandbekleding is gekarakteriseerd op basis van hun viskeuze resistiviteit, inertiële resistiviteit en ruwheid. Verschillende poreuze bekledingen zijn experimenteel getest. Het doel was om hun impact op de aerodynamische eigenschappen van de grenslaag van de windtunnel, de generatie van spuriëuze geluiden en de absorptie van akoestische reflecties te analyseren. De resultaten tonen aan dat de ideale keuze van bekleding bestaat uit een bekleding: met een hoge viskeuze resistiviteit, wat leidt tot hoge akoestische absorptie; met lage ruwheid, om de impact op de grenslaag van de windtunnelwand te verminderen; en met lage inertiële resistiviteit, om de generatie van spuriëuze geluiden te verminderen. Het beste bekledingsmateriaal dat

werd getest was melamine schuim.

De verbetering die wordt veroorzaakt door het bekleden van een windtunnel met een gesloten sectie werd geanalyseerd door een enkel gedeelte van het tunnelcircuit, de testsectie, te bekleden met melamine schuim. Het was mogelijk om een duidelijke vermindering van de nagalmtijd te verifiëren door uitsluitend dit gedeelte van het circuit te bekleden. Belangrijker nog, de akoestische interferentie bij de microfoons wordt drastisch verminderd door de testsectie te bekleden. Aan de andere kant werd de nagalming die werd veroorzaakt door de resterende secties van het windtunnelcircuit als verwaarloosbaar beschouwd in de invloed op de akoestische interferentie op de microfoonlocaties bij de frequenties van belang. Verdere vermindering van de nagalming in het windtunnelcircuit wordt als voordelig beschouwd voor het verlagen van de achtergrondruis tijdens de metingen.

De akoestische propagatie en akoestische interferentie in een windtunnel testsectie met gesloten wanden werd voorspeld met een FEM akoestische solver. De propagatie werd gemodelleerd op een basistestsectie en op testsecties met beklede wanden. De wanden van de basistestsectie worden als volledig reflecterend beschouwd. De numerieke resultaten bleken een zeer accurate voorspelling van de akoestische experimentele tests te geven. Het was mogelijk om de numerieke resultaten te gebruiken om de post-processing van experimentele gegevens te verbeteren. De Green’s functie die wordt gebruikt om experimentele microfoongegevens te verwerken met beamforming werd gecorrigeerd met behulp van de numerieke resultaten. Beamforming met de Green’s functie gecorrigeerd voor de akoestisch verstoorde omgeving leidde tot een hogere ruimtelijke resolutie bij beamforming. Bovendien zijn de geschatte geluidsniveaus nauwkeuriger wanneer de correctie wordt toegepast. Deze verbeterde benadering bleek te werken voor de post-processing van experimentele metingen van een monopoolgeluidsbron die in het midden van de testsectie was geplaatst, met en zonder vrije-stroom. Voor de gevallen met stroming helpt het verbeteren van de ruimtelijke resolutie van beamforming met de gecorrigeerde Green’s functie ook de signaal-ruisverhouding te verhogen.

Het onderzoek in dit proefschrift presenteert een belangrijke stap naar het bereiken van optimale akoestische testomstandigheden in akoestisch verstoorde omgevingen, zoals windtunnels met gesloten secties of hybride testsecties. Het begrip van de fysica van de state-of-the-art holtes voor microfoonwandplaatsing werd uitgebreid, het begrip van de voordelen van het bekleden van een windtunnelcircuit werd verkend, en de post-processing van akoestische gegevens die in een verstoorde omgeving werden geregistreerd, werd verbeterd. Er zijn echter nog veel verbeteringen te maken op het gebied van aeroakoestisch experimenteren. De bevindingen van dit proefschrift

suggereren dat verder onderzoek naar het beste ontwerp voor beklede microfoonholtes in de windtunnel moet worden uitgevoerd met puur akoestische numerieke studies, aangezien drukfluctuaties akoestisch naar de microfoons kunnen propageren. De voordelen van het bekleden van andere secties van het windtunnelcircuit (naast de testsectie) zouden moeten worden onderzocht door de impact op de nagalming en daarmee op de achtergrondruis te analyseren. Ten slotte zouden de FEM akoestische voorspellingen die in dit proefschrift zijn gepresenteerd, moeten worden uitgebreid naar andere akoestische bronnen, zoals lijnbronnen, roterende lichamen en bronnen met een andere directiviteit, bijvoorbeeld dipolair. Dit zal de nauwkeurige schatting van geluidsniveaus van windturbinebladen, windturbines en propellers op basis van gegevens van windtunnels met gesloten of hybride testsecties mogelijk maken, door de post-processingmethodologie die in dit proefschrift wordt voorgesteld te gebruiken.

1

INTRODUCTION

Scientific knowledge is a body of statements of varying degrees of certainty – some most unsure, some nearly sure, none absolutely certain.

Richard P. Feynman

Noise pollution causes discomfort and health problems to both humans and animals [1]. The aviation, automotive, and renewable energy industries strive to mitigate noise emitted by their new technologies. Besides acknowledging the need to reduce the impact of noise pollution on the environment, these industries face the need to comply with noise regulations [2, 3]. These regulations limit the noise which can be emitted in a certain area. In the aviation industry, these noise regulations may limit the number of flights for each airport, and delay a widespread adoption of Urban Air Mobility vehicles [4]. In the wind energy industry, regulations and noise concerns limit the growth of onshore wind turbine farms [5]. This effectively reduces renewable energy generation from wind, and has a negative impact on the climate crisis [6].

The study of aerodynamically generated noise and the development of innovative noise mitigation technologies needs proper verification, through numerical and experimental tests. Experimental tests may be carried out in wind tunnel facilities and outside in the field [7]. Computational AeroAcoustics (CAA) methods make use of Computational Fluid Dynamics (CFD) solvers in order to numerically calculate aerodynamic phenomena which leads to noise radiation. In CAA, noise at a receiver can be calculated directly by the CFD solver, or by post-processing of the numerical aerodynamic data. CAA calculations are computationally too expensive to cover as large

parametric studies as laboratory experiments, but have the advantage of providing more complete data, for instance detailed flowfield data. Combining wind tunnel experiments and CAA in a study is beneficial, and is also commonly used for validation of the simulations [8, 9]. Field measurements are important for quantifying the overall benefit of a given noise mitigation technology, in the most realistic scenario. Examples of state–of–the–art wind turbine noise field measurements are the studies by Oerlemans et al. [10] and Luesutthiviboon [11].

1.0.1. AEROACOUSTIC EXPERIMENTAL MEASUREMENTS

Aeroacoustic experimental investigations are most frequently carried out using wind tunnel facilities. The aerodynamic conditions in a wind tunnel should be realistic or scalable to real field conditions [12]. Aerodynamic wind tunnel measurements aim at quantifying the aerodynamic response of the test model to the prescribed inflow parameters. Acoustic measurements are directed at investigating pressure fluctuations generated during the test. These relatively low-energy fluctuations propagate as waves, away from their source and towards the far–field. During aeroacoustic experiments, acoustic pressure fluctuations are typically recorded with microphone measurements [13].

Common examples of test objects in aeroacoustic studies are aircraft components, such as jet–engines [14], propellers [15] or landing gears [16]; and wind turbine components, such as their airfoil sections [17]. As noise mitigation technologies evolve, measuring the noise of improved test models in free-field or wind tunnel tests becomes more challenging, due to the lower noise of the model in comparison with the background noise during the test. Therefore, wind tunnel facilities must be designed (or adjusted) to achieve optimal aeroacoustic measurement capabilities.

Traditionally, there are two types of wind tunnel test sections used for aeroacoustic testing: open–jet and closed test sections. Closed test sections have the advantage of constraining the wind tunnel jet, leading to more controlled aerodynamic conditions. Open–jet test sections have less realistic conditions when the test model causes a strong jet–deflection. Jet-deflection can cause changes on a wing model's effective angle of attack of over 50 % [18]. The pressure distribution over a wing may also vary, depending on the ratio between jet width and frontal wetted area of the wing [18]. This second effect is more challenging to correct for [19]. Indeed, Sanders et al. [20] obtained a difference in pressure of close to 0.4 of the free-stream dynamic pressure, between the suction peak of an airfoil in an open-jet section and the reference values, for the same lift coefficient of the airfoil. In closed test section wind tunnels, the necessary aerodynamic corrections are smaller and more precise [20]. Closed test section wind tunnels have a superior aerodynamic fidelity [21].

On the other hand, open–jet test sections are more easily adapted for acoustic measurements, e.g., by applying acoustic liners to the walls [22]. Reflections on an unlined closed test section lead to acoustic interference [23]. Furthermore, background noise can be over 20 dB Hz^{-1} higher on a closed test section than on the open-jet configuration of the same aeroacoustic wind tunnel. This considerable background noise difference was recorded at low frequencies, close to 500 Hz, at the Aeroacoustic Wind Tunnel of the University of Twente [20].

Recent developments in hybrid test section design result in a compromise between completely closed and open–jet test sections, as both aerodynamic fidelity and acoustic fidelity are equally accounted for, in the design. Hybrid test sections make use of permeable walls to constrain the jet, leading to a considerably lower jet-deflection than in open-jet test sections [20]. However, closed sections remain the only test section class for which the boundaries of the wind tunnel jet are completely fixed in space. The permeable Kevlar walls of the 1.8 m by 1.8 m Virginia Tech Stability Wind Tunnel hybrid test section have been recorded to get displaced by 0.1 m, in their perpendicular direction, due to the pressure field of a 0.9 m NACA0012 airfoil at high angle of attack [19].

1.0.2. CHALLENGES WITH CLOSED−SECTION WIND TUNNEL AEROACOUSTIC TESTS

Several closed wind tunnel facilities are adapted for aeroacoustic measurements, e.g., the Deutsche WindGuard aeroacoustic tunnel at Bremerhaven [24, 25]. The main aeroacoustic wind tunnel design challenges originate from background noise sources, and from the test section's acoustic response, which, dominantly due to reflections, may be extremely different from a free–field response.

REDUCTION OF THE GENERATION OF BACKGROUND NOISE

Background noise contaminates acoustic measurements, leading to difficulties in separating this noise from aerodynamic noise sources of interest. This noise propagates acoustically through the wind tunnel circuit and can have different origins, e.g., aerodynamically generated noise, or the noise from electric devices, such as the wind tunnel motor [11]. Improving the aeroacoustic design of wind tunnel components which generate noise can significantly improve the acoustic quality of the facility [26].

By improving the design of wind tunnel fan blades, Neise et al. have been able to decrease the peaks of their tonal noise by up to 30 dB. Inside the empty test section, the background noise at the most affected 1/12-octave bands reduced by close to 10 dB, at 42 m s^{-1} free-stream velocity. This resulted in a reduction of the overall

A-weighted background noise inside the empty test section of 3 dB(A) [26].

MICROPHONE PLACEMENT

Turbulent pressure fluctuations in the boundary layer of the wind tunnel walls are also recorded by microphones, which is commonly referred to as hydrodynamic noise. A poorly placed microphone may record hydrodynamic noise orders of magnitude stronger than the acoustic signal from the aerodynamic noise source of interest. In open–jet or hybrid test sections, this problem is solved by placing the microphones outside the jet. However, this is not possible in closed test section wind tunnels. In closed wind tunnels, microphone arrays are usually mounted along the test section walls.

Placing wall mounted microphones inside cavities can lead to a strong reduction of the recorded hydrodynamic noise [27]. The objective of improving microphone placement in a wind tunnel consists not only in reducing hydrodynamic noise, but in effectively improving the signal to noise ratio of the measurements. The signal to noise ratio describes the relative strength of the acoustic source of interest, at the microphone location, with respect to the background noise strength. For cavity mounted microphones, this means that the cavity needs to minimise the propagation of hydrodynamic noise towards the microphone, while not decreasing the propagation of the acoustic signal from the source of interest [28, 29].

REFLECTION MITIGATION

For an acoustically untreated wind tunnel, reflections through the circuit lead to the propagation of spurious noise towards the test section, where microphone measurements are taken. This can lead, e.g., to the propagation of strong tonal noise from the wind tunnel fan to the acoustic measurement location [26, 30].

Additionally, reflections in the test section itself can lead to strong acoustic interference at the microphone location. This acoustic phenomenon can lead to deviations of more than 10 dB with respect to the direct (i.e. unreflected) noise signal [23]. A common solution to lessen this problem is to reduce the reflection coefficient of the test section walls by covering the walls with an acoustic liner [30]. The choice of liner in terms of material and thickness needs to be made taking into account the frequencies of interest for the aeroacoustic studies. The characteristics of the flow inside the test section should also be analysed, so that the liner does not disturb the aerodynamic fidelity of the tunnel. An excessively rough liner leads to a thicker and more turbulent boundary layer over the tunnel walls [31]. This contributes towards an increase in background noise generation, and

towards a reduction of the effective test section area. A smaller test section area would increase the aerodynamic blockage effect [32]. Wind tunnel liners need, therefore, to be designed with both the acoustic and aerodynamic impact in mind.

POST–PROCESSING (ALGORITHMS)

For an acoustic source in the free-field, measurements with an isolated microphone may be sufficient to completely characterise the sound emissions. In aeroacoustic studies [33], it is common practice to measure noise with a phased–microphone array. Simply adding the signals from all microphones already mitigates the error which originates from the occurrence of acoustic interference at the measurement location, assuming that this interference pattern varies along the several microphone positions. However, to best exploit the potential of phased–array measurements it is necessary to develop more advanced post–processing methods. Beamforming techniques allow for the usage of the microphones' phase information to distinguish between sound sources and to separate the noise of a given sound source from background noise [34]. In a closed environment, beamforming may also be used to distinguish a sound source from its reflections [35].

In practice, the benefits of each beamforming formulation are limited. The spatial resolution that allows the localisation of different sources in an experimental setup is finite. The increase in signal to noise ratio which can be achieved with beamforming is also dependent on the setup (e.g., number of microphones) and on the beamforming formulation used [34]. The development of new beamforming methods and of new computational tools for increasing the precision of acoustic experimental results needs therefore to be a continuous effort.

1.0.3. RESEARCH OBJECTIVES AND OUTLINE

There are many challenges associated with performing successful aeroacoustic experimental studies. An experimental aeroacoustic test can be considered successful when it is possible to achieve controlled and well characterised aerodynamic conditions for the test object, to perform reliable acoustic measurements, and to obtain a precise quantification of the test object's noise emissions. For wind tunnel experimental investigations, closed test section wind tunnels provide the most reliable aerodynamic conditions. This thesis has the goal of improving the reliability of acoustic data measured in acoustically disturbed environments, with particular focus on data obtained with closed test section wind tunnels. This is achieved by reducing sources of error in the measurement of acoustic pressure fluctuations and by improving the post-processing of the experimental data.

It is interesting to note that aeroacoustic experimental studies may also be carried out without the direct measurement of pressure fluctuations. An example is the measurement of density gradients in the flow, with the Schlieren technique [36, 37]. However, these types of measurements are outside the scope of this thesis.

Following from the previous discussion, the research objective can be divided into the following sub–objectives:

- **Microphone cavity design**: the goal is to understand how wind tunnel microphone cavities should be designed. This requires a complete understanding of the aerodynamic and acoustic phenomena that occur in these cavities when grazed by a turbulent boundary layer. The investigation is carried out by simulating microphone cavities with a high–fidelity numerical solver, based on the Lattice–Boltzmann method.

- **Wall liners for acoustic absorption**: the goal is to provide recommendations on how to best choose the material to line a wind tunnel wall. To achieve this, the impact of lining a wall on the aerodynamic and acoustic characteristics of the wind tunnel test is evaluated. The liners investigated are characterised based on their viscous resistivity, inertial resistivity and roughness. The study makes use of wind tunnel experiments with a simplified single wall setup, in an open-jet anechoic wind tunnel test section.

- **Lining a segment of the circuit**: the goal is to investigate the benefit of lining exclusively a small portion of the wind tunnel circuit. It is investigated how lining the test section influences reverberation through the circuit, background noise at the measurement location, and reflections from a source placed inside the test section. The study is based on experimental tests performed at a closed test section wind tunnel, where the test section was installed in lined and unlined configurations.

- **Modelling the wind tunnel acoustic response**: the end goal is to improve the post-processing of acoustic data recorded in environments where acoustic interference caused by reflections is a dominant phenomenon. This is the case in closed wind tunnel test sections. The improved post-processing is based on the usage of a more precise propagation function. The propagation function of a closed test section is determined by modelling its acoustic response with a numerical acoustic solver. The acoustic modelling is validated against wind tunnel experiments.

With these objectives in mind, the dissertation is structured as follows. The theoretical background that supports the research done in this work

is presented in Chapter 2, along with the state–of–the–art research in the field of wind tunnel aeroacoustic testing.

The methodology employed in the research is described in Chapter 3. This chapter describes the experimental approach, including the facilities and the measurement techniques used. The computational approach is also described. Subsequently, this chapter describes the post–processing techniques used.

The research of the aerodynamic and acoustic response of cavities for microphone placement is presented in chapter 4. The numerical Lattice–Boltzmann method assesses the performance of cavities with varying geometries, when grazed by a turbulent boundary layer. The performance of each cavity is analysed in an uncovered and covered setup. Permeable cloth cavity covers had been shown to improve the signal to noise ratio of acoustic measurements in a wind tunnel. However, prior to this research, the understanding of the physical phenomena that primarily influence the response of covered cavities was very limited.

The resistivities and the roughness of sound absorbing wall liners is varied, and tested experimentally. The aerodynamic response of these liners to a grazing turbulent boundary layer is analysed. The improvement in the acoustic measurement of a point source placed in front of a wall, when this wall is lined, is quantified. The acoustic measurements are obtained from tests with and without flow in the test section. The results are presented and discussed in Chapter 5. The best liner is used to treat the walls of a closed–section wind tunnel at TU Delft, the Low Turbulence Tunnel (LTT). The benefits of lining the test section of this tunnel are explored in Chapter 6.

Although lining a wind tunnel test section results in a strong mitigation of reflections, it is found to be extremely challenging to achieve free–field conditions inside the facility. Modelling the acoustic response of a closed wind tunnel makes it possible to correct the results, by improving the post–processing of the microphone array data. FEM simulations are used to predict the sound propagation in a closed test section, for both lined and baseline (unlined) test section configurations. These FEM results are presented in Chapter 7, along with the approach suggested for using FEM acoustic modelling to improve the post–processing of the measured microphone signals. This approach is successfully validated with experimental data.

Chapter 8 summarizes the main findings of this research. The findings are used as basis for recommendations of future research, so that acoustically disturbed environments, such as closed test section wind tunnels, may become fully reliable for aeroacoustic testing.

2

THEORETICAL BACKGROUND

The idealized condition for performing acoustic measurements is the free–field. This means that the acoustic pressure fluctuations are measured by microphones placed outside the flow, in a quiescent fluid region. It is also ideal to perform these acoustic measurements with the microphones placed in a location where sound reflections do not reach, and background noise is relatively low, so that the sound waves radiated by the test object are the dominant source of pressure fluctuations at the measurement points. A free–field test setup is sketched in Fig. 2.1. When the measurement is performed in free–field conditions, it can be assumed that the sound propagation from the source to a measurement point, at distance r, follows:

$$g_{(\text{free–field})} = \frac{\exp\left(-2\pi i f \Delta t\right)}{r}, \tag{2.1}$$

where c is the speed of sound and $\Delta t = r/c$ is the sound propagation time. $2\pi f \Delta t$ is the phase change for a sound wave of frequency f during its propagation. $g_{(\text{free–field})}$ is therefore the Green's function of sound propagation of a spherical wave, in undisturbed conditions.

However, aeroacoustic studies often rely on acoustic measurements recorded in non–ideal conditions. When the environment contains walls or objects which alter the propagation of sound with respect to free–field conditions, this is named an acoustically disturbed environment. Closed test section wind tunnels, besides modifying the propagation of the sound radiated from a test object, also contain potentially strong sources of background noise [22]. This chapter provides the necessary theoretical background for understanding the challenges with wind tunnel aeroacoustic tests, and how these have been tackled in previous literature.

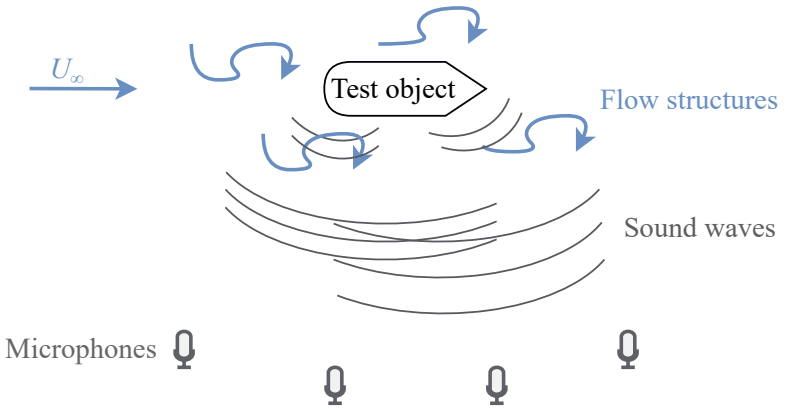

Figure 2.1: Sketch of idealized free–field microphone measurements.

2.1. ACOUSTICALLY DISTURBED ENVIRONMENTS

This section discusses the acoustic phenomena which disturb the propagation of sound in wind tunnels, particularly for facilities non–optimized for aeroacoustic testing. Solid walls or objects in the facility cause sound reflections and diffraction. The interaction between the flow and sound waves also disturb their propagation. The flow conditions may lead to the convection of sound and to an increased dissipation (i.e., loss of sound transmission). The phenomena introduced in this section leads to a modification of the Green's function of sound propagation with respect to the free–field case (eq. 2.1).

2.1.1. REFLECTIONS

The study of acoustic reflections is inherently part of the design of facilities designed for optimum acoustic performance. This assessment is done in the design of anechoic rooms [38], concert halls [39] or wind tunnels [23]. The study of reflections is important in room acoustics because reflections lead to acoustic interference, e.g., with a direct (non–reflected) sound wave. The acoustic interference between a direct sound wave and its reflections is constructive or destructive [40], depending on the wavelength and the geometry of the room. When occurring at a measurement point, constructive and destructive acoustic interference can cause, respectively, the overprediction or the underprediction of source noise levels by over 10 dB [23]. Furthermore, reflections in an enclosed space cause reverberation. Reverberation is the prolongation of sound in the room after a sound source has stopped emitting noise. The reverberation time T_{20} is the time required for sound to decrease by 20 dB. A room's reverberation time can be estimated with Sabine's equation [41]:

$$T_{20} = \frac{0.161V}{3\sum_{i=1}^{n} S_i \alpha_i}, \tag{2.2}$$

where V is the volume of the room, n is the number of absorbing surfaces, S_i is the area of each wall and α_i is its absorption coefficient.

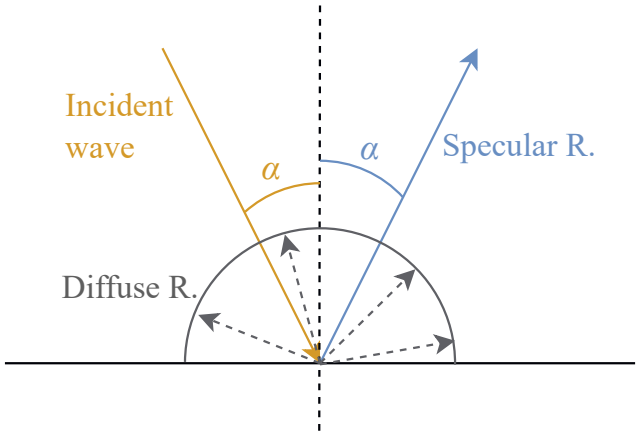

Figure 2.2: Sketch of specular and diffuse reflections.

Reflections on solid boundaries can be divided into specular and diffuse [42]. In specular reflections, the reflection angle is equal to the angle between the incoming sound wave and the wall. Diffuse reflections propagate in all directions, from the reflection point. These phenomena can be visualised in Fig. 2.2. For a flat and smooth surface, all reflections are specular. In fact, the roughness of a solid surface is an important parameter for predicting the percentage of acoustic energy reflected with a specular path, or as a diffuse reflection [42]. The irregularities in the surface should be analysed with respect to the wavelength of the incident waves, as irregularities much smaller than the wavelength have a negligible effect on the reflection path. Irregularities much larger than the wavelength should be considered as curved surfaces, in case the reflection path is to be predicted.

The scattering coefficient is the ratio of diffuse reflections' energy to the total reflected acoustic energy [42]. A scattering coefficient of 0 means that purely specular reflections occur. Vorländer and Mommerz measured this coefficient experimentally, for different combinations of rough surfaces and sound wavelengths [43]. For a surface roughness consistent of hemicylinders, the scattering coefficient has been found to approximately vary from 0.1 to 0.8 when the ratio of the hemicylinder's diameter to the sound wavelength increases from 0.1 to 1.4.

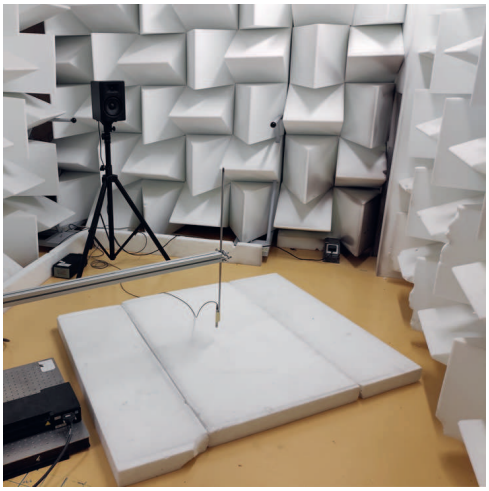

Figure 2.3: Experimental characterization of the sound absorbing properties of a wall liner [44].

Reflections can be dampened by applying treatments to the surfaces. A common approach is to line surfaces with sound absorbing materials, such as melamine foam. When a sound wave enters these highly porous materials, friction between the fluid and the material's fibres causes the acoustic energy to dissipate into heat, i.e., via viscous dissipation [45]. The viscous resistivity is a key parameter for predicting sound absorbing performance of a porous material [46]. The thickness of the liner, with respect to sound wavelength, is also an important parameter. Figure 2.3 shows the testing of a flat porous liner, with respect to the absorption of sound waves at oblique incidence angles. It is relevant to notice that the walls of the room in Fig. 2.3 are lined with wedged foam, to improve the performance of the room for acoustic testing, i.e., to reduce reflections in the room. Wedged liners have been found to lead to a higher absorption than flat liners, for constant liner depth and porous material [38, 47]. However, for many practical applications, it can be more convenient to line solid surfaces with flat liners, e.g., when these liners are expected to be in contact with the flow.

2.1.2. DIFFRACTION

When sound waves reach a solid obstacle or an opening between obstacles, they propagate to regions for which there is no direct or reflected path, from their source. Such physical problem can be described through the solution of the Helmholtz wave equation of sound propagation (Eq. 3.7), considering that the spatial gradient of pressure at the walls of the obstacle(s) is zero in their wall normal direction [48].

The difference between the resultant sound field and the geometric acoustic field (i.e. the sound field which includes the direct and reflected waves) is referred to as the diffracted wave field [48].

Figure 2.4 shows an illustration of sound diffraction around a barrier. Solving the Helmholtz wave equation in the presence of a wedge barrier gives that the complex pressure fluctuation of the diffracted wave, $\hat{p}_{\text{diff}}$, is approximately [48]:

$$\hat{p}_{\text{diff}} = \frac{\hat{S}}{2\beta_{\text{wedge}}} \left(\frac{2\pi}{kL_{\text{edge}} r_r r_s} \right)^{1/2} e^{i(kL_{\text{edge}} + \pi/4)} D_v(\phi_r, \phi_S), \tag{2.3}$$

where $\hat{S}$ is the complex pressure fluctuation at the monopole point source, $2\pi - \beta_{\text{wedge}}$ is the wedge angle, r_s is the shortest distance from the point source to the edge of the barrier, and r_r is the shortest distance from the receiver to the edge of the barrier. $D_v(\phi_r, \phi_S)$ is a function dependent on the angle between the barrier and the receiver, ϕ_r, and on the angle between the barrier and the source, ϕ_s. k is the sound wavenumber and L_{edge} is the shortest distance from the source to the edge of the barrier and then to the receiver.

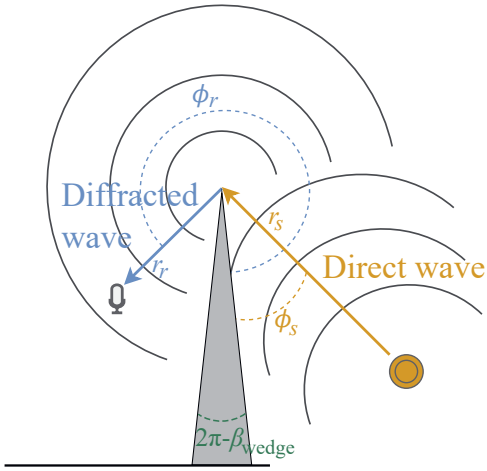

Figure 2.4: Sketch of sound diffraction around a wedge barrier.

In Fig. 2.4, it is clear that the receiver would be in a shadow region, in case the waves would propagate as rays. Equation 2.3 shows that the phase variation of the diffracted wave is proportional to kL_{edge}. Thus, the diffracted wavefronts have a constant L_{edge}. Indeed, diffraction is commonly perceived as the bending of waves around an opening or an obstacle [49]. Diffraction around an infinitely thin edge may also be

understood as the scattering of waves by this edge, when reached by sound waves [50].

Acoustic diffraction is a phenomenon of critical importance for many applications. These include room and building acoustics, as well as the study of the propagation of noise in public areas [51]. This phenomenon is also expected to play an important role in the acoustic behaviour of facilities designed for aeroacoustic experimental testing.

2.1.3. SOUND CONVECTION AND REFRACTION

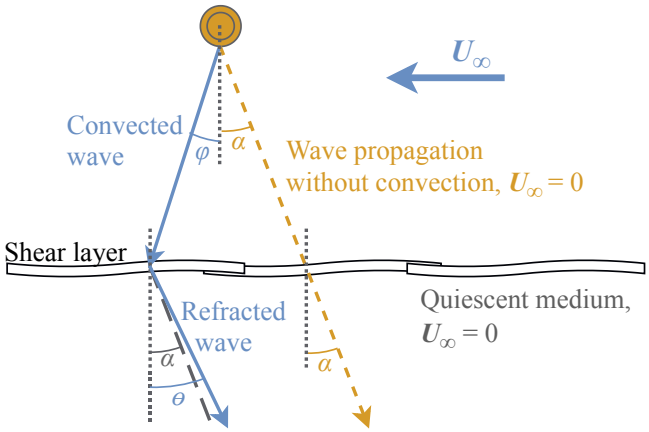

Figure 2.5: Sketch of sound convection by the mean flow and refraction at the shear layer.

When propagating through a fluid, sound waves are convected by the local flow velocity [52]. This means that the propagation velocity of the sound wave, at each point of the wavefront is given by $\vec{v}_{\text{soundwave}} = \vec{c} + \vec{u}$, where $\vec{u}$ is the local flow velocity. $\vec{c}$ is the velocity of propagation of the sound wave, at that point of the wavefront, considering the wave to be propagating in a quiescent medium. When a sound wave propagates through a shear layer between a moving fluid and a fluid with zero mean velocity, its direction of propagation appears to change, as represented in Fig. 2.5. In addition to the sound not being convected in a quiescent fluid, waves experience refraction when passing through a shear layer [53]. This phenomenon further changes the propagation direction of a sound wave.

Sound convection and refraction are important phenomena to be taken into account for many aeroacoustics applications, including experimental wind tunnel investigations [54] and atmospheric sound

propagation models [55]. For acoustic studies in open–jet wind tunnels, the relation between the angles φ and θ (as defined in Fig. 2.5) can be found with the analytical model derived in Ref. [56].

2.1.4. TRANSMISSION LOSS

When a sound wave propagates through an obstacle, it is expected for this wave to experience a transmission loss, i.e., the transmitted wave is likely to have less acoustic energy than the incident wave. The obstacle may be a solid medium, a porous material, or a shear layer, as depicted in Fig. 2.5. In aeroacoustic testing, the transmission loss in a shear layer may be a critical phenomenon, particularly for experiments at a high free–stream Mach number (M_∞). The transmission loss trough a shear layer, e.g. in a open–jet wind tunnel, is caused not only by partial dissipation of the sound wave which is being transmitted, but also by partial reflection of the incident wave [53].

Devenport et al. [57] characterised the transmission loss of sound waves transmitted through a Kevlar cloth, commonly used in aeroacoustic testing, and through shear layers, in this case the boundary layer of wind tunnels walls. Results are shown in Fig. 2.6. The transmission loss through a boundary layer shows a strong dependence on free–stream velocity. For $U_\infty \geq 36\,\mathrm{m\,s^{-1}}$, the transmission loss through a shear layer should be taken into account, when analysing results at high frequencies. The transmission loss through the Kevlar cloth starts being non–negligible from 6 kHz.

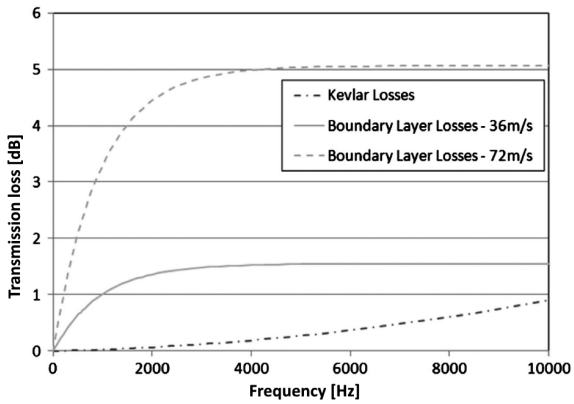

Figure 2.6: Transmission loss when a sound wave propagates through a Kevlar cloth and through a boundary layer, when the free–stream velocity of the flow is $U_\infty = 36\,\mathrm{m\,s^{-1}}$ and $U_\infty = 72\,\mathrm{m\,s^{-1}}$. Adapted from [57].

Fischer et al. [58] studied the influence of the pressure difference

through a Kevlar membrane on the acoustic transmission loss of sound waves passing through it. At $U_\infty \geq 33\,\mathrm{m\,s^{-1}}$, deflecting an airfoil by 4° (inside a Kevlar-walled wind tunnel test section) caused a frequency dependent shift in the Kevlar's transmission loss of up to 1 dB. This effect increases with U_∞ (due to increasing pressure gradients).

2.2. BACKGROUND NOISE IN A WIND TUNNEL

2.2.1. ACOUSTIC NOISE SOURCES

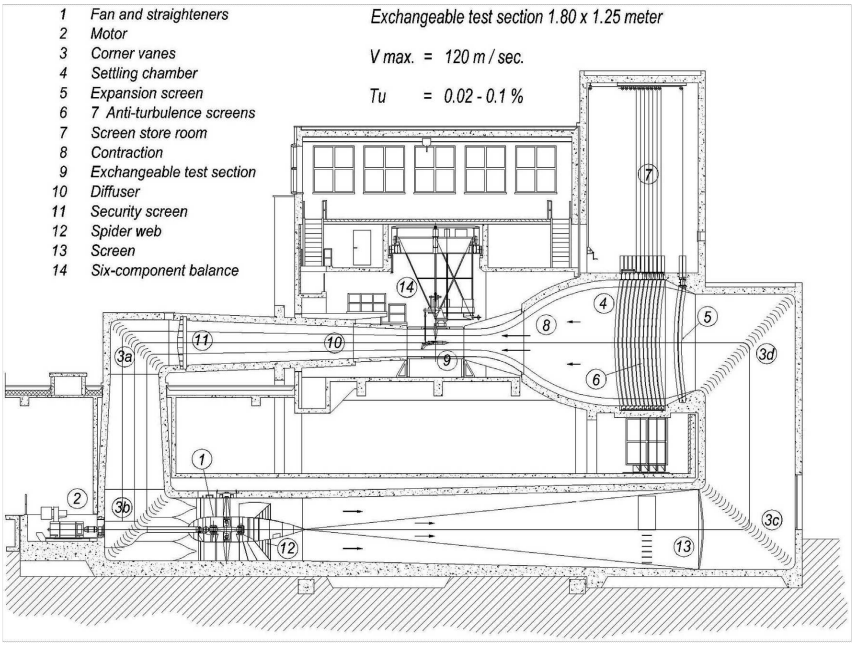

Figure 2.7: Low Turbulence Tunnel circuit [59], at Delft University of Technology.

Spurious sound waves present during a wind tunnel test are predominantly of aerodynamic origin, e.g., originating from the unsteady interaction between the flow in a wind tunnel and components of the circuit [60]. Figure 2.7 shows the circuit of a closed loop closed test section wind tunnel at TU Delft, the Low Turbulence Tunnel (LTT). There are several possible sources of aerodynamic noise in in this type of wind tunnels, which reach the test section. The directivity characteristics of the noise emitted depends on the physical generation mechanism. This is important to identify, as the scaling of noise produced with free-stream Mach number also depends on how noise is being generated. The directivity of aerodynamically generated sound can be:

- Monopole: this occurs when a body moves, displacing fluid. The displacement of fluid particles causes the emission of sound, uniformly in all directions. This type of noise is also named thickness noise, as the volume of fluid displaced increases with the thickness of the moving body, increasing the magnitude of the sound waves produced. The power of the noise radiated scales with M_∞^2 [61].

- Dipole: the generation of sound with a dipole directivity occurs due to the unsteady interaction between a fluid flow and a solid boundary [52]. More specifically, due to variations in fluid pressure at the solid boundaries or due to the movement of a pressure field along with the movement of a solid body. The power of the noise radiated approximately scales with M_∞^6 [61].

- Quadrupole: this occurs when sound is produced by unsteady fluctuations in a fluid, without a direct contribution of a solid body towards the sound generation. A typical example is sound produced by free–stream turbulence. The power of the noise radiated scales with M_∞^8 [52].

These noise generation mechanisms can be associated with several components, in a wind tunnel circuit. It is important to identify these components, in order to understand how to mitigate the noise emissions. Common background noise sources in a wind tunnel are:

- Wind tunnel fan: as in Fig. 2.7, the fan that powers the flow in a wind tunnel is often placed opposite to the test section, within a closed wind tunnel circuit. However, the sound generated at the fan can still reach the test section, by propagating and reflecting through the circuit. Rotating components, as a wind tunnel fan, produce strong tonal noise at the blade passing frequency and subsequent harmonics (multiples of the blade passing frequency) [62]. This tonal noise has both monopole and dipole nature, and is present when the aeroacoustic problem is analysed from a non-rotating reference frame. The fan may also produce strong broadband noise [63], e.g., from the interaction of turbulence in the flow with the leading edge of the fan blades (dipole noise), or from the interaction between the turbulent boundary layer over the fan blades with the blades' trailing edge (dipole noise).

- Free-stream turbulence: the turbulent fluctuations in the wind tunnel jet also lead to the generation of noise, in this case with a quadrupole directivity [52]. This turbulence can be found in the wake of components of the wind tunnel circuit, such as the wind tunnel fan. This phenomenon is already mitigated by trying to improve the flow quality in the test section, as wind tunnels are

designed with turbulence screens, usually placed between the fan and the test section, for reducing free–stream turbulence intensity.

- Corner or guide vanes and safety screens: the interaction of turbulent structures with vanes or with security screens also leads to the generation of broadband dipole noise [60]. In the case of the LTT, it can be understood from Fig. 2.7 that turbulent fluctuations originating in the test section, due to the model being tested, are likely to impinge in the metal grid downstream of the diffuser (safety screen) and on the guide vanes immediately downstream. The leading edges of these components can become dominant sources of background noise in the test section. The corner vanes upstream of the test section, on the other hand, are typically located in a section of the circuit where the velocity of the flow is lower, due to the larger area [64]. These upstream corner vanes are therefore less likely to lead to the generation of strong background noise.
- Wind tunnel walls and discontinuities: the turbulent boundary layer over the walls of the tunnel also results in the radiation of noise. Smooth wall surfaces result in the mirroring of this quadrupole noise source [60]. On the other hand, discontinuities on the walls or on the setup are expected to contribute towards a considerable increase of noise generation. This is due to the interaction between these irregular solid boundaries and the turbulent structures in the wind tunnel boundary layer [65] (dipole noise).

Furthermore, in wind tunnel tests there may also be sources of background acoustic noise of non–aerodynamic nature [17]. These can be, for example, the motor that powers the wind tunnel fan, or electric devices used to operate the tunnel.

2.2.2. PSEUDO-SOUND IN TURBULENT BOUNDARY LAYERS

The turbulent pressure fluctuations which do not radiate as sound waves into the far-field may be referred to as pseudo-sound [66]. These fluctuations are recorded by microphones placed in the turbulent region, and their propagation is perceived to follow the local mean flow velocity [67]. This is because turbulent structures are convected by the local flow. In reality, pseudo-sound also propagates from its source at sound speed. Due to the fast decay with respect to distance, the pseudo-sound field is typically small enough that any time delay is negligible [66].

Pseudo-sound is relevant because, in a turbulent region, the amplitude of its pressure fluctuations is orders of magnitude higher than that of the sound waves being generated. In a subsonic jet flow, only 10^{-4} of the turbulent energy radiates as sound [66]. For high Mach number rocket flows, this ratio is still below 10^{-2}. Another interesting characteristic

of pseudo-sound is that its magnitude is mostly uninfluenced by compressibility. For this reason, broadband pseudo-sound is commonly referred to as hydrodynamic noise [66]. This is the case of turbulent pressure fluctuations in boundary layers, e.g. the turbulent boundary layer over wind tunnel test section walls [68, 69].

Microphone placement in a wind tunnel needs to be decided considering the presence of acoustic and hydrodynamic background noise. Furthermore, measurement devices should be as less intrusive as possible, in order to avoid disturbing the aerodynamic and acoustic testing conditions in the wind tunnel test section. Common solutions include the placement of microphones away from the jet, in open–jet or hybrid test sections (described in more detail in the following section). For closed test section wind tunnels, it is common to place the microphones at the wind tunnel walls. This type of acoustic measurements is non–intrusive, but may suffer from increased hydrodynamic spurious noise.

For the placement of wall mounted microphones, it is a common solution to try to recess the microphones with respect to the wind tunnel wall surfaces. This can be done, e.g., by recessing individual microphones in a cavity, or by placing a set of microphones in a recessed plate [68]. Prior research also indicates that covering a microphone cavity with a cloth helps to reduce hydrodynamic fluctuations at the microphone, while allowing for acoustic fluctuations from a test model to be measured [27]. Figure 2.8 is illustrative of a state–of–the art strategy for placing a microphone on a wind tunnel wall. Figure 2.9 shows a result from a previous study where the hydrodynamic noise at a wind tunnel wall was quantified, by a microphone installed at the wall surface, and by a microphone recessed at the bottom of a cylindrical cavity [68]. For this microphone cavity design, covering the recessed microphone with a mesh cloth resulted in a clear attenuation in the spectra of the hydrodynamic noise, at most frequencies investigated. At 2 kHz, the noise attenuation was close to 20 dB.

The acoustic transfer function of a microphone cavity is defined as the ratio between the magnitude of acoustic pressure fluctuations at the cavity bottom, and the magnitude of the incoming acoustic waves which enter from the top of the cavity. This transfer function is also an important research topic, as the cavity geometry may lead to the generation of strong acoustic modes inside the cavity. Ideally, these acoustic modes should be minimised, especially at the frequencies of interest. Otherwise, if the cavity's acoustic transfer function is not perfectly characterised, this will lead to experimental errors. Prior research shows that cavities with a conical shape, i.e., where the opening is larger than the bottom surface of the cavity, lead to optimum acoustic measurements [28]. Finding a cavity design which leads to an optimal compromise between its acoustic transfer function and the

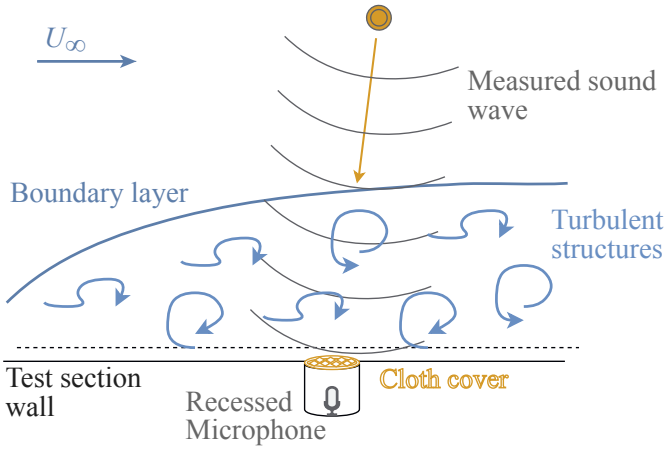

Figure 2.8: Sketch of a cavity designed for wind tunnel wall microphone placement.

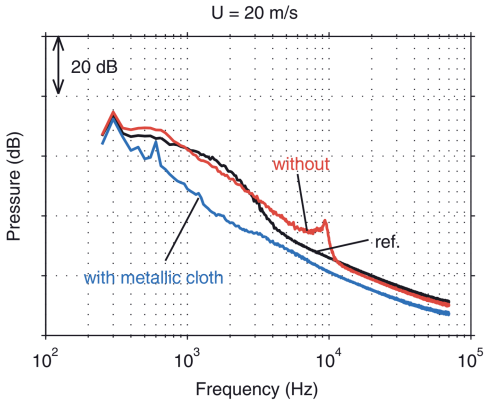

Figure 2.9: Hydrodynamic noise at the surface of a wind tunnel wall (reference), at the bottom of an uncovered cylindrical cavity, and at the bottom of a cylindrical cavity covered with a metallic cloth [68]. Free–stream velocity $U_\infty = 20\,\mathrm{m\,s^{-1}}$.

minimisation of hydrodynamic noise remains a topic of large interest.

2.3. ANECHOIC WIND TUNNEL DESIGN

Wind tunnels, when conceived for improved aeroacoustic testing, are designed with the challenges discussed in the previous two sections in mind. The facility is designed in order to cause the least disturbance possible to sound propagation in the test section, at the frequencies of

interest. The wind tunnel circuit is designed in order to lead to the least propagation of background noise towards the measurement locations in the test section. A commonly referred anechoic wind tunnel design goal is to reach a background noise at least 10 dB lower than the sound of any test object, at the measurement locations [22, 30, 60].

2.3.1. WIND TUNNEL CIRCUIT

As previously mentioned, there may be numerous sources of background aerodynamic noise through a wind tunnel circuit. These include the fan, the corner guide vanes, protection or turbulence mitigation screens and any discontinuities through the walls of the circuit. Gomes et al. [30], as shown in Fig. 2.10, suggest an approach for aeroacoustic wind tunnel design which distinguishes the airline circuit design (see first and second airline cross legs) from the design of the wind tunnel drive fan and of the test section (an anechoic open–jet section in the figure).

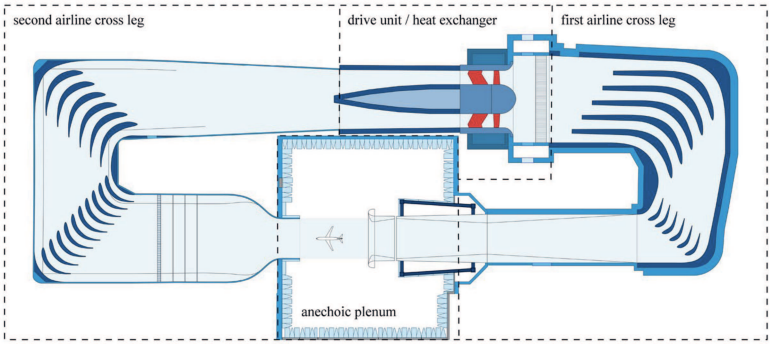

Figure 2.10: Sketch of the Low speed wind tunnel Braunschweig (NWB) of the German–Dutch Wind Tunnels Foundation (DNW) [30]. Dark blue areas correspond to acoustically treated surfaces).

Figure 2.10 shows that, in a state–of–the–art aeroacoustic wind tunnel, there are large areas of the circuit which are treated acoustically. These include airline walls, the corner vanes, the fan tail cone and the walls immediately downstream of the drive unit. The lining applied through the wind tunnel circuit helps to absorb sound waves, in order to avoid these waves from reaching the test section. However, acoustic treatments applied through the circuit should not lead to a poorer aerodynamic performance of the wind tunnel. If the pressure loss through the circuit were to increase, the drive fan would have to work at a higher power setting, in order for the same free–stream velocity to be reached in the test section [30]. As the wind tunnel fan may be one of the dominant sources of background noise, it is desirable to have this

component operating at lower rotational velocities and with minimum blade loading.

The noise from a wind tunnel drive fan can be expected to scale with the 5^{th} power of the flow velocity, with respect to each blade section [70]. This explains why reducing the rotational velocity of the fan is crucial for reducing background noise. For achieving the necessary static pressure increase at the fan, while reducing fan velocity, it is recommended to use state–of–the–art aerodynamic design tools, such as Computational Fluid Dynamics (CFD) [30]. Possible practical solutions may be to increase the solidity of the fan, either by increasing the number of blades or the blade chord.

For a rotor–stator configuration of the drive unit, additional sound sources are added at the stator stage [30]. These are mainly caused by strong variations of loading at the stator, due to the non–uniform inflow, and due to the impingement of turbulent eddies on the leading edge of the stator blades. These noise sources can be reduced by increasing the distance between the rotor and the stator, so the stator's inflow becomes more uniform. However, a too large distance may result in an aerodynamic penalty. Adding sweep to the blades may also reduce tonal noise generation at the stator stage [71].

Besides the targeted aeroacoustic design of the drive unit, also the corner guide vanes may be adapted. The corner vanes seen in Fig. 2.10 are longer than typical corner vanes designed exclusively for aerodynamic performance (compare, e.g., with vanes in Fig. 2.7). The reason is that aeroacoustic wind tunnel guide vanes should be designed with space for acoustic treatments, while not decreasing their aerodynamic performance, i.e., while successfully causing the mean flow to turn, without an increase in drag. The noise generated by the turning vanes upstream of the test section also decreases when the contraction ratio is increased, at the contraction stage. This causes the flow upstream of the contraction to reach lower velocities, due to the increased section area of the second airline cross leg of the circuit.

2.3.2. TEST SECTION

The test section design is key for the aeroacoustic testing capability of a wind tunnel. Open–jet test sections provide the most flexibility for improving the acoustic performance. Closed test section wind tunnels are typically able to provide the highest aerodynamic fidelity [72]. Hybrid wind tunnels attempt to achieve the benefits of both open–jet and closed–section wind tunnels [73].

OPEN–JET

In the test section of an open–jet circuit, the jet of the tunnel is not closely surrounded by walls. Instead, the jet is surrounded by a

quasi–quiescent fluid, which typically occupies most of the test section space. The main acoustic advantage of open–jet sections is that the test section walls, not being grazed by high–velocity flow, may be treated with highly absorbent liners. This lining possibility has allowed TU Delft's anechoic open-jet test section to reach a reverberation time T_{60} of 0.22 s, which is considered *acoustically dead*, i.e. anechoic, by the ISO norm 3382 [22]. The possibility to install free–field microphones outside the moving flow, relatively far from spurious hydrodynamic noise, is also an important upside of these test sections [22]. The out–of–stream background noise, in an anechoic open-jet test section, may reach a 25 dB noise reduction with respect to the in–airstream spurious noise [33].

Figure 2.11 shows the anechoic chamber of the DNW–NWB wind tunnel. As discussed in Sec. 2.1.1, wedged liners are able to provide a higher sound absorption than flat configurations, and are for this reason applied to the DNW–NWB test section, outside the flow. Open–jet test sections are designed with a large collector, as seen in Fig. 2.11, where the jet and shear layer enter the remaining closed sections of the wind tunnel loop. A collector with dimensions lower than the shear layer width could lead to a strong generation of noise, at the collector lips, besides leading to a decreased aerodynamic efficiency of the tunnel. Figure 2.10 also illustrates the large area of the collector, with respect to the jet nozzle area.

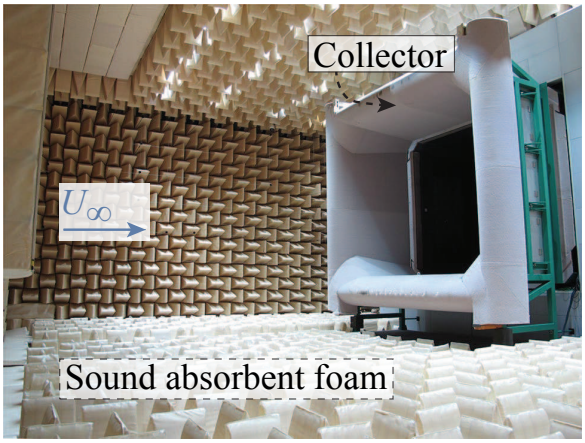

Figure 2.11: Anechoic test section of the DNW–NWB wind tunnel, in Braunschweig. Adapted from [30].

Similarly to the DNW-NWB wind tunnel, the Audi open-jet wind tunnel has also been designed with the goal of maximising acoustic performance. The main efforts include the design of the wind tunnel fan, with an increased number of fan blades for decreased fan noise;

a high contraction ratio from the settling chamber to the test section, to decrease flow velocities and, consequently, noise generation in the settling chamber; the application of sound absorbing lining in the test section walls and throughout the circuit; and the reduction of low frequency noise associated with pulsation of the jet, by improving the design of the collector and by active noise control of the sound field. By using a loudspeaker to emit sound waves in antiphase which respect to the phase of jet pulsation, it was possible to reduce the pressure fluctuations associated with this pulsation by 20 dB, and to completely eliminate the associated velocity fluctuations [74, 75]. The advanced acoustic features of this wind tunnel lead to a reduced background noise in the test section, with an overall sound pressure level 30 dB(A) lower than a comparable aerodynamic wind tunnel and 15 dB(A) lower than a previous generation of automotive aeroacoustic wind tunnels [30, 74].

The main disadvantages of open–jet test sections are associated with their aerodynamic behaviour. When a test model experiences strong lift forces, or any strong aerodynamic forces with a direction is perpendicular to the jet axis, this leads to a deflection of the jet. This reduces the effective angle of attack perceived by the test model. For an airfoil placed in an open-jet section, its effective angle of attack (in radians) can be estimated from [76]:

$$\alpha_{\text{eff.}} = \alpha_{\text{meas.}} - \frac{\sqrt{3\sigma}}{\pi} c_{l\,\text{meas.}} - \frac{2\,\sigma}{\pi} c_{l\,\text{meas.}} - \frac{\sigma}{\pi}\left(4\, c_{m\frac{1}{4}\,\text{meas.}}\right), \tag{2.4}$$

where

$$\sigma = (\pi^2/48)(c/h)^2, \tag{2.5}$$

being c is the airfoil chord and h the vertical open-jet dimension, considering that the wing span is aligned with the horizontal direction. The subscript meas. stands for the values measured during the test. α is the angle of attack, c_l is the sectional lift coefficient, and $c_{m\frac{1}{4}}$ is the quarter chord moment coefficient. The correction of Eq. 2.6 considers $c_{l\,\text{eff.}} = c_{l\,\text{meas.}}$.

Sanders et al. [20] tested a DU97W300 cambered airfoil with 0.25 m chord in an open-jet test section with $h = 0.9\,\text{m}$. At $U_\infty = 55\,\text{m}\,\text{s}^{-1}$ and $c_{l\,\text{meas.}} = 1$, this led to a correction $\alpha_{\text{eff.}} - \alpha_{\text{meas.}} \approx -4^\circ$, according to Eq. 2.6. In comparison, testing this airfoil in a closed test section with the same height led to $\alpha_{\text{eff.}} - \alpha_{\text{meas.}} \approx 0^\circ$, at the same free-stream velocity and airfoil sectional lift coefficient. This highlights the need to accurately correct the operating conditions in open-jet facilities.

Besides leading to a change in effective angle of attack, jet deflection also leads to a change in effective camber line of the airfoil [76]. This causes the pressure distribution over the airfoil to be different than in

free-field conditions, even if the angle of attack correction is accounted for. Moreau et al. [18] also studied the effect of jet deflection on the pressure distribution over an airfoil and concluded that, at $c/h = 1$, the airfoil pressure distrubtion resembles more the distribution of a cascade airfoil than that of an isolated one.

CLOSED–SECTION

Closed test section wind tunnels are commonly preferred for aerodynamics research, due to their high aerodynamic fidelity. As the wind tunnel jet remains always bounded by walls, the jet does not experience deflection or interaction with a collector. Instead, the wind tunnel walls cause a blockage effect which, for example, increases the lift experienced by a wing at a high angle of attack [32]. However, blockage in a closed section alters the aerodynamic behaviour of a test model considerably less than jet-deflection in an open-jet experiment. In a closed section wind tunnel, the angle of attack of an airfoil (in radians) can be corrected with [20, 77]:

$$\alpha_{\text{eff.}} = \alpha_{\text{meas.}} + \frac{57.3\sigma}{360}\left(c_{l\,\text{meas.}} + 4\,c_{m\frac{1}{4}\,\text{meas.}}\right), \tag{2.6}$$

which leads to a considerable smaller difference $\alpha_{\text{eff.}} - \alpha_{\text{meas.}}$ than Eq. 2.6. According to Barlow et al. [77], if $c/h < 0.7$, any wall blockage effects on the lift distribution can be neglected.

Figure 2.12 shows the airframe of a model aircraft being tested at DNW–LST wind tunnel. A microphone array is mounted on the wind tunnel wall, aligned in the streamwise direction with a potential noise source of the model, the aircraft wing. As mentioned in Sec. 2.2.2, wall–mounted microphones are expected to record high levels of hydrodynamic background noise, which is a main disadvantage of closed test section facilities for aeroacoustic studies.

The closed test section configuration seen in Fig. 2.12 has solid, fully reflective walls. This is expected to cause a strong disturbance to the propagation of sound in the test section, as sound waves generated by the test model have multiple reflection paths towards the array. The phenomenon causes the Green's function of sound propagation in a closed test section to largely deviate from the Green's function in free–field conditions (Eq. 2.1). Correctly estimating source noise levels from measurements in highly reflective environments therefore requires the extra (non–trivial) work of estimating the exact acoustic transfer function from a source to the microphones.

In contrast with the open–jet test section seen in Fig. 2.11 the lack of wall lining in the test section of Fig. 2.12 is expected to cause background noise to easily propagate through the test section, with minimal dampening. As it is not feasible to line closed sections of a

wind tunnel with foam cones, it is more difficult to reduce the reflection coefficient of these walls to optimum values (close to 0). This means that reverberation and, consequently, acoustic background noise are expected to be higher in closed test section wind tunnels.

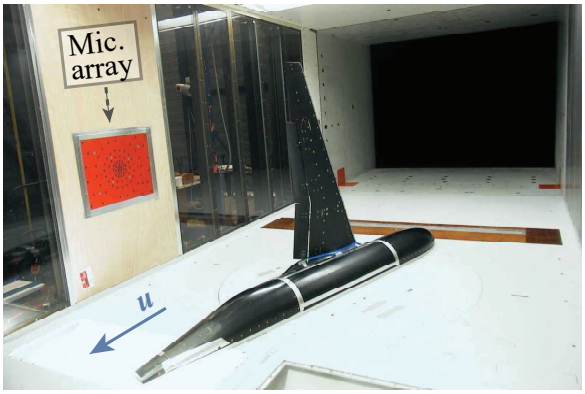

Figure 2.12: Closed test section aeroacoustic testing of an aircraft model, at DNW–LST wind tunnel. Adapted from [78].

HYBRID TEST SECTION

Hybrid wind tunnel test sections are designed to make use of the advantages of both closed and open–jet test sections [61, 79]. This leads to reduced aerodynamic corrections (compared to open-jet tunnels) and relatively low background noise in the acoustic measurements [80]. Figure 2.13 shows the hybrid anechoic test section at Virginia Tech. The side walls of the rectangular test section have been replaced by Kevlar windows (see Fig. 2.13a). These hybrid walls are designed to allow sound to be transmitted, while keeping the wind tunnel jet bounded, i.e., in order to avoid jet deflection [79]. The measurement device (microphone array) may in this way be placed outside the jet, where hydrodynamic pressure fluctuations are lower, as in an open–jet wind tunnel. Figure 2.13b shows two anechoic chambers, one at each side of the test section. The walls at these rooms are lined with sound absorbing wedged foam, which absorbs background noise and reflections from the test model.

Hybrid test sections, however, also have drawbacks. Precisely predicting the aerodynamic behaviour of a test section bounded by Kevlar walls is more complex than for closed sections. In a hybrid test section, wall blockage is usually reduced by the flow outside the Kevlar panels [19]. In the facility of Fig. 2.13, this is caused by interaction, or leakage, between the flow of the two lined chambers [69]. On the other hand, the pressure field around a high lifting model causes

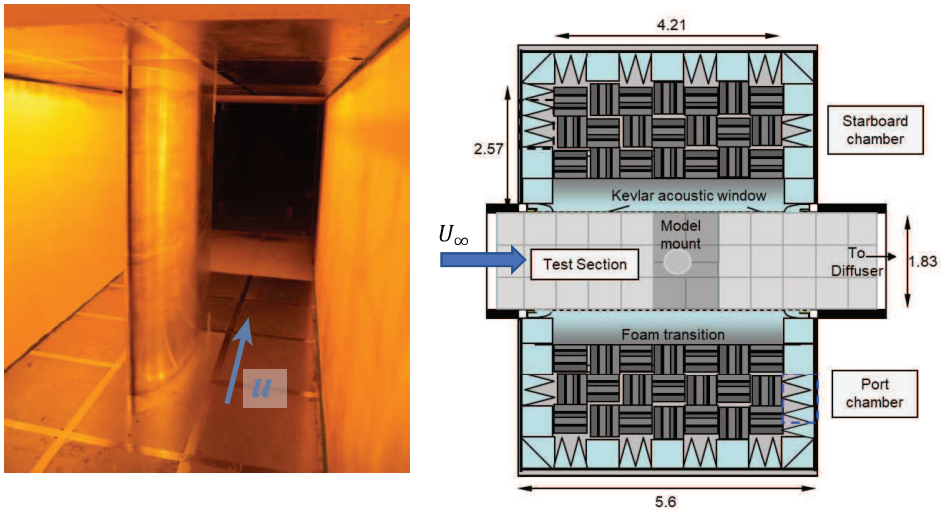

(a) Hybrid test section (b) Sketch of the anechoic chamber

Figure 2.13: Hybrid anechoic test section at Virginia Tech Stability wind tunnel (VTSWT) [69].

a displacement of the Kevlar sheets, which reduces the test section size. This second phenomenon increases wall blockage. Brown et al. [19] estimated the streamwise velocity increase due to blockage in the hybrid test section of the VTSWT, during the testing of a 0.91 m chord NACA0012 airfoil. The experiments were carried at $M_\infty = 0.2$ and at the chord based Reynolds number $Re_c = 4 \times 10^6$. The open area of the Kevlar fabric was used to characterise its porosity. For the Kevlar panels with an open area of 1.2 %, the streamwise velocity increase due to blockage varies between 2 % and 4 % of U_∞, depending on the airfoil's angle of attack. In comparison, the streamwise velocity increase at a closed section of the same dimensions would be approximately 1 % of U_∞, independently of α.

Additionally, when a model is tested at high lift, transpiration through the Kevlar panels is associated with a negative transverse velocity component in the test section. This contributes towards a decrease of the model's free-stream angle of attack. This phenomenon opposes the angle of attack deviation due to an increased blockage. For the Kevlar fabric with 1.2 % open area, the NACA0012 experiences an effective increase in angle of attack of 0.2° and an increase in maximum lift coefficient of $0.13C_{l,\max.}$ [19]. Instead, a Kevlar fabric with 5.9 % open area led to $\alpha_{\text{eff.}} - \alpha_{\text{meas.}} \approx 0.1°$ and to an increase in maximum lift by $0.07C_{l,\max.}$ [19]. This shows the influence of Kevlar porosity and permeability on the test. A comparable NACA0012 airfoil test in an

open-jet section leads to angle of attack corrections of over 7° [19]. Independently of the characteristics of the Kevlar fabric selected, the aerodynamic interference between a model and the testing facility is considerably lower in a hybrid test section than in an open-jet section.

Although Kevlar windows allow for a high transmission of sound, there is also a percentage of the incident acoustic energy which is either reflected or dissipated, as discussed in Sec. 2.1.4. In addition, it may not be possible to design a perfectly anechoic hybrid test section (see, e.g., floor and ceiling in Fig. 2.13a). This means that acoustic propagation in hybrid test sections is still different from the free–field. Aeroacoustic investigations carried out in hybrid test sections therefore also benefit from continuous improvements in the fields of acoustic modelling and signal processing.

3

METHODOLOGY

Measure what is measurable, and make measurable what is not so.

Galileo Galilei

The previous two chapters presented the challenges of aeroacoustic wind tunnel measurements. The physical phenomena associated with those challenges were introduced. The present chapter explains the methodology followed in order to tackle these challenges and improve wind tunnel experiments, particularly for the case of closed test section wind tunnels.

The improvements to aeroacoustic testing proposed in this work were validated experimentally, in wind tunnels at TU Delft. Section 3.1 describes the wind tunnels and measurement techniques used. The propagation of sound in wind tunnels may be disturbed by undesirable acoustic phenomena, as discussed in Sec. 2.1. A prediction of these phenomena was attempted with a geometric modelling method, which is described in Sec. 3.2, and with a higher fidelity numerical method. The problem of hydrodynamic noise propagation towards measurement points, introduced in Sec. 2.2.2, was also investigated making use of a numerical solver. The numerical methods used in this thesis are described in Sec. 3.3. Finally, Sec. 3.4 describes the state–of–the–art methods of processing pressure fluctuation measurements which were used in this thesis.

3.1. EXPERIMENTAL

3.1.1. FACILITIES

The research results presented in this thesis are either based on or validated with experimental campaigns. These campaigns were carried at two different wind tunnels at Delft University of Technology: an open–jet wind tunnel and a closed section wind tunnel.

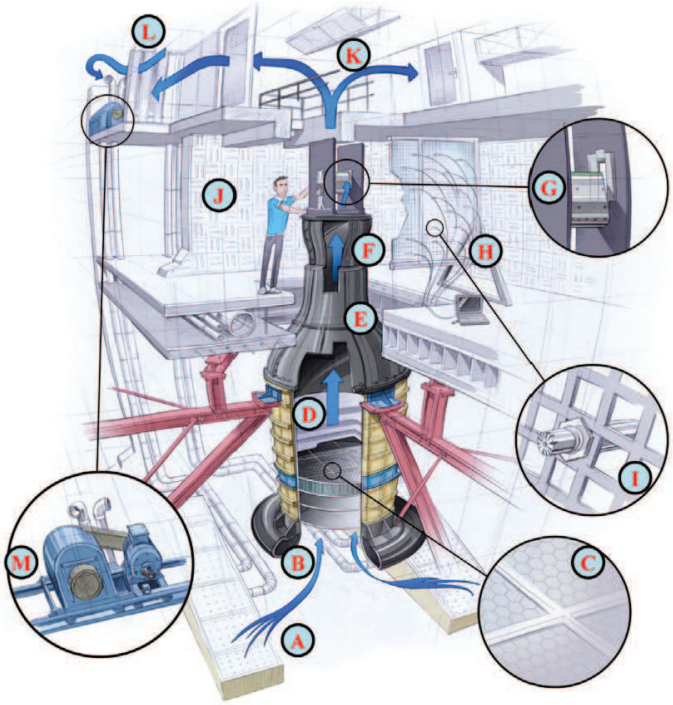

Figure 3.1: Sketch of the A–tunnel circuit [22].

ANECHOIC TUNNEL

The A–tunnel is the anechoic wind tunnel facility at TU Delft. This tunnel has a closed circuit, with a vertical open–jet test section. The facility was particularly designed for research in the aeroacoustics and flow–control fields [22]. Figure 3.1 shows the circuit of the anechoic tunnel. The circuit is powered by two centrifugal fans, each with 10 rotor blades. Each of the fans is connected to a 30 kW motor. As in the open–jet tunnels described in Sec. 2.3.2, the walls of the A-tunnel test section (see Ⓙ in Fig. 3.1) are lined with sound absorbing wedged foam, in this case melamine foam. This allows for accurate acoustic measurements in the test section from 200 Hz [22].

The interchangeable nozzle is located at Ⓕ. For the experiments carried in this thesis, a $40 \times 70\,\text{cm}$ nozzle was used. With this nozzle, the free-stream turbulence intensity is below 0.1 % of the free–stream velocity, U_∞, from $10\,\text{m}\,\text{s}^{-1}$ up to the maximum reachable velocity of $35\,\text{m}\,\text{s}^{-1}$ [22]. At the nozzle exit, the flow is uniform within this free-stream velocity range, with spanwise variations lower than $0.01U_\infty$ [22].

LOW TURBULENCE TUNNEL

The Low Turbulence Tunnel is a closed test section wind tunnel, initially designed for aerodynamic testing. The circuit is powered by a six-bladed wind tunnel fan, which is connected with a 525 kW DC motor. The flow in the test section of $1.8 \times 1.25\,\text{m}$ can reach free–stream velocities, U_∞, up to $80\,\text{m}\,\text{s}^{-1}$ with an average turbulence intensity, Tu, below 0.05 % [81]. The wind tunnel circuit has been previously shown in Fig. 2.7, along with a discussion of its possible background noise sources. As the tunnel has not been designed for aeroacoustic testing, reflections throughout the wind tunnel circuit contribute towards a long reverberation time.

Acoustic reflections at the LTT test section are dictated by its elongated octagonal shape, which can be seen in the computer-aided design (CAD) diagram reported in Fig. 3.2a. This test section has been adapted for aeroacoustic tests. The floor and ceiling have been acoustically treated, with 3 cm flat melamine foam. The foam panels have ramps at the leading edge and trailing edge, in order to avoid undesirable aerodynamic phenomena, such as separation at the trailing edge of the lining, or strong streamwise loads. The test section side–panels have also been modified, for maximising sound absorption. The treated panels contain 5 cm thick wedged melamine, covered by a tensioned Kevlar sheet, as sketched in Fig. 3.2b.

In addition to the absorption of reflections, the test section has been modified in order to reduce hydrodynamic background noise at the measurement location. Shown in Fig. 3.2, the microphone array is installed (15 cm) behind a tensioned Kevlar panel. As discussed in Sec. 2.3.2, this approach is characteristic of hybrid wind tunnel test section designs. Luesutthiviboon et al. [17] have assessed the aerodynamic performance of the LTT aeroacoustic test section (without floor and ceiling lining). Air transpiration through the hybrid wind tunnel side–wall was found to modify the lift polar of an airfoil at large angles of attack, $\alpha \geq 10\,\text{degree}$, due to the modification of the wall blockage effect experienced by this test model. This test was made with a 0.9 m chord NACA63_3–018 airfoil, at $Re_c = 3 \times 10^6$ [17].

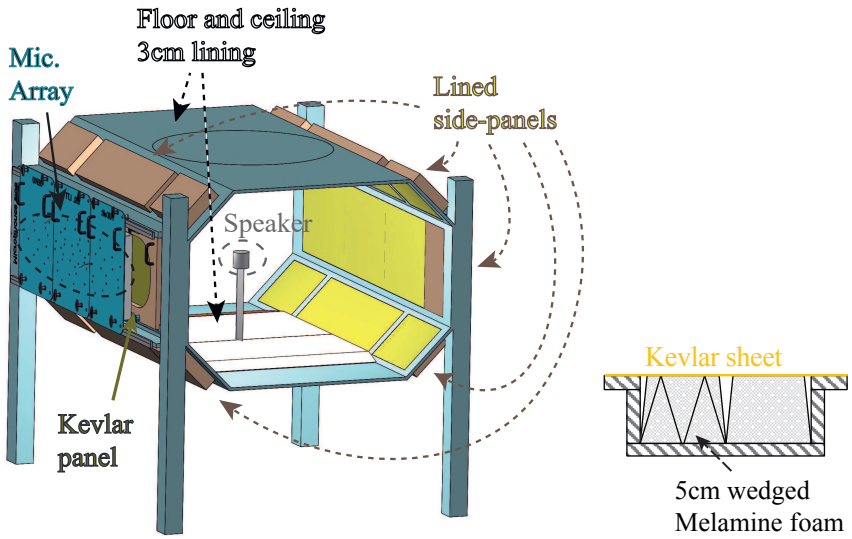

(a) Test section (b) Lined side–panels

Figure 3.2: Aeroacoustic test section of the Low turbulence tunnel. CAD of the lined test section, as seen from the inlet (left) and representation of the lined melamine side–panels (right). b) has been adapted from [11].

3.1.2. MEASUREMENT TECHNIQUES

The experimental data collected during this thesis was collected to characterise the flow and acoustic fields during the tests. The hot–wire technique and the surface measurements were taken to characterise the flow, whereas the acoustic microphone measurements were taken out–of–flow.

HOT–WIRE

The flow velocity measurements were made with the hot–wire technique. In this technique, a thin wire is placed in the flow, at the measurement location. The wire is heated, in the case of this experimental work to 340 °C, in order to allow for the flow to receive energy from the wire through convection. The temperature of the wire is kept constant by an electric current. The voltage required to keep the wire at this temperature is then recorded, and is related to the flow velocity after calibrating the sensor. The highest source of error in hot-wire measurements is typically the temperature variation in the room. During measurements, the ambient temperature and pressure were continuously measured, in order to correct for the temperature

variations, as discussed in [22].

The hot–wire probe used was a Dantec Dynamics hot-wire 55P15 probe. This probe is specifically designed to measure velocities in a boundary layer, without disturbing the flow. Figure 3.3 shows the probe installed and measuring at the A-Tunnel. The wire in this figure is placed parallel to the wall and perpendicular to the free–stream flow, in order to measure the streamwise velocity in the lined plate's boundary layer.

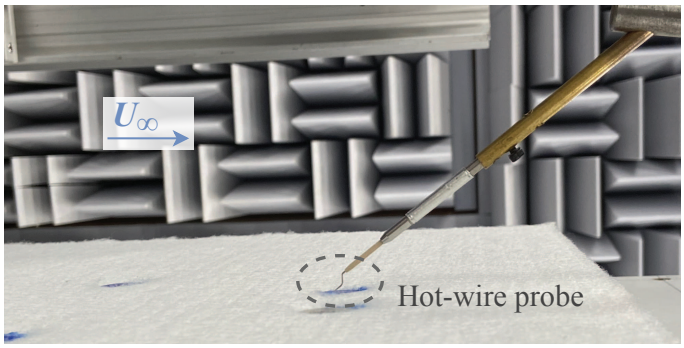

Figure 3.3: Hot–wire probe measurements of a turbulent boundary layer, at TU Delft's A–Tunnel.

SURFACE PRESSURE FLUCTUATION MEASUREMENTS

The measurement of turbulent pressure fluctuations was taken with microphones mounted on a surface. This was done to measure the magnitude of pressure fluctuations in a boundary layer, e.g. over the plate seen in Fig. 3.3, and at the bottom of cavities. Cavities have been designed for reducing the magnitude of these hydrodynamic fluctuations at the measurement location, as discussed in Sec. 2.2.2.

These surface measurements were taken with three microphone types: a Linear–X M51 microphone and small electret Sonion 8044 and Sonion 8010T microphones. The Linear–X has been designed for free–field measurements, and was used for redundancy, as this microphone is capable of measuring very high pressure fluctuation magnitudes, up to 150 dB. The Sonion microphones have the advantage of having a small membrane (diaphragm of the microphone) of 0.05 mm, which allows for the measurement of smaller eddies. This translates into a higher measurement frequency range. However, these smaller microphones are only able to measure up to 130.5 dB (Sonion 8044) and 119 dB (Sonion 8010T), at 1 kHz.

ACOUSTIC MEASUREMENTS

Acoustic measurements were taken both at the A–Tunnel and at the LTT. These measurements were taken with microphone arrays placed outside the flow. The microphone array of the A–Tunnel consisted of 64 G.R.A.S. 40PH free-field microphones. The free-field microphones have an uncertainty of 1dB, from 50 Hz to 5 kHz [82]. The microphones have been installed in a grid, as sketched in Fig. 3.1, ①. The array has an elliptical shape, formed by 7 spiral arms, and extending 2 m in the streamwise direction (vertical) and 1 m in the horizontal direction. The location of the microphones in the spiral arms of the array was optimised in order to maximize spatial resolution and minimize side lobe levels in the A-tunnel [83].

The array used in the LTT consists of 62 PUI AUDIO 665–POM–2735P–R microphones. The microphone coordinates were defined by scaling from the A–Tunnel array design. The LTT array extends 1.6 m in the streamwise direction (horizontal) and 0.4 m in the vertical direction, and is shown in Fig. 3.4a. The microphones are held by a solid plate, lined with 5 cm plane melamine foam. The microphones are positioned flush with the foam surface. During measurements, the microphones are recessed 15 cm behind a stretched aviation-standard Kevlar 49 T 965 sheet (see Figs. 3.2a and 3.4b).

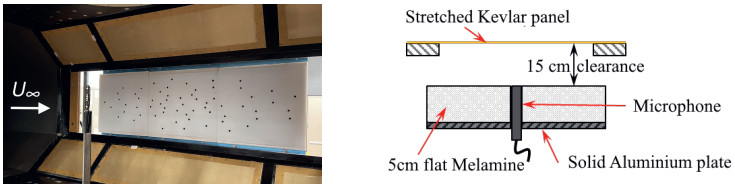

(a) Installed array (b) Microphone placement.

Figure 3.4: Low Turbulence Tunnel microphone array: array installed in test section, without the array's Kevlar panel (left); and microphone placement, behind the Kevlar panel (right). Figure b) adapted from [84].

3.2. SOUND WAVE GEOMETRIC MODELLING

A geometric modelling algorithm was developed, in order to predict the propagation of sound in a reflective environment. The algorithm is based on the mirror–source method, and has corrections for reflections on lined walls and for the convection of sound waves by the mean flow.

3.2.1. MIRROR–SOURCE METHOD

The mirror–source method is an efficient technique for predicting reflections on flat and smooth walls, particularly when the wall is large with respect to the wavelength. This method considers reflections to be specular, neglecting the existence of diffuse reflections. Diffraction is also neglected in the present model. The mirror–source method assumes the modelled walls to be infinite, and loses accuracy at lower frequencies, when the acoustic wavelength becomes comparable to the size of the walls [42].

The LTT test section has an octagonal shape, as seen in Fig. 3.2. The primary reflections on the three larger walls of the test section (floor, ceiling and wall opposite to the array) can be modelled as a mirror–source, as represented in Fig. 7.3. The effect of lining was taken into account in this geometric model by considering the complex valued surface reflection coefficient of the lined walls, $\underline{R}_c(f)$. The reflection coefficients of the lining were used in the algorithm, by adjusting the amplitude and phase of each mirror reflection signal, $\underline{S}_{MR}(f)$, with respect to the direct source signal, $\underline{S}_{DS}(f)$:

$$\underline{S}_{MR}(f) = \underline{S}_{DS}(f)\underline{R}_c(f). \tag{3.1}$$

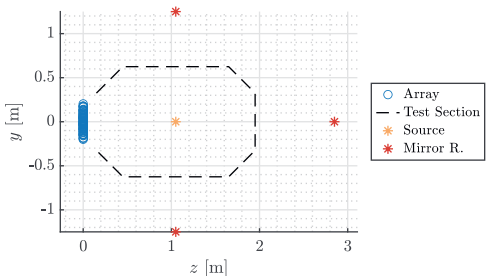

Figure 3.5: Setup for simulation of the acoustic response of the LTT test section, with the mirror–source method. Modelling of the primary reflections on the floor, ceiling and wall opposite to the array.

3.2.2. FLOW CORRECTION

The conventional mirror-source method does not take into account the convection of the sound wave by the tunnel jet. However, this phenomenon may considerably alter the propagation of sound in a wind tunnel environment, as represented in Fig. 2.5. For the flow-on cases, the path of each sound ray from the mirror source to the receivers (microphones) is re-calculated taking into account convection by the flow. The method used to calculate the path of the sound

ray, from each mirror–source to the receiver, resembles the ray tracing technique discussed by Savioja [42]. With the present method, the number of reflections to be calculated for each mirror source equals the number of receivers. In contrast with the widely used stochastic ray tracing techniques, this modelling tool is thus deterministic, as the "conventional" mirror–source methods [42].

3

3.3. NUMERICAL METHODS

Two numerical solvers have been used in this thesis, for aiding the investigation of solutions to improve wind tunnel aeroacoustic tests. A Lattice–Boltzmann method (LBM) solver has been used to simulate aerodynamic phenomena, including acoustic fluctuations generated aerodynamically. A Finite Element Method solver has been used to simulate the acoustic response of wind tunnel test sections, with a higher fidelity than the geometric model previously introduced, but at the expense of higher computational cost.

3.3.1. LATTICE–BOLTZMANN METHOD

The numerical flow simulations were performed with the commercial software SIMULIA PowerFLOW 6-2019, which is based on the Lattice–Boltzmann method, coupled with a Very-Large Eddy Simulation (VLES) approach. The LBM is based on kinetic models which take into account mesoscopic processes in order to obtain reliable continuum flow quantities, in agreement with the macroscopic dynamics of a fluid. PowerFLOW solves the LBM equation on a lattice, i.e., a Cartesian grid. The lattice consists of cubic cells, referred to as voxels, with 19 degrees of freedom. The LBM-VLES solver considers a discrete form of the lattice-Boltzmann equation, which can be written as [8]:

$$F_i(\boldsymbol{x} + V_i\Delta t, t + \Delta t) - F_i(\boldsymbol{x}, t) = C_i(\boldsymbol{x}, t) \tag{3.2}$$

where $\boldsymbol{x}$ and t are the space and time coordinates. F_i is the particle distribution function along the i^{th} lattice direction, and V_i is the discrete particle velocity in the same direction. The collision operator, C_i, is based on the Bhatnagar–Gross–Krook kinetic model [85], and is defined as:

$$C_i = -\frac{\Delta t}{\tau}\left[F_i(\boldsymbol{x}, t) - F_i^{eq}(\boldsymbol{x}, t)\right], \tag{3.3}$$

where $F_i^{eq}(\boldsymbol{x}, t)$ is the equilibrium distribution function, estimated from statistical physics considerations [86]. τ is the viscosity dependent collision relaxation time [86].

In a LBM-VLES approach, the small scales of turbulence are accounted for by correcting the relaxation time used in the calculation of the collision term. Following the work of Ref. [87], a two-equation $k-\epsilon$ renormalization group is used to compute a turbulent relaxation time that is added to the viscous relaxation time, such that the effective relaxation time reads as:

$$\tau_{\text{eff}} = \tau + C_\mu \frac{k^2/\epsilon}{(1+\eta^2)^{0.5}}, \tag{3.4}$$

where k is the turbulent kinetic energy and ϵ is the rate of dissipation of turbulent kinetic energy. $C_\mu = 0.09$ and η are a combination of the local strain, local vorticity and, local helicity. The term η mitigates the sub-grid scale viscosity in presence of large resolved vortical structures. The solver can realistically represent boundary layer profiles at large Reynolds numbers, without resolving the flow in the viscous sub–layer of the boundary layer, by using a pressure gradient–dependent wall model [86].

POROUS MODEL

The LBM–VLES solver allows for the simulation of flow through a porous material, without fully resolving its fibre structures. This is done through modelling the volume occupied by the porous material, e.g. a lining foam, as a porous medium. This model uses the material's viscous and inertial resistivities, R_v and R_i, to impose Darcy's law in the porous medium. Darcy's law relates the pressure drop across the porous medium, Δp, to the Darcy's velocity, v_d, according to [8]:

$$\frac{\Delta p}{t_{\text{pm}}} = R_v \boldsymbol{v_d} + \rho R_i \boldsymbol{v_d}^2, \tag{3.5}$$

where t_{pm} is the thickness of the porous medium and ρ is the density of air. Previous literature [8] suggests this simulation approach is capable of predicting the influence of a porous region on a grazing turbulent boundary layer.

3.3.2. FINITE ELEMENT METHOD ACOUSTIC MODELLING

The FEM solver *COMSOL Multiphysics* was used to solve the wave equation:

$$\frac{1}{c^2}\frac{\partial^2 p}{\partial t^2} - \nabla \cdot (\nabla p) = 0, \tag{3.6}$$

where c is the sound speed, p is pressure, t is time, and ∇ is the nabla operator. The *Pressure Acoustics Frequency Domain interface*,

part of the *Acoustics module*, was used. The iterative solver assumes the acoustic source terms and consequent pressure fluctuations to be time–harmonic, to reduce Eq.3.6 to the Helmholtz equation:

$$\nabla \cdot (\nabla p) + \frac{\omega^2}{c^2} p = 0, \tag{3.7}$$

where ω is the angular frequency. In this study, an acoustic monopole source was introduced in the simulations by adding a sphere whose surface was defined by the normal acceleration boundary condition:

$$\boldsymbol{n} \cdot \nabla p = \rho a_n, \tag{3.8}$$

where $\boldsymbol{n}$ is the wall normal vector and a_n is the inward normal acceleration. Both the speed of sound and the fluid density, ρ, were assumed constant. The corresponding ambient temperature was 15 °C. The sound hard boundary and the symmetry boundary conditions were included in the simulation by imposing Eq. 3.8 with $a_n = 0$ at these boundaries [88].

ACOUSTIC WAVE DISSIPATION

The porous liners over the wind tunnel walls were modelled by defining an equivalent fluid domain, at the location of the lining [88]. In these porous fluid regions, pressure waves are dissipated according to the Delany–Bazley–Miki model [89]. This empirical model allows for the prediction of sound absorption in a porous liner with a porosity close to 1, as is the case of Melamine foam, based on the material's viscous resistivity [46]. The porous materials are the only regions inside the test section where acoustic dissipation occurs, as any other thermoviscous effects were neglected. Atmospheric dissipation was considered negligible, due to the relatively small size of the numerical domain. Furthermore, these acoustic simulations were conducted for flow-off scenarios, in which no viscous losses associated with shear layers occur.

3.4. POST–PROCESSING

The recording of acoustic pressure fluctuations in the wind tunnel tests was done in this thesis with phased–microphone arrays. This allows to preserve the phase information between microphones. Beamforming is a post–processing technique which uses this phase relation between microphone measurements to localise acoustic sources and to more accurately quantify each noise source [34]. Beamforming facilitates noise quantification, e.g., by increasing the signal to noise ratio with respect to the background noise.

The processing of microphone signals in this thesis was mostly done in the frequency domain, i.e., after converting the recorded pressure fluctuations from the time–domain. The conversion was made by means of a Discrete Fourier Transform (DFT):

$$X[f] = \sum_{n=0}^{N_s-1} x[n_s] \cdot e^{-i2\pi f \frac{n}{F_s}}, \tag{3.9}$$

where $x[n_s]$ is the time domain input signal at discrete time index n_s, N_s is the total number of samples of this measured signal, and F_s is the sampling frequency of the measurement. n_s/F_s is the time coordinate at which each sample was recorded. $X[f]$ is the frequency domain output of the DFT, at the frequency f.

3.4.1. CONVENTIONAL BEAMFORMING

The beamforming technique used in this thesis is the conventional frequency domain beamforming, from here on referred to in this thesis as Conventional Beamforming (CBF). This post–processing technique is widely used in aeroacoustics research, e.g., in Refs. [90, 91], as this is an intuitive and robust beamforming method [34]. In CBF, the measured signals of the N microphones in the array are treated in the frequency domain:

$$\boldsymbol{p}(f) = \begin{pmatrix} p'_1(f) \\ \vdots \\ p'_N(f) \end{pmatrix}, \tag{3.10}$$

where p'_n is the pressure fluctuation recorded at each microphone, n. N stands for the number of microphones in the array. The propagation of the sound wave is considered in beamforming in the definition of the steering vector, $g_{j,n}$. The steering vector takes into account the sound wave's spherical spreading and phase shift from a scan grid point, j, to a microphone n, by assuming the wave to propagate in free–field conditions (see discussion of Eq. 2.1):

$$g_{j,n\ \text{(free–field)}} = \frac{\exp\left(-2\pi i f \Delta t_{j,n}\right)}{\|\boldsymbol{x}_n - \boldsymbol{\xi}_j\|}, \tag{3.11}$$

where $\Delta t_{j,n} = \left\|\boldsymbol{x}_n - \boldsymbol{\xi}_j\right\|/c$ is the sound propagation time from the grid point location ξ_j to the receiver at x_n. c is the speed of sound. $\|\cdot\|$ is the Euclidean norm of a vector. The vector $\boldsymbol{x}_n$ contains the coordinates of all microphones in the array. For each grid point, the noise levels are estimated from:

$$A(\boldsymbol{\xi}_j) = \frac{\boldsymbol{g}_j^*(\boldsymbol{p}\boldsymbol{p}^*)\boldsymbol{g}_j}{\|\boldsymbol{g}_j\|^b}, \tag{3.12}$$

$\boldsymbol{p}\boldsymbol{p}^*$ is a $N \times N$ matrix, commonly referred to as Cross-Spectral Matrix (CSM), where the asterisk, $(\cdot)^*$, represents the complex conjugate transpose. b is a scalar and is set to 2 or 4, depending, respectively, on whether it is intended to compute the noise levels at the observer (microphone array) or at the source.

For beamforming experimental wind tunnel data, it is common to consider a 2D scan grid parallel to the array, which includes the expected location of sources within the test model/ setup. Figure 3.6 shows the beamforming map obtained from experimental microphone array data, recorded with the LTT array. This purely acoustic test, carried without flow, was made with a small omnidirectional source (speaker) positioned at the streamwise and vertical centre of the array, $(x, y) = (0, 0)$m. The source was positioned 1.05 m away from the array plane, and this measurement is representative of free–field conditions. Sound Pressure Level is here defined as:

$$\mathrm{SPL} = 20 \log_{10}\left(\frac{p'_{\mathrm{rms}}}{p_{\mathrm{ref}}}\right), \tag{3.13}$$

where p'_{rms} is the root mean square of the pressure fluctuations, and the reference pressure, p_{ref}, is 2×10^{-5} Pa.

From Fig. 3.6, it is easy to identify the streamwise location of the speaker. However, the speaker noise spreads in the vertical direction, in this beamforming map. The reason for this difference in resolution between the streamwise and vertical direction is the horizontally oriented array shape. The LTT microphone array is 4 times longer on the horizontal direction than on the vertical direction. If we assume sound waves to propagate in a direction close to perpendicular to the array, resolution of a conventional beamforming map can be approximated by [83]:

$$RL(f) = h_{\mathrm{scan}} \tan\left(1.22 \frac{c}{f L_{\mathrm{array}}}\right), \tag{3.14}$$

where h_{scan} is the scan plane distance to the array plane, c is the sound speed, and L_{array} is the array length in a specific direction. $RL(f)$ is the frequency dependent Rayleigh Limit, in that same direction.

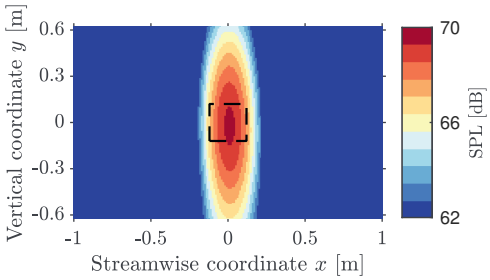

Figure 3.6: Beamforming map of the reference speaker measurement, for the 1 kHz centered third–octave band. Speaker located at a 1.05 m distance from the LTT array. A Source Power Integration region is represented by the dashed line.

3.4.2. SOURCE POWER INTEGRATION

After calculating the beamforming maps, the speaker noise levels can be obtained with the Source Power Integration (SPI) method [54]. Figure 3.6 shows a $24\times24\,\mathrm{cm}^2$ SPI region, centered at the source position. In the SPI method, the experimental CSM is normalised with the CSM of a simulated point monopole source, with unit strength. This is done in order to quantify the noise levels of the experimental source:

$$A_{\mathrm{SPI}}(f) = \frac{\sum_{j=1}^{K} A\left(\boldsymbol{\xi}_j\right)_{\mathrm{exp.}}}{\sum_{j=1}^{K} A\left(\boldsymbol{\xi}_j\right)_{\mathrm{sim.}}}, \tag{3.15}$$

where K is the number of grid points considered in the integration. The simulated map is typically calculated from [92]:

$$A\left(\boldsymbol{\xi}_j\right)_{\mathrm{sim.}} = \frac{\boldsymbol{g}_j^{*}(\boldsymbol{g}_k\boldsymbol{g}_k^{*})\boldsymbol{g}_j}{\|\boldsymbol{g}_j\|^{b}}, \tag{3.16}$$

where $\boldsymbol{g}_k$ is the steering vector to the kth grid point, usually selected as the grid point at the centre of the SPI region.

4

MICROPHONE PLACEMENT: CAVITY DESIGN

Microphone measurements in a closed test section wind tunnel are affected by turbulent boundary layer (TBL) pressure fluctuations. These fluctuations are mitigated by placing the microphones at the bottom of cavities, usually covered with a thin, acoustically transparent material. Prior experiments showed that the cavity geometry affects the propagation of TBL pressure fluctuations towards the bottom. However, the relationship between the cavity geometry and the flowfield within the cavity was previously not well understood. Therefore a very large–eddy simulation was performed using the Lattice–Boltzmann method. A cylindrical, a countersunk and a conical cavity were simulated with and without a fine wire-cloth cover, which is modelled as a porous medium governed by Darcy's law. Adding a countersink to an uncovered cylindrical cavity is found to mitigate the transport of turbulent structures across the bottom by shifting the recirculation pattern away from the cavity bottom. Covering the cavities nearly eliminates this source of hydrodynamic pressure fluctuations. The eddies within the boundary layer, which convect over the cover, generate an acoustic pressure field inside the cavities. As the cavity diameter increases compared to the eddies' integral length scale, the amount of energy in the cut–off modes increases with respect to the cut–on modes. Since cut–off modes decay as they propagate into the cavity, more attenuation is seen. The results are in agreement with experimental evidence.

This chapter is based on the work published in Physics of Fluids **34**, 10 (2022) [93].

4.1. INTRODUCTION

The signal–to–noise ratio (SNR) of flush mounted microphone array measurements in closed test section wind tunnels is reduced by the presence of a turbulent boundary layer (TBL) over the tunnel walls. The amount of SNR reduction by the TBL pressure fluctuations can be minimized, relative to a microphone mounted flush to the tunnel wall, by placing microphones within cavities. Research on flow over cavities has focused primarily on radiated noise from the interaction of the shear layer over rectangular cavities. The research presented in this article focuses on how the pressure fluctuations at the bottom of axisymmetric cavities, resulting from turbulent flow, are affected by cavity geometry.

Pressure fluctuations within cavities are produced by several mechanisms, which include the Rossiter feedback loop, turbulence within the shear layer, and the transport and production of turbulence due to recirculation within the cavity. The Rossiter feedback loop [94–96] is a self–sustaining noise generation mechanism produced by Kelvin–Helmholtz type vortices [97] shed from the cavity upstream edge. When the vortices impinge on the downstream wall, pressure waves are produced [98, 99] that perturb the shear layer, which further produces vortex shedding. The feedback loop is characteristic of cavities exposed to a boundary layer with relatively large momentum thickness, with respect to the cavity aperture [100]. For rectangular cavities, these vortices extend along the spanwise length of the cavity [101] and their impingement produces tonal peaks in the far-field noise spectra. Axisymmetric cavities exhibit similar behavior [102], however the vortices shed by cylindrical cavities are affected by the curved cavity edge [103]. Specifically, the vortex spanwise length is smaller than the cavity diameter and they are shed from multiple spanwise locations along the upstream edge [104]. This results in a weaker and broader spectral peak compared to rectangular cavities [95].

In addition to the shed vortices, the shear layer contains randomly fluctuating turbulence, which produces pressure fluctuations that propagate into the cavity, referred to as turbulent rumble [105]. The strength of these fluctuations increases from the leading edge towards the downstream edge as shown by PIV measurements [104]. The shape of the upstream edge influences the stability of the shear layer because non–sharp edges can cause the location of the separation point to vary in time [106], which affects the amplitude of the turbulent rumble [107].

Recirculation of the fluid due to the flow entering the cavities results in the presence of turbulent pressure fluctuations at the cavity bottom [108]. For deep cylindrical cavities, the recirculating flow is symmetric with respect to the cavity centerline [109]. The recirculation patterns within these deep cavities are stable, in contrast to shallower cavities, which feature unsteady and asymmetric recirculation patterns [110, 111]. The recirculating flow causes strong wall shear, which generates

fluctuations as high as ≈ 35% of the local velocity [108]. These velocity fluctuations are highest between the downstream bottom corner and the cavity center, along the cavity centerline [102, 111]. This region of increased turbulence corresponds to a region of higher static pressure [111].

These phenomena can excite acoustic cavity modes that radiate acoustic noise into the far-field. For example, the Rossiter mode produces strong acoustic tones if they are locked on with an acoustic cavity mode [112–114]. Acoustic depth modes are also excited by the turbulent rumble as well as the acoustic energy produced by the shed vortices [98]. For the deep cavities, defined as $L/D \leq 1$, acoustic depth modes are the most significant [115, 116].

A previous study [68] characterized how axisymmetric cavities with different diameters, depths, countersink depths, coverings, and wall angles affect the pressure fluctuations, produced by the TBL, at a microphone placed at the bottom. Cavities with angled walls, e.g., cavities with a countersink, reduce the TBL noise more than cylindrical cavities [68]. Additionally, covering the cavity with Kevlar [117] or finely woven stainless–steel cloth [68] reduces the amplitude of pressure fluctuations at the microphone location by 10 - 20 dB [117]. This reduction is assumed to be caused by the cover preventing flow into the cavity, reducing the hydrodynamic source of pressure fluctuations. Previous experiments, conducted as part of this project [27, 29], have measured the effect that cylindrical cavities, with and without a countersink, and conical cavities, as illustrated in Fig. 4.1, have on the attenuation of pressure fluctuations due to the TBL. When these three cavities are uncovered, the countersunk cavity attenuates the TBL pressure fluctuations the most, followed by the cylindrical one. The conical cavity performs the worst as the pressure spectra at the bottom are higher than the spectra measured by a flush mounted microphone. Covering the cavities alters this trend: the conical cavity attenuates the pressure spectra at the bottom more than the countersunk and cylindrical cavities. However, better insight into the relationship between the mechanisms that produce pressure fluctuations and cavity geometry is needed to further optimize the geometry. Currently, there is a lack of literature describing the physical mechanisms that affect the amplitude of pressure fluctuations at the bottom of axisymmetric microphone cavities, especially for covered cavities.

The objective of this work is to understand the effect of aperture size, different countersink depth ratios, i.e., the ratio between the cavity depth and the countersink depth, wall angles, and the presence of a covering have on the recirculation within the cavities, vortex shedding, and turbulence generation, which contribute to the pressure fluctuations at the cavity bottoms. Given the size and geometry of the cavities, non–intrusive velocity–field measurements to identify and study the flow

phenomena within the cavity are challenging. Hence, a very–large eddy simulation (VLES) was performed using a Lattice–Boltzmann method (LBM) solver, SIMULIA PowerFLOW. This article is organized as follows: Section 4.2 describes the cavity geometries and the PowerFLOW simulation parameters, the validation measurements, and the post-processing used in this analysis. Section 4.3 discusses the simulation verification and validation. Section 4.4 analyses the flowfield and pressure field in the time–averaged, instantaneous, and wavenumber domains. Section 4.5 evaluates the porous covering's effect on the flowfield in the time–averaged, frequency, and wavenumber domains. Additionally, the effect of geometry on the propagation of the pressure fluctuations is analyzed. Finally Section 4.6 summarizes the major findings of this article.

4.2. METHODOLOGY

4.2.1. COMPUTATIONAL SET-UP

The LBM–VLES simulations are performed with the commercial software SIMULIA PowerFLOW 6-2019. The equations behind this numerical method have been previously described, in Sec. 3.3.1.

GEOMETRY

The following axisymmetric cavity geometries are studied: a cylindrical cavity with and without a countersink, and a conical cavity. These three cavities and their geometric parameters are shown in Fig. 4.1. These cavity geometries were chosen because they are representative of the cavities commonly used in wind tunnel experiments [27, 29]. Each cavity is investigated with and without a stainless–steel cloth cover. The following cavity geometric parameters are defined in Table 4.1: aperture size (L), depth (D), countersink depth ratio (d_c/D), ratio of aperture size to BL momentum thickness (L/θ), and wall angle (ψ). For the cylindrical cavity, the aperture diameter is $L = 2.5\theta$, where θ is the momentum thickness of the incoming boundary layer (described in Sec. 4.3.2). The relatively small L/θ is expected to avoid the cavity wake mode described in Ref. [100]. For an array of microphone cavities, the cavity wake mode would likely cause the downstream cavities to experience a highly turbulent incoming flow.

Table 4.1: Cavity geometric parameters.

Cavity	L, cm	D, cm	d_c/D	L/θ	ψ
Cylindrical	1.0	1.0	0.0	2.5	90°
Countersunk	1.6	1.0	0.3	4.1	45°
Conical	4.5	1.23	1.0	11.4	30°

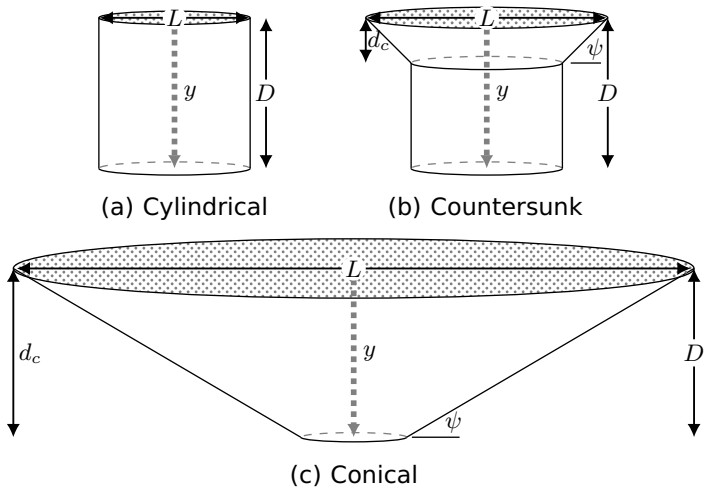

Figure 4.1: Simulated cavity geometries: a) Cylindrical, b) Countersunk, and c) Conical.

POROUS MODEL

The covered cavities are covered with a finely woven stainless–steel cloth, which has a wire diameter of 2.6×10^{-3} cm and a density of 200 wires per cm^2. This cloth was used in prior cavity experiments [29] and for this work is modelled as a porous medium, as proposed in Ref. [118]. This porous medium model has been previously introduced in Sec. 3.3.1.

In order to have sufficient cells inside the porous region, so that the solver can simulate the relationship between flow velocity and pressure gradient, the thickness of the porous medium in the simulation is approximately three times larger than the thickness of the physical stainless–steel cloth. To account for this, the resistivity values R_v and R_i were multiplied by the ratio between the thickness of the measured sample and the thickness of the porous medium in the simulation. A permeability tube simulation was performed (with the numerical setup described in Ref. [119]) to confirm that the porous medium with increased thickness, and corrected R_v and R_i, matches the experimental $\Delta p/t$.

DOMAIN AND OPERATING CONDITIONS

The computational domain for the circular and countersunk cavities is shown in Fig. 4.2. The bottom of the domain is a flat plate with a no-slip condition at the wall. The cavity, which also contains no-slip walls, is

placed at the origin of the domain, i.e., at the center with respect to the length of the streamwise and spanwise domain lengths. This center is located 150 cm (150 $L_{\text{Cylindrical}}$) downstream of the inlet. At the inlet, a turbulent boundary layer mean velocity profile, based on experimental measurements from Ref. [29], is imposed ($\delta_{99} = 1.4$ cm at the inlet). A zigzag trip is placed downstream of the inlet, introducing coherent vortices in the boundary layer. The (no-slip) zigzag trip is 0.16 cm high and has 0.427 cm length, 0.427 cm pitch and 90° of top angle (dimensions as defined in Ref. [120]). The boundary layer downstream of the zigzag trip is turbulent. The free-stream velocity, U_∞, is set at 32 m s^{-1}, which is within the U_∞ range of interest for closed wind tunnel wind turbine airfoil aeroacoustic testing [90]. As shown in Fig. 4.2, the sides of the domain have a periodic boundary condition (BC). The span of the domain was chosen to minimize the influence of the boundaries on the cavity flowfield. For the cylindrical and countersunk cavities, a value of $3.2L_{\text{Countersunk}}$ was selected. The distance from the cavity to the boundaries is larger than the spanwise coherence length of the pressure fluctuations in the boundary layer, which is typically on the order of the boundary layer displacement thickness [121]. The span of the domain for the conical cavity simulations is increased to $1.7L_{\text{Conical}}$ (covered configuration) and $2.6L_{\text{Conical}}$ (uncovered). The top of the domain is bounded by a free-slip wall and is located 136 cm above the bottom wall (flatplate). The outlet of the domain imposes an ambient static pressure (sea level pressure). Figure 4.2 shows a representation of the variable resolution (VR) regions in the computational domain. The VR regions specify the amount of lattice refinement, where VR0 is the finest and VR5 the coarsest, for the uncovered cavities. The VR regions are similar for the covered cavity simulations, which have an additional finer resolution region around the location of the cloth cover, as shown in Fig. 4.3. The Appendix in Ref. [93] contains additional details on the domain and VR dimensions.

4.2.2. EXPERIMENTAL SET-UP

CAVITY PRESSURE MEASUREMENTS

The experimental data used for validation were measured in the TU Delft A–Tunnel using the same procedure as described in Ref. [29]. The tunnel is described in Sec. 3.1.1. The cavities in Fig. 4.1 were made of poly–carbonate and mounted on a plate flush with the exit nozzle. The cavities were placed 76 cm downstream of the tunnel nozzle exit. Two plates with dimensions of 110 cm × 40 cm were used. One was uncovered and the other was covered with a 200 threads per cm^2 (#500) stainless–steel cloth. A flush-mounted microphone was placed 3.2 cm downstream with a spanwise offset of 4.5 cm. The three cavities were tested in each plate. The tunnel flow speed was 32 m s^{-1} at the

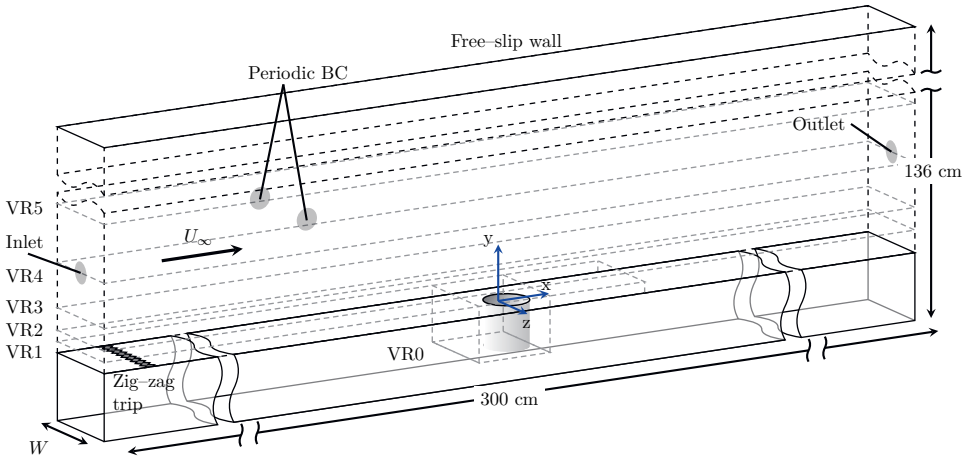

Figure 4.2: Representation of the computational domain

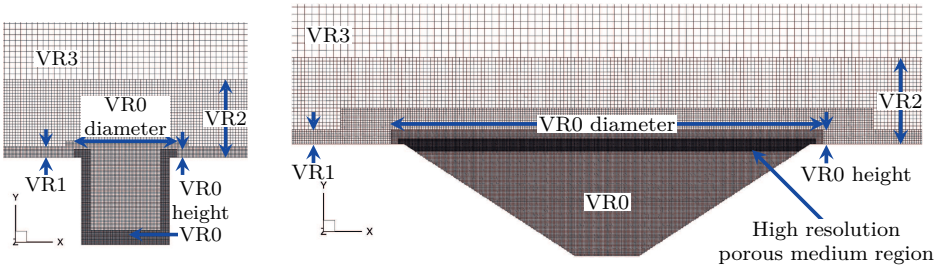

(a) Cylindrical – uncovered

(b) Conical – covered

Figure 4.3: Grid topology at the cavities location: a) uncovered cylindrical cavity; b) covered conical cavity.

cavity's location.

Sonion 8010T omni-directional MEMS microphones were used to measure the pressure fluctuations. This microphone has an outer diameter of 2.5 mm and a transducer diameter of 0.05 mm. The microphones were center mounted on a 7 mm diameter holder in order to fit securely within the cavities. All the microphones were calibrated individually using a *G.R.A.S. 42AG* pistonphone following the guidelines of Mueller [33]. The microphones have a flat frequency response within ±1 dB from 100 Hz to 10 kHz. The data acquisition system consists of a *National Instruments* (NI) *NI9215* analog input module mounted in the NI *cDAQ-9178 CompactDAQ* with 16–bit resolution. The sampling frequency of the measurements was 51.2 kHz and the data were recorded for 45 s.

STAINLESS–STEEL CLOTH PERMEABILITY MEASUREMENTS

A 7.5×10^{-3} cm thick stainless–steel cloth sample was installed in a permeability tube to determine the viscous and inertial resistance of the cloth. The pressure drop, Δp, across the sample as well as the volumetric flow, Q, through the sample were measured. The Darcy velocity, v_d, is calculated as follows: $v_d = Q/A$, where A is the cross–sectional area of the tube. The measured Δp and v_d are fit to the Hazen-Dupuit-Darcy equation (Eq. 3.5) using a least squares fit method [91, 122] to determine the permeability, $K = \frac{\mu}{R_v}$, and the form drag coefficient, $C = R_i$, where μ is the viscosity of air. Further details on the permeability tube can be found in Refs. [91, 122].

The cloth sample was mounted between two 9.0 cm × 9.0 cm polycarbonate plates each with 5.1 cm diameter holes at the center. Epoxy was applied to one polycarbonate plate and the cloth was then stretched across the plate so that the material was tensioned across the opening. Pressure taps within the tube are located 5 cm upstream and downstream of the sample [91]. The static pressure was measured with a Mensor 2101 differential pressure sensor, which has a range of 1.2–15 kPa and an accuracy of 2 Pa. The volumetric flow rate was controlled using an Aventics pressure regulator and measured by a TSI4040 volumetric flowmeter. The Darcy's velocity flow range in the tube is between 0 and 2.5 m s^{-1}, and the permeability tube has a cross–sectional area of 2.04×10^{-3} m^2. The flowmeter has an accuracy of 2% [91, 122]. The pressure drop was measured at 22 discrete velocities ranging from 0 to 2.2 m s^{-1}. The resulting permeability K, the form drag coefficient C, inertial resistance, and viscous resistance are provided in Table 4.2.

Table 4.2: Experimentally measured stainless–steel cloth permeability characteristics with 95% confidence intervals.

K, m^{-2}	C, m^{-1}	R_v, s^{-1}
3.0×10^{-11}	3.1×10^{4}	5.0×10^{5}
$\pm\ 1.0 \times 10^{-14}$	$\pm\ 1.6 \times 10^{5}$	$\pm\ 1.7 \times 10^{2}$

4.2.3. POST-PROCESSING METHODS

SPECTRAL ANALYSIS

The power spectral density (PSD) of the pressure field at a given point within the cavity, P_{xx}, was calculated using the Welch's method [33]. A Hanning window was used with 50% overlap when computing the spectra. For all cavities, with and without a covering, a window size of 512 samples was used. The PSD was converted to a decibel scale with a reference pressure of 2×10^{-5} Pa.

WAVENUMBER ANALYSIS

A wavenumber-frequency spectral analysis was performed to decouple the acoustic and hydrodynamic contribution to pressure fluctuations propagation within the cavity. The acoustic region contains the pressure fluctuations' propagation at the speed of sound. The acoustic wavenumbers, k_0, associated with this region are between $-\frac{f}{c}$ and $\frac{f}{c}$. The hydrodynamic region is defined by wavenumbers outside of the acoustic region. However, at low frequencies, the hydrodynamic wavenumbers are difficult to decouple from the acoustic wavenumber. Therefore, a limiting frequency is defined, below which the distinction between acoustic and hydrodynamic spectra is uncertain. This frequency is defined as [123] $f \leq U_\infty \Delta k$, where Δk is the wavenumber resolution.

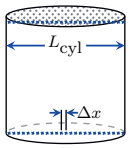

Figure 4.4: Illustration of the sampling location of p' along the centerlines at the top and bottom of the cylindrical cavity, with a spacing of Δx.

The wavenumber spectra were calculated using a 2-D Fourier transform applied to the pressure fluctuations sampled along the cavity centerline, as illustrated for the cylindrical cavity in Fig. 4.4. A Hanning window with 50% overlap was applied in the time domain using the approach described in Ref. [123]. The data were sampled with a spacing of $\Delta x = 1.5 \times 10^{-2}$ cm at the top and bottom of each cavity in the streamwise direction. For the covered cavities, the pressure was sampled just below the interface between the porous region and the cavity volume. The sampling rates, number of time steps, Hanning window size (N_{fft}), and sampling locations are defined in Table 4.3.

PROPER ORTHOGONAL DECOMPOSITION

Proper orthogonal decomposition (POD) was used to decompose the pressure fluctuations into a linear combination of orthogonal modes to identify coherent structures [124, 125]. The tool *MODULO* [126] was used to perform this decomposition. The pressure fluctuations were sampled from the PowerFLOW simulation output with an equal spacing of $\Delta x = \Delta z = 2.5 \times 10^{-2}$ cm. *MODULO* requires a Cartesian grid of equally sampled points, thus a square grid was used. As the cavity cross-sections are circular, the data for the region outside of the cavities are padded with zeros. The sample rate and sampling location with respect to cavity depth (y) are the same as described in Table 4.3. The

Table 4.3: Wavenumber—Frequency spectrum calculation parameters for each cavity, normalized by $L_{cyl} = 1.0\,cm$.

	Cylinder	Countersunk	Conical
		Uncovered	
Sample Rate, kHz	15.32	15.32	15.32
# Time steps	4307	4307	10052
N_{fft}	512	512	512
Δf, Hz	29.9	29.9	29.9
Δx, cm	0.015	0.015	0.015
Top Sampling Location, y/D	0.0	0.0	0.0
Top Sample Length, cm	1.0	1.6	4.5
Bot. Sampling Location, y/D	-1.0	-1.0	-1.0
Bot. Sampling Length, cm	1.0	1.0	0.7
		Covered	
Sample Rate, kHz	183.8	183.8	367.6
# Time steps	7353	7353	14705
N_{fft}	2048	2048	2048
Δf, Hz	89.7	89.7	179.4
Δx, cm	0.015	0.015	0.015
Top Sampling Location, y/D	-0.015	-0.015	-0.024
Top Sample Length, cm	1.0	1.6	4.5
Bot. Sampling Location, y/D	-1.0	-1.0	-1.0
Bot. Sampling Length, cm	1.0	1.0	0.7

resulting modes are defined in terms of their spatial structures, $\boldsymbol{\phi}$, and temporal bases, $\boldsymbol{\psi}$, [125]. The estimated energy, i.e., the amplitude, of each mode, σ_r is weighted by $\sqrt{N_s N}$, where N_s are the number of sampled spatial points and N are the number of time samples [125].

4.3. GRID AND DATA VALIDATION

4.3.1. GRID RESOLUTION VALIDATION

The effect of grid resolution on the flat plate's boundary layer profile and the pressure spectrum inside the cylindrical cavity (covered and uncovered) were evaluated using five grid refinement levels. For the uncovered simulations, these levels are specified in Table 4.4. The smallest voxels are located inside the uncovered cavities. The minimum size of the voxels above the flat plate, upstream of the cavity, is twice the minimum voxel size inside the cavity. Table 4.4 lists as well the non-dimensional wall distance, y^+, from the center of the smallest voxels to the flat plate wall. The non-dimensional wall distance is defined as:

$$y^+ = \frac{y u_\tau}{\nu}, \tag{4.1}$$

where y is the vertical coordinate, u_τ is the friction velocity, and ν is the kinematic viscosity. The value of u_τ is measured $3L_{\text{Cylindrical}}$ upstream of the cavity center. Table 4.4 shows the relative cell size between grids, h_i/h_1, where h_1 is the smallest voxel size of the finest grid tested, and h_i is the smallest voxel size of grid i. The timestep in the LBM simulation is set to maintain a Courant-Friedrichs-Lewy number of 1, considering the sound speed, and is therefore dependent on voxel size. For the different grids, the timestep at VR0 is shown in Table 4.4.

Table 4.4: Grids used in the convergence study (uncovered cylindrical cavity).

Grid i	Min. voxel size outside the cavity [m]	Min. y^+ outside the cavity	h_i/h_1	Min. timestep at VR0 [µs]
Very Coarse	4.00×10^{-4}	15	3	0.34
Coarse	2.67×10^{-4}	10	2	0.23
Medium	2.00×10^{-4}	8	1.5	0.17
Fine	1.60×10^{-4}	6	1.2	0.14
Very Fine	1.33×10^{-4}	5	1	0.11

The convergence of the boundary layer velocity profile, 3.0 cm upstream of the cavities, is analyzed with respect to the displacement thickness, $\delta^\star$, and the boundary layer momentum thickness, θ. The grid dependence of $\delta^\star$ and θ is shown in Fig. 4.5a. Figure 4.5b shows the convergence of the pressure fluctuations at the bottom center of the cylindrical cavity (covered and uncovered), for the one–third-octave band centered at 6.3 kHz since this band contains the acoustic depth mode for the cylindrical cavity. Furthermore, this band is associated with smaller eddies (at higher frequencies), which are therefore expected to be more sensitive to the cell size.

The fits shown in Fig. 4.5 are defined by:

$$f(h_i) = \phi_0 + \alpha h_i^c, \tag{4.2}$$

where α is a constant, c is the order of convergence, ϕ_i is the parameter (e.g., $\delta^\star$) obtained from the simulation with grid i, and ϕ_0 is the estimated exact solution, i.e. the solution for a grid with infinite resolution. The order of convergence is 3 [8]. ϕ_0 and α are calculated with the least squares regression described in [127]. Figure 4.5a indicates that the grids with a medium, fine, and very fine resolution (see Table 4.4) result in approximately equal values of $\delta^\star$ and θ. Figure 4.5b also shows that

the medium grid ($h_i/h_1 = 1.5$) results in a Φ_{pp}, at the bottom of the cavity, close to the estimated exact solution, i.e., the value at $h_i/h_1 = 0$ for the 6.3 kHz one–third-octave band.

Based on the previous results, the fine resolution is chosen for the cylindrical and countersunk cavities (covered and uncovered). The conical cavity simulations use the medium grid resolution because it has a larger outer diameter, which increases the computational costs, particularly for the simulation with the cloth cover.

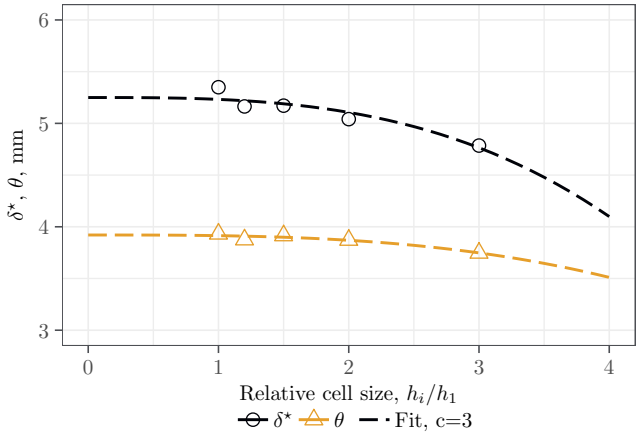

(a) Displacement and momentum thicknesses

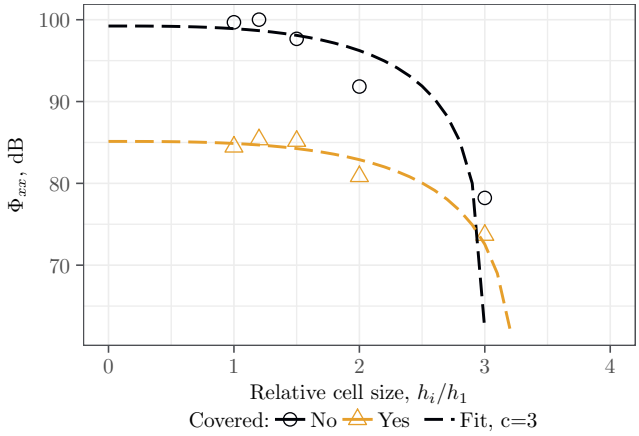

(b) Pressure fluctuations

Figure 4.5: Grid convergence study comparing the following variables: a) BL displacement and momentum thicknesses, $\delta^\star$ and θ, and b) pressure fluctuations (in the 6.3 kHz centered one–third–octave–band) at the bottom of the cylindrical cavity.

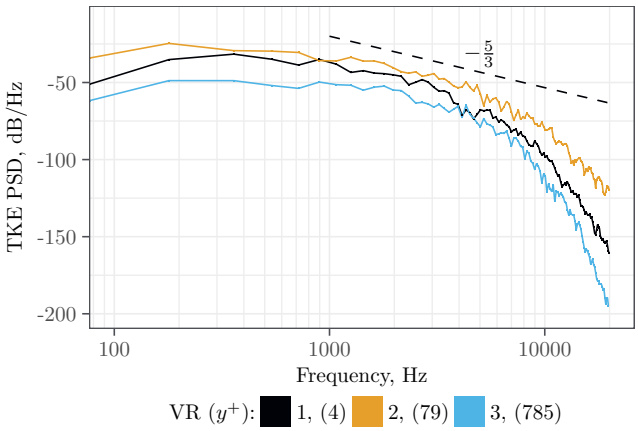

Figure 4.6: PSD of the turbulent kinetic energy (TKE) at 3 VR regions over the flatplate, from the uncovered conical cavity simulation.

Figure 4.6 shows the PSD of the turbulent kinetic energy (TKE) of the simulated boundary layer at four VR regions. The TKE was calculated from the sampled turbulence (u', v', w') upstream of the conical cavity for the medium grid (Table 4.4). The VR1, VR2, and VR3 data were sampled at x = −3.0 cm. This figure shows that the voxel sizes for the VLES simulation are sufficiently small to simulate the turbulent eddies for this work.

Figure 4.7 shows the spanwise correlation of turbulent pressure fluctuations at $x = 0$ and $y = 0$, keeping as reference a point at the spanwise location of the periodic boundary. The figure shows the correlation coefficient, r, for the flatplate and uncovered cavities simulation. The correlation between pressure fluctuations at the boundary condition and at the spanwise location where each cavity begins (cavity edge) is below $r = 0.1$, being close to the minimum correlation calculated: $r_{\text{noise}} \approx 0.05$. The figure indicates that the spanwise length of the domain is sufficient for a low influence of the boundary condition in the cavity flowfield. In wall units, the distance between the periodic boundary condition and the countersunk cavity edge is $z^+ = 1.4 \times 10^3$. The spanwise distance is one order of magnitude larger than the spanwise extent of the turbulent structures characteristic of high-amplitude pressure peaks, as expected in a zero-pressure gradient turbulent boundary layer, with a similar Re_θ [128].

4.3.2. COMPARISON WITH EXPERIMENTS

Figure 4.8 shows the experimental and simulated streamwise velocity, u, and turbulence intensity (TI) profiles of the boundary layer, measured upstream of the cavity location. The profiles from the simulation are

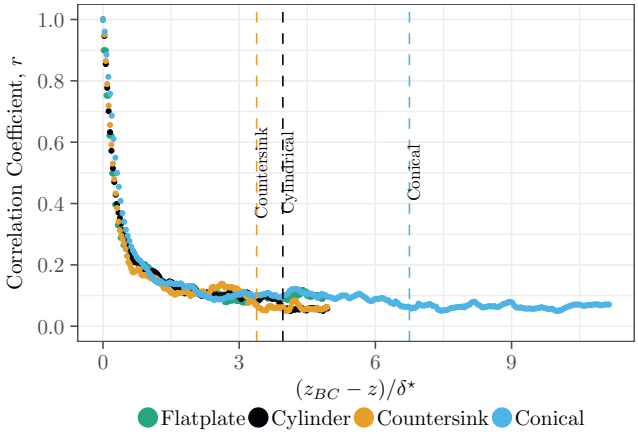

Figure 4.7: Spanwise variation of correlation coefficient for the flatplate and uncovered cavities simulation. The points are sampled at the streamwise centre of the domain, and at the flatplate surface height, i.e., at $x = 0$ and $y = 0$. The reference point is the spanwise location of the periodic boundary (positive z). The vertical dashed lines are the spanwise location of the cavity edges.

measured 3 cm upstream of the cylindrical cavity center and the profiles for the experimentally measured profiles were sampled 10 cm upstream of the cylindrical cavity. The turbulence intensity is defined as:

$$\mathrm{TI} = u'/U_\infty, \tag{4.3}$$

where u' is the root mean square (RMS) of the streamwise velocity fluctuations in the boundary layer. The profiles are normalized with the free–stream velocity, U_∞. Figure 4.8a indicates that the simulated TBL has a slightly higher velocity deficit than the experimental TBL. The boundary layer thickness is 3.3 cm in the simulation and 3.7 cm in the experiment. This leads to a negligible difference in momentum thickness between the experiment and the simulation (below 3%). The ratio θ/L has been identified as a dominant driving parameter for cavity flow [100, 130], and the simulation and experiment have equivalent ratios. The momentum thickness–based Reynolds number is therefore also identical in the experiment and the simulation: $Re_\theta = 8.6 \times 10^3$. The shape factor of $\delta^*/\theta = 1.3$ is indicative of a fully developed simulated turbulent boundary layer [131].

Figure 4.8b shows that, for $y^+ > 100$, the boundary layer TI levels in the simulation are close to those from the experiment. $y^+ \approx 50$ was the lowest wall distance at which experimental hot-wire measurements were made, due to limitations of the hot–wire measurement system.

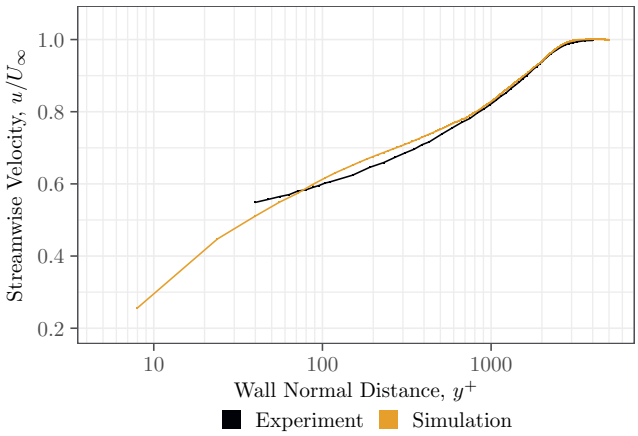

(a) Velocity profile

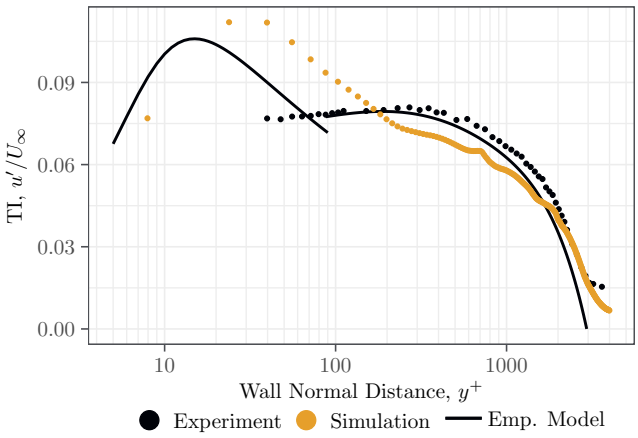

(b) TI profile

Figure 4.8: Simulated and experimental boundary layer profiles: a) Velocity profile and b) turbulence intensity profile. Empirical turbulence intensity profiles were obtained with Marusic's model [129].

Marusic's empirical model was used to estimate the boundary layer TI profile close to the wall [129], using experimental data as input. Marusic's empirical model estimates a boundary layer TI profile from the inputs: δ_{99}, U_∞ and u_τ. The experimental u_τ is obtained from Re_θ, using the Kármán–Schoenherr (KS) formula [132]. Figure 4.8b shows a reasonable agreement between the simulated and empirical TI profiles, with the model's estimate of TI having a lower peak. This result indicates that the highest TI levels in the simulation may be slightly higher than in the experiment. The result is associated with the

(approximately 10%) higher wall shear in the simulation, in comparison with the experiment. The study focuses on the relative difference between the turbulent fluctuations upstream of the cavities and at the cavity bottoms. Therefore, small differences in turbulence levels over the flat plate, between experiment and simulation, are assumed to have minimal effect on the analysis.

Figure 4.9 compares the wall pressure spectra at the bottom of each cavity from the experiment with those of the simulations. ΔSPL is defined as the difference between the wall pressure spectrum at the bottom of the cavity and the wall pressure spectrum upstream of the cavity, i.e., the flush microphone measurement:

$$\Delta\mathrm{SPL} = \mathrm{SPL}_{\mathrm{cavity}} - \mathrm{SPL}_{\mathrm{flush}}. \tag{4.4}$$

Figure 4.9 shows a good agreement between the numerical and experimental ΔSPL for each uncovered cavity. This indicates that the flow features that lead to pressure fluctuations at the cavity bottoms are realistically represented in the simulations. Only for frequencies above 4 kHz, do the simulations over–predict the pressure fluctuations at the bottoms. Figure 4.9 shows that the simulations for the covered cavities show a reduction of the TBL pressure spectra at the bottom of the cavities with respect to the flush spectrum. These trends agree with the experiment but under–predict the amount of attenuation. This result suggests that the attenuation, caused by the stainless–steel cloth cover, is higher in the experiment than in the simulation, especially towards higher frequencies. The results suggest that, when eddy size becomes small in comparison with cavity aperture diameter (see discussion of Fig. 4.10), the validity of the equivalent fluid approach for simulating covered cavities is reduced. The discrepancy in the amount of attenuation is independent of the cavity geometry, and is therefore considered to not affect the conclusions of this investigation.

Figure 4.10 shows the coherence length of the TBL pressure fluctuations calculated from a flat plate simulation without a cavity present. The sampling location of the data was centered at $x = 0$, i.e., at the cavities' streamwise location. Figure 4.10a shows that the streamwise coherence length, which is indicative of eddy size, is comparable to the cylindrical and countersunk cavity aperture diameters at low frequencies (at 1000 Hz). The spanwise coherence length of the pressure fluctuations, is considerably smaller than the cylindrical cavity's diameter, for frequencies higher than 350 Hz). As seen in previous experimental studies, e.g., Refs. [133, 134], the coherence length agrees with Efimtsov empirical model (see dashed line) at high frequencies.

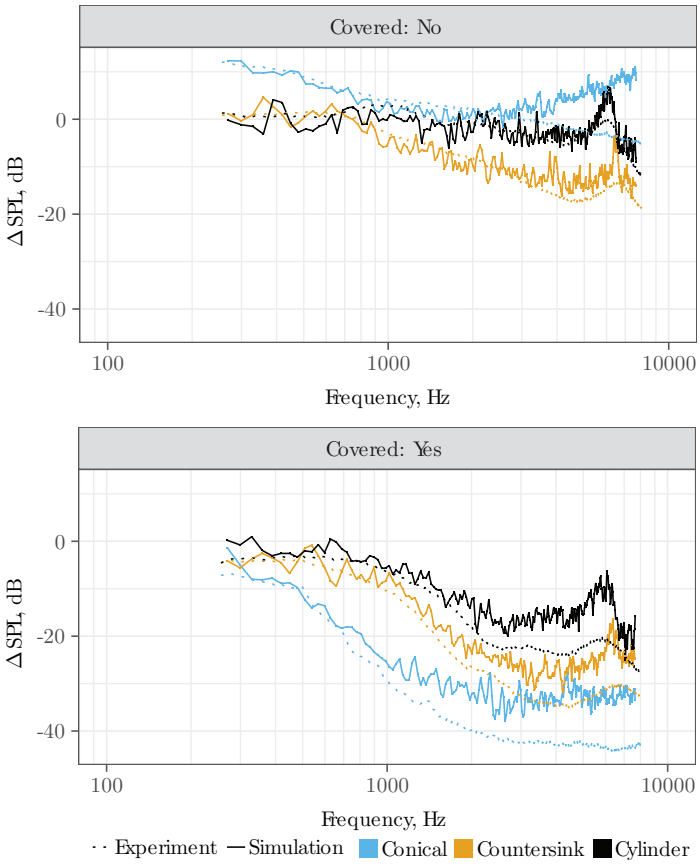

Figure 4.9: Simulated and experimental pressure spectra: difference between the spectra at the bottom of the cavities, and the spectra over the flat plate for both uncovered cavities and covered cavities.

4.4. UNCOVERED CAVITIES

4.4.1. EFFECT OF CAVITY GEOMETRY ON THE TIME–AVERAGED FLOWFIELD

Figure 4.11 presents the average streamwise velocity, u, and static pressure coefficient:

$$C_p = (p_s - p_\infty)/q_\infty, \tag{4.5}$$

inside the uncovered cavities. p_s is the static pressure, p_∞ is the free-stream static pressure and q_∞ is the free-stream dynamic pressure. Figure 4.11 shows u/U_∞ and C_p in a plane aligned with the cavity

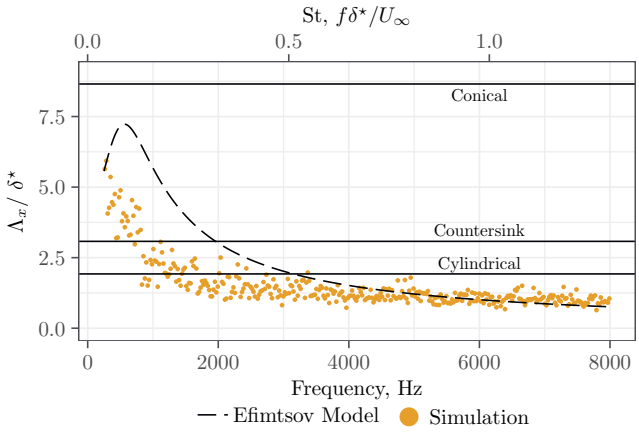

(a) Streamwise

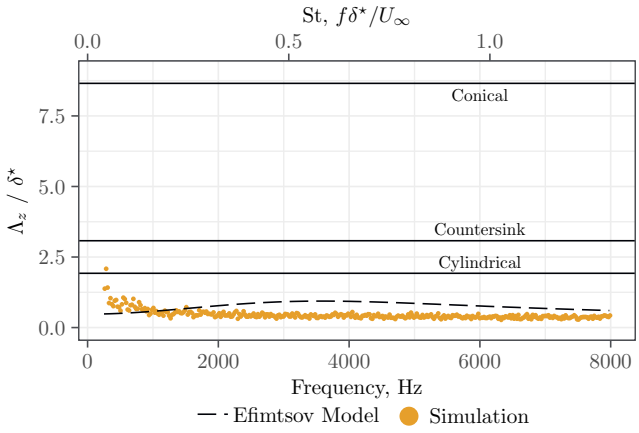

(b) Spanwise

Figure 4.10: Coherence length of the pressure fluctuations at $y = 0$ for the flat plate simulation, in comparison with Efimtsov empirical models: a) Streamwise coherence length and b) Spanwise coherence length. The cavity diameters are shown for reference as horizontal lines. Data extracted from a flat plate simulation (without cavity), at $x = 0$.

center–line, $z = 0$. The streamtraces in Fig. 4.11 are defined as lines which follow the local in–plane velocity vector.

The comparison of Figs. 4.11a and 4.11b indicates that decreasing the wall angle ψ from 90° to 45° and increasing d_c/D to 3, for the case of the countersunk cavity, shift the center of recirculation away from the bottom, resulting in a lower velocity along the bottom when compared to the cylindrical cavity. Figure 4.11c indicates that further

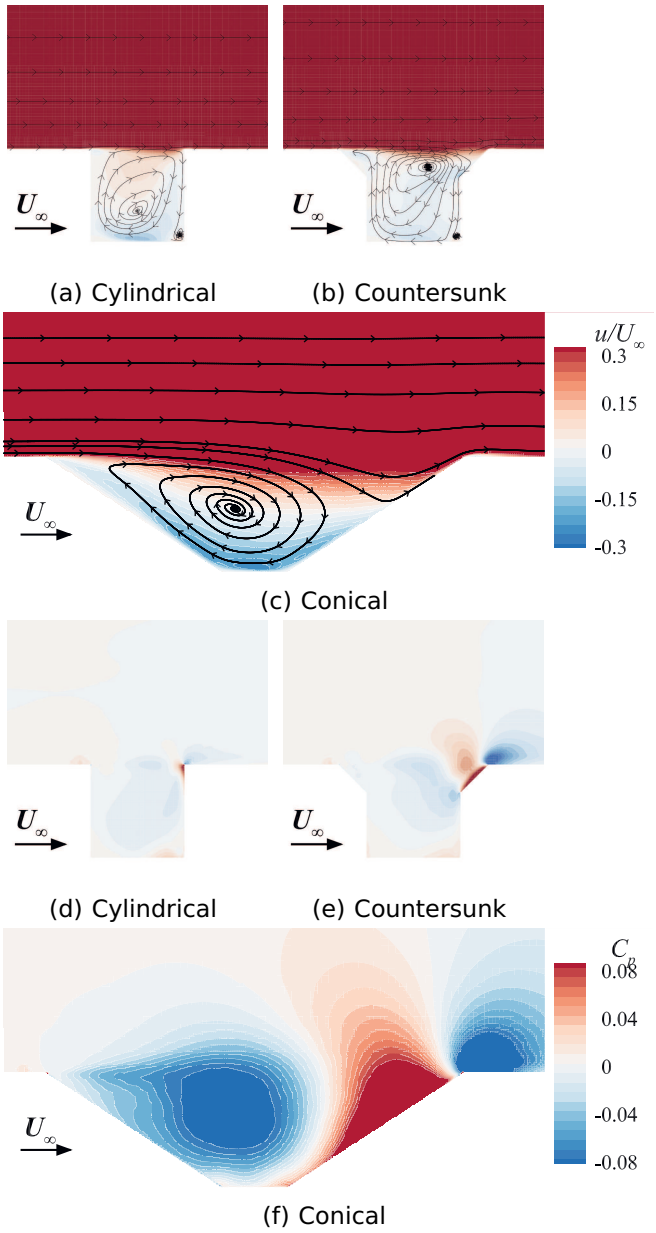

Figure 4.11: Uncovered cavities average flowfield, located at the $z = 0$ plane (center of the cavities). Streamwise velocity contours and in–plane streamtraces: a) cylindrical, b) countersunk, and c) conical. Pressure coefficient contours: d) cylindrical, e) countersunk, and f) conical.

increasing d_c/D to 1.0 (see Fig. 4.1) and increasing the cavity aperture, increases the recirculation velocities at the bottom, in contrast with the countersunk cavity. Furthermore, the streamtraces in Fig. 4.11c indicate that, due to the upstream wall angle, the stagnation point on the downstream cavity wall moves toward the bottom, changing the recirculation pattern. Shifting the recirculation towards the bottom of the cavity increases pressure fluctuations at the bottom, as it leads to the convection of eddies from the boundary layer towards the bottom. Additionally, higher velocities inside the cavity are associated with higher shear forces, which generate turbulence. The wall friction due to increasing cavity wetted area has minimal effect on recirculation because the reduction in velocity at the bottom does not increase substantially with the increasing wetted area.

A comparison of Figs. 4.11d and 4.11e shows that the downstream angled wall of the countersunk cavity leads to regions of higher positive and negative C_p, with a corresponding larger pressure gradient. The downstream edge of the conical cavity also leads to a high C_p region at the stagnation point inside the cavity (Figs. 4.11c and 4.11f). Pressure gradients can accelerate or decelerate the flow inside the cavity, further increasing the shear forces acting on the fluid.

Figure 4.12 shows average spanwise velocity, w, contours in the $x = -0.25L$ plane. The angled walls of the countersink and conical cavities increase the spanwise velocity at the top, compared to the cylinder, as shown in Figs. 4.12b and 4.12c. This result and the previous one indicate that the upstream angled wall of the countersunk and conical cavities cause stronger velocity fields within the cavities that contribute towards increased pressure fluctuations, i.e., turbulence, at the top of the cavity.

4.4.2. Influence of wall angle and countersink depth on pressure fluctuations

Figure 4.13 shows the contours of the root mean square of the pressure fluctuations, p'_{rms}, for the uncovered cavities. This figure shows that p'_{rms} is higher in the shear layer at the top of the cavities due to the local turbulence generation and vortex shedding. Beneath the shear layer, the differences between the cavities are associated with the cavities' respective recirculation patterns, as discussed previously. p'_{rms} increases near the downstream walls and the bottoms of the cavities compared to the upstream wall where the local velocity is lower. Decreasing the recirculation velocity at the bottom results in lower values of p'_{rms} as seen when comparing the countersunk cavity in Fig. 4.13b to the cylindrical (Fig. 4.13a) and conical cavities (Fig. 4.13c).

Decreasing the downstream wall angle from 90° (Fig. 4.13a) to 45° (Fig. 4.13b) or from 45° to 30° (Fig. 4.13c), increases the levels

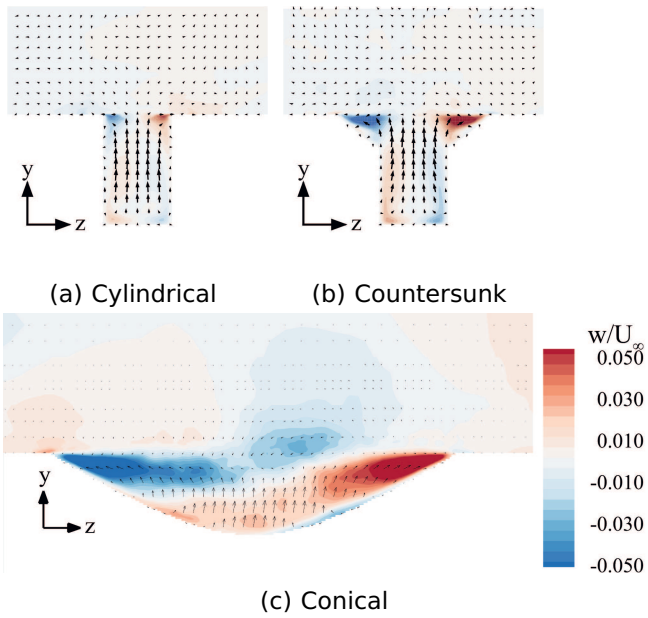

(a) Cylindrical (b) Countersunk

(c) Conical

Figure 4.12: Average spanwise velocity, w, contours and in-plane vectors ($x = -0.25L$ plane) for the following uncovered cavities: a) cylindrical, b) countersunk, and c) conical.

of p'_{rms} in the vicinity of the stagnation point. This location is where vortex impingement and subsequent deformation occurs, due to strong pressure gradients in the region. However, the effect of decreasing downstream wall angle on p'_{rms} at the bottom is minimized when the cavity has a countersink depth ratio of 0.3, as indicated by the comparison between cylindrical and countersunk cavities (Figs. 4.13a and 4.13b). Decreasing the upstream wall angle from 90° to 30° increases p'_{rms} within the shear layer. This is in line with the inclined angle backward facing step flow results presented in Ref. [107].

Figure 4.14 shows the pressure contours and the vortices present in an instantaneous streamwise slice at $z = 0$. The λ_2 criterion is used to identify vortices, where $\lambda_2 < 0$ indicates vortex structures [135]. The streamtraces show instantaneous convection paths for vortices within the cavities.

The shedding location of the Kelvin–Helmholtz type vortices [99] is near the spanwise center ($z = 0$) of the upstream edge of the cylinder in Fig. 4.14a. For the cylindrical cavity, these vortices are of approximately constant size in the spanwise direction. The vortices are convected within the shear layer until they impinge on the downstream wall, emitting a pressure wave, or are convected towards the cavity bottom.

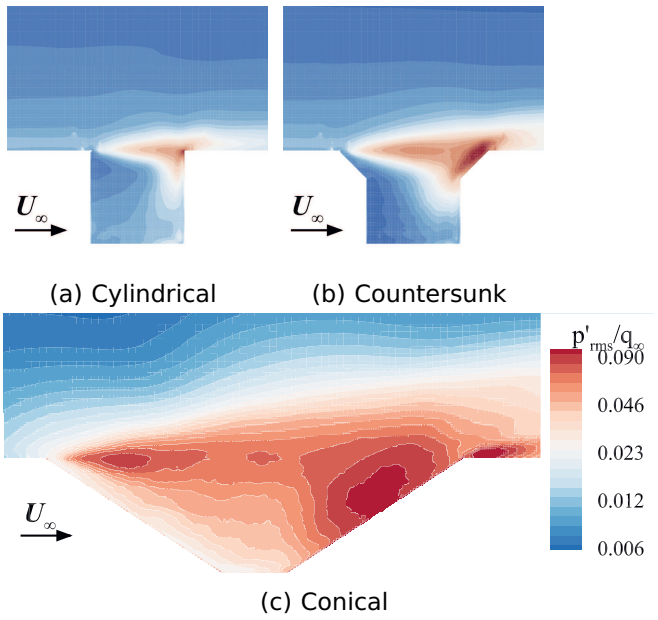

(a) Cylindrical (b) Countersunk

(c) Conical

Figure 4.13: Contours of the root mean square of the pressure fluctuations, for the uncovered cavities: a) cylindrical, b) countersunk, and c) conical.

Decreasing the wall angle alters the convection path of the vortices and results in the vortex shedding behavior becoming increasingly unsteady. This is shown in Figs. 4.14b and 4.14c. When ψ decreases to 45° for the countersunk cavity, the vortices exhibit similar shedding behavior as the cylindrical cavity. However, the recirculation region at the angled downstream wall entraps and distorts the shed vortices, which partially explains the larger region of elevated turbulence spread along the angled downstream wall shown in Fig. 4.13b. This is in contrast to the cylindrical cavity where the region of elevated turbulence is concentrated in the shear layer. However, unlike the cylindrical cavity with $d_c/D = 0$, the vortices for the $d_c/D = 0.3$ case tend to be transported away from the cavity bottom, reducing p'_{rms} at the cavity bottom. For the conical cavity, the large region of pressure fluctuations shown in Fig. 4.13c, is explained by the vortices not following a well–defined streamtrace, and thus impinging at random locations along the downstream wall as well as the flowfield induced by the conical cavity's upstream angled wall increasing the deformation of the vortices.

The regions of negative C_p, shown in blue in Figs. 4.14a and 4.14b for the cylindrical and countersunk cavities, correspond to the vortex cores [99], an example of which is indicated with an arrow in Fig. 4.14a. When

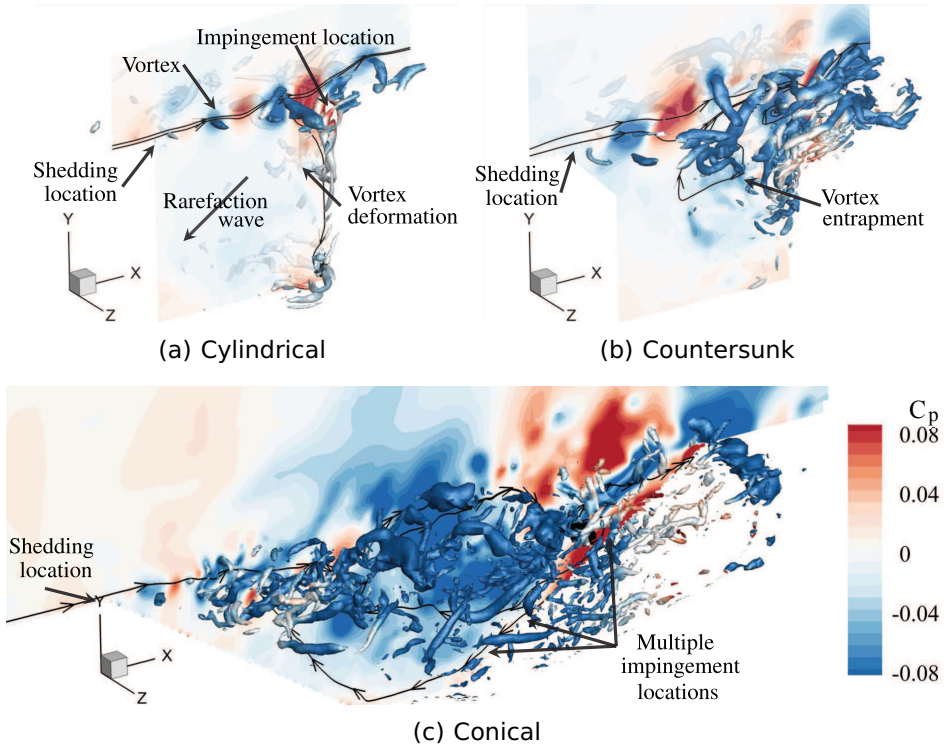

Figure 4.14: Instantaneous visualization of the pressure fluctuation contours, p', vortex shedding, and velocity streamtraces. Vortex cores are identified using the λ_2 criterion with the isosurfaces defined by $\lambda_2 < -2 \times 10^8$ for the following cavities: a) cylindrical, b) countersunk, and c) conical.

these vortices impinge on the downstream wall, a rarefaction acoustic wave is produced and propagates from the impingement location [99]. The resulting negative pressure from this wave can be seen within the cylindrical cavity in Fig. 4.14a. Acoustic compression waves are generated in between the impingement of these vortices, as described by Ref. [98]. Unlike the cylindrical and countersunk cavities, the pressure fluctuations within the conical cavity are not substantially influenced by vortex impingement.

HYDRODYNAMIC AND ACOUSTIC COMPONENTS OF THE PRESSURE SPECTRA

The wavenumber–frequency spectra at the bottom of the uncovered cavities are shown in Fig. 4.15. In this figure, the contributions to the spectrum by both the hydrodynamic and acoustic phenomena are seen. The spectra within the hydrodynamic regions are concentrated near

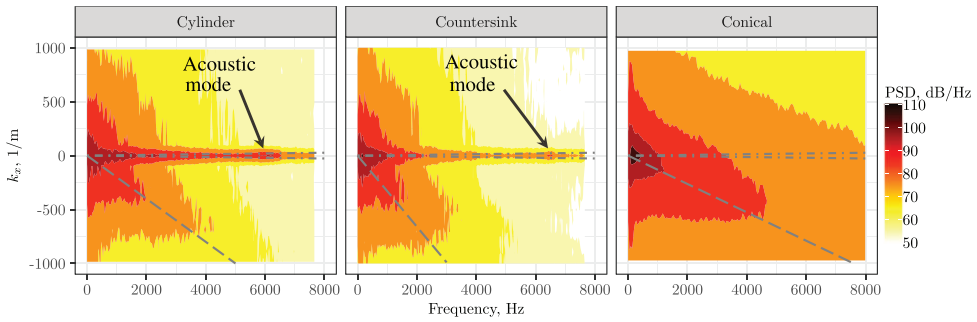

(a)

Figure 4.15: Wavenumber - frequency spectra across the bottom of the uncovered cavities (- -) lines represent the hydrodynamic peak due to recirculation, (– •) represents the area between the acoustic region. $p_{\text{ref}} = 2 \times 10^{-5}$ Pa.

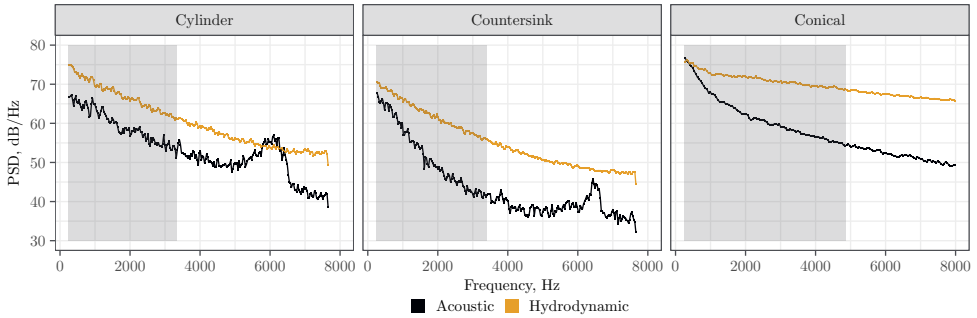

Figure 4.16: Wavenumber spectra decomposed into acoustic and hydrodynamic components for all three uncovered cavities. Shaded area is the region of uncertainty, defined as $f \leq U_\infty \Delta k$.

the wavenumbers, $k = \frac{f}{U_c}$, associated with the recirculation velocity, i.e., U_c along the bottom of the cavity. This velocity is $-4.9\,\mathrm{m\,s^{-1}}$, $-3.0\,\mathrm{m\,s^{-1}}$, and $-7.6\,\mathrm{m\,s^{-1}}$ for the cylindrical, countersunk, and conical cavities. The spectrum levels within the hydrodynamic region decrease with decreasing recirculation velocity due to the reduced transport of turbulence across the bottom. The spectra in and near the acoustic regions, seen for the cylindrical and countersunk cavities, are due to the pressure waves from the vortices impinging on the downstream wall. Peaks at 6.0 kHz and 6.3 kHz are the cylindrical and countersunk cavity acoustic depth modes. However, the conical cavity does not have a well–defined acoustic region. This suggests that the scattered

energy due to the vortex impingement seen in Fig. 4.14c does not result in strong pressure waves from the downstream wall. At the top of all cavities (not shown), the spectrum levels are highest near the TBL convective wavenumber, k_c, which is defined as $k_c = \frac{f}{U_c}$. The flow at the top of the cavities has a convective velocity, $U_c = 18\,\mathrm{m\,s^{-1}}$, which is 52% of the free stream velocity, U_∞.

Figure 4.16 shows the pressure spectra for the acoustic and hydrodynamic components of the pressure field. The acoustic component is calculated by integrating the spectrum within the acoustic wavenumber domain, while the hydrodynamic component is represented by the integrated spectrum outside this acoustic region. In these simulations the cavity diameters are smaller than the acoustic wavelength, i.e., for frequencies below 34 kHz for the cylindrical cavity. Therefore the wavenumber resolution, Δk_x, is larger than the acoustic wavenumber, $k_0 = f/c_0$, below this frequency. $\Delta k_x = 1/L$ is $100\,\mathrm{m^{-1}}$ for the cylinder and countersunk cavities, and is $142\,\mathrm{m^{-1}}$ for the conical cavity. As a result, the spectral energy of the acoustic region is concentrated in the $k_x = 0$ region. The shaded area in the figures highlights the frequency bands where differentiating between acoustic and hydrodynamic propagation is difficult.

The hydrodynamic components of the spectra in Fig. 4.16 are dominant relative to the acoustic component for all three cavities. The cylindrical cavity's acoustic depth mode at 6.0 kHz is identifiable in the spectrum of the acoustic component and has an amplification of 8.5 dB with respect to the broadband spectrum level. The frequency of this depth mode agrees with predictions, using the expression $f = \frac{(2n+1)c_0}{4D+\delta}$, where n is the mode number beginning at 0, c_0 is the speed of sound, and δ is the correction term for the cavity diameter [28]. The acoustic component is higher for the cylindrical cavity than those of the other cavities due to the stronger pressure waves generated by the impinging vortices. The countersunk cavity's hydrodynamic component is lower than that of the cylindrical cavity due to the lower recirculation velocity. The countersunk cavity's depth mode at 6.3 kHz is also identifiable within the acoustic component of the spectrum. The countersunk cavity's acoustic mode is amplified by 7.5 dB, which is less than the cylindrical case due to the higher countersunk ratio of 0.3 resulting in a shallower straight walled portion [28]. The conical cavity's hydrodynamic component is higher than its acoustic component because the vortex impingement produces lower amplitude pressure waves compared to the other cavities. Additionally, the flow along the downstream wall transports turbulence across the bottom resulting in higher pressure fluctuations. This explains the higher hydrodynamic spectral levels for the conical cavity compared to the other two cavities. The depth mode for a conical cavity is estimated to be at $f = 5.0$ kHz using the method described in Scavone [136]. This mode is not identifiable, presumably

because conical cavities have much weaker depth modes than straight walled cavities due to their lower quality factor [28].

4.5. COVERED CAVITIES

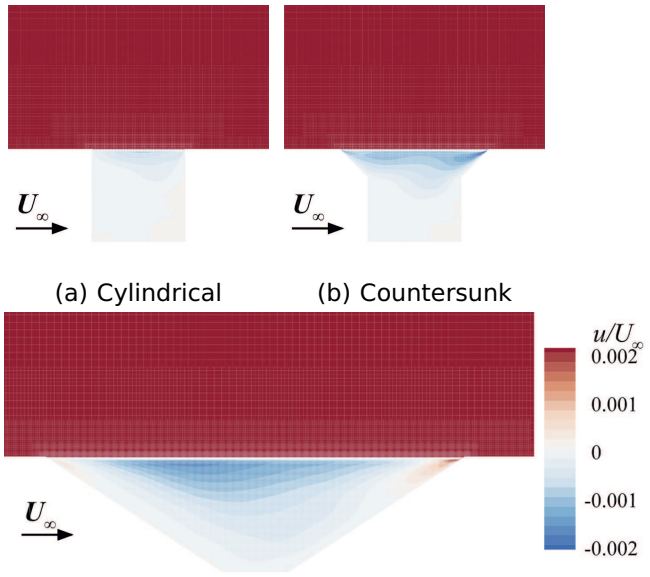

Figure 4.17: Average streamwise velocity field for the following covered cavities: a) cylindrical, b) countersunk, and c) conical.

In contrast to the uncovered cavities, the streamwise velocity magnitudes of the covered cylindrical, countersunk, and conical cavities are below $0.002U_\infty$, as shown in Fig. 4.17. Therefore, the flow beneath the cover is nearly stagnant. Covering the cavities eliminates the dominant propagation mechanism of the pressure fluctuations. As expected, eliminating recirculation partially explains why the covered cavity spectra in Fig. 4.9 are lower than the uncovered cavities.

4.5.1. PRESSURE FLUCTUATIONS DUE TO TBL EDDIES OVER THE COVERING

Figure 4.18 shows the band–pass filtered pressure at the 1 kHz one–third–octave band for each cavity. This frequency band was chosen because the integral length scale of the eddies, as shown in Fig. 4.10a, is of the order of the diameter of the cylindrical cavity. The TBL eddies convect across the top of the covering at the boundary layer

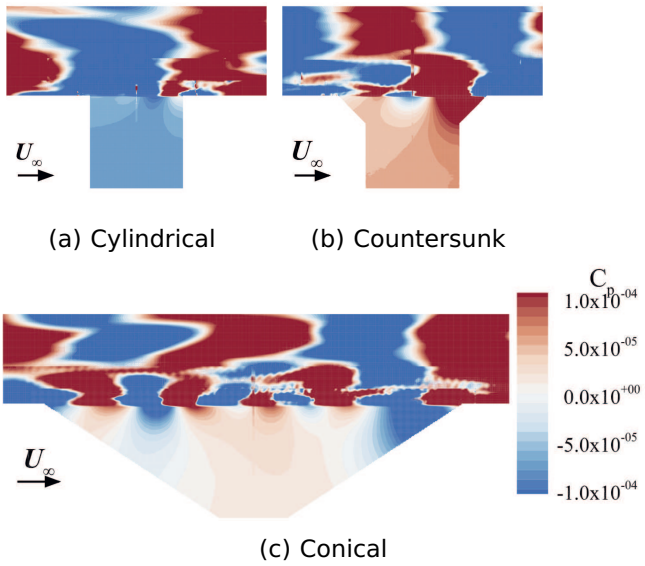

(a) Cylindrical (b) Countersunk

(c) Conical

Figure 4.18: Band–pass filtered pressure fluctuations at the 1.0 kHz one–third–octave frequency band. The streamwise slice is centered at z = 0.0 cm for the following covered cavities: a) cylindrical, b) countersunk, and c) conical.

convective velocity, U_c [137]. Immediately above the covering, y = 0.0 cm, the pressure fluctuations due to the eddies are visible. The distance between these eddies is indicative of the TBL streamwise coherence length, which approximates the size of the eddies. The eddies immediately above the cover create a pressure field inside the cavity. This pressure field decays as it expands within the cavity volume. This pressure field is the dominant source of noise (p') at the bottom of the covered cavities and can be considered a near field acoustic perturbation.

The cylindrical cavity band–passed pressure field is shown in Fig. 4.18a. The pressure field within the cavity is almost spatially uniform (coherent) due to the eddies at the top of the cavity being close in size to the cavity aperture size. As a result the pressure field within the cavity is highly coherent with respect to the microphone location (center of the cavity bottom). The countersunk cavity in Fig. 4.18b exhibits similar behavior as the cylindrical cavity with the pressure field becoming increasingly uniform towards the cavity bottom. At the top, the eddies are smaller than the aperture size. This results in a more complex pressure field at the top of the cavity, especially near the

angled walls. The pressure field within the conical cavity, shown in Fig. 4.18c, is much less uniform than the other cavities. This is due to the aperture being approximately a factor of 4.5 larger than the eddies, as indicated by Fig. 4.10a. The resulting pressure field within the conical cavity is the summation of the rarefactions and compressions at the top. The eddies immediately above the conical cavity center contribute to p' at the microphone location. This is shown by Fig. 4.18c.

HYDRODYNAMIC AND ACOUSTIC COMPONENTS OF THE PRESSURE FLUCTUATIONS

The wavenumber–frequency spectra for the cylindrical cavity are shown in Fig. 4.19. Figure 4.19a shows the spectrum just beneath the covering, $y = -1.5 \times 10^{-3}$ cm. The covering reduces the amplitude of the spectrum at the top of the cavities compared to the uncovered case in Fig. 4.15 by approximately 20 dB. The spectral energy is more concentrated near the convective wavenumber, k_c, as shown by a similar wavenumber analysis in Ref. [138]. This convective ridge is due to the convecting eddies within the TBL being the primary source of pressure fluctuations. At the bottom of the cylindrical cavity, shown in Fig. 4.19b, the spectrum is highest at or near the acoustic wavenumber, k_0, i.e., at the bottom of the cavity the pressure fluctuations propagate primarily at the speed of sound. The countersunk and conical cavities exhibit similar wavenumber-frequency spectra.

Figure 4.20 compares the hydrodynamic and acoustic components of the spectra at the bottom of all three covered cavities. The acoustic component is dominant at the bottom of all covered cavities. For the covered cylindrical cavity, the acoustic contribution is approximately 20 dB higher than the hydrodynamic contribution at the bottom. The depth mode is visible near 6.0 kHz with a reduced amplitude compared to the uncovered cavity in Fig. 4.16. The porous cover changes the acoustic impedance at the top of the cavity and consequently reduces the quality factor of the cavity [28]. The countersunk cavity's spectrum levels are 5–10 dB lower than the cylindrical cavity. The depth mode is also visible at 6.3 kHz. The covered conical cavity reduces the acoustic spectrum by an additional 10 dB for frequencies greater than 4.0 kHz compared to the countersunk cavity. A small peak near the conical cavity's predicted depth mode can be seen near 4.5 kHz. The acoustic component of the TBL spectra levels at the bottom decrease with increasing cavity aperture size.

MODAL DECOMPOSITION OF p'

Proper orthogonal decomposition was performed on the pressure fluctuations in the 2–D plane at the top (under the covering) and bottom of the covered cavities. Figure 4.21 shows the first three mode shapes, $\boldsymbol{\phi}_r$, sorted by the energy content of each mode, σ_r, at the top of a

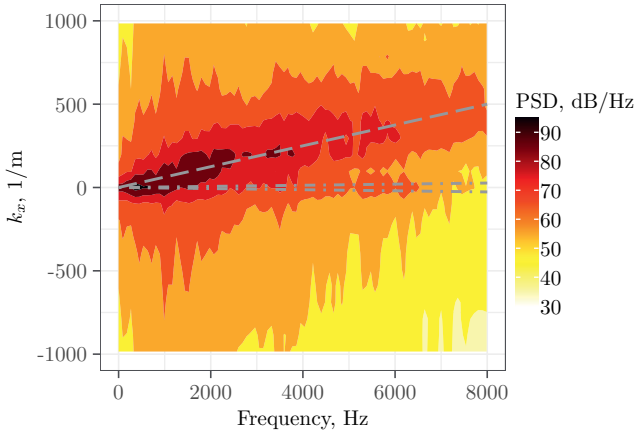

(a) Cylindrical, covered, top

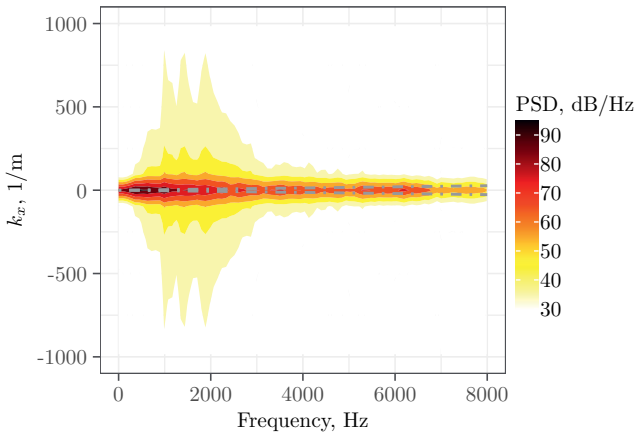

(b) Cylindrical, covered, bottom

Figure 4.19: Wavenumber - frequency spectra across the covered cylindrical cavity (- -) lines represent the hydrodynamic peak, (– •) represents the area between the acoustic region. $p_{\text{ref}} = 2 \times 10^{-5}$ Pa. a) Top of the cylindrical cavity; b) Bottom of the cylindrical cavity.

covered cylindrical cavity. The energy of each mode, as a percentage of the sum of the energy of all the modes, is illustrated by the vertical grey bar. The first mode contains about 61% of the total energy and resembles an acoustic plane wave mode ($m = 0$, $\mu = 1$), where m is the azimuthal mode number, and μ is the radial mode number [139]. This work uses the numbering convention where the radial mode number index begins at 1, per the Refs. [140] and [139]. This mode is dominant because the cavity diameter is close to the eddy size for frequencies

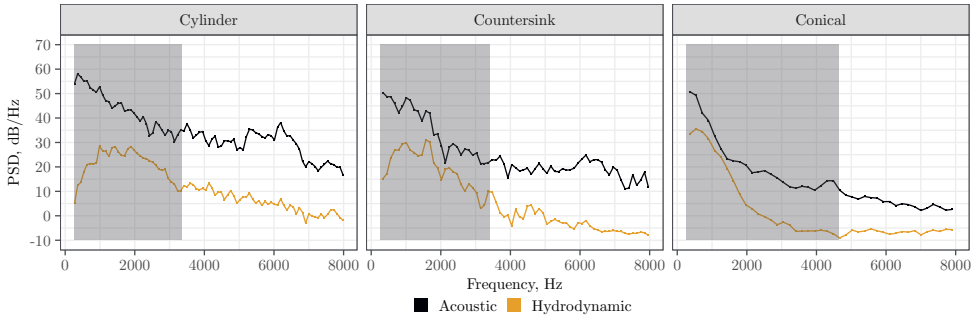

Figure 4.20: Decomposition of the wavenumber spectra into acoustic and hydrodynamic components for all three covered cavities. Shaded area is the region of uncertainty.

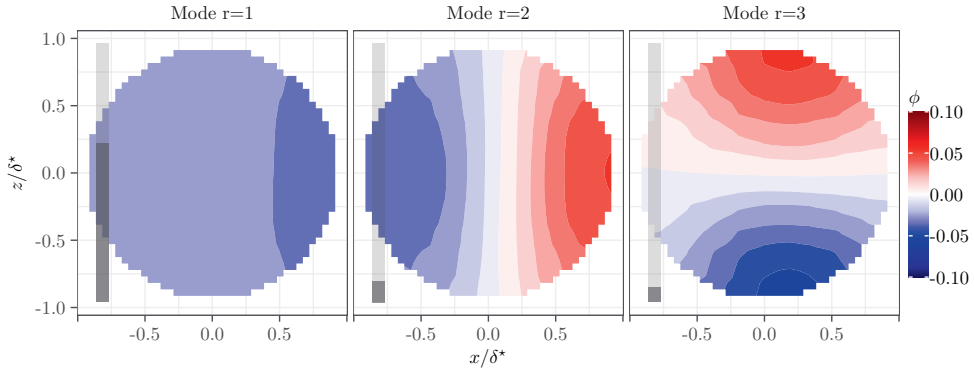

Figure 4.21: First three mode shapes, ϕ, at the top of the covered cylindrical cavity, y $= -1.5 \times 10^{-2}$ cm. The modes are sorted by energy content, with the grey bars indicating the percentage of total energy, $\sum \boldsymbol{\sigma}$, each mode contains.

below 2.0 kHz, shown in Fig. 4.10. Modes 2 and 3 have the same shape as the acoustic modes in a circular duct [139]. Specifically, they are the $m = 1$, $\mu = 1$ acoustic mode. Thus, Fig. 4.21 suggests that acoustic modes are dominant when the eddy size is larger than the cavity aperture.

The first three POD modes at the top of the covered conical cavity are shown in Fig. 4.22. Unlike the cylindrical cavity, whose first mode represents the majority of the energy in the pressure field, the energy at the top of the conical cavity is spread out across more modes, with the first mode having only 1.3% of the total energy. This is due to the conical aperture diameter being larger than the TBL streamwise coherence length, as shown in Fig. 4.10. The mode shapes do not correspond to acoustic mode shapes as the pressure fluctuations are

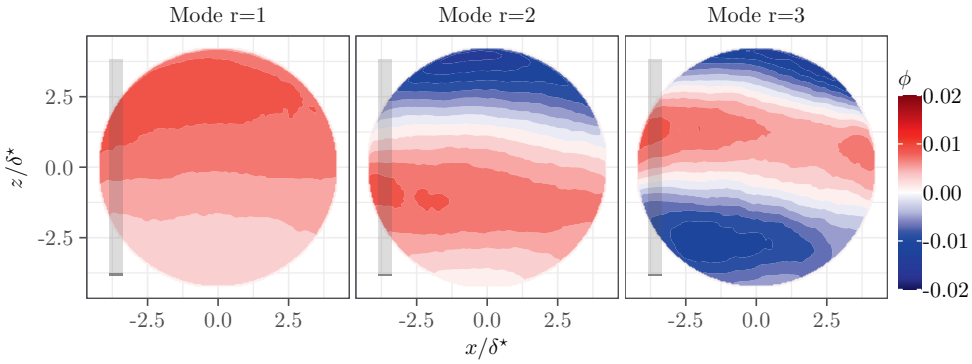

Figure 4.22: First three mode shapes, ϕ, at the top of the covered conical cavity, y = -1.5×10^{-2} cm. The grey bars indicate the percentage of total energy, $\sum \boldsymbol{\sigma}$, each mode contains.

not coherent with a single eddy due to the conical cavity diameter being a factor of 4.5 larger than the cylindrical diameter.

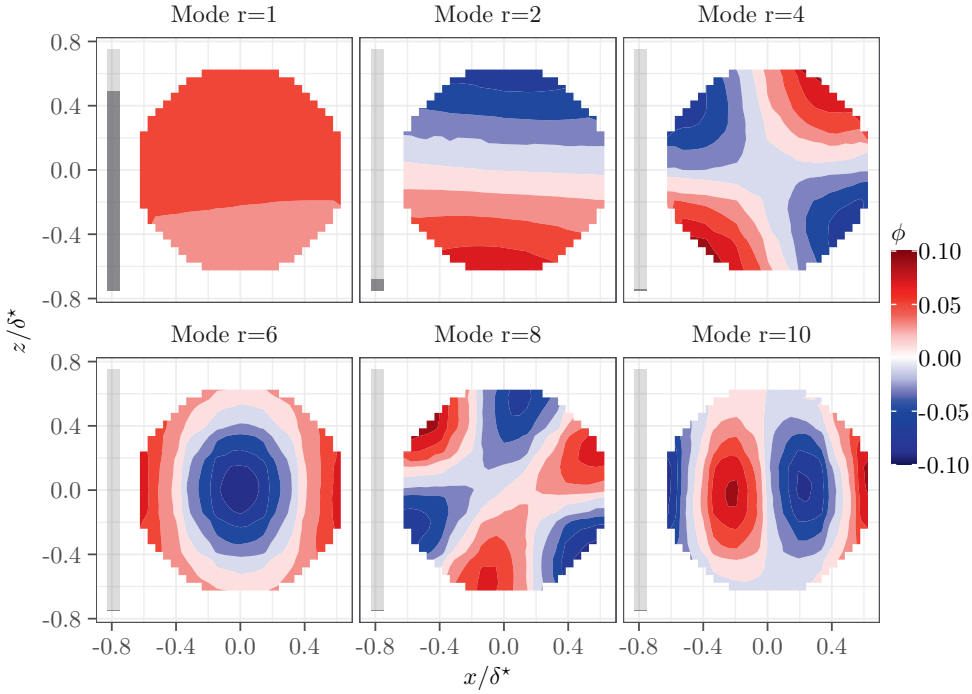

Figure 4.23: First six unique modes, $\boldsymbol{\phi}$, at the bottom of the covered conical cavity. The grey bars indicate the percentage of total energy, $\sum \boldsymbol{\sigma}$, each mode contains.

At the bottom of the covered cavities, the mode shapes correspond to the acoustic mode shapes of a circular duct. This is shown in Fig. 4.23 for the conical cavity. POD mode 1 is similar to the acoustic plane wave mode, ($m = 0$, $\mu = 1$), mode 2 corresponds to the acoustic mode ($m = 1$, $\mu = 1$), mode 4 is similar to the acoustic mode ($m = 2$, $\mu = 1$), mode 6 matches the ($m = 0$, $\mu = 2$) mode, mode 8 is the ($m = 3$, $\mu = 1$) acoustic mode, and mode 10 is the ($m = 1$, $\mu = 2$) mode. The first POD mode contains the largest percentage of the total estimated energy, 83%. This is in contrast to the same mode at the top in Fig. 4.22. The explanation is that the higher order modes are cut off in the cavity and thus exponentially decay as they propagate towards the bottom of the cavity [139, 141]. The first mode and its associated energy propagates to the cavity bottom resulting in it containing the majority of the energy at the cavity bottom. The cut-off condition is defined by the following expression,

$$\frac{\omega a}{c_0} > \alpha_{m\mu} \tag{4.6}$$

where a is the cavity aperture radius and $\alpha_{m\mu}$ is the radial wave number. The radial wavenumber is the Bessel (of the first kind) derivative root [139]. For example, for mode $n = 2$ in Fig. 4.23 ($m = 1, \mu = 1$) the root of the Bessel function of the first kind derivative is $\alpha_{11} = 1.8412$. Eq. 4.6 states that for the cylindrical cavity with a diameter of 1.0 cm the first non-planar acoustic mode will propagate for frequencies above 20.1 kHz. Therefore, only mode 1, the planar mode, is cut on for the frequencies of interest and propagates without decaying.

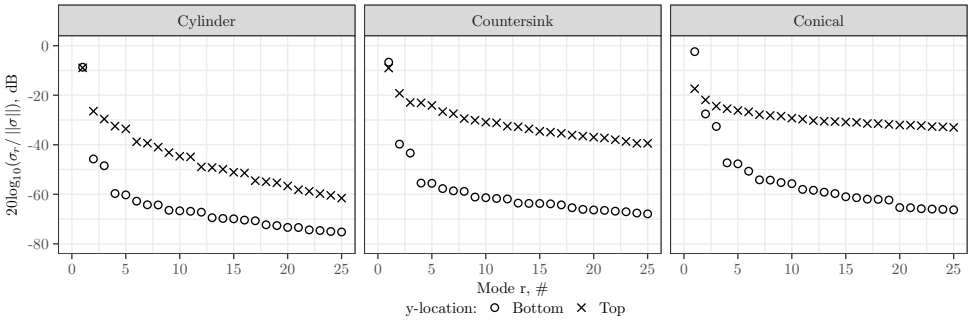

Figure 4.24: Normalized energy per mode, $\sigma_r/\|\boldsymbol{\sigma}\|$, at the top and bottom of the cavities with a stainless steel cloth covering.

The effect of cavity aperture size on the attenuation of the TBL spectra is shown in Fig. 4.24. This figure shows the normalized energy content of each mode, $\sigma_r/\|\boldsymbol{\sigma}\|$, where $\|\boldsymbol{\sigma}\| = \sqrt{\sigma_1^2 + \sigma_2^2 + \cdots + \sigma_r^2}$, at the cavity top and bottom for all three covered cavities. At the top of the cylindrical

cavity, the normalized amplitude of the first mode is 18 dB higher than the next highest mode. As the cavity aperture diameter increases for the countersunk and conical cavities, the difference between the first two modes at the cavity tops decreases to 10 dB and 5 dB. Thus, the energy of the TBL pressure field is increasingly spread across the higher order POD modes for larger cavities. This is due to the cavity aperture size increasing with respect to the coherence length of the TBL and therefore the number of pressure rarefactions and compressions present at the top of the larger cavities, due to the TBL eddies, increases. In contrast, the pressure fluctuations at the top of the smaller cavities can be represented primarily by the planar mode as it contains significantly more energy because the TBL eddies convecting over the cavity are larger than the cavity, as shown in Fig. 4.10a.

At the bottom of all cavities, the first mode has a 30–40 dB higher amplitude that the next highest mode. This is explained by this mode being planar and thus cut on. The higher–order modes are cut off, thus their energy decays exponentially as they propagate from the top to the cavity bottom. Furthermore, as the cavity aperture size increases, the energy at the bottom of the cavity is increasingly concentrated in the first mode, as shown by the conical cavity having a normalized amplitude 6 dB higher than the cylindrical cavity. This is attributed to the TBL energy being spread out over higher–order modes. Therefore, larger diameter covered cavities will attenuate the TBL pressure fluctuations more than smaller ones. This explains why the covered conical cavity attenuates the TBL pressure fluctuations the most, as plotted in Fig. 4.9.

An important result of the wavenumber and POD analyses is that the pressure field beneath a covered cavity exhibits behavior similar to an acoustic wave propagating in a duct. The wavenumber analysis in Fig. 4.20 shows that at the bottom of the cavity the pressure spectral energy is primarily contained within the acoustic wavenumber domain. The POD analysis shows that the pressure fluctuations at the bottom are decomposed into mode shapes that correspond to acoustic circular duct modes. This suggests that modelling the propagation of the TBL pressure field into a covered cavity can be simplified with an acoustic model.

4.6. CONCLUSIONS

The present study used the Lattice–Boltzmann based commercial software package PowerFLOW to simulate turbulent flow with a freestream velocity of $32\,\mathrm{m\,s^{-1}}$ over axisymmetric cavities placed in a flat plate. The following geometries were simulated: a cylindrical cavity, a countersunk cavity, and a conical cavity. In addition to simulating these open cavities, the effect of a finely woven stainless steel cloth covering is evaluated by using an equivalent fluid approach, modelled by

imposing Darcy's law, at the top of each cavity. The simulated pressure spectrum at the bottom of the cavities is validated with experimental measurements. Both show that the uncovered countersunk cavity has the lowest TBL spectrum, followed by the uncovered cylindrical and uncovered conical cavities. The simulated trend in covered cavity performance is also in agreement with the measurements. The covered conical cavity attenuates the pressure fluctuations at the microphone location (cavity bottom) the most and therefore performs the best. The covered countersunk cavity performs better than the covered cylindrical cavity. The porous medium model is found to be capable of modelling the effect of covering the cavities. This analysis identifies the behaviour of the hydrodynamic and acoustic components of the pressure fluctuations within these axisymmetric cavities.

Based on a wavenumber analysis, it is found that the pressure fluctuations at the bottom of uncovered cavities are dominated by hydrodynamic phenomena. These phenomena include recirculation and turbulence generation inside the cavities. Adding a countersink at the top of the cylindrical cavity is found to reduce recirculation towards the cavity bottom by shifting the center of recirculation away from the cavity bottom. However, extending the countersink to the bottom (conical cavity) increases the recirculation velocity and turbulence generation at the bottom. It is reasoned that the upstream angled wall deflects the flow downwards and thus moves the downstream shear layer reattachment point towards the bottom, increasing the recirculation velocity. This is most noticeable in the conical cavity. Furthermore, the angled downstream walls also cause strong pressure gradients inside the cavities, which are associated with turbulence generation in the region of vortex impingement. An optimal uncovered cavity should feature a perpendicular upstream wall to reduce turbulence generation and inflow, an angled downstream wall to reduce the strength of acoustic waves generated due to vortex impingement, and a countersink that does not extend to the bottom of the cavity to reduce the recirculation at the bottom.

Covering the cavity opening with the cloth reduces the flow across the covering, mitigating the entrance of turbulent structures into the cavity. The flow is mostly stagnant inside the covered cavities, and turbulent structures are not produced inside. The pressure field within the cavities is due to the pressure fluctuations generated by the eddies convecting across the top. The pressure field created by the TBL eddies propagates towards the bottom of the cavities at the speed of sound, as shown by the wavenumber analysis. The pressure field within the cavities is dependent on the cavity size relative to the eddy size. When the cavity diameter is nearly the same size as the eddy, the pressure field within the cavity is coherent with the pressure fluctuations corresponding to the convecting eddy. When the cavity is larger than the eddies, the pressure

field from individual eddies is evanescent resulting in attenuation of the pressure field at the cavity bottom.

The proper orthogonal decomposition (POD) analysis shows that the energy distribution of the resulting orthogonal modes at the top of each cavity is dependent on cavity aperture size. For smaller apertures, the energy is concentrated in the first mode due to the cavity size being close to that of the eddy size. For larger cavities, e.g., the conical cavity, a larger ratio of the energy is decomposed into higher order modes with less energy, relative to the smaller cavities, in the first mode. The spectra at the bottom of the cavities is attributed to the first POD mode as this mode is cut on. By shifting more energy into cut-off modes, the larger cavities have lower spectra levels at the cavity bottom. At the bottom of all cavities, the POD modes correspond to acoustic duct mode shapes. This is an important finding as it suggests that the propagation of TBL pressure fluctuations for covered cavities can be accurately modelled with an acoustic approach. The acoustic modeling could be performed using the same approach as Ref. [28]. With this approach, a pressure field representative of the TBL at the top of the cavity could be simulated as propagating acoustically into the cavity.

Covered cavities reduce the TBL spectral levels at the bottom of the cavity more than uncovered cavities. Therefore, future optimization of the cavity geometry should start with a covered cavity. The present work suggests that the propagation of the pressure fluctuations into a covered cavity can be simplified by solving only the wave equation. This may enable optimization of cavity shape and wall material, with affordable computational costs. However, the very-large eddy simulation using the Lattice–Boltzmann method is capable of simulating the propagation of the TBL pressure fluctuations into a cavity and therefore is suitable for evaluating future cavity designs, to improve the attenuation of the turbulent boundary layer pressure fluctuations.

5

WIND TUNNEL WALL LINING FOR AEROACOUSTIC MEASUREMENTS

Sound absorbing porous materials are used to line a wind tunnel wall, in order to reduce reflections. However, lining can have a detrimental effect on acoustic measurements due to an increase in the noise radiated from the walls. In addition, the aerodynamic fidelity of the tunnel can be affected. In the present study, the influence of porous materials on boundary layer aerodynamic characteristics is assessed. The consequent aerodynamic noise scattering is also studied, and compared against the acoustic benefit from absorbing reflections in the test section. Geometric modelling is used to understand the influence of varying absorbing materials in reducing the acoustic interference caused by reflections. The aerodynamic and acoustic results are related to the roughness, and to the viscous and inertial resistivities of the three porous materials studied. The material with highest roughness (polyester wool) is found to result in the strongest turbulent fluctuations in the boundary layer. However, it is the material with the thickest fibre diameter (PU foam), and consequent highest inertial resistivity, which generates the strongest surface noise scattering. Materials with high viscous resistivity, together with low inertial resistivity, are found to provide good sound absorbing capabilities. The results therefore indicate that the best choice of sound absorbing wall treatment for wind tunnel applications results from minimizing roughness and inertial resistivity, while maximizing viscous resistivity.

This chapter is based on the work published in Applied Acoustics **199** (2022) [142].

5.1. INTRODUCTION

Aeroacoustic wind tunnels may suffer from strong reflections, unless acoustically treated. Following from the discussion of Sec. 2.3.2, reflections in open–jet test sections can be mitigated with relative ease, by installing liners outside the flow. On the other hand, closed test section wind tunnels have solid walls at the boundaries of the wind tunnel jet. Hybrid test sections often have walls in this condition as well [79]. These wind tunnels would therefore benefit from the installation of liners which are at the same time acoustically and aerodynamically efficient.

Lining closed wind tunnel walls with a porous material affects the aerodynamic characteristics of the wind tunnel walls' boundary layer. The changes in boundary layer profile can affect (closed) wind tunnel aerodynamic corrections, e.g. if the displacement thickness, δ^*, increases and the effective area of the tunnel reduces. Moreover, increases in the turbulence levels in the boundary layer can increase the scattering of spurious noise sources in the tunnel, e.g. from discontinuities [65]. The influence of porous materials on boundary layers is widely studied (e.g. by [143, 144]). However, literature is lacking studies with a complete trade-off of lining materials for wind tunnels, considering both the aerodynamic changes in the boundary layer, the consequent scattered noise, and the absorption of sound reflections.

The prediction of reflections over lined walls were done in this study with a Geometric Modelling method, previously introduced in Sec. 3.2. Guidatti et al. proposed a similar image-source method in order to obtain a reflection canceller, and in this way to improve experimental beamforming maps [145]. More recent studies have also used the image-source method in order to provide theoretical modifications to the Green's function used in the beamforming algorithm [23, 146]. The post–processing methods discussed in previous studies can be applied to wind tunnel test sections with fully reflective walls, as well as lined walls, by considering the actual reflection coefficient of the walls. However, most of the methods have been tested against experiments with hard-walled wind tunnels. Literature is lacking studies on the applicability of geometric modelling methods, and in particular the image-source method, to the prediction of reflections in lined wind tunnel test sections. The present study helps to fulfil this gap, but the main focus is on investigating the effect of the aerodynamic and acoustic properties of the lining materials, on the aerodynamic and acoustic fidelity of a wind tunnel.

Three sound absorbing materials were tested in the A-Tunnel, at TU Delft. The wind tunnel models consist of acoustically treated plates, each with its own reflection coefficient. The lining materials also have different surface roughness and flow resistivity. The influence of the

lining in the aerodynamic properties of the boundary layer (BL), and, consequently, in the background noise of the tunnel, is characterized. The positive effect of lining the plates is accessed, by analysing the interference between the sound emitted by a known source, with the reflections at each plate. The acoustic measurements are compared against predictions based on geometric modelling. The geometric modelling tool developed in the present study is based on the image source method. For the cases with flow-on, the position of the image source is corrected, in order to take into account the convection of the reflected sound wave.

The methodology followed in the present study is described in Section 5.2. The section includes a description of the experimental setup, of the measurement techniques and computation methods used. Section 5.3 characterises the influence of the lining materials used in the aerodynamic properties of the boundary layer, and consequently on the aerodynamic noise sources in the tunnel, when the flow is on. Sections 5.4 and 5.5 show the comparison between experimental results and geometric modelling predictions, for the flow-off case and for the flow-on case, respectively. Finally, section 5.6 presents an overview of the findings.

5.2. METHODOLOGY

5.2.1. FACILITY AND MODELS

The experiment was carried out in the A–Tunnel, previously described in Sec. 3.1.1. The 40 x 70 cm nozzle was used. At the bottom of the nozzle, the boundary layer is forced to turbulent by a zigzag trip. A vertical wooden plate was installed on the shorter side of the rectangular nozzle, for the baseline tests (hard–wall case). A smooth transition from the nozzle to the plate was ensured by using tape, in this way removing possible gaps. For the acoustically treated test cases, the smooth plate was lined with sound absorbing materials. Figure 5.1 shows that, for the lined plate case, a 0.1 m wooden plate is placed between the nozzle and the start of the lining foam. This wooden plate is flush with the nozzle. The difference in thickness between the 0.1 m wooden plate and each lining leads to a small step, no larger than 3 mm. Figure 5.1a shows the plate lined with polyurethane PU foam installed in the A-Tunnel. The microphone array is placed outside the jet, and parallel to the lined plate. As Fig. 5.1b shows, the speaker was placed 0.25 m outside the jet. The sound source is a miniature QindW speaker [147], which was verified to have very good omnidirectional characteristics up to 2 kHz. The speaker is placed between the plate and the array, so that the plate is representative of a closed wind tunnel back wall. Figure 5.1c indicates the location where flush microphones were installed on the plate. Microphones were installed 1m downstream

of the nozzle, at locations 0 and 1, with z-coordinates 0.02 m and −0.02 m, being $z = 0$ at the plate's spanwise centre. Locations 0c, 0l, 2 and 3 represent the locations where the flow velocity was measured with hot-wire anemometry. The respective physical coordinates are: (0.46, 0, 0)m, (0.46, 0, 0.045)m, (-0.42, 0, 0)m and (-0.46, 0, 0)m.

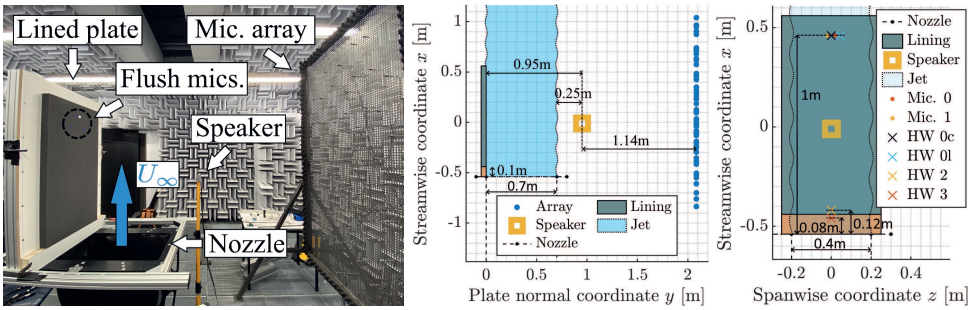

(a) Side-view (picture) (b) Side-view (sketch) (c) Front-view (sketch)

Figure 5.1: Experimental setup. Side-view of a lined plate (with PU foam) installed in the anechoic room (left). Representation of the setup with a lined plate: side-view (centre) and front-view (right).

Four different plates were tested. In addition to the acoustics, the aerodynamic characteristics of the surface also varied, since the plates have different roughness and resistivities. The baseline plate is a clean wooden plate, which is the most sound reflective test-case. The other 3 models consist of the clean plate lined with melamine foam, polyurethane (PU) foam, and polyester wool. The porous materials are shown in Fig. 5.2. The roughness of the materials was inferred from 3D scans of the porous surfaces, obtained with a Keyence VR-5000 series microscope. The arithmetical mean height parameter was used for evaluating surface roughness [148]. The flow viscous and inertial resistivities, R_v and R_i, were obtained from permeability tube experiments (setup described in [91]). The main parameters which affect the aerodynamic and acoustic performance of the test plates are summarized in Table 5.1. Both melamine and wool have very good sound absorption characteristics, whereas PU is more reflective. The sound absorption characteristics of the melamine and wool can be related to their higher viscous resistivity, according to Delany's empirical model [149]. A more detailed characterisation of the acoustic properties of the liners can be found in Section 5.2.3, where the impedance tube tests are discussed. The high viscous resistivity of the melamine and wool also make the materials less permeable to the incoming flow. The high inertial resistivity of the PU foam is also expected to avoid strong

flow velocities inside the material. The polyester wool was the roughest model tested.

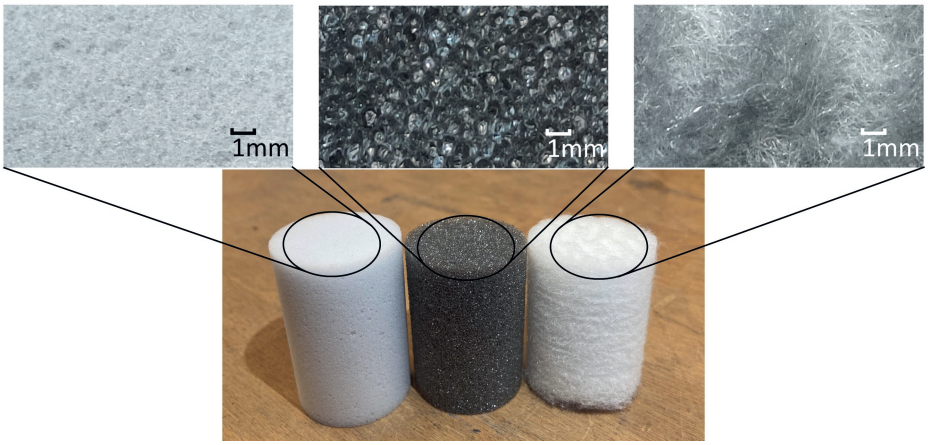

Figure 5.2: Samples of melamine foam (left), PU foam (center), and polyester wool (right).

Table 5.1: Acoustic and aerodynamic properties of the plates tested.

Plate	Average roughness size	Viscous resistivity R_v [kPa s m^{-2}]	Inertial resistivity R_i [kPa s^2 m^{-3}]
Clean	Low	-	-
Melamine	Medium (~ 0.1 mm)	9	2
PU	Medium (~ 0.1 mm)	2	40
Wool	High (~ 0.6mm)	8	2

5.2.2. MEASUREMENT TECHNIQUES

The present section describes the measurement techniques used in the experimental campaign. The flow velocity was measured with the hot-wire, the pressure fluctuations on the wall were measured with

surface microphones, and the acoustic measurements were made with a free-field phased microphone array.

FLOWFIELD MEASUREMENTS

The hot–wire flow measurement technique, discussed in Sec. 3.1.2, was used to measure the streamwise velocity over the plates. The measurements were taken at four locations. Two locations approximately 10 cm downstream of the nozzle, locations 2 and 3, and two locations 1m downstream of the nozzle, locations 0c and 0l (see Fig. 5.1c). At each location, the boundary layer profiles were taken with a 60 point-distribution, following an exponential function. The distribution of the points provides a higher resolution close to the wall, where the velocity gradients are the highest. The minimum sampling frequency used was 25.6 kHz, and the measurement time was 10 s. The velocity measured with the hot-wire was calibrated based on a 4^{th} order polynomial, with respect to the output voltage. A Pitot tube was used as reference, during calibration. The repeatability of the results was confirmed by comparing measurements at equal streamwise location, e.g. locations 0c and 0l.

WALL PRESSURE MEASUREMENTS

The plate was instrumented with a small electret Sonion 8044 microphone, placed at location 0, and a Linear-X M51 microphone, at location 1 (see Fig. 5.1c). The surface measurements were taken to investigate the magnitude of the surface pressure fluctuations. The Sonion microphone was calibrated with the omnidirectional speaker, and using a reference free-field Linear-X M51 microphone. The Linear-X microphones were calibrated with a G.R.A.S. 42AA pistonphone. The surface microphone measurements were taken with a sampling frequency of 51.2 kHz, and with a measurement time of 20 s.

FREE-FIELD ACOUSTIC MEASUREMENTS

The free-field acoustic measurements were made with the phased microphone array shown in Fig. 5.1a. The array consists of 64 free-field microphones, and has been earlier introduced in Sec. 3.1.2. The microphones were calibrated with a G.R.A.S. 42AA pistonphone. The free-field microphone measurements were taken with a sampling frequency of 51.2 kHz, and with a measurement time of 20 s. The array was placed on the opposite side and parallel to the test plate, so that the mirror source reflection stayed directly behind the speaker, from the point of view of the array.

5.2.3. POST-PROCESSING ALGORITHMS

The present section describes the algorithms which were used in the present study. Beamforming was used to estimate the sound levels of the direct source, with a decreased influence from spurious noise sources. A geometric modelling tool was used to predict the reflections in the experiment.

CONVENTIONAL BEAMFORMING

The measurements from the phased microphone array were post-processed with conventional beamforming. This signal processing technique was previously been described in Sec. 3.4.1. The beamforming formulation used allows for quantification of the source noise levels at the receiver location (CBF formulation with $b = 2$ in Eq. 3.12). For estimating the speaker noise levels from the resulting beamforming map, the Source Power Integration (SPI) method outlined in Sec. 3.4.2 is applied.

In this paper, two beamforming scan-planes were considered: one including the location of the speaker, and one scan-plane at the plane of the test plate surface. Both planes are parallel to the array. The scan-plane at the test plate location was used in order to characterize the aerodynamic noise sources for the flow-on and speaker-off experimental test cases. For identifying aerodynamic noise sources at the plate, a correction for the convection of sound waves by the flow is applied in the formulation, as described in [54]. The aerodynamic noise sources were analysed for the test cases at the free-stream velocity, U_∞, of $30\,\mathrm{m\,s^{-1}}$.

ACOUSTIC GEOMETRIC MODELLING TOOL

The experimental acoustic results were compared against predictions from a geometric modelling tool (see description in Sec. 3.2). The tool was used to estimate the acoustic interference effect caused by the reflections on the test plate. This algorithm includes corrections for the sound absorption by the lined plates and for the convection of sound waves by the jet.

Figure 5.3 shows the baseline result of the simulations with the geometric modelling tool. Figures 5.3a and 5.3b show the prediction of the path of the sound rays, from mirror-source to receiver, for the flow-off and -on cases. For the flow-on cases, the perceived location of the mirror-source is above its flow-off location, and is dependent of receiver position. Figure 5.3c shows the predicted spectra, as perceived at the location of the microphone at the centre of the array, for the cases with and without a reflective plate. The spectra are shown as Sound Pressure Levels (see Eq. 3.13).

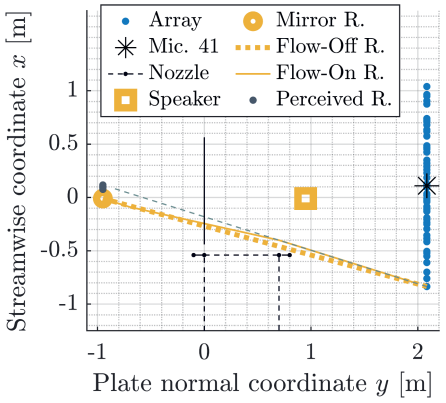

(a) Reflection path: Side-view

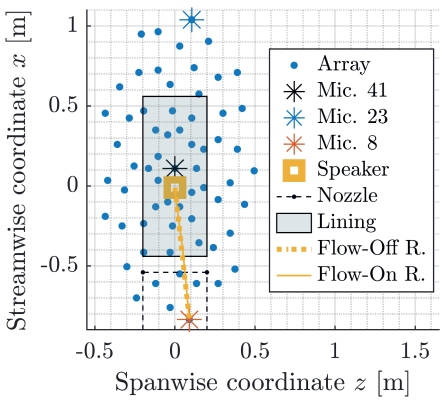

(b) Reflection path: Front-view

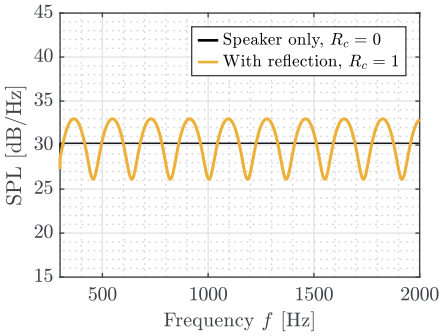

(c) Spectra with and without reflection

Figure 5.3: Prediction of the reflections with the geometric modelling tool. Reflection path for the flow-off and -on cases: side-view (top-left) and front-view (top-right). Predicted spectra for the flow-off cases without reflection and with perfect reflection, from the signal simulated for microphone 41, at the array centre (bottom).

The difference (in dB) between the two spectra shown in Fig. 5.3c is considered in the following sections as the measure of the acoustic interference caused by the test plate reflections, for both experimental and simulated microphone signals, at the receiver location. The acoustic interference is therefore estimated from the difference between the spectra measured with an installed plate and the spectra obtained from the measurement with the speaker in a free-field configuration, i.e. without any installed plate:

$$\Delta\text{SPL} = \text{SPL}_{\text{Test case}} - \text{SPL}_{\text{Free-field speaker}}. \tag{5.1}$$

Positive and negative peaks in ΔSPL are indicative of, respectively, constructive and destructive interference between the direct and reflected sound waves. The geometric modelling algorithm is validated for frequencies in the range 0.3 kHz to 2 kHz, where the speaker is omnidirectional. The speaker omnidirectionality was verified with measurements of the speaker in the empty A-Tunnel room. The measurements were taken with the speaker at constant distance from the array (≈ 1 m), and for different speaker orientations: 0°, 45°, 90° and 180°. The speaker was rotated with respect to a vertical axis aligned with the speaker's support (see Fig. 5.1a).

In order to predict the propagation of reflections with a mirror-source algorithm, it is essential to consider the complex valued impedance of the material [150]. The complex reflection coefficient, $\underline{R}_c$, of the lined plates was calculated based on surface impedance, $\underline{Z}_s$ [150]:

$$\underline{R}_c(f, \theta_0) = \frac{\underline{Z}_s(f) - Z_0/\cos\theta_0}{\underline{Z}_s(f) + Z_0/\cos\theta_0}, \tag{5.2}$$

with θ_0 the specular reflection angle, and Z_0 the impedance of air. The surface impedance was estimated based on normal-incidence impedance tests, which were carried out at the Netherlands Aerospace Centre (NLR). In the impedance tube tests, the samples were placed in front of a (fully reflective) solid wall, as in the two microphones' impedance tube setup described in [151]. Figure 5.4a shows the absolute R_c, and Fig. 5.4b shows the phase shift which occurs at the moment of the reflection. Figure 5.4 also shows the prediction based on Delany's empirical model for surface impedance [149]. Fig. 5.4a shows that the empirical model accurately predicts $R_c(f)$ for the melamine and wool linings. For the PU foam, the prediction is very poor at low frequency (around 700 Hz), where the empirical model predicts a stronger reflection. Delany's model makes use of the viscous resistivity for the surface impedance prediction, while neglecting the inertial resistivity. The empirical model is therefore most accurate for predicting the absorption of porous materials when viscous dissipation plays a dominant role. The PU foam has, however, a low viscous

resistivity and a very high inertial resistivity (see Table 5.1), which is in line with the less accurate prediction from the empirical model for this material.

In Fig. 5.4b, the theoretical phase shift, ϕ, corresponds to the phase shift that occurs, per frequency, for a sound wave which passes through the material and is fully reflected by the solid back plate:

$$\phi_{\text{Theoretical}} = -2d/\lambda, \tag{5.3}$$

being d the thickness of the material and λ the wavelength of the sound wave. Figure 5.4b shows that the phase shift given by the empirical model is, for all materials, similar to the theoretical. The empirical model therefore assumes that the reflection is almost completely at the solid back plate, identically to the theoretical prediction. This trend is similar to what is indicated by the experimental tests for melamine and wool. However, for the PU foam, the experimental phase shift during the reflection is close to 0, indicating that most of the reflection occurs directly at the surface of the foam. In practice, reflections can occur at two locations: at the surface of the foam and at the solid back wall. However, the impedance tube used in the present investigation only provides a single reflection (or absorption) coefficient. In order to take into account both reflections, it is required to have an estimation of the transmission, absorption and reflection capabilities of the material, for example by testing with a four microphones' impedance tube, as described in [151]. Considering both reflections (on the surface of the material and on the back wall) is expected to have a positive impact on predictions based in the mirror-source method. The present study considers one single reflection. The experimental and empirical reflection coefficients indicate different reflection locations, which influences the frequencies at which acoustic interference occurs, between the direct and the mirror sources (see Fig. 5.3).

5.3. EFFECT OF WALL TREATMENT ON BOUNDARY LAYER AERODYNAMIC CHARACTERISTICS AND AERODYNAMIC NOISE

The present section describes the turbulent boundary layer over the test plates (Sec. 5.3.1), and discusses its impact on the spurious aerodynamic noise (Sec. 5.3.2). The goal is to characterize the aerodynamic phenomena which can affect noise measurements in a wind tunnel, counter acting the acoustic improvement achieved.

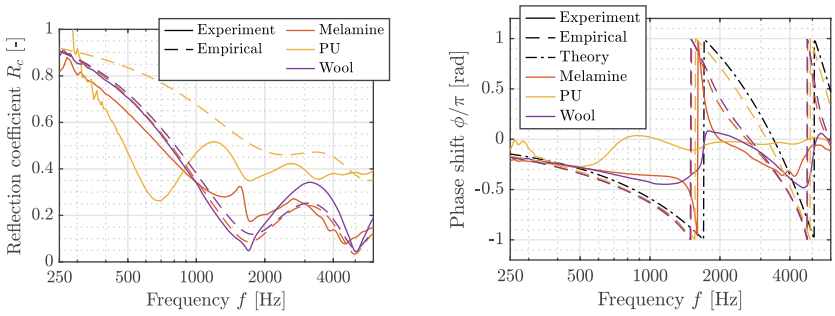

(a) Reflection coefficient (b) Phase shift

Figure 5.4: Acoustic characterization of melamine, PU and polyester wool when backed by a solid wall. Experimental data from the impedance tube and empirical data, from Delany's model. Absolute reflection coefficient (left) and phase shift at the surface of the foam (right), considering a normal incidence reflection ($\boldsymbol{\theta_0} = \mathbf{0}^\circ$).

5

5.3.1. TURBULENT BOUNDARY LAYER CHARACTERIZATION

Figure 5.5 presents the velocity and turbulence intensity,

$$\mathrm{TI} = u'_{rms}/U_\infty, \tag{5.4}$$

profiles for the clean and lined plates, measured at locations 0c and 0l (see Fig. 5.1c). u'_{rms} is the root mean square of the velocity fluctuations. Figure 5.5a also shows the velocity profile at location 3, measured with the clean plate. The shape of the velocity profile does not change along the clean plate, between locations 3 and 0c (0.92 m apart). Figure 5.5a highlights the increase in velocity deficit in the boundary layer, as the roughness of the liner increases. In Fig.5.5b, turbulence intensity is plotted versus streamwise velocity, in order to remove the error caused by the uncertainty in the distance from the measurement point to the wall [152]. For the roughest plate (wool) the hot-wire was located at least 0.5mm away from the wool surface, due to the risk of damaging the measurement tool. Figure 5.5b shows that the increase in turbulence intensity, with respect to the clean plate, is dominated by the increase in roughness. The differences in viscous and inertial resistivity between the melamine and PU plates are shown to play a negligible role in the velocity and turbulence intensity profiles. The agreement of the measurements at locations 0c and 0l is indicative of the negligible spanwise variations in boundary layer profiles between the two locations. For a clean plate, a sharp peak in turbulence intensity is expected close to the wall, at $y^+ \approx 15$, being y^+ the non-dimensional wall normal distance [129]. For the rough plates,

the peak in turbulence intensity is less sharp and further from the wall [153], and is shown in Figure 5.5b. The strong velocity fluctuations caused by the rougher surfaces indicate that these liners can cause stronger background aerodynamic noise, when applied to a closed wind tunnel. Figure 5.5 also indicates that the differences in viscous and inertial resistivity between melamine and PU foams (see Table 5.1) do not considerably affect the turbulent boundary layer properties.

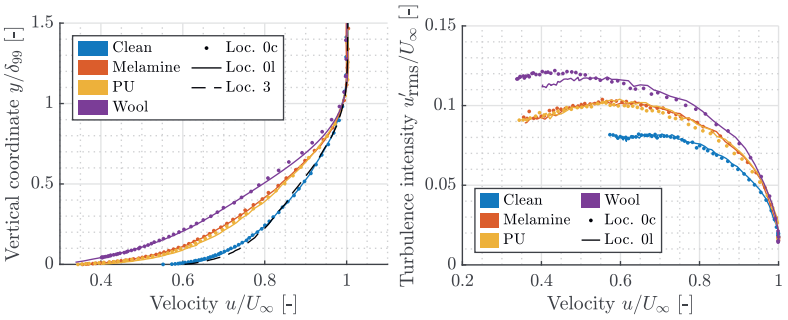

(a) Streamwise velocity profile (b) TI profile

Figure 5.5: Boundary layer velocity and turbulence intensity profiles at U_∞ =30 m s^{-1}, 1 m downstream of the nozzle, for the 4 plates tested.

Figure 5.6 presents the growth in boundary layer thickness, $\Delta\delta_{99}$, displacement thickness, $\Delta\delta^*$, and momentum thickness, $\Delta\theta$, from the streamwise location where the liner starts, location 2-3 (0.1 m downstream of the nozzle and 0.9 m upstream of location 0c). The boundary layer parameters 0.1 m downstream of the nozzle were obtained from averaging data collected at locations 2 and 3 (clean plate test case), respectively 0.12 m and 0.08 m downstream of the nozzle (see Fig. 5.1c). Each value is normalised with the growth of the specific boundary layer parameter for the clean plate, from location 2-3 to 0c. For the BL thickness, the normalisation value is:

$$\Delta\delta_{99\ (\text{Clean, Loc. 0c})} = \delta_{99\ (\text{Clean, Loc. 0c})} - \delta_{99\ (\text{Loc. 2-3})}. \tag{5.5}$$

The clean plate's BL parameters, at the free-stream velocity 30 m s^{-1}, are presented in Table 5.2. The boundary layer two dimensional friction drag was estimated from:

$$D/b = \rho U_\infty^2 \theta, \tag{5.6}$$

being b the wall length in the spanwise direction, and ρ the air density.

Table 5.2: Boundary layer characteristics, for the clean plate case, at $U_\infty = 30\,\mathrm{m\,s^{-1}}$.

Location	δ_{99} [mm]	δ^* [mm]	θ [mm]	D/b [N m^{-1}]
2-3	19	2.4	1.9	2.1
0c	31	4.1	3.2	3.6

Figure 5.6a shows that the boundary layer thickness is increased as roughness increases, having the wool plate a growth 50 % larger than the clean case. At $U_\infty = 20\,\mathrm{m\,s^{-1}}$ and $U_\infty = 30\,\mathrm{m\,s^{-1}}$, the difference in $\Delta\delta^*$ and $\Delta\theta$ between the clean and lined cases approximately doubles, as roughness is increased from ∼0.1mm (melamine and PU) to ∼0.6 mm (wool). At the present flow conditions, the rough wall lining materials tested are not expected to affect closed wind tunnel aerodynamic measurements. The changes in the boundary layer parameters are small when compared to the dimensions of closed wind tunnel test sections which are used for aeroacoustics research, e.g. the Low Turbulence Tunnel at TU Delft [27, 90]. However, when a liner is applied to a large portion of the wind tunnel's circuit (e.g. lining of diffuser walls in [154]), it is relevant to consider the increase in momentum losses in the circuit. Lining a large portion of the tunnel with a very rough material, such as polyester wool, can lead to a considerable increase in drag of the wind tunnel walls. This would require the tunnel's drive fan to work at a higher power setting. The drive fan is a strong contribution towards background noise in a wind tunnel test section, and can disturb acoustic measurements [30].

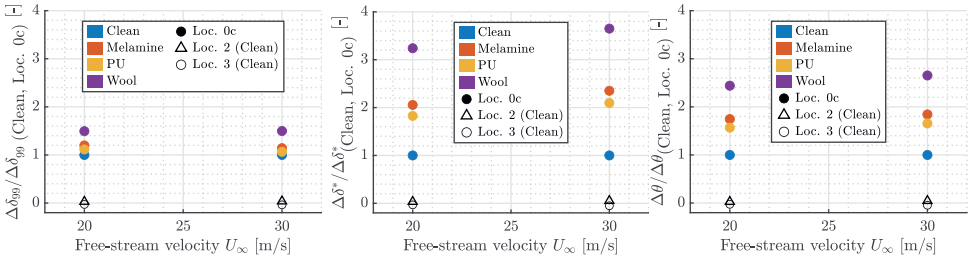

(a) BL thickness (b) BL displacement thickness (c) Momentum thickness

Figure 5.6: Effect of the lining materials on BL parameters of the flat plates, 1 m downstream of the nozzle (location 0c). Measurements taken at $U_\infty = 20\,\mathrm{m\,s^{-1}}$ and $U_\infty = 30\,\mathrm{m\,s^{-1}}$. The plots show the BL thickness (left), displacement thickness (centre) and momentum thickness (right).

Figure 5.7 shows the changes in wall pressure fluctuations spectra, caused by the three liners, for the free-stream velocity $30\,\mathrm{m\,s^{-1}}$. The results from the Sonion microphone of position 0 are in agreement with the spectrum from the Linear-X microphone of position 1 (equal streamwise location), which provides confidence in the result. At low frequency, below 1 kHz, the increase in roughness causes an increase in intensity of the wall pressure fluctuations, which is in line with the higher turbulence intensity seen in Fig. 5.5b.

According to Manes [143], who measured velocity fluctuations in permeable walls' boundary layers, the frequency band for which the fluctuations are highest becomes narrower as permeability increases, whereas the fluctuations over a smooth plate are distributed over a larger frequency band. In the present study, the plate with highest inertial resistivity (PU) shows a low gradient in the spectrum decay towards higher frequency, as in the impermeable case (clean plate). The materials with high viscous resistivity and low inertial resistivity (melamine and wool), are observed to result in a faster decay in wall pressure fluctuations' intensity, towards higher frequency, which is in line with the findings presented in [143]. The viscous resistivity of the materials may be associated with a higher dissipation rate of eddies at high frequencies, where the break down of eddies becomes more dominated by viscous forces. To the authors' knowledge, literature is however lacking thorough studies differentiating the effect of viscous and inertial resistivities in the velocity and pressure spectra of turbulent boundary layers, and, consequently, in the spectra of scattered aerodynamic noise. The aerodynamic noise scattered by the four plates is therefore experimentally characterized in the following sub-section.

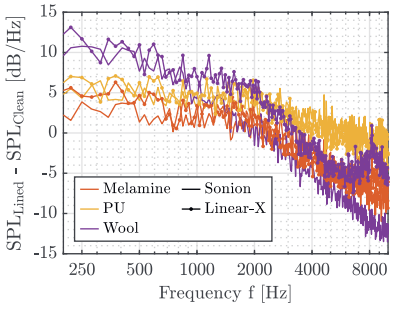

Figure 5.7: Spectra of the wall pressure fluctuations at $U_\infty = 30\,\mathrm{m\,s^{-1}}$, 1m downstream of the nozzle. Measurements with a Sonion microphone, at location 0, and with the Linear-X microphone at location 1. SPL difference between the clean plate and the lined plates.

5.3.2. AERODYNAMIC NOISE SOURCES

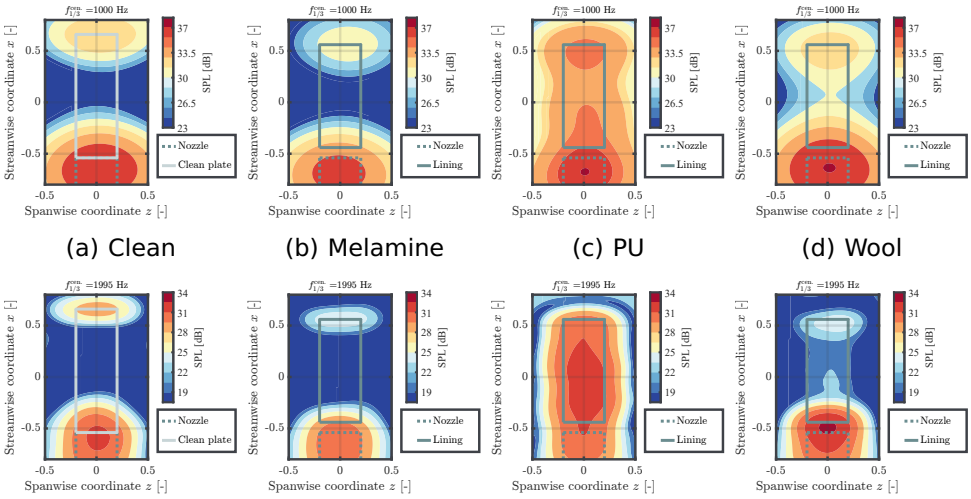

(a) Clean (b) Melamine (c) PU (d) Wool

(e) Clean (f) Melamine (g) PU (h) Wool

Figure 5.8: Beamforming maps at the plate location. Third-Octave bands centered at 1000 Hz (top) and 2000 Hz (bottom). Hard-wall (left) and lined plates (centre-left to right) cases. Free stream velocity, $U_\infty = 30\,\mathrm{m\,s^{-1}}$.

The purpose of analysing the aerodynamic noise sources in the experiment is twofold: to identify which properties of the materials lead to a higher aerodynamic noise, and to determine the dominance of the aerodynamic noise levels in the present experiment, with respect to the speaker noise. The beamforming maps of Fig. 5.8 show the noise source in the plane of the test plate, for the four plates tested, and for the one-third octave bands centered at 1 kHz and 2 kHz. At 1 kHz, the four maps identify the trailing edge of the plate and the nozzle exit as noise sources. For the clean, melamine and wool plate cases the nozzle and trailing edge noise sources are also visible at 2 kHz.

Following from the discussion of Sec. 5.3.1, the boundary layers over the melamine and PU plates are very similar, both in terms of velocity profiles and intensity of the turbulent fluctuations. However, Figs. 5.8c and 5.8g, relative to the PU plate, show higher noise levels than the beamforming maps of the melamine plate (see Figs. 5.8b and 5.8f). At 1 kHz, the intensity of the trailing edge noise is clearly higher for the PU plate. At higher frequency, the figure indicates that the strongest source of noise, for the PU plate case, is originated at the foam surface. The results, therefore, indicate that porous materials with a higher inertial resistivity (see Table 5.1) result in higher noise scattering, both from a trailing edge and from the porous surface. The higher inertial

resistivity of the PU foam (see Table 5.1) is associated with the higher fibre diameter of this material, which increases the ratio of inertial to viscous forces inside the porous medium [155].

Figure 5.9 shows the comparison between speaker noise levels (without flow) and the scattered aerodynamic noise in the flow-on tests. The aerodynamic noise was measured with the speaker off, and for five setup configurations: only wind tunnel nozzle (no plate installed), clean plate (baseline), and for the three lined plates. Figure 5.9a presents the spectra averaged over the 64 microphones in the array. The figure shows that the speaker noise is higher than the aerodynamic noise of the configurations tested from approximately 700 Hz. Figure 5.9b shows the spectra obtained from source power integration of the beamforming maps, at the source plane. The region of integration is the same as shown in Fig. 5.8. The speaker noise levels obtained from source power integration are higher than the background noise from 400 Hz, meaning that the beamforming results presented in section 5.5 are essentially unaffected by aerodynamic sources.

Figure 5.9 highlights the higher aerodynamic noise which is scattered by the PU plate. As indicated by Figure 5.8, the PU plate results in both higher trailing edge noise, as well as higher noise from the entire foam surface, resulting from the interaction with the turbulent boundary layer. The results indicate that a porous material with a higher fibre diameter, and consequently a higher inertial resistivity, leads to more aerodynamic noise. The figures indicate that lining materials with a high inertial resistivity should be therefore avoided, in closed wind tunnels.

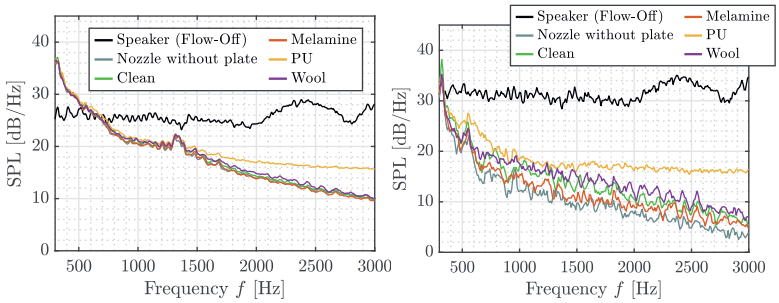

(a) Average of the 64 microphones

(b) Beamforming

Figure 5.9: Comparison between the speaker noise levels (without an installed plate, and without flow) and background noise of the tunnel with the flow-on, at $U_\infty = 30\,\mathrm{m\,s^{-1}}$. Spectra averaged from the 64 microphones in the array (left); and spectra obtained from SPI at the source plane, from conventional beamforming.

5.4. EFFECT OF WALL TREATMENT ON ACOUSTIC SOURCE CHARACTERIZATION

The present section presents and discusses the acoustic results, which refer to the test cases without flow. The goal of the section is to evaluate the acoustic benefit of the lining materials in a controlled environment. The experimental results are compared with the geometric modelling results for a more complete understanding. The measurements are analysed by considering a single receiver, in Sec. 5.4.1, and by analysing the beamforming results, in Sec. 5.4.2.

5.4.1. SINGLE RECEIVER - MEASUREMENT PERFORMANCE

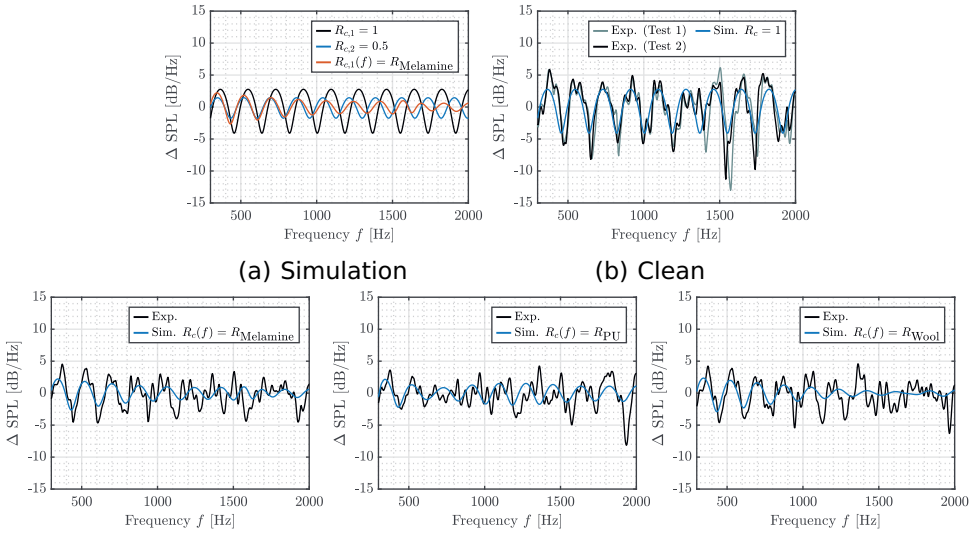

(a) Simulation (b) Clean

(c) Melamine (d) PU (e) Wool

Figure 5.10: Acoustic interference caused by a reflection vs. frequency, for a receiver located at the centre of the array (microphone 41). Comparison of simulations, considering different reflections: $R_{c,1} = 1$, $R_{c,2} = 0.5$ and $R_{c,1}(f) = R_{\text{Melamine}}$ (top-left). Clean plate, measurement and simulation, considering $R_{c,1} = 1$ (top-right). Lined plates, measurement and simulation, considering $R_{c,1} = R_{\text{Foam}}$ (bottom). Reflection coefficient of the lined plates obtained from experimental impedance tube data. Flow-off case, $U_\infty = 0\,\text{m}\,\text{s}^{-1}$.

Figure 5.10 shows the acoustic interference caused by the reflection in the measurements by a point receiver. The receiver considered is located at the centre of the array. Figure 5.10a shows the simulation

results, considering a complete reflection at the location of the foam surface ($R_{c,1} = 1$), a partial reflection at the solid wall behind the foam ($R_{c,2} = 0.5$), and a reflection on a plate lined with melamine, considering the surface reflection coefficient obtained from the impedance tube ($R_{c,1}(f) = R_{\text{Melamine}}$). Figure 5.10a shows that, according to the prediction, the lining causes a shift in the frequencies of constructive and destructive interference (positive and negative ΔSPL, respectively). The cases with $R_{c,1}(f) = R_{\text{Melamine}}$ and $R_{c,2} = 0.5$ produce similar results, at low frequencies (between 0.4 and 1 kHz). The result could be expected, since at low frequency the reflection coefficient of the melamine plate is high, and also because the reflection occurs mostly at the back plate (from the impedance tube data shown in Fig. 5.4). The comparison between simulation and clean plate experiment can be seen in Fig. 5.10b. The results indicate that the mirror-source method is capable of predicting the interference caused by the reflections, with the present setup, for the case of a highly reflective plate. Furthermore, Fig. 5.10b shows the repeatability of the results, for the acoustic data measured in tests 1 and 2. The two experimental data sets were acquired with 21 days difference.

Figures 5.10c, 5.10d, and 5.10e, compare the simulated and measured spectra for the test cases with the melamine, PU and wool linings, respectively. The results indicate that the algorithm predicts well the frequencies of interference, and the interference levels, for the melamine and wool cases at low frequency (below 1 kHz). At higher frequency, the acoustic absorption of the melamine and wool are high, and the error in the measurement can be dominated by acoustic phenomena not predicted by the geometric modelling tool, e.g. diffuse reflections and diffraction, or noise in the measurement device (see uncertainty in Sec. 3.1.2). Furthermore, for smaller sound wavelengths, predicting the frequencies of interference can be more challenging, since the result is more prone to inaccuracies, resulting e.g. from an imprecise reflection coefficient obtained from the impedance tube measurements. For the PU foam (Fig. 5.10d), the simulation provides a reasonable prediction at very low frequencies. At higher frequencies, i.e. from 0.7 kHz, when R_{PU} is low (see Fig. 5.4), the experimental result appears to be dominated by noise, e.g. due to diffuse reflections. As discussed in Sec. 5.2.3, the fact that only one mirror-source is considered in the simulation can be a source of added errors. It is possible that, at certain frequencies, the reflections at the foam surface and at the back plate can have constructive or destructive interference with each other, at the receiver location.

5.4.2. BEAMFORMING PERFORMANCE

Figure 5.11 presents conventional beamforming maps, at the source plane, for the simulated and experimental cases of a free-field speaker (Figs. 5.11a and 5.11d), speaker with a highly reflective back wall installed (Figs. 5.11b and 5.11e), and speaker with a melamine plate installed (Figs. 5.11c and 5.11f). The results show that the difference between the beamforming maps is negligible, when the purpose is to locate the position of the direct source in the scan plane. The next step was to apply source power integration in a region close to the source, in order to evaluate the consequence of installing a back wall in the assessment of the source noise levels. The integration area is specified in Fig. 5.11.

The ΔSPL in source level estimation with source power integration caused by the reflections is presented in Fig. 5.12. Figure 5.12a presents

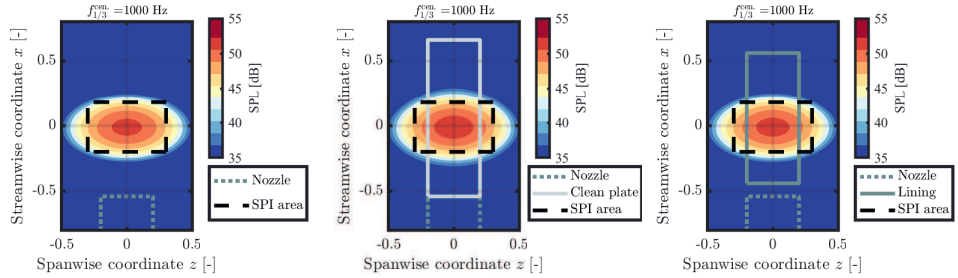

(a) $\boldsymbol{R_c = 0}$, Speaker Only (b) $\boldsymbol{R_c = 1}$, clean plate (c) $\boldsymbol{R_c(f) = R_{Melamine}}$, melamine plate

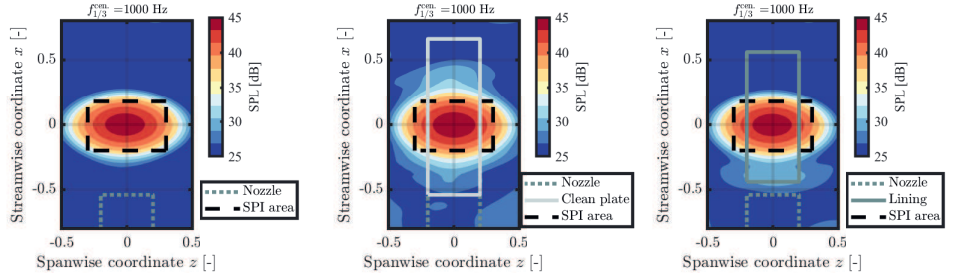

(d) Experimental, Speaker Only (e) Experimental, clean plate (f) Experimental, melamine plate

Figure 5.11: Beamforming of the simulated (top) and experimental (bottom) microphone signals, at the source plane. The maps are for the 1000 Hz third-octave band. Free-field speaker case (left), speaker with the clean plate installed (centre), and speaker with a melamine plate installed (right). Flow-off case, $U_\infty = 0\,\mathrm{m\,s^{-1}}$.

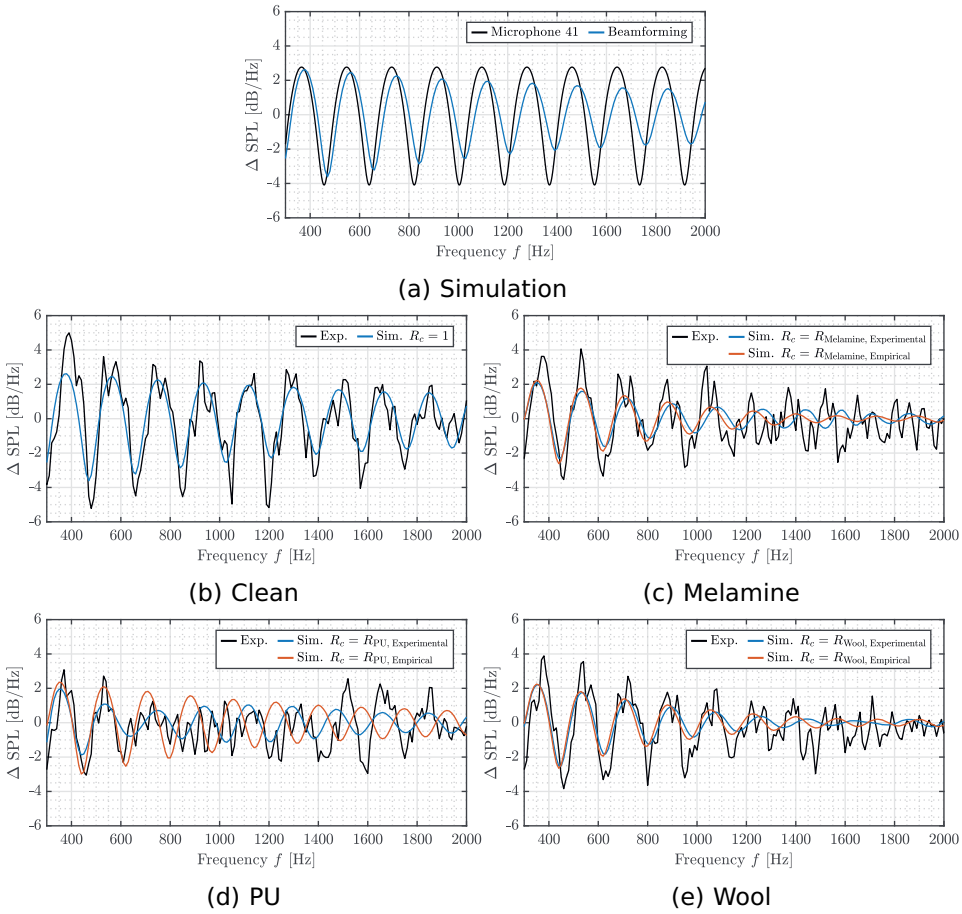

(a) Simulation

(b) Clean

(c) Melamine

(d) PU

(e) Wool

Figure 5.12: Acoustic interference caused by a reflection vs. frequency. Simulation: isolated microphone (41) and beamforming spectra (top-left). Beamforming of experimental data with the clean plate and beamforming of the simulated data, with $\boldsymbol{R_c = 1}$ (top-right). Beamforming of experimental data with the lined plates and beamforming of the simulated data (bottom). Results obtained from Source Power Integration of the beamforming maps. Flow-off case, $U_\infty = 0\,\mathrm{m\,s^{-1}}$.

the results for the simulated signals. Figure 5.12a compares the ΔSPL when a single receiver is considered (in this case microphone 41) to the error when the spectrum is obtained from source power integration. The results indicate that beamforming is capable of largely reducing the error caused by the back plate reflection, particularly at high frequency, close to 2 kHz. The agreement in Fig. 5.12b indicates that the geometric

modelling tool is capable of predicting the performance of beamforming when the back plate is highly reflective (case without lining).

Figures 5.12c, 5.12d and 5.12e, show that the geometric modelling tool is capable of incorporating the complex reflection coefficient of the materials. The prediction is particularly good at low frequency, when the performance of geometric modelling tools is most uncertain, as the ratio between setup geometry sizes and sound wavelength reduces [42]. Figures 5.12c, 5.12d and 5.12e show the simulated spectra obtained using both the experimental and empirical reflection coefficients (see Fig. 5.4). The results for the melamine and wool cases indicate a slight improvement in the prediction at high frequency (above 1 kHz), when the empirical reflection coefficient is used. The result therefore indicates that most of the reflection occurs at the back solid wall, as predicted by Delany's empirical model (see Fig. 5.4). For the PU plate, however, both the magnitude of the peaks and the frequencies of interference are more accurately predicted when the experimental impedance tube data is used. As discussed in section 5.2.3, Delany's model only takes into account the viscous resistivity, whereas the PU foam has a very high inertial resistivity (see Table 5.1). The reflection location is therefore mispredicted by the empirical model, resulting in errors in the prediction of the interference between direct source and reflections. Figure 5.12 is indicative of the importance of knowing the exact reflection location, when using a geometric modelling tool.

5.5. ACOUSTIC WAVE - FLOW INTERACTION: FLOW-ON REFLECTION PREDICTION

The present section discusses the interaction between the acoustic reflected wave and flow, and its effect on the acoustic measurements. To this end, Sec. 5.5.1 discusses the effect of the flow in the measurements from isolated receivers, and Sec. 5.5.2 describes the consequence of the interaction between acoustic wave and flow in the beamforming results.

5.5.1. SINGLE MICROPHONE

Figure 5.13 presents the acoustic interference occurring during the measurement of the speaker noise levels, due to the reflection, for the flow-off and -on cases. Both the experimental and the simulated results are shown. The data was obtained by three isolated receivers: microphone 8, at the bottom of the array, microphone 23, at the top of the array, and microphone 41, at the centre of the array (see Fig. 5.3b). The simulation predicts that, when the reflected wave is convected by the flow, the receiver sees a shift in the frequencies of interference between the direct and reflected sound waves. The flow convection

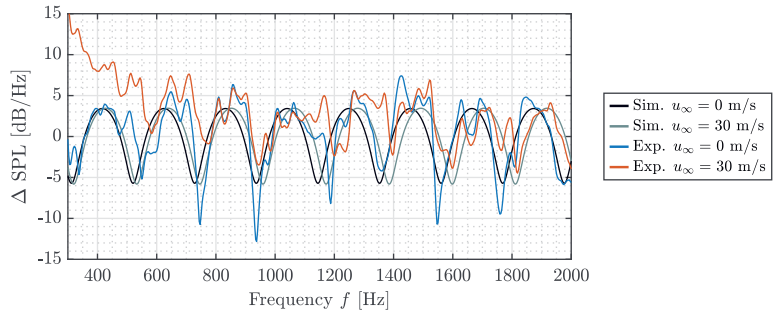

(a) Top Microphone (23)

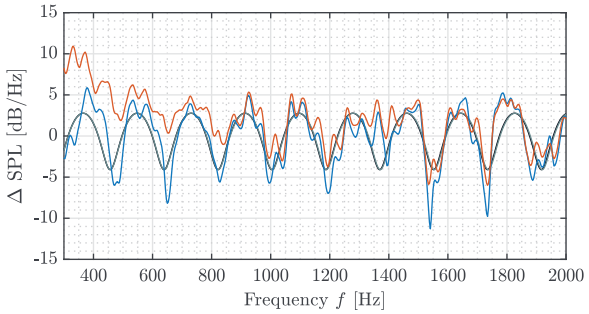

(b) Centre microphone (41)

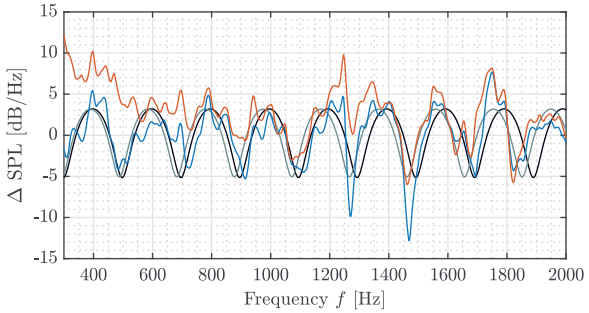

(c) Bottom microphone (8)

Figure 5.13: Acoustic interference caused by a reflection (and aerodynamic noise) vs. frequency, as perceived by isolated receivers. Comparison between simulation with flow-off and -on, and experiment with flow-off and -on. Microphones at the bottom of the array (left), at the middle of the array (centre) and at the top of the array (right). Clean plate test case, at the free stream velocity, $U_\infty = 30\,\mathrm{m\,s^{-1}}$.

influences the travel time of the reflected wave, from source to receiver. The shift in frequency depends on the location of the receiver. For receivers located below the speaker, e.g. microphone 8, the reflected wave is convected in the opposite direction of its path, and takes longer to reach the receiver. The frequencies of interference therefore shift towards lower frequency at the location of microphone 8, when the flow is on. For a receiver above the speaker, however, the convection of the reflected wave reduces the sound wave's travelling time. Microphone 23, therefore, sees a shift in the frequencies of interference towards higher frequency, as the flow velocity is increased. For receivers at a height close to the speaker height, the travel time of the reflected wave is essentially unchanged by flow convection, at the velocities considered. Microphone 41, at the centre of the array, is predicted to perceive equal interference between the reflected and direct sound waves, at the free-stream velocities $0\,\mathrm{m\,s^{-1}}$ and $30\,\mathrm{m\,s^{-1}}$.

The experimental data in Fig. 5.13 shows very similar results for the $0\,\mathrm{m\,s^{-1}}$ and $30\,\mathrm{m\,s^{-1}}$ case, from 700 Hz. Below 700 Hz, the results for the $30\,\mathrm{m\,s^{-1}}$ case are dominated by background aerodynamic noise, as indicated by the results of Sec. 5.3.2. Figures 5.13a and 5.13c show a slight shift in the frequencies of interference in the experimental data, as indicated by the geometric modelling prediction. However, the experimental shift is very small compared to the noise in the results. The following subsection analyses data from all the microphones in the array, which helps reducing the influence of spurious acoustic noise sources, e.g. diffuse reflections.

5.5.2. CONVENTIONAL BEAMFORMING

Figure 5.14 shows the error caused by acoustic interference in the beamforming estimate of the speaker levels, for the flow-off and -on cases. The spectra were obtained from source power integration of the beamforming maps, with an equal scan plane and region of integration as in Fig. 5.11. The figure shows that, according to the simulation, the presence of the flow does not affect the beamforming results in the present setup. The result is aligned with the discussion of the previous sub-section (Sec. 5.5.1), where it was referred that the flow causes a shift in the frequencies of interference, which is dependent on the position of the receiver. Since the 64 microphones are approximately equally spread above and below the speaker (see Fig. 5.3), when all the microphones are considered, the shift in frequency of interference becomes negligible.

The experimental results presented in Figs. 5.14a, 5.14b, 5.14c and 5.14d correspond to the test cases with the clean, melamine, PU and wool plates, respectively. The experimental results are in agreement with the predictions, since the difference in experimental spectra at

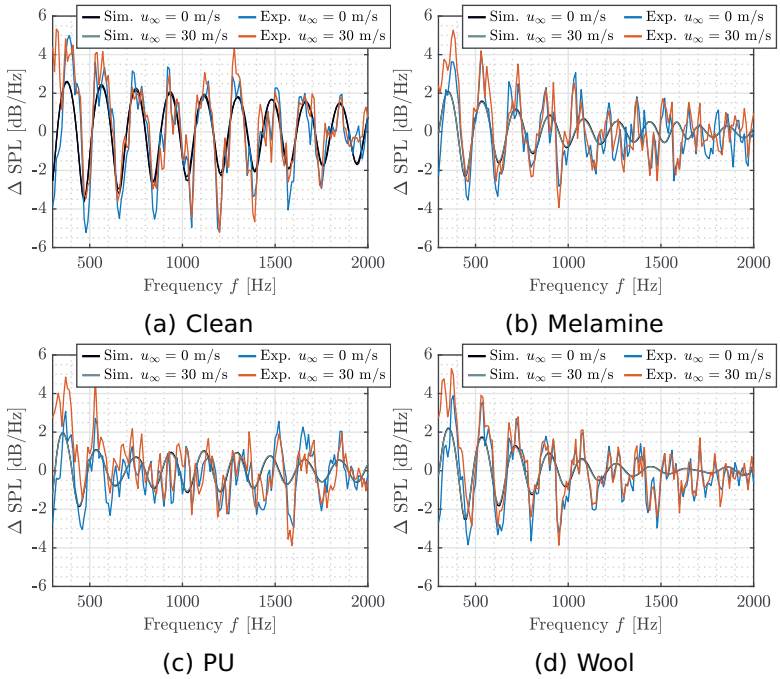

Figure 5.14: Acoustic interference caused by a reflection, in the spectra obtained from beamforming. Comparison between the flow-off and -on ($U_\infty = 30\,\mathrm{m\,s^{-1}}$) cases. Spectra obtained from SPI of the beamforming maps at the source plane. Experimental and simulated data relative to the clean (top-left) and lined plates (top-right and bottom). Reflection coefficient of the lined plates obtained from experimental impedance tube data.

$0\,\mathrm{m\,s^{-1}}$ and $30\,\mathrm{m\,s^{-1}}$ is also negligible. Small differences can be seen at very low frequency, below 500 Hz, due to aerodynamic background noise. Considering the frequencies $500\,\mathrm{Hz} < f < 2000\,\mathrm{Hz}$, the correlation between the spectra with and without flow is high for the 4 plates tested. The correlation coefficient is 0.8, 0.7, 0.6 and 0.9 for the clean, melamine, PU and wool test cases, respectively. The results are therefore indicative that flow phenomena which are neglected by the geometric modelling tool, such as transmission loss or refraction in shear layers, play a minor influence in the experiment carried out in the A-tunnel.

As discussed in section 5.4.2, a good estimation of the location of the reflections, which can be at the surface of the foam or at the solid back wall, is a dominant factor for an accurate prediction of the geometric modelling algorithm. Figure 5.14 shows that, also for the flow-on cases,

the interference peaks are approximately predicted by the geometric modelling algorithm, as long as the reflection coefficient of the back wall is sufficiently high, i.e. $R_c(f) > 0.4$ (see Fig. 5.4). For frequencies where the reflection coefficient is low, the result becomes dominated by spurious noise, which can be associated with diffuse reflections and diffraction. When beamforming is applied, the convection of a reflected wave by the flow can be neglected, as long as the direct sound source is (approximately) aligned with the centre of the microphone array.

5.6. CONCLUSION

An experimental campaign was carried out in an anechoic open-jet wind tunnel, in order to evaluate the influence of lining materials on the aerodynamic and acoustic fidelity of wind tunnel test sections. The test models consisted of plates lined with sound absorbing porous materials. The porous materials were characterized based on their surface roughness, viscous and inertial resistivities, and reflection coefficient. The study focuses on the influence of the liners on the boundary layer of the wind tunnel's wall, on the boundary layer aerodynamic noise, and on the absorption of sound reflections. A geometric modelling algorithm was developed in order to improve the understanding of the effect of lining the wind tunnel wall on the acoustic measurements.

For the flow-on tests, the aerodynamic properties of the boundary layer of each test plate were initially characterized. The turbulent fluctuations in the boundary layer where confirmed to be most increased for the roughest material tested, polyester wool, particularly at low frequencies. However, it was the lining material with largest fibre diameter (PU), and consequently higher inertial resistivity, which was found to scatter most aerodynamic noise, both from the surface and from the trailing edge.

During the acoustic tests, a well characterized speaker was placed in front of the lined wall. Measurements were taken with a phased acoustic array. The results show that the modelling algorithm is capable of predicting the interference caused by acoustic reflections, for the clean wall and lined cases. For the lined cases, however, at high frequencies, when the absorption from the lining materials is increased, acoustic spurious noise sources become more dominant in the experimental data. Both the geometric modelling algorithm and the experiments show that the highest improvement on the acoustic measurements occurs for the lining materials with highest viscous resistivity, melamine and wool, due to their increased sound absorption capabilities. The results indicate that the best choice of acoustic lining material, for a closed wind tunnel, results from maximizing viscous resistivity, while reducing roughness and inertial resistivity.

The present study highlighted the advantages and limitations of porous wind tunnel lining materials with varying roughness, viscous resistivity and inertial resistivity. The capabilities of a geometric modelling tool to predict the acoustic benefit of each lining material were also assessed. Future aeroacoustic investigations would benefit from the validation of geometric modelling methods in closed wind tunnel environments, with walls lined with sound absorbing materials. The presence of the wind tunnel walls perpendicular to the array increase the amount of specular and diffuse reflections, increasing the complexity of the acoustic problem.

6

AEROACOUSTIC MEASUREMENTS IN A LINED CLOSED WIND TUNNEL

Aeroacoustic tests in closed wind tunnels are affected by reflections in the tunnel circuit and background noise. Reflections can be mitigated by lining the tunnel circuit. The present study investigates if lining exclusively the most accessible segment of a closed wind tunnel circuit, in particular the test section, is an approach which improves acoustic measurements. Previous investigations show that a wind tunnel lining material should have high acoustic absorption, low inertial resistivity and low surface roughness. Therefore, the test section of TU Delft's closed Low Turbulence Tunnel is lined with melamine foam wall liners. A total of 4 test section configurations were tested: baseline; test section with lining on the floor and ceiling; test section with lined side–panels; and test section lined at all surfaces (floor, ceiling and side–panels). An omnidirectional speaker is used for evaluating the wind tunnel's acoustic performance. A geometric modelling algorithm, based on the mirror-source method, is used to predict the effect of lining on primary reflections in the test section. In addition, reflections in the test section and in the tunnel circuit are characterized experimentally. The results show that the closed loop of the tunnel circuit is responsible for a long reverberation time in the test section. However, reflections inside the test section itself are the dominant source of acoustic interference at the microphone array location. The low fidelity geometric modelling algorithm is shown to be a valuable approach for an initial estimation of the acoustic benefit of lining, for both flow–off and –on conditions.

This chapter is based on the work presented in AIAA AVIATION 2023 FORUM [156].

Lining of the test section walls significantly reduces reflections from the reference source, as well as the aerodynamic background noise that reaches the array.

6.1. INTRODUCTION

Lining of an aeroacoustic wind tunnel circuit has a strong influence on the acoustic performance, and is often considered to be a justifiable investment (e.g. in Refs. [30, 79]). However, lining a closed wind tunnel with a porous material also affects the aerodynamic characteristics of the wind tunnel walls' boundary layer. An increase in the turbulence levels in the boundary layer can affect the scattering of spurious noise sources in the tunnel, e.g. from discontinuities [65]. The influence of porous materials on boundary layers is widely studied (e.g. by [143, 144]). The noise scattering from wall porous liners has been investigated, and is discussed in the previous chapter of this thesis. The results presented in Chapter 5 indicate that a good closed wind tunnel liner has a low surface roughness and inertial resistivity, and a high viscous resistivity, which leads to high acoustic absorption. As a following step, closed wind tunnel designs can benefit from research which assesses the improvement obtained from lining individual segments of the circuit, e.g., the diffuser or the test section. This can be very helpful for performing a trade–off, e.g., when resources for designing or refurbishing a wind tunnel are limited.

The present study investigates the benefit of applying wall treatments to the test section of a closed wind tunnel. The study focuses on the trade-off between different lining configurations, with respect to a baseline (fully reflective) test case. Measurements of a known sound source (omnidirectional speaker) with each configuration, are used to assess the improvements achieved with each different lining. Measurements were taken with and without flow, in order to take into account the modifications in background noise. The experimental campaign was conducted in the Low Turbulence Tunnel (LTT), at TU Delft. The LTT is a closed wind tunnel intensively used for aerodynamic and aeroacoustic research, see e.g. [17, 157, 158].

The present document is structured as follows: Sec. 6.2 describes the facility, the measurement techniques, and post processing algorithms used. Section 6.3 presents and discusses the experimental results. Finally, Sec. 6.4 highlights the main conclusions.

6.2. METHODOLOGY

6.2.1. FACILITY AND MODELS

The wind tunnel analysed with this experimental campaign, the LTT, has been designed as a closed test section wind tunnel. As described in Sec. 3.1.1, the LTT aeroacoustic test section features a Kevlar panel in replacement of a wind tunnel wall, which is most characteristic of hybrid test section designs (see Sec. 2.3.2). In the present experiment, 7 out of 8 test section walls were kept closed (solid or lined walls), and no strong pressure gradients were present at the Kevlar wall. Therefore, the aerodynamic conditions in the test section are considered most representative of closed test section wind tunnels.

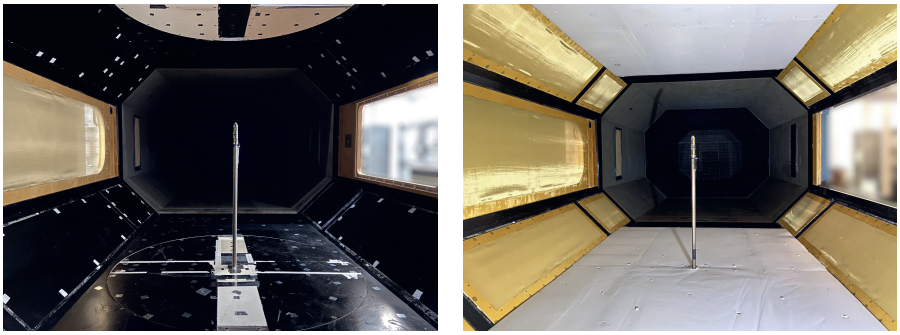

(a) Without lining (b) With lining

Figure 6.1: Low turbulence tunnel aeroacoustic test section (view from the inlet): test section with baseline reflective walls (left) and fully lined test section (right).

Figures 6.1a and 6.1b show, respectively, a speaker installed in the baseline (fully reflective) test section and in the fully lined test section. The Kevlar wall, behind which the microphone array is placed, is seen in both configurations (see the left side–panel).

REFERENCE ACOUSTIC SOURCE

The acoustic source seen in Fig. 6.1 is a miniature QindW speaker model, developed by QSources [147]. As mentioned in the previous chapter, this speaker has been verified to be omnidirectional at low frequencies, up to 2kHz. The speaker is placed at the centre of the test section, being aligned with the streamwise centre of the microphone array. The aerodynamic shape of the speaker results in low aerodynamic self–noise.

For the flow-off tests, the speaker's input was based on an in–built white–noise signal, in the range 300 Hz to 6300 Hz. For the flow–on tests, the signal provided to the speaker was based on a sum of

sine waves, with constant amplitudes, at the frequencies of interest. This solution allows for the increase of the speaker's noise signature at each frequency, f. Three distinct signals were provided to the speaker: a sum of sinusoids in the range $f_1 = 325\,\text{Hz}$ to $f_{\text{end}} = 825\,\text{Hz}$ (low–frequency, narrow band), a sum of sinusoids in the range $f_1 = 775\,\text{Hz}$ to $f_{\text{end}} = 1275\,\text{Hz}$ (mid–frequency, narrow band), and a sum of sinusoids in the range $f_1 = 325\,\text{Hz}$ to $f_{\text{end}} = 2175\,\text{Hz}$ (broadband). The signals, $v(t)$, were calculated from:

$$v(t) = \sum_{f \in F} \sin\left(2\pi f t + \phi_{\text{rand}}\right), \tag{6.1}$$

where $F = \{f_1, f_1 + 5\,\text{Hz}, f_1 + 10\,\text{Hz}, \ldots, f_{\text{end}}\}$, ϕ_{rand} is a random phase shift applied to each sinusoid, and t is the time coordinate.

AEROACOUSTIC TEST SECTION LINING

The experimental campaign evaluates four different test section configurations (Table 6.1). The baseline (most reflective configuration) is seen in Fig. 6.1a. The octagonal baseline test section contains 7 solid fully reflective walls. The Kevlar left side–panel is present in all four configurations, to allow measurements with the microphone array. The plate that holds the microphones is lined with 5 cm thick plane Basotect melamine (see Fig. 3.4). The most anechoic configuration (Figs. 3.2a and 6.1b), as described in Sec. 3.1.1, has the floor and ceiling lined with 3 cm flat melamine foam, and has lined side–panels. These consist of 5 cm wedged melamine covered by Kevlar. Two intermediate test sections were also tested: one with the top and bottom flat melamine lining, and with the baseline side–panels, and the second with the baseline top and bottom, and with the lined side–panels.

Table 6.1: Low Turbulence Tunnel test sections tested

Test section	Mic. array recessed behind Kevlar	Top and bottom flat 3 cm melamine lining	Kevlar side–panels, with 5 cm wedged melamine
A	✓	-	-
B	✓	✓	-
C	✓	-	✓
D	✓	✓	✓

The high viscous resistivity of the melamine foam (specified in Sec. 5.2.1) leads to a high acoustic absorption. Figure 6.2 shows the reflection characteristics of the melamine lining, when placed in front of

a solid wall, and considering a 90° reflection. The figure shows that the thicker melamine lining leads to a higher reflection mitigation, especially at frequencies below 2 kHz.

The experimental values were obtained from normal-incidence impedance tube measurements at the Netherlands Aerospace Centre (NLR). The empirical values were obtained from Delany's empirical model for surface impedance, with the methodology described in 5.2.3.

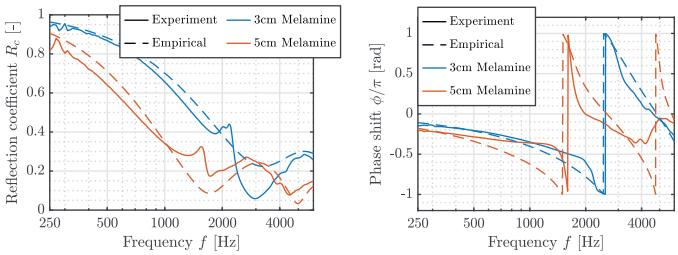

(a) Reflection coefficient (b) Phase shift

Figure 6.2: Acoustic characterization of the plane Basotect melamine foam. Absolute reflection coefficient (left) and phase shift at the foam surface (right) for a normal incidence reflection.

6.2.2. GEOMETRIC MODELLING

The primary acoustic reflections in the LTT test section, from the source to the microphone array, were predicted with a geometric modelling (GM) algorithm. The algorithm is explained in Sec. 3.2, which includes a representation of the setup used to model the primary reflections on the LTT test section (see Fig. 3.5). The correction for the convection of sound waves by the flow was implemented, in this investigation. This geometric modelling method provides a good initial prediction of acoustic reflections on a single wall, with similar dimensions to the dimensions of the LTT test section walls (i.e. of the same order of magnitude), for both fully reflective and lined (with melamine foam) cases [142].

In order to model the lined walls, the experimental reflection coefficients shown in Fig. 6.2 were used in the algorithm. The lining on the wall opposite to the array was simplified with respect to the experiment, from 5 cm wedged melamine (covered by Kevlar) to 5 cm plain melamine.

6.2.3. ACOUSTIC MEASUREMENTS AND SIGNAL PROCESSING

The data was recorded with 62 PUI AUDIO 665–POM–2735P–R microphones. The phased microphone array configuration and installation

have been discussed in more detail in Sec. 3.1.2. In this study, the microphones were calibrated with a Brüel & Kjaer 4230 pistonphone, at the frequency of 1 kHz. Each measurement was taken with a measurement time of 20 s and a sampling frequency of 50 kHz.

The spectra of the isolated microphones were obtained with the Welch's method [159]. The 20 s signals were divided into chunks of 0.1 s, with a 50 % overlap. Each chunk was multiplied by the Hanning window. The spectrograms analysed in the study were obtained by dividing the 20 s signals in time blocks of 0.05 s, with 50 % overlap. SPL, defined in Eq. 3.13, was calculated considering a reference pressure of $p_{\text{ref}} = 2 \times 10^{-5}$Pa.

Acoustic interference in the test section was quantified by the difference between the measurements in the reverberant environment and the reference speaker measurement, which was taken outside the wind tunnel test section, in a large room (with low reverberation) and with the microphone array described in Sec. 3.1.1. ΔSPL is defined as:

$$\Delta\text{SPL} = \text{SPL}_{\text{Speaker inside the test section}} - \text{SPL}_{\text{Reference, speaker}}, \tag{6.2}$$

being positive and negative ΔSPL, respectively, indicative of constructive and destructive interference between direct source and reflections, at the measurement location. $\Delta\text{SPL} = 0$ indicates that, at that specific frequency, the measurement inside the test section is not disturbed by reflections. The main assumptions are that the reference speaker measurement is representative of free–field conditions; and that the speaker's response is consistent throughout all the tests.

CONVENTIONAL BEAMFORMING

The acoustic data from the microphone array was processed with conventional beamforming, previously introduced in Sec. 3.4.1. The beamforming formulation used outputs an estimation for the sound levels at the array, of the noise originating from each scan grid point. This is equivalent to setting $b = 2$ in Eq. 3.12.

The microphone data were processed considering two different beamforming scan grids. For identifying the sound sources in the empty test section, a 3D scan grid was designed, which covers the 8 walls of the octagonal test section. This grid can be visualised in Fig. 6.3. For estimating the noise levels of the speaker, when installed in the test section, a 2D plane parallel to the array was considered. The 2D grid is at a 1.05 m distance from the array, and passes through the spanwise centre of the test section, i.e. through the speaker location. An equivalent scan grid was used for processing the reference speaker measurements, for which the resulting beamforming map, at 1 kHz, is shown in Fig. 3.6. After calculating the beamforming maps, the speaker

noise levels were obtained with the Source Power Integration (SPI) method described in Sec. 3.4.2. In this study, a 24×24 cm integration region was considered, as illustrated in Fig. 3.6.

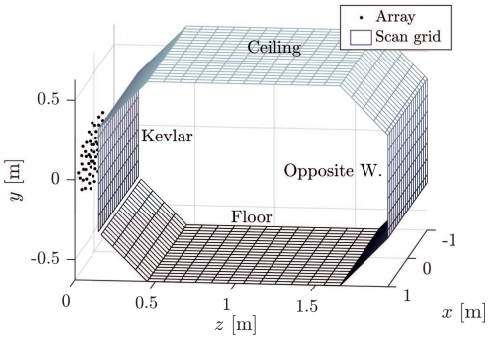

Figure 6.3: Scan grid along the 8 walls of the LTT test section. Microphone array located behind the Kevlar panel, which is also evaluated with the grid.

6.3. WIND TUNNEL ACOUSTIC CHARACTERIZATION

The present section analyses the results obtained from the experimental data, and compares these with the results obtained from the geometric modelling tool. The acoustic properties of the tunnel are characterized by analysing the acoustic reflections in the test section (Sec. 6.3.1). The background noise is analysed in Sec. 6.3.2 by evaluating speaker–off measurements. In Section 6.3.3, the measurements with the flow and speaker –on are analysed.

6.3.1. ACOUSTIC REFLECTIONS IN THE WIND TUNNEL CIRCUIT

The prolongation of sound, due to reflections in the wind tunnel circuit, was analysed with intermittent speaker measurements. During these measurements, the speaker was paused at the time t_0. To characterize reverberation at the different test section configurations, the spectrogram of the data was produced. The spectrograms of Fig. 6.4 were obtained by averaging the sound powers obtained from all the microphones in the array, for each timestep, being therefore indicative of the acoustic energy in the test section. The results are shown for the third-octave band centres, $f_{1/3}^{\text{cen.}}$. Test section C, which has the baseline top and bottom, and lining on the side–panels (see Table 6.1), was also tested outside the wind tunnel circuit (Fig. 6.4e). The reverberation

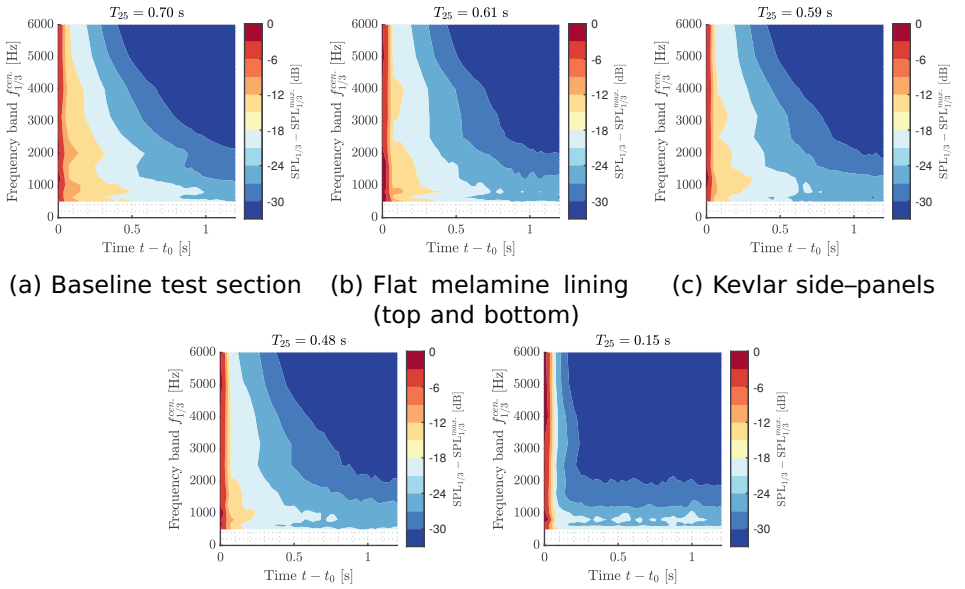

(a) Baseline test section (b) Flat melamine lining (top and bottom) (c) Kevlar side–panels

(d) Most anechoic test section (e) Test section C outside the WT loop

Figure 6.4: Spectrogram of the acoustic data obtained from the intermittent speaker tests. The spectrogram shows the development of reverberation in the test section from the moment the speaker is interrupted. The plots a) to d) refer to the test cases with the LTT test section installed in the tunnel circuit: test sections A (top–left), B (top–centre), C (top–right), D (bottom–left). Test section C, with the wedged melamine Kevlar side–panels, was also tested outside the wind tunnel circuit (bottom–right).

time, T_{25}, is also shown in Fig. 6.4. T_{25} is the time in which the overal sound pressure level reduces by 25 dB, after turning off the speaker. T_{25} was calculated considering the frequencies shown in Fig. 6.4.

Figure 6.4 shows that both the flat melamine (top and bottom lining) and the lined side–panels are efficient in reducing reverberation in the test section, as reverberation reduces faster in Figs. 6.4b and 6.4c than in Fig. 6.4a. There is however little difference between the performance of the two lining solutions in reducing reverberation, as Figs. 6.4b and 6.4c show a similar pattern. When both linings are used simultaneously, the improvement in reducing reverberation is further noticeable (see Fig. 6.4d). The linings are particularly efficient at reducing reverberation at high frequency, which is consistent with the reflection coefficients shown in Fig. 6.2. Figure 6.4e indicates that reverberation in the

test section is negligible, when the test section is placed outside the tunnel circuit. The reverberation time, for the test sections installed in the wind tunnel circuit, is considerably longer than at other facilities commonly used for aeroacoustics research, e.g. TU Delft's Anechoic Tunnel ($T_{60,\mathrm{A-Tunnel}} = 0.22\,\mathrm{s}$) [22]. The results suggest that it can be advantageous to line further sections of the tunnel circuit, e.g. the diffuser (see Fig. 6.1a).

ACOUSTIC INTERFERENCE INSIDE THE TEST SECTION

The present section investigates the acoustic interference that occurs at the microphone array location, between a direct sound source and reflections in the circuit. The objective is to quantify the disturbance caused by primary reflections, which directly reflect towards the microphones, by secondary reflections (here meant as any non-primary reflections) in the test section, and by reverberation caused by the remaining parts of the circuit. The final goal is to identify which parts of a closed tunnel are beneficial to treat with acoustically absorbent materials.

Reflections inside the test section lead to frequency dependent constructive or destructive interference patterns at the microphone locations. Figure 6.5 shows the interference mitigation achieved with lining, from both experimental and simulation data. The spectra were obtained by averaging the source powers between all microphones in the array. A good test section acoustic performance is reached when ΔSPL becomes close to 0 dB.

Figure 6.5a shows the acoustic interference caused by the three primary (specular) reflections in the test section that reach the microphone array from the acoustic source (see the GM setup in Fig. 3.5). The figure shows that, for the four test sections, the primary reflections cause a strong constructive interference peak for frequencies in the vicinity of 600 Hz, which is followed by a destructive interference peak, near 800 Hz. Below 1000 Hz, the reflection coefficient of the lined walls is still relatively high (see Fig. 6.2). Above 1000 Hz, Fig. 6.5a shows that, for the baseline test section (A), the interference caused by the primary reflections is approximately 3 dB. For the most anechoic configuration, configuration D, ΔSPL becomes close to 0 dB at high frequencies. The result of Fig. 6.5a indicates that reducing the reflection coefficient of the test section walls which cause the primary reflections is important for achieving accurate acoustic measurements.

Figure 6.5b shows the acoustic interference patterns which occur in test section C, for the case where the test section is installed in the tunnel circuit, and for the case where the test section is outside the circuit. As seen from Fig. 6.4, the wind tunnel circuit is responsible for a long reverberation time, when the test section is installed. However, Fig. 6.5b indicates that installing the test section in the wind tunnel

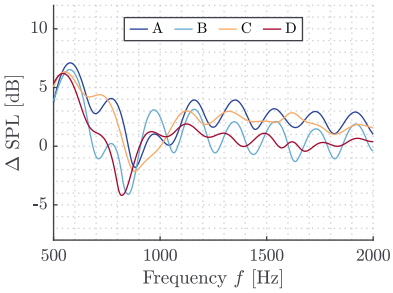

(a) GM simulation of primary reflections

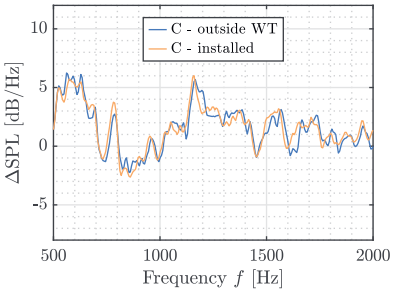

(b) Experiment: installed vs. uninstalled

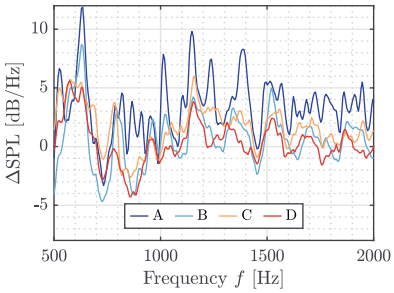

(c) Experiment: installed test sections

Figure 6.5: Acoustic interference caused by the reflections: difference between the measurement inside the test section and the reference speaker measurement. Primary reflections in the test section, simulated with geometric modelling (top–left); difference between installed and uninstalled test section, from experimental data (top–right); and each installed test section, from experimental data (bottom). Average from the 62 microphones in the array.

circuit does not change the dominant acoustic interference phenomena. The result indicates that, at these frequencies, and in the absence of aerodynamic background noise in the tunnel, reverberation caused by the remaining parts of the circuit (besides the test section) is not visible in the acoustic measurements.

Figure 6.5c, obtained from the experimental measurements with the test sections installed, presents the acoustic interference pattern caused by primary and secondary reflections in the test section, and by reverberation in the tunnel. The comparison of Figs. 6.5a and 6.5c shows that the experimental ΔSPL is noisier than for the simulated case, where only the primary reflections are present. This is associated with the fact that, besides likely experiencing diffraction, reflections

in the experimental case are infinite. The experimental ΔSPL is also higher: for the baseline configuration, the difference with respect to the reference measurement is, for a wide range of frequencies, close to 5 dB. For the lined cases, the experimental ΔSPL is non-negligible also at high frequencies, when the primary reflections on the lined walls are relatively weak. This result indicates that secondary reflections in the test section (i.e. any non-primary reflections) noticeably affect the transfer function from the source to the microphone array. Figure 6.5 shows that it is beneficial to line as much area of the test section walls as possible, for reducing acoustic interference at the measurement location.

6.3.2. AERODYNAMIC NOISE SOURCES

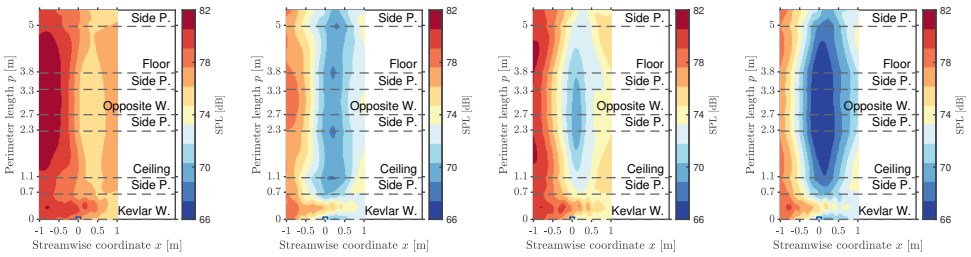

(a) Baseline configuration

(b) Melamine on floor and ceiling

(c) Kevlar side–panels

(d) Most anechoic configuration

Figure 6.6: Beamforming along the (empty) test section walls, for the 1 kHz third–octave band. Free-stream velocity 40 $\mathrm{m\,s^{-1}}$. Test sections A (left), B (centre–left), C (centre–right) and D (right).

Figure 6.6 shows the beamforming maps of the empty test section measurements, with the wind tunnel operating at $U_\infty = 40\,\mathrm{m\,s^{-1}}$. The scan plane is placed along the test section walls (see Fig. 6.3). For the four test sections, the beamforming maps indicate that most background noise originates from downstream of the test section (where $x < -1\,\mathrm{m}$). This can be e.g. from the diffuser's boundary layer, or discontinuities in the circuit, such as a gap between the test section and the diffuser. Furthermore, the result indicates noise sources at the Kevlar panel location. The figure also shows that, when lined, the noise from a given wall/ side–panel is reduced. This occurs despite of the higher surface roughness of the liner with respect to a solid wall, which increases boundary layer turbulence [142]. Figures 6.6c and 6.6d show the strong reduction in noise from the opposite wall, when the lined side panels are installed. This can be explained by the reduction in reflection

of background noise at the opposite wall, when the wall's reflection coefficient is reduced.

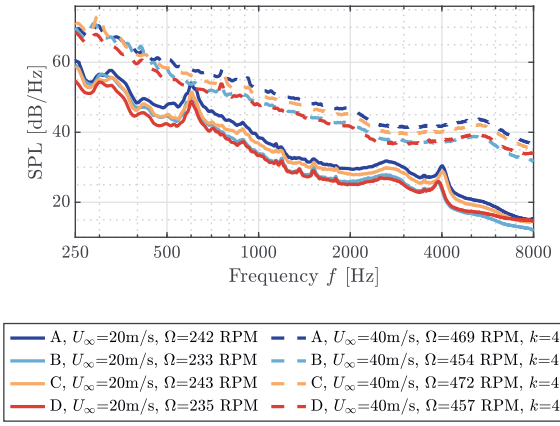

Figure 6.7: Background noise of the 4 empty test sections, at $U_\infty = 20$ m s^{-1} and $U_\infty = 40$ m s^{-1}. Average between the 62 microphones in the array. The angular velocity of the wind tunnel fan, for each test, is specified in rotations per minute (RPM).

Figure 6.7 shows the background noise of the empty test sections, at $U_\infty = 20\,\mathrm{m\,s^{-1}}$ and $U_\infty = 40\,\mathrm{m\,s^{-1}}$. Test sections A and C operated with the wind tunnel fan at a higher angular velocity than B and D, for reaching the same U_∞. Test sections B and D include the top and bottom flat melamine panels, which reduce the effective cross–sectional area of the tunnel, without noticeably increasing the pressure loss in the circuit. For test sections B and D, a lower wind tunnel fan rotational speed, Ω, is therefore required. As a consequence of the higher wind tunnel fan power setting, test sections A and C feature the highest background noise. This result indicates that the aerodynamic background noise sources produced in the wind tunnel circuit, outside the test section, are dominant at the array location. These noise sources can be e.g. the wind tunnel fan, or physical discontinuities throughout the circuit. The scaling, k, of the aerodynamic noise levels with free-stream velocity was obtained from:

$$\left(\frac{U_{\infty,2}}{U_{\infty,1}}\right)^k = \left(\frac{p'_{\mathrm{rms},2}}{p'_{\mathrm{rms},1}}\right)^2, \tag{6.3}$$

where p'_{rms} was calculated considering the frequencies shown in Fig. 6.7. The high SPL peaks at $f = 600\,\mathrm{Hz}$, for the measurements at $U_\infty = 20\,\mathrm{m\,s^{-1}}$, have been previously identified to originate from

electrical devices used to power the wind tunnel [11]. The third octave frequency band centered at $f = 630\,\text{Hz}$ has therefore been filtered out, for the calculation of k. For the four test sections, k has a value between 4 and 5. This indicates that most aerodynamic noise is generated due to fluid–solid interaction. A value of $k = 8$ is considered to be ideal for aeroacoustic wind tunnels, since it is indicative that jet–noise has the strongest contribution to aerodynamic noise [22].

Figure 6.7 also shows that installing the wedged melamine Kevlar side–panels (compare e.g. test sections A and C) reduces the background noise by approximately $1 - 2\text{dB}$. This result is consistent with the lower levels found in the beamforming maps of Fig. 6.6, for the test sections with lined side–panels. The results of Figs. 6.6 and 6.7 highlight the effectiveness of test section lining solutions, for reducing the disturbance caused by background noise on acoustic measurements.

6.3.3. ACOUSTIC WIND TUNNEL MEASUREMENTS - WITH FLOW

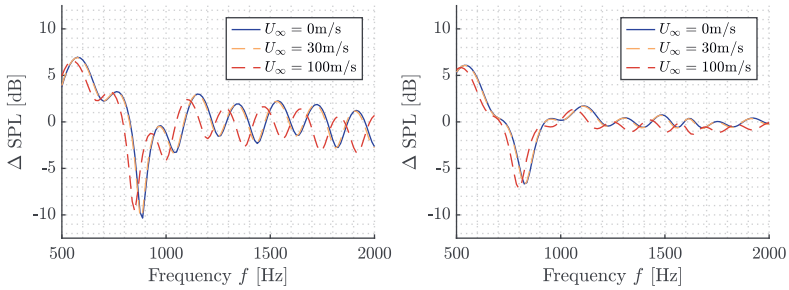

(a) Baseline test section - A (b) Most anechoic test section - D

Figure 6.8: Acoustic interference caused by the primary reflections, in the geometric modelling data, for varying free-stream velocity in the test section. Baseline test section (left), and most anechoic test section configuration (right). Spectra obtained from source power integration of the beamforming maps.

The effect of having the wind tunnel flow–on on the acoustic measurement of a source inside the test section was initially assessed with geometric modelling. The simulated spectra of Fig. 6.8 were obtained from source power integration of the beamforming maps of simulated data. The results obtained for the baseline (Fig. 6.8a) and most anechoic (Fig. 6.8b) test sections show that, up to $U_\infty = 30\,\text{m}\,\text{s}^{-1}$, i.e. at relatively low wind tunnel free-stream Mach number ($M = U_\infty/c = 0.09$), the convection of the sound waves by the flow does not affect the acoustic interference pattern at the microphone

array location. At higher Mach number ($M = 0.29$), the convection caused by the flow causes a significant shift of the interference pattern. The intensity of the mirror sources, as perceived by the microphones, is however not visibly affected, as the magnitude of the interference peaks remains unchanged.

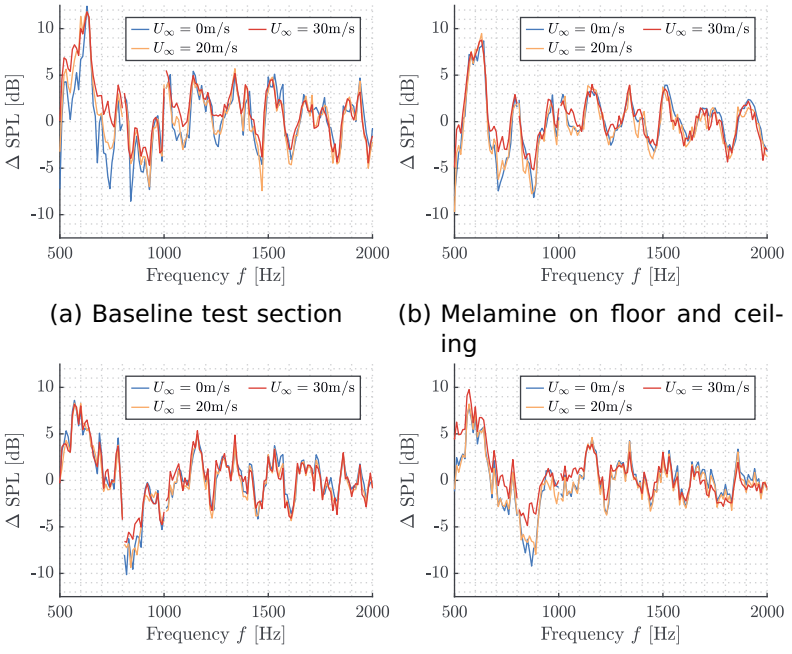

(a) Baseline test section

(b) Melamine on floor and ceiling

(c) Kevlar side-panels

(d) Most anechoic test section

Figure 6.9: Acoustic interference caused by the reflections, in the experimental data. Test sections A (top–left), B (top–right), C (bottom–left) and D (bottom–right). Spectra obtained from source power integration of the beamforming maps.

Figure 6.9 shows the SPI spectra obtained experimentally with each test section configuration, for the free-stream velocities: $U_\infty = 0\,\mathrm{m\,s^{-1}}$, $U_\infty = 20\,\mathrm{m\,s^{-1}}$ and $U_\infty = 30\,\mathrm{m\,s^{-1}}$. Below 1 kHz, the broadband and the white noise signals emitted by the speaker are relatively low, in comparison with the background noise. Therefore, the experimental spectra of Fig. 6.9 in the ranges 500 Hz to 800 Hz, 800 Hz to 1000 Hz, and 1000 Hz to 2000 Hz correspond, respectively, to the measurements with the speaker emitting the low–frequency narrow band noise, the mid–frequency narrow band noise, and broadband noise (see description of the signals in Sec. 6.2.1).

In agreement with the geometric modelling data, the experimental data indicates that the magnitude and the frequencies of the acoustic

interference peaks remain unchanged, at low free-stream velocities. The spectra of Fig. 6.9 also show that, at $U_\infty = 30\,\mathrm{m\,s^{-1}}$, there are frequencies for which the SPL is higher for the flow–on case than at $U_\infty = 0\,\mathrm{m\,s^{-1}}$ (most noticeable for f close to 850 Hz). This indicates that, at these frequencies, the background noise is comparable or higher than the noise levels from the acoustic source. The disturbance caused by the aerodynamic background noise in the measurement is most noticeable for the baseline test section configuration (Fig. 6.9a), which is consistent with the higher background noise levels seen in Figs. 6.6 and 6.7, for this test section.

The results of Figs. 6.8 and 6.9 show that, for aeroacoustics experiments at relatively low free-stream velocity ($M < 0.1$), the disturbance on acoustic measurements caused by reflections in the test section can be assessed without flow. The limit for which the flow–off acoustic measurements are valid can be investigated with a geometric modelling algorithm, based on the mirror–source method.

6.4. CONCLUSION

An experimental campaign was conducted in TU Delft's closed test section Low Turbulence Tunnel. Four test section configurations were tested, as the test section was progressively lined with sound absorbing treatments. An omnidirectional speaker was used as reference acoustic source. The resulting acoustic signals were measured with a phased microphone array. The disturbance in the acoustic measurement of the source signal was analysed by assessing the effect of reflections in the test section, reverberation in the wind tunnel, convection of acoustic waves by the free-stream flow, and aerodynamic background noise. A geometric modelling algorithm was developed for predicting the disturbance caused by primary reflections in the test section on acoustic measurements, for each lining configuration.

The experimental results show that reverberation in the wind tunnel circuit is reduced with test section lining. Reverberation caused by walls outside the test section (both upstream and downstream), although strong, is shown to cause a negligible disturbance in the microphone array measurements, in the flow–off tests. For the flow–on experimental measurements, aerodynamic noise originating outside the test section was identified to be a dominant cause of pressure fluctuations at the array location. Lining over the test section walls was an effective approach for reducing the aerodynamic noise reaching the microphones. The geometric modelling results demonstrate that a strong improvement of the acoustic capabilities of a wind tunnel can be achieved, by reducing the reflection coefficient of the test section walls for which there is a direct reflection path from the source to the microphone array. The experimental acoustic tests show that the remaining test section walls

should also be lined, for approaching anechoic conditions in the test section. The convection of sound waves by the free-stream flow, at low Mach number ($M < 0.1$), was demonstrated to cause a negligible change in the acoustic interference pattern at the microphone array.

Based on the results of this study, it can be concluded that acoustic reflections in a wind tunnel designed for aeroacoustic studies can be investigated with a speaker, without flow. The flow conditions for which the flow–off acoustic measurements are valid should be assessed, e.g. with a geometric modelling algorithm. Measurements of aerodynamic background noise should be performed with an empty test section, and lining can be used to reduce the background noise that reaches the microphone array. Future studies should investigate the benefits obtained from lining other sections of the tunnel, such as the diffuser, for reducing aerodynamic noise in the circuit. The use of higher fidelity methods for predicting acoustic interference in the test section is also expected to further help with designing acoustically treated test sections.

7

SOUND PROPAGATION IN ACOUSTICALLY DISTURBED WIND TUNNELS

Sound propagation in closed test section wind tunnels suffers from reflections and diffraction, which compromise acoustic measurements. In this article, it is proved possible to improve the post–processing of phased–array microphone measurements by using an approach based on the combination of numerical acoustic simulations and beamforming. A Finite Element Method solver for the Helmholtz equation is used to model the acoustic response of the experimental facility. The simulations are compared with acoustic experiments performed at TU Delft's Low Turbulence Tunnel, using both fully reflective (baseline) and lined test sections. The solver accurately predicts the acoustic propagation from a monopole sound source at the centre of the test section to the microphones in the phased–array, for frequencies in the range $500\,Hz < f < 2000\,Hz$*. It is shown that a (lower fidelity) geometric modelling method is unable to precisely predict the acoustic response of the Low Turbulence Tunnel at these frequencies, due to strong acoustic diffraction. The numerical results are used to implement corrections to the post-processing of experimental data. A corrected version of the Source Power Integration method is able to increase the accuracy of the source's noise levels calculation, based on a single numerical simulation with the source at the same location as in the experiment. A Green's function correction increases the beamforming resolution and the source's noise levels estimation accuracy from the beamforming*

This chapter is based on the work published in Journal of Sound and Vibration **600** (2025) [160] and in 4TU.ResearchData [161].

maps, without a priori knowledge of the source's location. Both corrections perform well at processing flow–on acoustic measurements, and the Green's function correction shows an additional benefit. The improvement in beamforming spatial resolution leads to an increase of the signal to noise ratio.

7.1. INTRODUCTION

Most commonly, conventional beamforming takes into account the sound propagation (through the Green's function) from a source to an observer by assuming the source to behave as a free–field monopole. However, this can lead to errors, when the acoustic propagation is disturbed by the environment or by its boundaries. Previous literature has been directed at reducing the effect of non–free–field conditions, e.g. reflections in the setup, on beamforming results.

Guidati et al. [145] and Fenech and Takeda [146] used a geometric modelling algorithm to predict and correct for the influence of mirror–reflections on the propagation of sound in a rectangular wind tunnel test section. Sijtsma and Holthusen [35] reduced the influence of specular reflections in the beamforming map with a "Mirror Minimisation" technique, a correction which is less dependent on the assumed strength and location of the mirror sources. Fischer and Doolan [23] improved beamforming in a closed hard–walled wind tunnel by calculating corrected Green's functions based on the mirror–source method and on experimental measurements. The Green's function obtained experimentally achieved better results, however, it requires a complex measurement procedure. The experimental Green's function had to be measured for each beamforming scan grid location. Gombots et al. [162] used a Finite Element Method (FEM) for estimating the Green's function of sound propagation in a disturbed environment, which has been shown to be accurate for identifying and quantifying sources simulated numerically. Lehmann et al. [163] also employed a numerical method, the Boundary Element Method, for calculating the acoustic Green's function in a disturbed environment. The numerical Green's function has been shown to improve the beamforming maps of experimental data, measured with a setup representative of a fan in a heat exchanger, e.g., by reducing the main lobe width.

Preceding literature has, however, not yet been able to demonstrate that a numerically obtained Green's function correction improves the estimation of an experimental source's noise levels. In this study, simulations of an acoustic source inside a wind tunnel test section were done with a FEM solver for the Helmholtz equation. The numerical results are validated with an acoustic experiment carried out at TU Delft's LTT wind tunnel, described in 3.1.1. Following, two methods are proposed for correcting the acoustic experimental results, making use of the FEM

simulations. In the first method, the Green's function is corrected, similarly to the approach employed in literature, e.g., [162, 163]. In the second method, only the Source Power Integration (SPI) step is modified, making use of prior knowledge of the source location. SPI is a technique commonly used to estimate source noise levels from beamforming maps [92]. The second method removes the need of having to compute the Green's function in the entire test section, or at the beamforming scan plane. To quantify the benefits achieved with each correcting method, an experimental measurement of the source in an undisturbed environment is used as reference. To the authors' knowledge, this is the first time that the approach of lining a closed wind tunnel test section is combined with the approach of numerically simulating the wind tunnel's acoustic response, for improving the experimental beamforming results.

The study is structured as follows. Section 7.2 describes the methodology employed in the study, including the computational approach, the experimental campaign, and the post–processing methods. Section 7.3 covers the validation and verification of the results presented. Section 7.4 describes the dominant acoustic phenomena present in the wind tunnel test section, based on the computational solutions. Section 7.5 presents the results obtained after implementing the numerically obtained corrections for processing the experimental data with beamforming. The discussion of the applicability of the post-processing methodology proposed in this paper to flow–on measurements is presented in Sec. 7.6. Finally, Sec. 7.7 highlights the main conclusions from the study.

7.2. METHODOLOGY

7.2.1. NUMERICAL MODELLING OF SOUND WAVE PROPAGATION

The acoustic propagation inside the LTT test section was predicted with the FEM solver described in Sec. 3.3.2. This study evaluates each test case for the acoustic frequencies in the range $300\,\text{Hz} \leq f \leq 2000\,\text{Hz}$, with steps of $\Delta f = 10\,\text{Hz}$.

NUMERICAL SETUP

Figure 7.1 shows the numerical setups defined for understanding the acoustic behaviour of the different wind tunnel test section (TS) configurations. Figure 7.1a shows the setup defined for the reference simulation, the simulation of a free-field monopole source. The acoustic domain has a cylindrical shape, with streamwise (x–direction) length $L_c = 1.65\,\text{m}$ and radius $R_c = 1.8\,\text{m}$. Reflections at the boundary of the simulation domain were avoided by defining Perfectly Matched Layer (PML) regions, where outgoing waves are dampened. The thickness of the PML regions depend on the acoustic wavelength, λ, of each

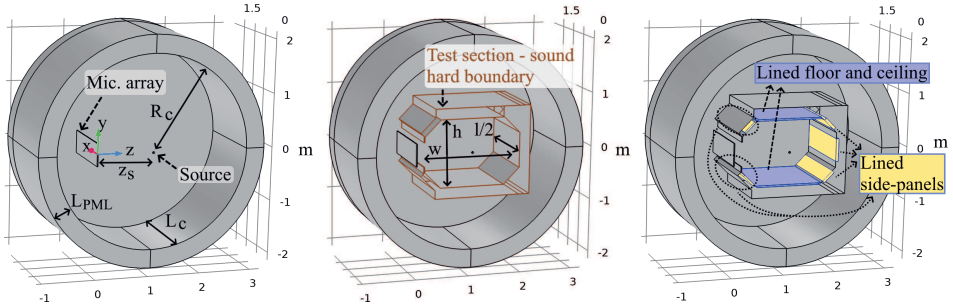

(a) Free–field (b) Baseline test section (c) Fully lined test section

Figure 7.1: Numerical setup used for the Finite Element Method acoustic simulations: setup defined for the simulation of a free-field monopole (left), setup of the baseline wind tunnel test section (centre) and setup of the fully lined test section configuration (right).

simulation: $L_{\mathbf{PML}} = 2\lambda$. As in [28], this approach allowed for the simulation of an acoustically open domain [88].

The monopole source is a sphere of radius 0.02 m, placed at the centre of the cylindrical domain, with coordinates $(x_s, y_s, z_s) = (0, 0, 1.05)$m. Only half of the sphere is simulated, as a symmetry boundary condition is placed at the streamwise plane that passes through the centre of the source. This plane is defined by $x = 0$. The microphone array used to measure the source's noise levels in the simulation is placed at $z = 0$ and is confined within $-0.4\,\text{m} < y < 0.4\,\text{m}$ and $x < 0.8\,\text{m}$.

The vertical and spanwise coordinates of the 62 microphones that make up the array are the same as in the wind tunnel experiment (described with more detail in Sec. 7.2.3). The streamwise coordinates of the simulated array are $x_{\text{simulation}} = |x_{\text{experiment}}|$, where $|\cdot|$ is the modulus, so that all microphones have a positive streamwise coordinate, and are thus placed inside the simulation domain. A rectangular box is seen in Fig. 7.1a which encloses the microphone array. The box has been exclusively defined for increasing cell refinement at the measurement location.

Figure 7.1b shows the simulation setup of the baseline wind tunnel test section. The test section has an octagonal shape with a constant angle between walls of 135°. The test section's height, spanwise width and streamwise (half) length are $h_{\text{TS}} = 1.25\,\text{m}$, $w_{\text{TS}} = 1.8\,\text{m}$ and $l_{\text{TS}}/2 = 1.4\,\text{m}$. l_{TS} is larger in the simulation than in the experiment to allow for the assumption that the simulated test section is infinite in the streamwise direction, from the perspective of the microphone array (see description of the post–processing technique in Sec. 7.2.4). Figure 7.1c shows the setup of the fully lined test section configuration.

The floor and ceiling are lined with 3 cm thick melamine panels, simply placed over the baseline floor and ceiling (seen in Fig. 7.1b). The side panels are lined with 5 cm thick melamine, installed in panels which are mounted on the walls, effectively increasing the fluid volume inside the test section. The melamine side panels are enclosed (on 5 sides) by walls, where the sound hard wall boundary condition is imposed. Sound reflections still occur at these walls, mainly at lower frequencies. The sound absorption characteristics of Melamine foam panels with 3 cm and 5 cm thickness placed over a solid wall are dictated by Melamine's viscous resistivity, $R_v = 9\,\mathrm{kPa\,s\,m^{-2}}$, and are detailed in Ref. [156].

Table 7.1 describes the different setups evaluated in this study. The Reference, Test section A and Test section D simulation domains are shown, respectively, in Figs. 7.1a, 7.1b and 7.1c. B and C are configurations with intermediate lining, between the baseline (A) and the fully lined (D) cases. Besides simulating the complete test sections, the dominance of specular reflections and diffraction was also evaluated by performing simulations with a reduced number of wind tunnel walls. This is done in order to isolate each of the dominant acoustic phenomena. For these simulations, the domain streamwise length and the walls' half streamwise length were reduced, respectively, to $L_c = 1.25\,\mathrm{m}$ and $l/2 = 1\,\mathrm{m}$. The remaining setup geometrical characteristics and boundary conditions, as shown in Fig. 7.1, are uniform for all setups described in Table 7.1.

Table 7.1: Numerical setups designed for the FEM simulations of a monopole sound source.

Setup designation	Details	Bottom and top 3 cm melamine lining	Side–panels lined with 5 cm melamine
Reference	Free–field monopole	-	-
Test section A	Baseline section	-	-
Test section B	Lined section	✓	-
Test section C	Lined section	-	✓
Test section D	Fully lined TS	✓	✓
2 walls	Floor and opposite wall	-	-
3 walls	Floor, ceiling and opposite wall	-	-
Walls + corner(s)	Corner(s) between the floor/ ceiling and opposite wall	-	-
Walls + edge(s)	Being edges the angled walls between floor/ ceiling and the array	-	-

DISCRETIZATION

Figure 7.2 shows the coarse computational grid generated for studying the response of the fully lined test section, with the source emitting

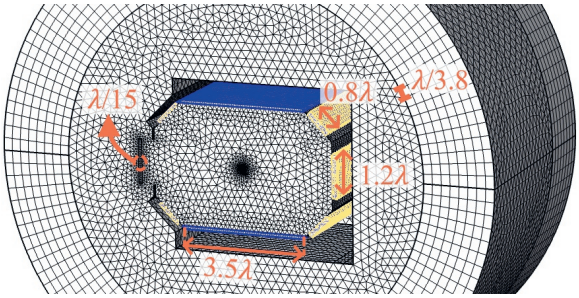

Figure 7.2: Computational grid generated for the numerical simulation of test section D, the fully lined configuration. Element size correspondent to the simulation of the source emitting noise at $f = 1\,\text{kHz}$, with the coarse grid settings. The elements coloured with blue represent the melamine lining regions over the floor and ceiling, and the elements coloured with yellow represent the lined side–panels.

noise at 1000 Hz. The figure shows that the grid is unstructured, except for the PML domains, where a swept grid was introduced. For each computed frequency, the size of the mesh elements was defined based on the sound wavelength, λ. For the medium grids, the cell size has been defined to be not larger than $\lambda/5$. Regions of increased refinement include the inner walls of the test section, the acoustic source and the porous media. The region where the microphones are located have cells smaller or equal to $\lambda/20$, in order to avoid complex interpolations (i.e. non-linear interpolations) between cell elements during post-processing. A grid refinement study was conducted to find the optimum grid refinement. For the coarse and fine grids, the cell length settings of the medium grid were divided by 0.75 and 1.5, respectively. The results of the grid dependence study are discussed in Sec. 7.3.1.

7.2.2. GEOMETRIC MODELLING

The GM algorithm described in Sec. 3.2 is used to understand the influence of specular reflections in the acoustic behaviour of the octagonal wind tunnel test section. The comparison with FEM allows for the understanding of how the remaining acoustic phenomena, such as diffraction, alter the test section's acoustic behaviour.

The specular reflections on the three larger walls of the test section (floor, ceiling and wall opposite to the array) are modelled as a mirror–source, as shown in Fig. 7.3. Primary, secondary and tertiary reflections refer to waves which reflect over one, two or three walls on the path between the source and a microphone. As in the numerical (FEM) setup, the microphones in Fig. 7.3 are located slightly (15 cm)

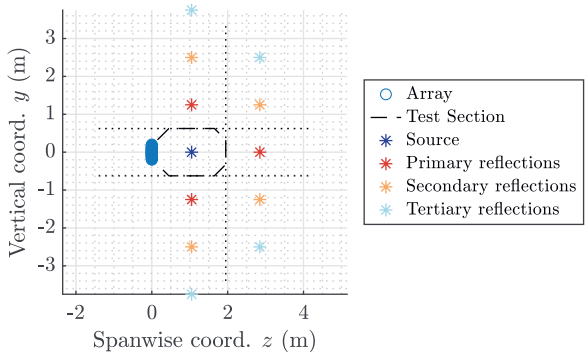

Figure 7.3: Setup of the geometric modelling simulations. The reflections on the three largest test section walls (floor, ceiling and wall opposite to the array) are modelled with the mirror–source model.

outside the test section in the z direction. This is done in order to replicate the experimental installation of the microphone array. The experimental setup is detailed in the following sub–section.

7.2.3. EXPERIMENTAL VALIDATION CASE

The wave propagation modelling method described in Sec. 7.2.1 has been validated against measurements taken at the LTT wind tunnel, at TU Delft. This wind tunnel is introduced in Sec. 3.1.1 and the experimental campaign is described in Sec. 6.2.1.

All 4 LTT test section configurations described in Table 6.1 have been analysed in this study. The experimental data analysed corresponds to measurements taken with the following free–stream velocities in the test section: $U_\infty = 0\,\mathrm{m\,s^{-1}}$, $U_\infty = 20\,\mathrm{m\,s^{-1}}$ and $U_\infty = 30\,\mathrm{m\,s^{-1}}$.

ACOUSTIC MEASUREMENTS

The LTT acoustic array is described in Sec. 3.1.2 and shown in Fig. 3.4a. The campaign's measurement procedure is detailed in Sec. 6.2.3. The main difference between the experimental and the numerical microphone array setups is that the simulated microphones are placed as free–field microphones, i.e., without the lined plate holder and without the Kevlar sheet (shown in Fig. 3.4b). The lined holder can cause an offset in the measured absolute noise levels at low frequencies, but this offset is negligible when evaluating the difference between the noise spectra of two test cases, e.g. the difference between the reference simulation and the simulation with a test section.

The influence of the Kevlar panel on the measurements was verified

by performing an additional measurement of the speaker noise with test section C without the Kevlar panel, i.e., with an open wall, as shown in Fig. 3.4a. This was possible since this measurement was taken at 0 free–stream velocity.

7.2.4. POST-PROCESSING ALGORITHMS

The numerical microphone data was extracted for each frequency, as the simulations were done with the frequency domain formulation. The experimental microphone data was instead measured in the time domain. The experimental microphone signals were converted to the frequency domain with the Welch's method [159]. The 20 s signals were divided into windows of 0.1 s, with a 50 % overlap. Each window was multiplied by the Hanning function. The following steps in the post–processing were equally applied to both the experimental and the numerical microphone data, in the frequency domain.

As in Chapter 6, acoustic interference in the test section was quantified as the difference between the measurements in the reverberant environment and the reference speaker measurement, ΔSPL (see Eq. 6.2).

CONVENTIONAL BEAMFORMING

The experimental and simulated acoustic data from the microphone array were processed with conventional beamforming, which has been introduced in Sec. 3.4.

In this study, the diagonal of the beamforming CSM (see Eq. 3.12), i.e., the auto–powers, has been kept for the processing of the purely acoustic results (flow–off), i.e. the results presented in Secs. 7.3, 7.4 and 7.5, and has been removed for obtaining the results presented in Sec. 7.6, relative to the flow–on test cases. Furthermore, for the flow–on cases, $\Delta t_{j,n}$ (see Eq. 3.11) was recalculated taking into account the flow convection of sound waves.

For beamforming, the acoustic data were processed considering a 2D scan grid parallel to the array. The 2D grid is at a 1.05 m distance from the array, and passes through the spanwise centre of the test section, i.e., through the speaker location. After calculating the beamforming maps, the speaker noise levels were obtained with the Source Power Integration (SPI) method, previously described in Sec. 3.4.2.

Figure 3.6 shows a beamforming map of the reference speaker measurement. A $24\times24\,\mathrm{cm}^2$ SPI region is illustrated. This SPI region was used in this study to estimate the noise levels from the beamforming maps obtained with the free–field Green's function.

For the experimental beamforming maps calculated with a corrected Green's function, a $2\times2\,\mathrm{cm}^2$ SPI region was considered. The reason is that correcting the Green's function influences the resolution of the

beamforming map. Equation (3.15) should not be used for integrating noise levels in regions of the scan plane where the experimental beamforming map (present on the numerator of Eq. (3.15)) has a different resolution than the simulated beamforming map (present on the denominator of Eq. (3.15)). This issue can also be overcome by simultaneously using the Green's function correction and the SPI correction, both described in the following sub–section.

CORRECTIONS TO THE EXPERIMENTAL RESULTS

The numerical method described in Sec. 7.2.1 was used to model the acoustic behaviour of a source inside closed wind tunnel test sections. The numerical results were used in this study to correct the experimental measurements taken in the LTT, in order to make these acoustic results closer to the reference measurement of the source (the omnidirectional speaker). Two methods were tested for improving the post–processing of experimental data. The first focuses on refining the Green's function used for beamforming (see Eq. (3.11)). The second is based on changing the denominator of Eq. (3.15), in this way improving the SPI method.

The reference numerical simulation models a free–field monopole source. Therefore, the propagation in this simulation follows the Green's function described by Eq. (3.11). However, for the simulations where the wind tunnel test section is present, the propagation of sound is altered. For each numerical simulation, $p'_{s,o}(f)$ is the pressure fluctuation at the observer position o, when the source is located at s. $p'_{s,o}(f)$ is complex valued and, therefore, contains both magnitude and phase information. For each o and s, the Green's function of a monopole inside the simulated wind tunnel test section (i.e. in non-free field conditions) is then:

$$g_{s,o\ \text{(WT, corrected)}} = g_{s,o\ \text{(free–field)}} \frac{p'_{s,o}(f)_{\text{WT simulation}}}{p'_{s,o}(f)_{\text{Ref. simulation}}}. \tag{7.1}$$

Equation (7.1) was used for correcting the Green's function used for post–processing the experimental acoustic measurements with beamforming. This correction requires that the Green's functions of sound propagation in the experimental and numerical wind tunnel setups are equivalent. This is true when the computational modelling of the experimental setup is accurate. The validation of the simulations is discussed in the following Section.

To correct the Green's function, $g_{s,o\ \text{(WT)}}$ is calculated for all beamforming scan plane positions. The beamforming map of Fig. 3.6 was generated for scan plane positions spaced by 0.01 m, i.e., 24000 positions. The most straight–forward approach for calculating $g_{s,o\ \text{(WT)}}$ for the entire scan plane is to perform simulations with the source at

each scan plane position. However, this is computationally expensive. Three assumptions were made to reduce the number of simulations required. Firstly, the wind tunnel setup was considered to be symmetric in the vertical direction, with respect to the horizontal plane which passes by the source, the plane $y = 0$. In this way, simulations were performed for source locations defined by $y_s \geq 0$. To obtain the value of $g_{s,o\ (\mathrm{WT})}$ for $y_s < 0$, the observer and source's vertical coordinates were instead mirrored: $y'_s = -y_s$ and $y'_o = -y_o$ (see sketch in Fig. 7.4a). This first consideration reduces the number of numerical simulations required to approximately half. Secondly, the test section walls were defined (in the numerical setup) with constant y and z coordinates, leading to a constant test section area with respect to the streamwise direction (whereas the experimental test section walls feature a slight expansion). The simulated test section was also assumed to be infinite, in the streamwise direction. To increase the validity of this assumption, the streamwise test section length was increased in the simulation. As described previously, the test section had been assumed to be symmetric with respect to $x = 0$. Based on these assumptions, it was possible to run simulations exclusively for source positions at the streamwise centre of the test section, $x_s = 0$. To obtain the value of $g_{s,o\ (\mathrm{WT})}$ for $x_s \neq 0$, the observer's streamwise coordinate was instead moved: $x'_s = 0$ and $x'_o = |x_s - x_o|$ (see sketch in Fig. 7.4b). Thirdly, $p'_{s,o}(f)_{\mathrm{WT\ simulation}}$ and $p'_{s,o}(f)_{\mathrm{Ref.\ simulation}}$ were assumed to vary linearly, for relatively short variations of the source's vertical position. The simulations were done for source locations spaced by $\Delta y_s = 0.04m$. For scan plane locations at a vertical location which had not been simulated, $p'_{s,o}(f)_{\mathrm{WT\ simulation}}$ and $p'_{s,o}(f)_{\mathrm{Ref.\ simulation}}$ were estimated by linear interpolation. With this approach, it is possible to obtain $g_{s,o\ (\mathrm{WT})}$ for the scan plane seen in Fig. 3.6 by simulating the source at 16 different locations, instead of 2400. In this study, the computational cost was further decreased by reducing the scan plane to $0.8 \times 0.32\,\mathrm{m}^2$.

The second correction validated in this study was a correction to the SPI method. This was implemented by correcting the denominator in Eq. (3.15):

$$A(\boldsymbol{\xi}_j)_{\mathrm{sim.,\ correction}} = \frac{\boldsymbol{g}^*_{j(\mathrm{free\text{–}field})}(\boldsymbol{pp}^*)_{\mathrm{FEM}}\boldsymbol{g}_{j(\mathrm{free\text{–}field})}}{\|\boldsymbol{g}_{j(\mathrm{free\text{–}field})}\|^b}, \tag{7.2}$$

where $(\boldsymbol{pp}^*)_{\mathrm{FEM}}$ is the cross–spectral matrix calculated from the numerical acoustic data. Considering the properties of the logarithmic function, the corrected SPI for a source inside the test section can equivalently be calculated from:

$$\mathrm{SPL}_{\mathrm{SPI\ corr.}} = (\mathrm{SPL}_{\mathrm{WT}})_{\mathrm{SPI,\ Exp.}} - (\mathrm{SPL}_{\mathrm{WT}})_{\mathrm{SPI,\ FEM.}}. \tag{7.3}$$

In this study, each correction was tested separately, i.e., the SPI

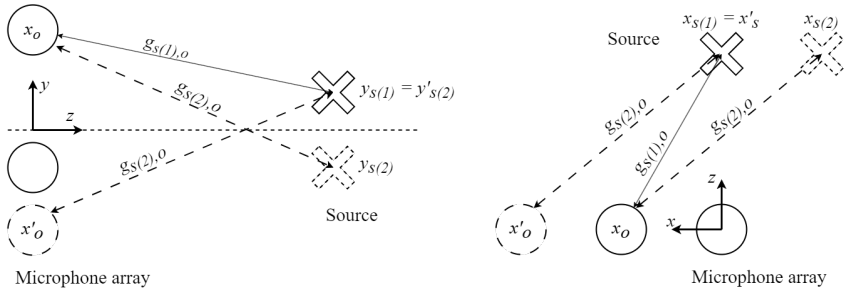

(a) Mirror plane at $y = 0$

(b) Constant section – streamwise direction

Figure 7.4: Method of calculating the Green's function. Mirror with respect to $y = 0$ (left) and assumption that the test section is constant and infinite in the streamwise direction (right).

correction was applied to process beamforming data obtained with the free-field Green's function. This was done to evaluate the benefits from the two correction methods separately. The two corrections may, however, be used simultaneously, which can be beneficial when the SPI area is relatively large, as previously mentioned.

SUMMARY OF THE PROPOSED APPROACH

The diagram of Fig. 7.5 summarizes the methodology proposed in this paper for improving the post–processing of experimental acoustic data obtained in a disturbed environment, e.g., a closed test section wind tunnel. The numerical FEM setup is discussed in Sec. 7.2.1, and the acoustic wind tunnel experimental setup is described in Sec. 7.2.3. The measurement (or extraction) of the pressure fluctuations from the FEM results is discussed in Sec. 7.2.4, along with the calculation of the corrected Green's function. The beamforming and (uncorrected) SPI methods are introduced in Sec 7.2.4. The correction to the SPI method is described in Sec. 7.2.4.

The two alternative paths tested in this study (black and blue paths in Fig. 7.5) represent, respectively, the proposed Green's function correction and the proposed SPI correction. The dashed lines suggest possible alternatives to the methodology validated in this paper.

7.3. VALIDATION

7.3.1. GRID DEPENDENCE STUDY

Figure 7.6 shows the results from the grid dependence study of the FEM simulations. Results are shown for the baseline test section (A)

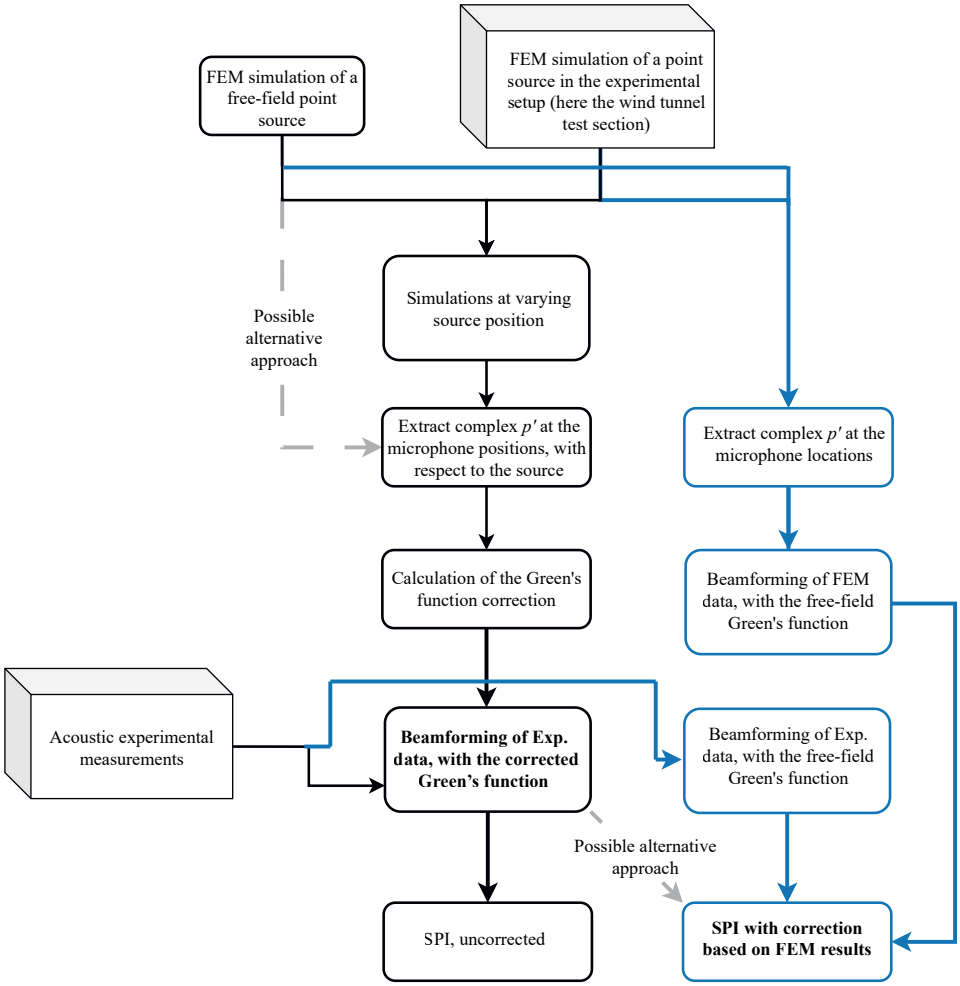

Figure 7.5: Summary of the methodology proposed, for using FEM simulations to improve the post–processing of experimental acoustic data collected in a disturbed environment. The black and blue arrows refer to the two approaches suggested and validated in this paper.

and for one of the lined configurations (B). For each test section, three simulations with increasing grid refinement were carried out (grids previously described in Sec. 7.2.1). The fine grid simulations were computed for fewer frequencies, by setting $\Delta f_{\text{Fine}} = 20\,\text{Hz}$. For the baseline test section, the numerical calculations with the medium and fine grids had equivalent results (Fig. 7.6a), while differences are visible for the coarse one. For the lined test section, it can be seen that the

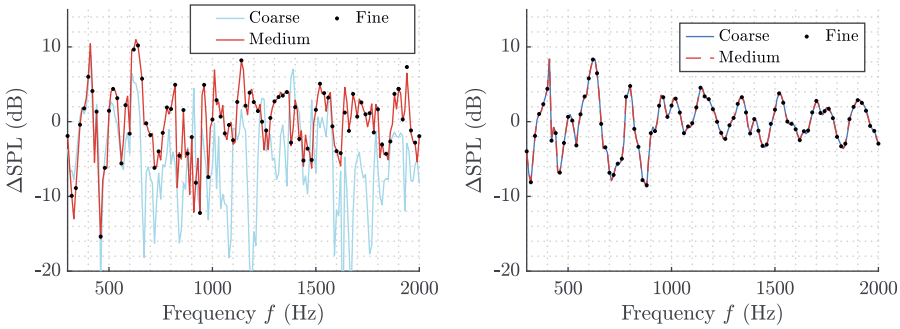

(a) Spectra TS A

(b) Spectra TS B

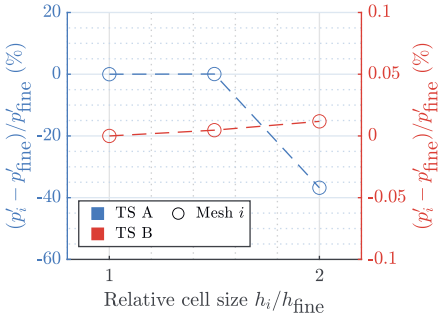

(c) Overall noise level

Figure 7.6: Grid dependence study of the FEM simulations: spectra of the Baseline test section A (top-left); spectra of the lined configuration B (top-right); and overall noise level, for both test sections (bottom). Spectra obtained from Source Power Integration of the conventional beamforming maps, within a $24 \times 24\,\text{cm}^2$ region. The overall noise level is obtained from the SPI spectra, considering frequencies in the range $300\,\text{Hz} \leq f \leq 2000\,\text{Hz}$, with steps of $\Delta f = 20\,\text{Hz}$. ΔSPL as defined in Eq. (6.2).

spectra matches for all three grids (Fig. 7.6b).

The dependence of the overall noise levels with respect to grid refinement is shown in Fig. 7.6c. The quantity analysed, p'_i, is obtained by integrating the noise levels shown in the spectra of Figs. 7.6a and 7.6b, for each grid resolution i. The convergence of p'_i is analysed with respect to the relative cell size between each grid and the fine resolution grid, h_i/h_{fine}. Based on the lined test section results, p'_i is not expected to vary from the coarse grid to a grid with finer resolution, i.e., with h_i/h_{fine} approximating 0. For the baseline test section, Fig. 7.6c highlights the large difference in result between the coarse grid and the remaining grids.

Based on the results of Fig. 7.6, the resolution of the coarse grid was deemed sufficient to simulate the lined test sections. For the baseline test section, however, it was concluded that the medium resolution had to be used. For the simulations with a reduced number of walls, the medium refinement was also selected.

7.3.2. REFLECTIONS THROUGHOUT THE WIND TUNNEL CIRCUIT

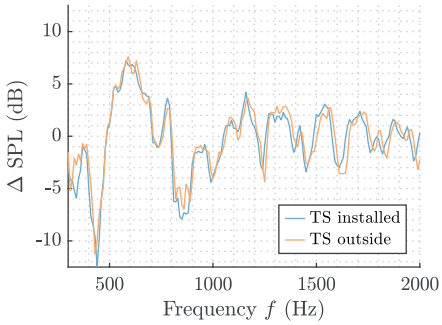

Figure 7.7: Acoustic interference caused by the reflections: difference between the measurement inside the test section and the reference speaker measurement. Comparison between installed and uninstalled test section, from experimental data, for test section C. Spectra obtained from Source Power Integration of the conventional beamforming maps, within a $24 \times 24\,\mathrm{cm}^2$ region.

The simulations of the acoustic behaviour of a source inside the wind tunnel were made by modelling the test section. However, this approach does not account for possible contamination caused by reflections in the remaining sections of the wind tunnel circuit. In order to quantify this disturbance, an additional acoustic test was made. One of the lined test sections (test section C) was removed from the wind tunnel circuit, and placed in a large room, where reverberation is negligible. The reverberation in this room and in the LTT circuit was quantified and discussed in more detail in Ref. [156]. The acoustic measurements conducted with test section C installed in the wind tunnel circuit and placed outside the circuit were compared. The results are shown in Fig. 7.7. The resulting spectra show negligible differences between the two cases. This indicates that, when the experimental phased–array data is processed with beamforming, the reflections in the wind tunnel circuit, outside of the test section, have a negligible influence in the resulting spectra. Therefore, it is assumed sufficient to model the test section, with the numerical acoustic solver.

7.3.3. VALIDATION OF THE FEM SIMULATIONS

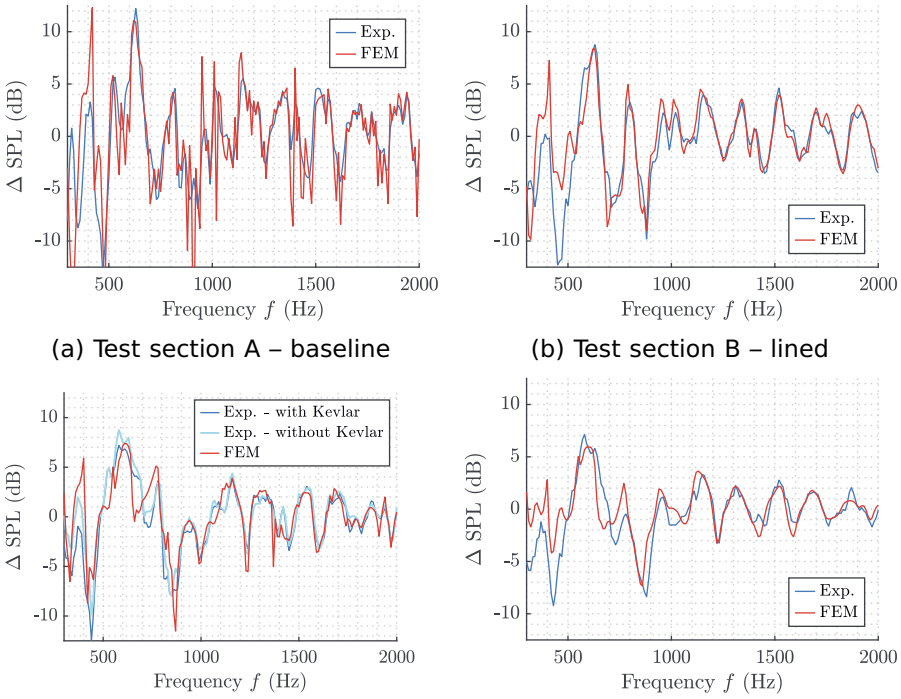

(a) Test section A – baseline

(b) Test section B – lined

(c) Test section C – lined

(d) Test section D – fully lined

Figure 7.8: Validation of the numerical acoustic simulations. Comparison between the simulated and experimental spectra, for the test cases with a monopole source at the centre of each test section. Spectra obtained from Source Power Integration of the conventional beamforming maps, within a $24 \times 24\,\mathrm{cm}^2$ region.

To validate the FEM numerical method, the simulated acoustic spectra were compared against the experimental ones. The comparison was done for the test cases with the monopole acoustic source inside each of the four test sections. The experimental data from test section C was obtained with and without the Kevlar wall placed in front of the microphone array, as discussed in Sec. 7.2.3. During the experimental measurements with test sections A, B and D, the Kevlar panel remained installed. The spectra were obtained from SPI of the conventional beamforming maps. Figure 7.8 shows the results. These spectra were calculated with a $24 \times 24\,\mathrm{cm}^2$ SPI region, although the spectra calculated with a smaller integration region, of $2 \times 2\,\mathrm{cm}^2$, are identical.

The agreement between experiment and simulation is very good for

all test cases, for frequencies above 500 Hz. At lower frequencies, the agreement is poorer due to differences between the experimental and numerical setups, which are associated with the assumptions previously discussed in Sec. 7.2.3. Figure 7.8c shows that the Kevlar panel is partially responsible for this difference between experiment and simulations at lower frequencies. The result appears to deviate from results reported in literature, where the acoustic transmission loss through Kevlar, without a grazing boundary layer, is shown to be negligible below 2 kHz [57]. This deviation is assumed to be due to the finite size of the Kevlar sheet and of the tunnel opening where it is installed (see Fig. 3.2a). This non–ideal installation causes an increase of the acoustic disturbance at $f < 500$ Hz, where diffraction is a relevant phenomenon (see discussion of Sec. 7.4.2). Due to the challenging comparison between experiments and simulations at low frequencies, the methodology proposed in this paper for improving the post–processing of experimental data based on the FEM results is applied for $f \geq 500$ Hz (results of the improved methodology presented in Secs. 7.5 and 7.6).

Figure 7.8 also shows that the best agreement between experiment and simulation was found for test section B (Fig. 7.8b). As mentioned in the previous section, this is the case for which the lining was most accurately modelled in the simulation: the side panels' wedged–melamine lining was simplified to flat melamine lining, for simulating test sections C and D (Figs. 7.8c and 7.8d). Figure 7.8a shows that the simulation of the baseline section captures sharper acoustic interference peaks than seen in the experimental result, possibly explained by the limited experimental measurement time (detailed in Sec. 7.2.4).

7.4. KEY ACOUSTIC PHENOMENA

The present section identifies the dominant acoustic phenomena which occur inside the octagonal LTT test section. Section 7.4.1 discusses the significance of mirror reflections in the test section, Sec. 7.4.2 describes the disturbance caused by diffraction on the test section's acoustic response, and Sec. 7.4.3 analyses the acoustic absorption which occurs in the lined configurations.

7.4.1. MIRROR REFLECTIONS

The relevance of mirror reflections on the acoustic interference at the microphone array location was analysed by simulating a reduced number of test section walls, both with the FEM solver and with the geometric modelling algorithm. The acoustic interference results, obtained from beamforming of the synthetic data, are shown in Fig. 7.9. Figure 7.9b

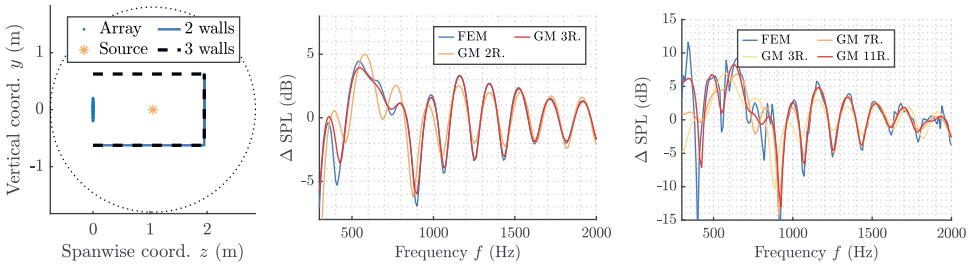

(a) Setup (b) Spectra: 2 walls (c) Spectra: 3 walls

Figure 7.9: Acoustic interference caused by specular reflections in the (fully reflective) test section, simplified to a reduced number of walls. Simulation setup (left), and comparison between FEM and geometric modelling of the two walls (centre) and three walls (right) cases. Spectra obtained from Source Power Integration of the beamforming maps of the simulated data, within a $24 \times 24\,\mathrm{cm}^2$ region.

shows that the reflections on the floor and opposite wall can be modelled by considering three mirror sources, i.e. by including the secondary reflection. The result shows that, for the two walls' setup (see Fig. 7.9a), specular reflections are dominant with respect to diffraction. The spectra shown in Fig. 7.9c indicates that the tertiary reflections should also be modelled for predicting the disturbance caused by specular reflections, in the three walls case.

This GM algorithm does not account for diffraction and diffuse reflections, thus it can only approximate the behaviour of the three main walls of the LTT test section. However, the FEM spectrum shown in Fig. 7.9c (3 main LTT walls) is considerably different from the spectra of Fig. 7.8a, i.e., the spectra for the baseline LTT test section. This indicates that the mirror source–method is insufficient for accurately predicting the acoustic response of the LTT's test section, even if an infinite number of mirror reflections is considered.

7.4.2. DIFFRACTION

The present section analyses the disturbance caused by acoustic diffraction inside the LTT test section. This effect is visible in Fig. 7.10, where the acoustic fields of the two walls FEM simulations are shown, for the frequencies $f = 500\,\mathrm{Hz}$ and $f = 2000\,\mathrm{Hz}$. The acoustic fields are taken at the $x = 0$ plane, from the FEM simulations. The two walls' acoustic fields are compared with the case where a 45° angled edge is added to the floor wall, close to the array (see Figs. 7.10b and 7.10e), and to the case where a 45° angled corner is added, between the floor

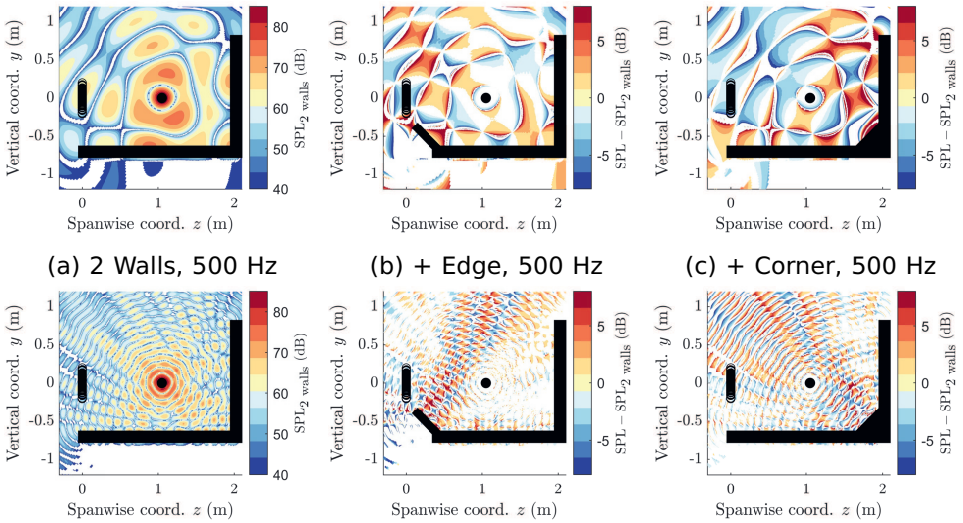

(a) 2 Walls, 500 Hz (b) + Edge, 500 Hz (c) + Corner, 500 Hz

(d) 2 Walls, 2000 Hz (e) + Edge, 2000 Hz (f) + Corner, 2000 Hz

Figure 7.10: Acoustic fields of the test cases with the floor and with the wall opposite to the array. Simulations of the 2 walls case (left), 2 walls with an angled edge (centre), and 2 walls with the angled corner (right). Calculations with the source emitting noise: at 500 Hz (top); and at 2000 Hz (bottom). Acoustic fields at the $x = 0$ plane, obtained from the Finite Element Method simulations. $\mathrm{SPL}_{2\ \mathrm{walls}}$ is the acoustic field of the 2 walls case (left), which in this figure is considered as reference.

and the wall opposite to the array (see Figs. 7.10c and 7.10f). In the test cases analysed in the previous sub–section (Fig. 7.9), each wall could be substituted by its mirror reflections. However, the additional angled edge and corner, which are part of the LTT test section, cannot be simulated with a geometric modelling algorithm (either the mirror source method or ray tracing), as there is no direct path from the primary reflections on these walls to the microphone array.

Figures 7.10b and 7.10c show that, at $f = 500$ Hz, the primary reflections on the angled walls lead to a considerable disturbance in the entire acoustic field. Acoustic diffraction leads to the propagation of reflected waves to locations for which there is no direct specular reflection path, including to the microphone array location. This is also a strong indication that, at low frequency (e.g. 500 Hz), the LTT test section's acoustic response cannot be modelled with a (lower fidelity) geometric modelling algorithm. Figures 7.10e and 7.10f show that, at higher frequency, reflections on the angled walls become closer to what

can be predicted with geometric modelling, i.e. by drawing the specular reflections path.

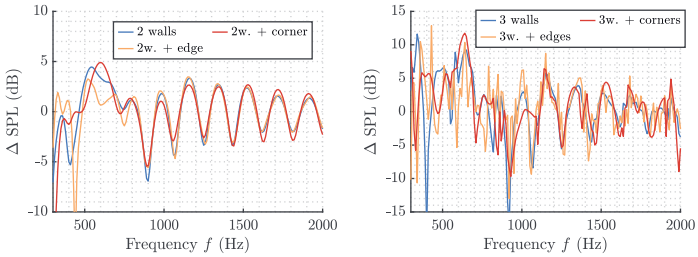

(a) 2 walls (b) 3 walls

Figure 7.11: Acoustic interference caused by specular reflections in the (fully reflective) test section, simplified to a reduced number of walls. Comparison between the baseline 2 walls (left) and 3 walls (right) cases and the cases where angled edges and corners are added to the FEM setup. Spectra obtained from Source Power Integration of the beamforming maps of the simulated data, within a $24 \times 24\,\mathrm{cm}^2$ region.

Figure 7.11 quantifies the change which occurs in the SPI spectra by adding the angled edges and corners to the two and three walls test cases. Figure 7.11a shows that, for the 2 walls case, the disturbances caused by the edge and corner are limited to low frequencies, $f < 1000\,\mathrm{Hz}$. For the 3 walls case, the number of reflections which reach the array becomes infinite, and the disturbance caused by edges and corners increases. For this reason, the spectra in Fig. 7.11b are dissimilar for all frequencies analysed. Still, the highest differences with respect to the baseline 3 walls case are found for low frequencies, i.e., for $f < 1000\,\mathrm{Hz}$, where diffraction is more relevant.

7.4.3. WAVE ABSORPTION BY LINING

Figure 7.12 shows the acoustic field inside each test section, with the simulated source emitting noise at the frequency $f = 1000\,\mathrm{Hz}$. Figure 7.12a indicates that, inside the baseline test section, the sound wave pattern is largely dominated by specular reflections. In the region where the microphones are placed, the waves appear to display a curvature around the test section opening, highlighting the importance of sound diffraction. Figures 7.12b, 7.12c and 7.12d show the difference in acoustic field between each lined test section and the baseline configuration. The figures clearly show that, as the lining over the walls is increased, the acoustic energy inside the test section is reduced. However, lining the test section walls also changes the acoustic interference pattern. For this reason, there are also locations inside

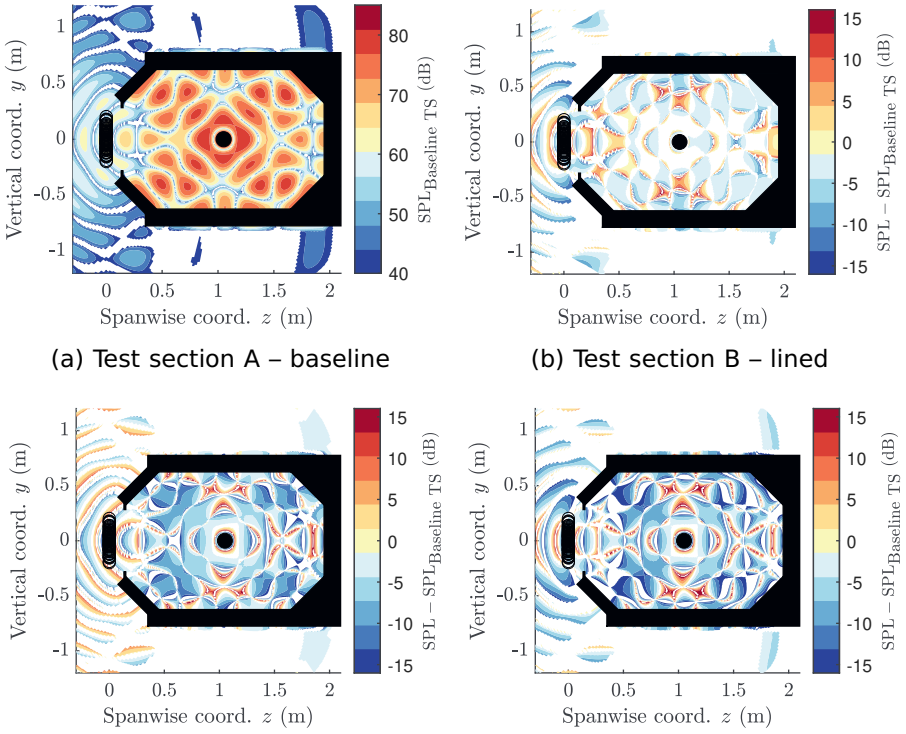

(a) Test section A – baseline

(b) Test section B – lined

(c) Test section C – lined

(d) Test section D – fully lined

Figure 7.12: Acoustic field inside each of the LTT test sections: baseline section A (top-left); test section B, with lining on the floor and ceiling (top-right); test section C, with lined side–panels (bottom-left); and fully lined test section D (bottom-right). Calculations with the source emitting noise at 1000 Hz. Acoustic fields at the $x = 0$ plane, obtained from the FEM simulations. $\mathrm{SPL}_{\mathrm{Baseline\ TS}}$ is the acoustic field of the baseline test section (top-left), which in this figure is considered as reference.

each of the lined test sections where acoustic energy at $f = 1000$ Hz is higher than for the baseline case. This result highlights the need to accurately model reflections inside each lined test section, e.g., with a high fidelity numerical tool, as demonstrated in this study.

7.5. IMPROVEMENTS TO THE BEAMFORMING TECHNIQUE

7.5.1. SOURCE IDENTIFICATION WITH BEAMFORMING

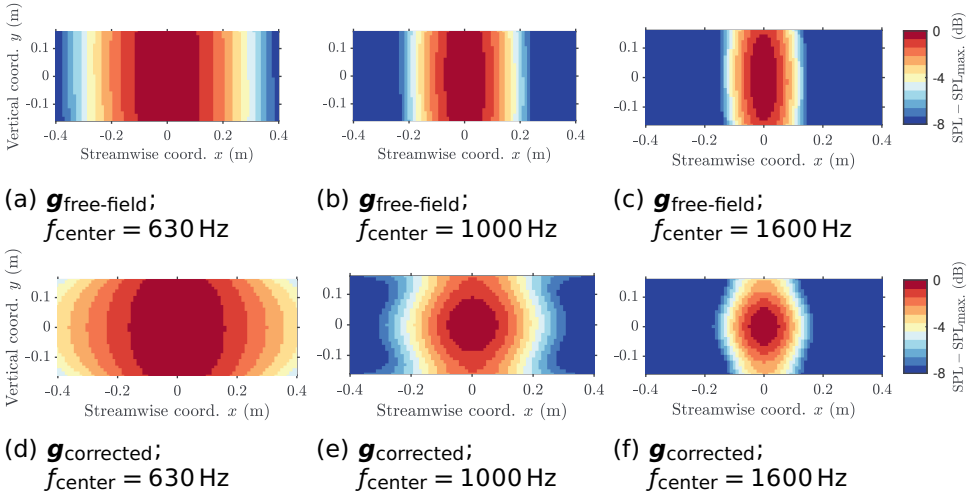

Figure 7.13: Beamforming maps obtained from the simulation of a source at the centre of test section B, which is lined on the floor and ceiling. Beamforming with the free-field Green's function (top) and with the corrected Green's function (bottom). Third–octave bands centered at 630 Hz (left), 1000 Hz (center) and 1600 Hz (right). Maps calculated with the $\|\boldsymbol{g}\|^2$ beamforming formulation.

The improvement of beamforming resolution in an environment disturbed by reflections, by correcting the (free–field) Green's function, is evaluated for the beamforming formulations with $b = 2$ and $b = 4$ (see Eq. (3.12)). Figure 7.13 shows the beamforming maps calculated from numerical data, correspondent to the simulation of a source inside test section B (lined floor and ceiling). The maps were obtained with the $\|\boldsymbol{g}\|^2$ beamforming formulation, i.e. with $b = 2$. The maps calculated with the uncorrected free–field Green's function are shown in Figs. 7.13a, 7.13b and 7.13c, whereas the maps obtained with the corrected Green's functions are shown in Figs. 7.13d, 7.13e and 7.13f. The results show a clear increase in beamforming resolution in the vertical direction. The reason for the high increase in resolution in the vertical direction is that the noise source inside the test section is aligned with its mirror reflections in the same direction (floor and ceiling reflections). The increase in resolution is noticeable for all frequencies tested.

The beamforming data of Fig. 7.13, at the source plane lines $x = 0$ and $y = 0$, can be analysed in more detail with Fig. 7.14. The figure clarifies

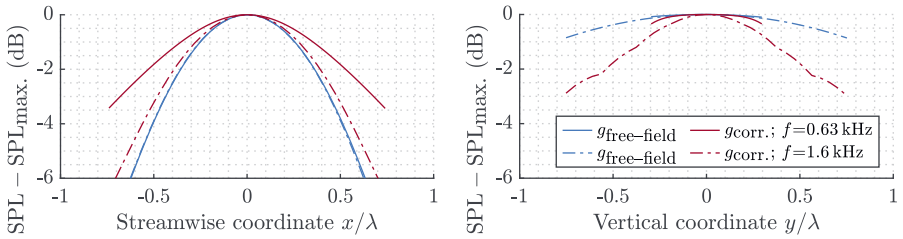

(a) Streamwise direction (b) Vertical direction

Figure 7.14: Resolution of the beamforming maps obtained with the free–field and with the corrected Green's functions. Resolution in the streamwise direction (left) and in the vertical direction (right). Synthetic data from the FEM simulation of a source at the centre of test section B. Results shown for the third–octave frequency bands centered at $f_{\text{center}} = 630\,\text{Hz}$ and $f_{\text{center}} = 1600\,\text{Hz}$.

that there is a strong increase in resolution in the vertical direction, whereas the resolution in the streamwise direction sees a negligible change when the Green's function is corrected. The streamwise resolution does not improve with this correction since all simulated tunnel walls are parallel with the streamwise direction vector, i.e., there is no mirror source that can be placed at a different streamwise location than the source, for describing the acoustic problem.

The beamforming of microphone data from the simulation of a monopole at the centre of test section B, with the $\|\boldsymbol{g}\|^4$ beamforming formulation, is shown in Fig. 7.15. For high frequencies, these results also show an increase in beamforming resolution when the corrected Green's function is used. However, the formulation with $\|\boldsymbol{g}\|^4$ leads to higher side–lobes in the beamforming map. Figure 7.15d shows that, for the third–octave band centered at $f_{\text{center}} = 500\,\text{Hz}$, the side–lobes' noise levels are higher than the noise levels of the primary source. At $f_{\text{center}} = 500\,\text{Hz}$, it is therefore impossible to identify the noise source, when the correction is used. This does not occur for the beamforming map with the free–field Green's function. Figure 7.15 therefore shows the disadvantage of the $\|\boldsymbol{g}\|^4$ beamforming formulation for processing acoustic data measured in a disturbed environment. The finding is in agreement with the results presented in Ref. [164], where similar Green's functions were implemented (formulations I and II of Ref. [164]) for localising an isolated source in an undisturbed environment, within a three–dimensional beamforming scan plane. In Ref. [164], formulation II of the Green's function, which is equivalent to the formulation with $\|\boldsymbol{g}\|^4$ in this study, was shown mathematically to not lead to a local maximum at the physical location of the source, in the beamforming map.

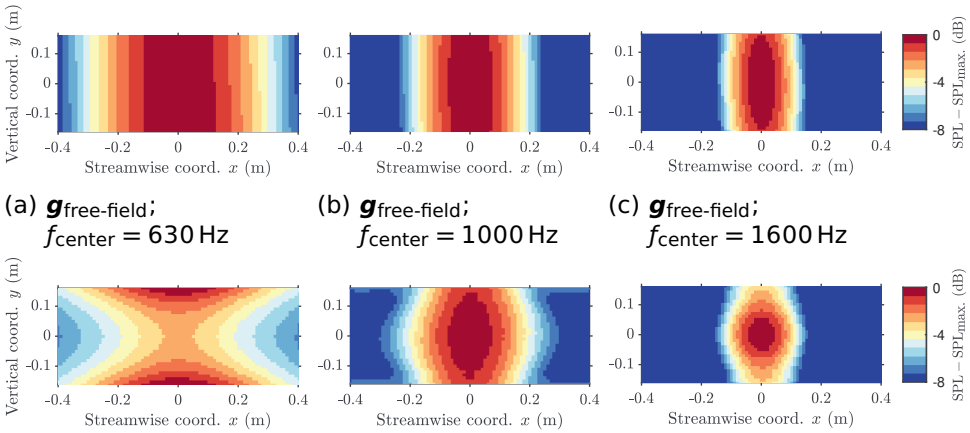

(a) $\boldsymbol{g}_{\text{free-field}}$; $f_{\text{center}} = 630\,\text{Hz}$ (b) $\boldsymbol{g}_{\text{free-field}}$; $f_{\text{center}} = 1000\,\text{Hz}$ (c) $\boldsymbol{g}_{\text{free-field}}$; $f_{\text{center}} = 1600\,\text{Hz}$

(d) $\boldsymbol{g}_{\text{corrected}}$; $f_{\text{center}} = 630\,\text{Hz}$ (e) $\boldsymbol{g}_{\text{corrected}}$; $f_{\text{center}} = 1000\,\text{Hz}$ (f) $\boldsymbol{g}_{\text{corrected}}$; $f_{\text{center}} = 1600\,\text{Hz}$

Figure 7.15: Beamforming maps obtained from the simulation of a source at the centre of test section B, which is lined on the floor and ceiling. Beamforming with the free-field Green's function (top) and with the corrected Green's function (bottom). Third–octave bands centered at 630 Hz (left), 1000 Hz (center) and 1600 Hz (right). Maps calculated with the $\|\boldsymbol{g}\|^4$ beamforming formulation.

As the beamforming formulation with $\|\boldsymbol{g}\|^2$ is found to provide a more accurate source localisation, this formulation was used to localise the noise source in the experimental data. Test section B is the case for which the numerical simulations give the best agreement with experiments (see discussion of Fig. 7.8), and is therefore the case analysed in Fig. 7.16. The figure compares the beamforming maps of the free–field case with the beamforming map of the omnidirectional source inside the lined test section. For the free–field test case, the figure shows both the beamforming Point Spread Function (PSF) of the free–field Green's function and the beamforming maps of the experimental reference measurement. This figure clearly shows that the proposed methodology is capable of increasing beamforming resolution during the post–processing of experimental data in a disturbed environment. The increase in resolution is observed in the direction where the direct source is aligned with its mirror reflections, i.e., the vertical direction, in this case.

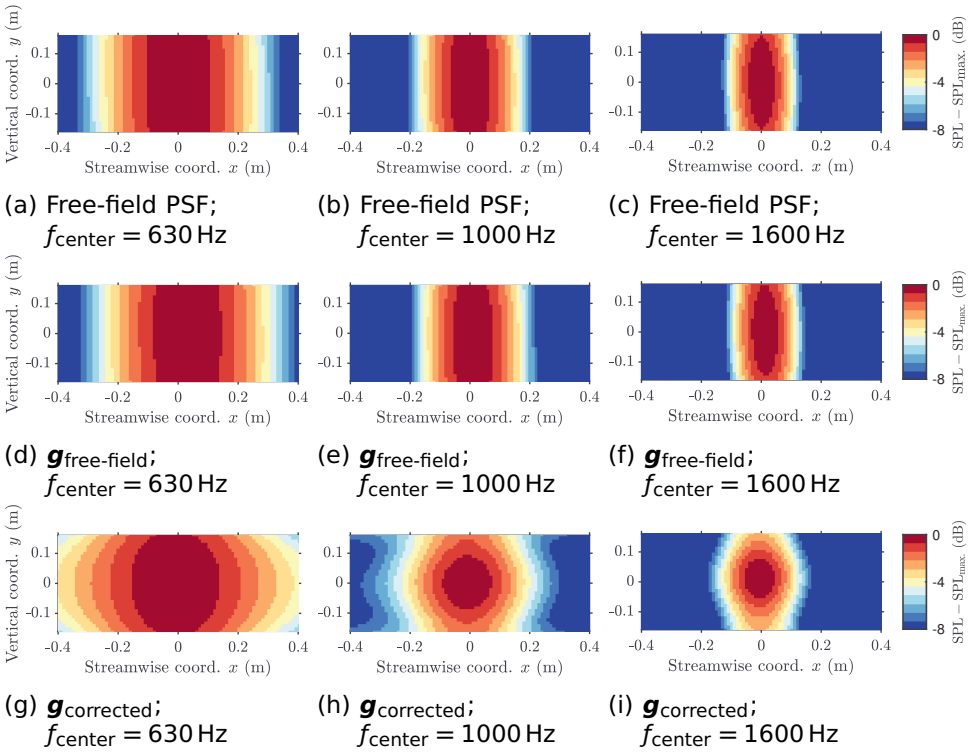

(a) Free-field PSF; $f_{\text{center}} = 630\,\text{Hz}$ (b) Free-field PSF; $f_{\text{center}} = 1000\,\text{Hz}$ (c) Free-field PSF; $f_{\text{center}} = 1600\,\text{Hz}$

(d) $\boldsymbol{g}_{\text{free-field}}$; $f_{\text{center}} = 630\,\text{Hz}$ (e) $\boldsymbol{g}_{\text{free-field}}$; $f_{\text{center}} = 1000\,\text{Hz}$ (f) $\boldsymbol{g}_{\text{free-field}}$; $f_{\text{center}} = 1600\,\text{Hz}$

(g) $\boldsymbol{g}_{\text{corrected}}$; $f_{\text{center}} = 630\,\text{Hz}$ (h) $\boldsymbol{g}_{\text{corrected}}$; $f_{\text{center}} = 1000\,\text{Hz}$ (i) $\boldsymbol{g}_{\text{corrected}}$; $f_{\text{center}} = 1600\,\text{Hz}$

Figure 7.16: Point Spread Function of the microphone array, calculated with the free–field Green's function (top); and beamforming maps obtained from the experimental measurements of a source in an environment with low reverberation (center), and at the centre of test section B, which is lined on the floor and ceiling (bottom). Third–octave bands centered at 630 Hz (left), 1000 Hz (center) and 1600 Hz (right). Maps calculated with the $\|\boldsymbol{g}\|^2$ beamforming formulation.

7.5.2. DETERMINATION OF THE SOURCE POWER LEVELS

The Green's function correction is shown to improve source localisation with beamforming. Simultaneously, it is important to evaluate the accuracy of the estimate of the source levels, when the correction is used. The error in source level's estimation, when using the free–field Green's function, can be seen in Fig. 7.8. The spectra obtained with the corrected Green's functions, for each test section, is shown in Fig. 7.17. As mentioned previously, $\Delta\text{SPL}(f) = 0$ represents a noise level estimation equal to the noise level calculation from the reference measurement, i.e., $\Delta\text{SPL}(f) = 0$ indicates a correct estimation. The figure shows that, when the $\|\boldsymbol{g}\|^4$ beamforming formulation is used, there is a

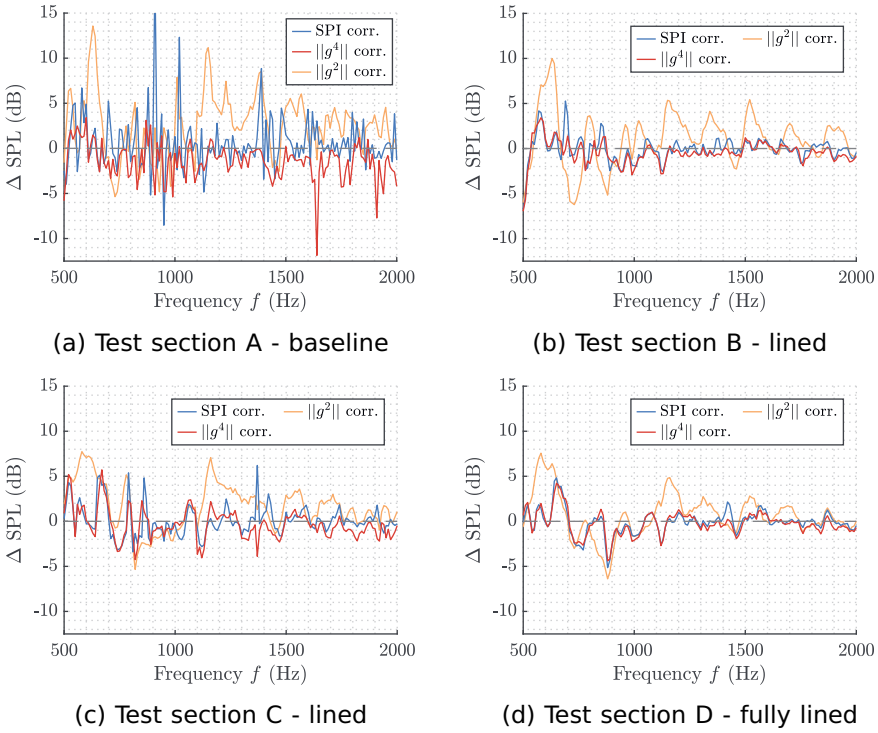

(a) Test section A - baseline

(b) Test section B - lined

(c) Test section C - lined

(d) Test section D - fully lined

Figure 7.17: Spectra of the experimental measurements of an acoustic monopole source at the centre of each test section, improved with the Source Power Integration correction and with the Green's function corrections. Acoustic signals measured in test section A (top-left), test section B (top-right), test section C (bottom-left) and test section D (bottom-right). Spectra obtained from Source Power Integration of the beamforming maps, within a $24 \times 24\,\mathrm{cm}^2$ region (SPI correction) and a $2 \times 2\,\mathrm{cm}^2$ region ($\|\boldsymbol{g}\|^2$ and $\|\boldsymbol{g}\|^4$ corrections).

significant improvement in the noise levels calculation. However, when the Green's function formulation with $\|\boldsymbol{g}\|^2$ is used, the source's noise levels estimation does not visibly improve with respect to the estimation with the free–field Green's function. This occurs because, with $\|\boldsymbol{g}\|^2$, the beamforming result indicates the noise levels at the microphone array, where reflections are also included. The formulation with $\|\boldsymbol{g}\|^4$ instead corrects for the acoustic interference which disturbs the measurement, and is able to provide an estimation of the noise levels without the reflections.

Figure 7.17 also shows the spectra obtained using the SPI correction. For the baseline test section, Fig. 7.17a shows that the Green's function correction outperforms the SPI correction. This is associated with the sharp acoustic interference peaks seen for the numerical calculation with the source at the centre of the baseline test section, which did not occur in the experiment (see Fig. 7.8a). As the corrected Green's function is obtained with simulations at varying source location, the presence of these sharp interference peaks in the corrected result is mitigated. For the lined test sections (Figs. 7.17b, 7.17c and 7.17d) the SPI correction provides the same improvement as the use of the Green's function formulation, with $\|\boldsymbol{g}\|^4$. This reveals an advantage of the SPI correction. This correction only requires a single numerical simulation for each test section, whereas correcting the Green's function requires several numerical computations. A main advantage of the Green's function correction, for the purpose of source noise levels calculation, is that this correction does not require a priori knowledge of the source location. For an experimental acoustic environment which is perfectly described by the computational model, both corrections are expected to lead to precise source noise level estimations.

Figure 7.17 also reveals that the corrected ΔSPL closest to 0 occurs for test section B. The lining on this test section clearly provides lower sound absorption than the lining on the remaining test sections (see Fig. 7.12). However, as shown in Fig. 7.8, the floor and ceiling flat melamine lining were the most accurately modelled liners. The result of Fig. 7.17 clearly indicates that, for experimental acoustic measurements corrected with numerical data, it is important to perform an accurate characterisation of the lined walls. This characterisation needs to be precise both in terms of the lining material, here described based on its viscous resistivity, and liner shape. This study also reveals that too strong acoustic reflections increase the challenge of matching experiment and simulations, i.e., lining a wind tunnel's test section allows for more accurate numerical predictions and consequent corrections.

7.6. APPLICATION OF THE POST–PROCESSING METHODOLOGY TO FLOW–ON TEST CASES

The previous results show that the most accurate acoustic predictions have been made for test section B, where the floor and ceiling of the wind tunnel are lined. The applicability of the proposed post–processing method to flow–on test cases is therefore analysed with this test section. Figure 7.18 shows the beamforming maps of the data obtained from the measurements of the speaker emitting broadband noise (signal description in Sec. 6.2.1), with a free-stream velocity in the test section of $30\,\mathrm{m\,s^{-1}}$. Figure 7.18a shows that, without taking into account the

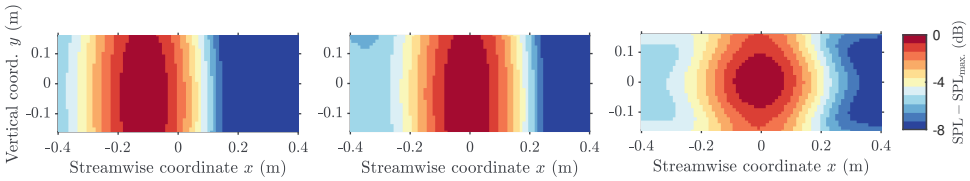

(a) $\boldsymbol{g}_{\text{free-field}}$ (b) $\boldsymbol{g}_{\text{with sound convection}}$ (c) $\boldsymbol{g}_{\text{corrected (sound convection and acoustic interference)}}$

Figure 7.18: Beamforming maps obtained from experimental acoustic data measured at the LTT test section B, with $U_\infty = 30\,\text{m}\,\text{s}^{-1}$. The speaker was located at the centre of the test section, and emitting broadband noise. Beamforming with the $\|\boldsymbol{g}\|^2$ beamforming formulation and with the CSM diagonal removed. The maps correspond to the third-octave band centered at $f_{\text{center}} = 1000\,\text{Hz}$. Beamforming with the free-field Green's function (left), with the Green's function calculated considering convection of sound by the flow (center), and with the Green's function simultaneously calculated considering sound convection and using the numerical (FEM) correction, which takes into account acoustic interference at the microphones (right).

convection of sound in the calculation of the Green's function, the speaker's streamwise location in the beamforming map is approximately 0.15 m downstream of its actual location ($x = 0$). Figure 7.18b shows that the accuracy of the the speaker's location in the beamforming map is improved by correcting for sound convection. However, as in Fig. 7.18b the correction for the sound reflections is not yet applied, the resolution of beamforming is relatively low (in agreement with the previous discussion, of Sec. 7.5.1). Figure 7.18c proves that, when both corrections are applied simultaneously, it is possible to correct the streamwise location of the source in the map and at the same time improve beamforming resolution.

It is relevant to note that the correction for the reflections was obtained without considering convection of sound in the FEM model. The correction method is therefore applicable to low free-stream Mach numbers, M_∞. $U_\infty = 30\,\text{m}\,\text{s}^{-1}$ corresponds to $M_\infty = 0.09$. Ref. [156] proposes the use of the mirror source method to analyse if M_∞ is large enough to significantly modify the acoustic interference pattern at a microphone array location. Based on the results presented in Ref. [156], it was expected that the post-processing methodology proposed in this study would be applicable to acoustic data measured at $M_\infty = 0.09$, but not to data measured with $M_\infty = 0.29$ ($U_\infty = 100\,\text{m}\,\text{s}^{-1}$) at the LTT.

7.6.1. DETERMINATION OF THE SOURCE POWER LEVELS

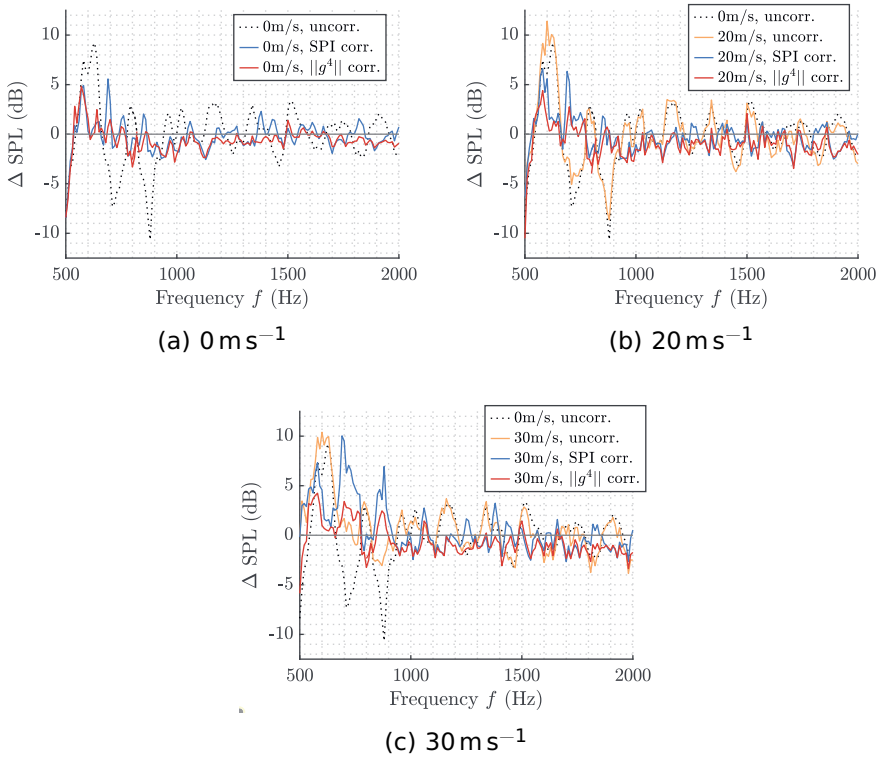

(a) $0\,\mathrm{m\,s^{-1}}$ (b) $20\,\mathrm{m\,s^{-1}}$

(c) $30\,\mathrm{m\,s^{-1}}$

Figure 7.19: Spectra of the experimental measurements of an acoustic monopole source at the centre of test section B, at varying free–stream velocity. The lines show the uncorrected spectra, and the spectra improved with the Source Power Integration correction and with the Green's function correction. Acoustic signals measured at $U_\infty = 0\,\mathrm{m\,s^{-1}}$ (top-left); $U_\infty = 20\,\mathrm{m\,s^{-1}}$ (top-right); and $U_\infty = 30\,\mathrm{m\,s^{-1}}$ (bottom). Sound convection was taken into account in the Green's function calculation, for all results in the figure (taking into account each U_∞). Spectra obtained from Source Power Integration of the beamforming maps, within a $2 \times 2\,\mathrm{cm^2}$ region, and with the $\|\boldsymbol{g}\|^4$ beamforming formulation.

Figure 7.19 shows the improvement in noise levels estimation by using the SPI and Green's function corrections, when processing flow–on test cases. The spectra in Fig. 7.19 were calculated considering sound convection in the beamforming formulation (as in Figs. 7.18b and 7.18c). These results were obtained by performing beamforming with

the diagonal of the CSM removed. The results at $f < 800\,\mathrm{Hz}$ shown in Fig. 7.19 correspond to measurements where the speaker was emitting the low frequency narrow band noise, and the results at $f > 800\,\mathrm{Hz}$ correspond to measurements where the speaker was emitting the broadband noise (description of the speaker input in Sec. 6.2.1). Figure 7.19a shows, for reference, results for the $U_\infty = 0\,\mathrm{m\,s^{-1}}$ case, processed in the same way as the flow–on cases. The spectra are identical to the spectra shown in Figs. 7.8b and 7.17b, confirming that the difference in post–processing technique (removal of the CSM diagonal) does not affect the previous conclusions.

As for the flow–off case, the $U_\infty = 20\,\mathrm{m\,s^{-1}}$ results (Fig. 7.19b) show the SPI and the Green's function corrections leading to similar results. This indicates that both methods can be used when background noise is relatively low.

At $U_\infty = 30\,\mathrm{m\,s^{-1}}$, however, the background noise during the test is noticeable in the resulting beamforming spectra for frequencies $f < 900\,\mathrm{Hz}$. This is indicated by the difference between the $0\,\mathrm{m\,s^{-1}}$ and $30\,\mathrm{m\,s^{-1}}$ uncorrected spectra in Fig. 7.19c. Consequently, at $f < 900\,\mathrm{Hz}$, the Green's function correction leads to a better spectra estimation than the SPI correction. Figure 7.19c demonstrates that the Green's function correction can also be used to improve the signal to noise ratio in the post–processing of experimental data. This is due to the improved spatial resolution of the corrected Green's function, which helps to differentiate the noise source of interest from spurious noise sources.

7.7. CONCLUSIONS

Numerical simulations were carried out for predicting sound propagation in complex–shaped closed wind tunnel test sections. The numerical solver uses a Finite Element Method to solve the Helmholtz equation for acoustic waves. These simulations were validated by comparing the numerical results with acoustic data obtained at the Low Turbulence Tunnel (LTT), a closed section wind tunnel at Delft University of Technology. This validation included a baseline wind tunnel test section, i.e., a test section with fully reflective walls, and lined test sections.

The numerical results show that, along with specular reflections, diffraction is a dominant acoustic phenomenon occurring at the LTT's octagonal test sections. Therefore, the test sections' acoustic response cannot be precisely predicted with lower fidelity methods, e.g., geometric modelling. The numerical results were used to improve the post–processing of experimental acoustic data recorded at the LTT. A corrected Green's function with the $\|\boldsymbol{g}\|^2$ formulation was capable of improving source localisation in the disturbed environment, by enhancing beamforming resolution. Furthermore, both the Source Power Integration correction and the $\|\boldsymbol{g}\|^4$ Green's function correction led to

more accurate estimations of the source's noise levels, by reducing the adverse effects of acoustic interference in each disturbed environment. While the uncorrected source noise levels estimation is more accurate for the most lined LTT test section, the noise estimations with the corrections are most accurate for the test section where the liners are most accurately described in the numerical model.

Up to the free–stream Mach number $M_\infty = 0.09$, the post–processing methodology proposed in this study was shown to be applicable to flow–on acoustic tests. For the flow–on test case with a relatively high background noise, the Green's function correction also showed the advantage of improving signal to noise ratio. This is due to an improvement in resolution of the beamforming map, which helps to differentiate between noise sources.

The present study shows the benefits of modelling acoustic propagation in a wind tunnel test section, when studying an omnidirectional noise source. Future studies should extend the proposed numerical prediction to cases with more complex sound sources, e.g., with a dipole directivity and/ or distributed over a line. This will make the method applicable to airfoil noise measurements. Furthermore, it is recommended that numerical acoustic simulations are conducted to support the design of new aeroacoustic wind tunnel test sections, as they can provide an accurate prediction of the facility's acoustic performance.

8

CONCLUSION AND RECOMMENDATIONS

You cannot solve a problem with the same mind that created it.

Albert Einstein

The research presented in this dissertation aims at improving aeroacoustic experiments in acoustically disturbed environments. Typically, aeroacoustic experiments are carried out with wind tunnel facilities. Acoustic propagation in wind tunnels is disturbed by obstacles, which cause reflections and diffraction of sound waves; and by the wind tunnel flow. In addition, hydrodynamic and acoustic background noise presents a limitation for acoustic measurements. Open–jet anechoic facilities present the least acoustically disturbed wind tunnel environments. However, these have a lower aerodynamic fidelity than closed section or hybrid test section wind tunnels. By improving the capability to perform accurate noise level estimations in challenging environments, it will become possible to make the best use of the facilities with higher aerodynamic performance.

This thesis analyses first how the background noise in wind tunnel measurements can be reduced. It is studied how the microphone placement aids in reducing hydrodynamic noise, particularly for wall mounted microphones. Acoustic background noise is reduced with sound absorbing wall liners. The influence of these liners on the aerodynamic characteristics of the tunnel and on the scattering of boundary layer noise is investigated. Besides the potential to reduce background noise, wall liners also alter the acoustic propagation from the noise source of interest to the receivers (microphones). This change of the acoustic

environment is predicted with a high fidelity numerical tool, whose results are compared against wind tunnel experiments. Subsequently, the results of the numerical tool are used to improve the post–processing of acoustic experimental data.

The main conclusions of the research are as follows:

- **Microphone placement on closed test section wind tunnels (Chapter 4)**: Microphone cavities are capable of decreasing the recording of hydrodynamic noise from the pressure fluctuations in the wind tunnel wall's boundary layer. Microphones are in this case installed at the cavity bottoms. When covered with a steel cloth, cavities show a superior performance, i.e., higher signal to noise ratio. This occurs due to a lower recording of boundary layer noise by the microphone. This thesis shows that the cavity cloth covers improve acoustic measurements by causing the flow inside the cavity to remain stagnated. The computed flow velocities inside the covered cavities are below 0.2 % of the simulated free-stream velocity ($U_\infty = 32\,\mathrm{m\,s^{-1}}$). This avoids the convection of pressure fluctuations towards the cavity bottom. Cavity cloth covers are modelled numerically in this research as a porous medium region, characterised by the cover's viscous and inertial resistivities. The comparison of the Lattice–Boltzmann method numerical results with experimental evidence validated the numerical approach.

  In the absence of recirculation inside a cavity, the wall's boundary layer noise propagates acoustically to the cavity bottom. The numerical results show that, in order to further reduce spurious noise at the microphone, the size of the cavity should be increased with respect to the size of the hydrodynamic pressure fluctuations at the frequencies of interest. The ratio of the cavity aperture diameter with respect to the coherence length of the incoming fluctuations is concluded to be an important indicator for predicting the performance of a covered cavity.

- **Wall liners for acoustic absorption (Chapter 5)**: Wall liners are used in order to absorb spurious background noise, and to reduce reflections from the source of interest of a given test model. However, these liners also influence the aerodynamic characteristics of the wind tunnel walls' boundary layer. This effect was investigated in this thesis by testing a single wall, installed in an open-jet test section, and lined over a 1 m by 0.4 m area grazed by the jet flow. The porous liners tested in this research were characterised by their roughness, viscous resistivity, and inertial resistivity. Viscous resistivity is the parameter which should be maximised, as this leads to higher acoustic absorption. Roughness should be minimised, in order to reduce the impact on the aerodynamic characteristics of the grazing boundary layer.

Higher roughness of the liner, with respect to the size of the boundary layer viscous sublayer, leads to increased boundary layer height, displacement thickness, and strength of its pressure fluctuations. Although the inertial resistivity of the liner was found to have a weak impact on the aerodynamic characteristics of the boundary layer, it was found to have a strong influence on scattered noise. The difference in surface noise scattering, at $U_\infty = 30\,\mathrm{m\,s^{-1}}$, can reach over 10 dB for two liners with similar roughness and different inertial resistivity (by a factor of 20), as seen at 2 kHz in the third-octave band beamforming maps. Inertial resistivity is therefore also a parameter which should be minimised, on a wind tunnel liner. Melamine foam was the best performing porous liner tested, due to its high viscous resistivity and relatively low roughness and inertial resistivity.

- **Lining the test section of the circuit (Chapter 6)**: Covering the entire wind tunnel circuit with wall liners is expected to reduce spurious background noise in the tunnel. This research investigated the benefits of lining exclusively the test section of a highly reverberant closed wind tunnel circuit. The lining consisted of melamine foam. Despite the decrease of reverberation, the circuit remained highly reverberant after applying the lining. Still, lining the test section resulted in a decrease of background noise. Decreasing reverberation time T_{25} by 0.1 s, by lining the test section side walls, resulted in a background noise reduction inside the test section of $1-2$dB, for the frequencies within the range 0.5 kHz to 5 kHz. Furthermore, acoustic reflections result in a strong interference with direct sound waves from the test object, at the array location. It is concluded that reflections upstream and downstream of the test section have, however, a minor influence on this interference. At the LTT wind tunnel, this influence is shown to be negligible for $f > 500$ Hz. Lining the test section is found to be an efficient method to make the acoustic transfer function from a test object to the array closer to free–field conditions.

- **Modelling the wind tunnel acoustic response (Chapter 7)**: the acoustic propagation of a monopole point source placed inside a closed section wind tunnel is modelled with a Finite Element Method (FEM). Only the test section geometry is included in the model, as it is understood from experimental data that the reverberation caused by reflections on the remaining parts of the circuit is negligible. The FEM simulations compare well against experimental data, for both hard walled (fully reflective) and lined test sections. Consequently, it is found that the numerical results can be used to correct experimental measurements contaminated by acoustic interference. Two correction methods are tested, both

in combination with conventional beamforming: a correction of the Green's function used for beamforming; and a correction of the Source Power Integration (SPI) step, where the sources' noise is estimated from the beamforming maps. Both corrections work well for improving the post–processing of acoustic data measured in tests with and without flow in the test section. As a consequence, the noise level estimation of an experimental monopole source is improved with both methods. The Green's function correction has the additional benefit of improving the resolution of the beamforming map. This leads to an increase in signal to noise ratio with respect to spurious noise sources, for the flow–on measurements.

RECOMMENDATIONS

The main takeaway from this research is that it is shown to be possible to perform accurate acoustic measurements in disturbed (or non–anechoic) wind tunnel environments. However, it is still important to reduce the negative impact of background noise, and to expand the knowledge on how to model acoustic propagation in these environments. The following recommendations are targeted at reaching these two objectives.

While the test section shape and boundary conditions are the main driver of its acoustic response, it is expected that lining additional sections of the circuit further reduce background noise in the measurements. However, this improvement has not been well quantified yet, which may reduce the willingness of wind tunnel designers to make an additional investment. Future wind tunnel background noise investigations should aim at predicting and quantifying the benefit of lining the additional portions of the tunnel circuit (besides the test section). A proposed methodology is to vary the reflection coefficient of the diffuser (and/ or other circuit sections) and to measure the changes in reverberation time and in the dampening of noise originating from downstream sources, such as turning vanes or the wind tunnel fan. This can be tested acoustically by placing a sound source (e.g., a speaker) at locations downstream of the diffuser. This study would be most helpful if equivalent results are achieved with a numerical acoustic modelling tool. This would prove that it is possible to model the complete acoustic response of a wind tunnel numerically, and to accurately estimate the acoustic performance during the wind tunnel design process.

For closed test section wind tunnels where the microphones are mounted on the wind tunnel walls, the design of microphone cavities can be improved. The current research shows that, in covered cavities, the spurious pressure fluctuations propagate acoustically towards the microphone location, i.e., without being convected by the flow. This indicates that it is possible to predict the performance of covered cavities by exclusively modelling the acoustic response of the cavity.

Such an approach would be computationally less expensive than solving Computational Fluid Dynamics (CFD) simulations. By using acoustic simulations, it would be possible to run an optimisation algorithm which minimises the spurious noise at the bottom of a covered cavity, while maintaining an efficient propagation of the sound of interest. In order to achieve this, it is recommended to model the incoming boundary layer pressure fluctuations accurately. An appropriate approach is to model the coherent boundary layer turbulent structures with the methodology proposed by Lima Pereira et al. [165].

The conclusion that it is possible to precisely measure a monopole source inside a closed wind tunnel should be followed up with the extension of the proposed method to more complex sound sources. The application to airfoil or wind turbine blade noise measurements requires the extension of the method to distributed dipole sources. The application of the method to propeller investigations requires the extension to rotating sources. For extending the applicability of the method to higher free-stream Mach numbers ($M_\infty \geq 0.2$) in hybrid test sections, it is recommended to include a Green's function correction for the transmission of sound through a Kevlar wall, e.g., following up on the approach proposed by Fischer et al. [166]. Following these steps will enable a fully reliable characterisation of aerodynamic sound sources in acoustically disturbed environments (such as closed or hybrid test section wind tunnels) without the need to aim for free-field acoustic testing conditions.

BIBLIOGRAPHY

[1] A. M. O. Mohamed, E. K. Paleologos, and F. M. Howari. “Noise pollution and its impact on human health and the environment”. In: *Pollution Assessment for Sustainable Practices in Applied Sciences and Engineering*. Elsevier Inc., 2020. Chap. 19, pp. 975–1026. isbn: 9780128095829. doi: 10.1016/B978-0-12-809582-9.00019-0.

[2] E. Peris. *Environmental noise in Europe - 2020*. 2020. doi: 10.2800/686249.

[3] A. L. Brown and I. van Kamp. *WHO environmental noise guidelines for the European region: A systematic review of transport noise interventions and their impacts on health*. Aug. 2017. doi: 10.3390/ijerph14080873.

[4] D. S. Little, J. Majdalani, R. J. Hartfield, and V. Ahuja. “On the prediction of noise generated by urban air mobility (UAM) vehicles. I. Integration of fundamental acoustic metrics”. In: *Physics of Fluids* 34.11 (2022). issn: 10897666. doi: 10.1063/5.0124134.

[5] V. Katinas, M. Marčiukaitis, and M. Tamašauskiene. “Analysis of the wind turbine noise emissions and impact on the environment”. In: *Renewable and Sustainable Energy Reviews* 58 (2016), pp. 825–831. issn: 18790690. doi: 10.1016/j.rser.2015.12.140.

[6] R. J. Barthelmie and S. C. Pryor. “Potential contribution of wind energy to climate change mitigation”. In: *Nature Climate Change* 4.8 (2014), pp. 684–688. issn: 17586798. doi: 10.1038/nclimate2269.

[7] R. Merino-Martinez, E. Neri, M. Snellen, J. Kennedy, D. G. Simons, and G. J. Bennett. “Comparing flyover noise measurements to full–scale nose landing gear wind–tunnel experiments for regional aircraft”. In: *23rd AIAA/CEAS Aeroacoustics Conference*. AIAA AVIATION Forum, 2017.

[8] C. Teruna, F. Manegar, F. Avallone, D. Ragni, D. Casalino, and T. Carolus. “Noise reduction mechanisms of an open-cell metal-foam trailing edge”. In: *Journal of Fluid Mechanics* 898 (2020). issn: 14697645. doi: 10.1017/jfm.2020.363.

[9] G. Romani, E. Grande, F. Avallone, D. Ragni, and D. Casalino. “Performance and Noise Prediction of Low-Reynolds Number Propellers using the Lattice-Boltzmann Method”. In: *Aerospace Science and Technology* 125 (2022), p. 107086. issn: 12709638. doi: 10.1016/j.ast.2021.107086.

[10] S. Oerlemans, P. Sijtsma, and B. Méndez López. “Location and quantification of noise sources on a wind turbine”. In: *Journal of Sound and Vibration* 299.4-5 (2007), pp. 869–883. issn: 10958568. doi: 10.1016/j.jsv.2006.07.032.

[11] S. Luesutthiviboon. “Assessing and improving trailing-edge noise reduction technologies for industrial wind-turbine applications”. PhD thesis. Delft University of Technology, 2022. doi: 10.4233/uuid:23e2f72e-2502-4f4a-9504-ba607bae0364.

[12] D. M. Bushnell. “Scaling: Wind tunnel to flight”. In: *Annual Review of Fluid Mechanics* 38 (2006), pp. 111–128. issn: 00664189. doi: 10.1146/annurev.fluid.38.050304.092208.

[13] T. J. Mueller. *Aeroacoustic Measurements*. 2002. isbn: 9783642075148.

[14] P. Sijtsma. “Using CLEAN-SC for determining the directivity of engine noise sources”. In: *AIAA AVIATION 2023 Forum*. June. 2023, pp. 1–12. doi: https://doi.org/10.2514/6.2023-3839.

[15] E. Grande, G. Romani, D. Ragni, F. Avallone, and D. Casalino. “Aeroacoustic Investigation of a Propeller Operating at Low Reynolds Numbers”. In: *AIAA Journal* 60.2 (2022), pp. 860–871. issn: 1533385X. doi: 10.2514/1.J060611.

[16] G. J. Bennett, J. Lai, G. O’brien, D. Ragni, F. Avallone, A. R. Carpio, and M. Pott-Pollenske. “Flow Control and Passive Low Noise Technologies for Landing Gear Noise Reduction”. In: *28th AIAA/CEAS Aeroacoustics Conference, 2022* (2022), pp. 1–20. doi: 10.2514/6.2022-2848.

[17] S. Luesutthiviboon, L. T. L. Pereira, D. Ragni, F. Avallone, and M. Snellen. “Aeroacoustic Benchmarking of Trailing-Edge Noise from NACA 633 –018 Airfoil with Trailing-Edge Serrations”. In: *AIAA Journal* 61.1 (2023), pp. 329–354. issn: 1533385X. doi: 10.2514/1.J061630.

[18] S. Moreau, M. Henner, G. Iaccarino, M. Wang, and M. Roger. “Analysis of Flow Conditions in Freejet Experiments for Studying Airfoil Self-Noise”. In: *AIAA Journal* 41.10 (2003), pp. 1895–1905. issn: 00011452. doi: 10.2514/2.1905.

[19] K. Brown, W. Devenport, and A. Borgoltz. “Exploitation of hybrid anechoic wind tunnels for aeroacoustic and aerodynamic measurements”. In: *CEAS Aeronautical Journal* 10.1 (Mar. 2019), pp. 251–266. issn: 18695590. doi: 10.1007/s13272-019-00385-2.

[20] M. P. Sanders, C. F. Koenjer, L. Botero-Bolivar, F. L. Dos Santos, C. H. Venner, and L. D. de Santana. “Trailing-Edge Noise Comparability in Open, Closed, and Hybrid Wind Tunnel Test Sections”. In: *AIAA Journal* 60.7 (2022), pp. 4053–4067. issn: 1533385X. doi: 10.2514/1.J061460.

[21] L. Cattafesta, C. Bahr, and J. Mathew. “Fundamentals of Wind-Tunnel Design”. In: *Encyclopedia of Aerospace Engineering*. 2010. isbn: 9780470686652. doi: 10.1002/9780470686652.eae532.

[22] R. Merino-Martínez, A. Rubio Carpio, L. T. Lima Pereira, S. van Herk, F. Avallone, D. Ragni, and M. Kotsonis. “Aeroacoustic design and characterization of the 3D-printed, open-jet, anechoic wind tunnel of Delft University of Technology”. In: *Applied Acoustics* 170 (2020), p. 107504. issn: 1872910X. doi: 10.1016/j.apacoust.2020.107504.

[23] J. Fischer and C. Doolan. “Beamforming in a reverberant environment using numerical and experimental steering vector formulations”. In: *Mechanical Systems and Signal Processing* 91 (2017), pp. 10–22. issn: 10961216. doi: 10.1016/j.ymssp.2016.12.025.

[24] C. Dollinger, M. Sorg, and P. Thiemann. “Aeroacoustic Optimization of Wind Turbine Airfoils by Combining Thermographic and Acoustic Measurement Data”. In: *DEWI Magagzin* 43.43 (2013), pp. 61–64.

[25] Ö. C. Yilmaz. “Examples of Wind Tunnels for Testing Wind Turbine Airfoils”. In: *Handbook of Wind Energy Aerodynamics: With 678 Figures and 33 Tables* (2022), pp. 631–658. doi: 10.1007/978-3-030-31307-4_28.

[26] W. Neise, W. V. Heesen, N. Lindener, and J. Hansen. “Blade tip cavity noise of a large axial-flow wind tunnel fan”. In: *2nd AIAA/CEAS Aeroacoustics Conference* May (1996). doi: 10.2514/6.1996-1692.

[27] C. P. VanDercreek, A. Amiri-Simkooei, M. Snellen, and D. Ragni. “Experimental design and stochastic modeling of hydrodynamic wave propagation within cavities for wind tunnel acoustic measurements”. In: *International Journal of Aeroacoustics* 18.8 (Nov. 2019), pp. 752–779. issn: 1475-472X. doi: 10.1177/1475472X19889949.

[28] C. P. VanDercreek, F. Avallone, D. Ragni, and M. Snellen. “Simulating the acoustic response of cavities to improve microphone array measurements in closed test section wind tunnels”. In: *The Journal of the Acoustical Society of America* 151.1 (Jan. 2022), p. 322. issn: 0001-4966. doi: 10.1121/10.0009274.

[29] C. P. VanDercreek, R. Merino-Martínez, P. Sijtsma, and M. Snellen. “Evaluation of the effect of microphone cavity geometries on acoustic imaging in wind tunnels”. In: *Applied Acoustics* 181 (Oct. 2021), p. 108154. issn: 0003682X. doi: 10.1016/j.apacoust.2021.108154.

[30] J. P. Gomes, A. Bergmann, and H. Holthusen. “Aeroacoustic wind tunnel design”. In: *CEAS Aeronautical Journal* 10.1 (2019), pp. 231–249. issn: 18695590. doi: 10.1007/s13272-019-00372-7.

[31] I. P. Castro. “Turbulent flow over rough walls”. In: *Advances in Turbulence XII: Proceedings of the 12th EUROMECH European Turbulence Conference*. 2009, pp. 381–388. isbn: 9783642030857. doi: 10.1007/978-3-642-03085-7.

[32] M. Selig, R. Deters, and G. Wiliamson. “Wind Tunnel Testing Airfoils at Low Reynolds Numbers”. In: *49th AIAA Aerospace Sciences Meeting including the New Horizons Forum and Aerospace Exposition*. January. 2011. doi: 10.2514/6.2011-875.

[33] T. J. Mueller. “Aeroacoustic measurements”. In: *Experimental fluid mechanics* (2002).

[34] R. Merino-Martínez, P. Sijtsma, M. Snellen, T. Ahlefeldt, J. Antoni, C. J. Bahr, D. Blacodon, D. Ernst, A. Finez, S. Funke, T. F. Geyer, S. Haxter, G. Herold, X. Huang, W. M. Humphreys, Q. Leclère, A. Malgoezar, U. Michel, T. Padois, A. Pereira, C. Picard, E. Sarradj, H. Siller, D. G. Simons, and C. Spehr. “A review of acoustic imaging methods using phased microphone arrays (part of the “Aircraft Noise Generation and Assessment" Special Issue)”. In: *CEAS Aeronautical Journal* 10.1 (2019), pp. 197–230. issn: 18695590. doi: 10.1007/s13272-019-00383-4.

[35] P. Sijtsma and H. Holthusen. “Corrections for mirror sources in phased array processing techniques”. In: *9th AIAA/CEAS Aeroacoustics Conference and Exhibit*. Hilton Head, South Carolina, 2003, p. 3196. isbn: 9781624101021. doi: 10.2514/6.2003-3196.

[36] A. Marsan, C. P. Arroyo, Y. Pasco, and S. Moreau. “Spectral and wavelet analysis of an aero-acoustic feedback loop in a transonic outflow valve based on Schlieren imaging To cite this version : HAL Id : hal-02376833 Spectral and wavelet analysis of

an aero-acoustic feedback loop in a transonic outflow val". In: (2019).

[37] D. Edgington-Mitchell. "Aeroacoustic resonance and self-excitation in screeching and impinging supersonic jets – A review". In: *International Journal of Aeroacoustics* 18.2-3 (2019), pp. 118–188. issn: 20484003. doi: 10.1177/1475472X19834521.

[38] L. Beranek and H. S. Jr. "The design and construction of anechoic sound chambers". In: *The Journal of the Acoustical Society ...* 18.I (1946), pp. 140–150. doi: 10.1121/1.1916351.

[39] T. J. Schultz. "Acoustics of the concert hall". In: *IEEE Spectrum* 2.6 (1965), pp. 56–67. issn: 00189235. doi: 10.1109/MSPEC.1965.5531663.

[40] R. Malkin, T. Todd, and D. Robert. "Quantitative imaging of acoustic reflection and interference". In: *Journal of Physics: Conference Series* 581.1 (2015). issn: 17426596. doi: 10.1088/1742-6596/581/1/012007.

[41] E. A. Lehmann and A. M. Johansson. "Prediction of energy decay in room impulse responses simulated with an image-source model". In: *The Journal of the Acoustical Society of America* 124.1 (2008), pp. 269–277. issn: 0001-4966. doi: 10.1121/1.2936367.

[42] L. Savioja and U. P. Svensson. "Overview of geometrical room acoustic modeling techniques". In: *The Journal of the Acoustical Society of America* 138.2 (2015), pp. 708–730. issn: 0001-4966. doi: 10.1121/1.4926438.

[43] M. Vorländer and E. Mommertz. "Definition and measurement of random-incidence scattering coefficients". In: *Applied Acoustics* 60.2 (2000), pp. 187–199. doi: 10.1016/S0003-682X(99)00056-0.

[44] S. Dupont, M. Melon, and A. Berry. "Characterization of acoustic material at oblique incidence using a spherical microphone array". In: *The Journal of the Acoustical Society of America* 147.5 (2020), pp. 3613–3625. issn: 0001-4966. doi: 10.1121/10.0001257.

[45] X. Wang, Y. Li, T. Chen, and Z. Ying. "Research on the sound absorption characteristics of porous metal materials at high sound pressure levels". In: *Advances in Mechanical Engineering* 7.5 (2015), pp. 1–7. issn: 16878140. doi: 10.1177/1687814015575429.

[46] D. Oliva and V. Hongisto. "Sound absorption of porous materials - Accuracy of prediction methods". In: *Applied Acoustics* 74.12 (2013), pp. 1473–1479. issn: 0003682X. doi: 10.1016/j.apacoust.2013.06.004.

[47] C. Jiang, S. Zhang, and L. Huang. “On the acoustic wedge design and simulation of anechoic chamber”. In: *Journal of Sound and Vibration* 381 (2016), pp. 139–155. issn: 10958568. doi: 10.1016/j.jsv.2016.06.020.

[48] A. D. Pierce. *Acoustics - An Introduction to Its Physical Principles and Applications*. 3rd ed. Springer, 2019. doi: https://doi.org/10.1007/978-3-030-11214-1.

[49] J. Piechowicz. “Sound wave diffraction at the edge of a sound barrier”. In: *Acta Physica Polonica A* 119.6 A (2011), pp. 1040–1045. issn: 1898794X. doi: 10.12693/APhysPolA.119.1040.

[50] J. J. Bowman, T. B. A. Senior, and P. L. E. Uslenghi. *Electromagnetic and acoustic scattering by simple shapes*. Tech. rep. 1970.

[51] U. J. Kurze. “Noise reduction by barriers”. In: *Journal of the Acoustical Society of America* 55.3 (1974), pp. 504–518. issn: NA. doi: 10.1121/1.1914528.

[52] M. J. Lighthill. “On sound generated aerodynamically I. General theory”. In: *Proceedings of the Royal Society of London. Series A. Mathematical and Physical Sciences* 211.1107 (1952), pp. 564–587. url: https://royalsocietypublishing.org/.

[53] R. K. Amiet. “Refraction of sound by a shear layer”. In: *Journal of Sound and Vibration* 58.4 (1978), pp. 467–482. issn: 10958568. doi: 10.1016/0022-460X(78)90353-X.

[54] P. Sijtsma. *Phased Array Beamforming Applied to Wind Tunnel and Fly-Over Tests*. Tech. rep. NLR-TP-2010-549. National Aerospace Laboratory (NLR), Amsterdam, The Netherlands, 2010. doi: 10.4271/2010-36-0514.

[55] F. Yunus, D. Casalino, F. Avallone, and D. Ragni. “Toward inclusion of atmospheric effects in the aircraft community noise predictions”. In: *The Journal of the Acoustical Society of America* 150.2 (2021), pp. 759–768. issn: 0001-4966. doi: 10.1121/10.0005733.

[56] R. K. Amiet. “Correction of open jet wind tunnel measurements for shear layer refraction”. In: *AIAA 2nd Aeroacoustics Conference*. 1975, p. 532.

[57] W. J. Devenport, R. A. Burdisso, A. Borgoltz, P. A. Ravetta, M. F. Barone, K. A. Brown, and M. A. Morton. “The Kevlar-walled anechoic wind tunnel”. In: *Journal of Sound and Vibration* 332.17 (2013), pp. 3971–3991. issn: 10958568. doi: 10.1016/j.jsv.2013.02.043.

[58] A. Fischer, O. Lylloff, A. S. Olsen, M. Gaunaa, and C. Bak. “Experimental investigation of the influence of aerodynamic loading on the transmission loss through Kevlar membranes”. In: *30th AIAA/CEAS Aeroacoustics Conference*. 2024. isbn: 9781624107207. doi: 10.2514/6.2024-3354.

[59] E. Llorente and D. Ragni. “Trailing-edge serrations effect on the performance of a wind turbine”. In: *Renewable Energy* 147 (2020), pp. 437–446. issn: 18790682. doi: 10.1016/j.renene.2019.08.128.

[60] E. Duell, J. Yen, J. Walter, and S. Arnette. “Boundary Layer Noise in Aeroacoustic Wind Tunnels”. In: *42nd AIAA Aerospace Sciences Conference*. 2004. doi: https://doi.org/10.2514/6.2004-1028.

[61] S. Glegg and W. Devenport. *Aeroacoustics of Low Mach Number Flows: Fundamentals, Analysis, and Measurement*. Academic Press, 2017.

[62] F. d. Monteiro, D. Ragni, F. Avallone, and T. Sinnige. “Low-order acoustic prediction tool for estimating noise emissions from distributed propeller configurations”. In: *AIAA AVIATION 2023 Forum*. June. 2023, pp. 1–13. doi: 10.2514/6.2023-4180.

[63] S. J. Majumdar and N. Peake. “Noise generation by the interaction between ingested turbulence and a rotating fan”. In: *Journal of Fluid Mechanics* 359 (1998), pp. 181–216. issn: 00221120. doi: 10.1017/S0022112097008318.

[64] P. Soderman and L. Hoglund. “Wind-tunnel fan noise reduction including effects of turning vanes on noise propagation”. In: AIAA 5th Aeroacoustics Conference, 1979. doi: 10.2514/6.1979-642.

[65] M. S. Howe. “Surface pressures and sound produced by turbulent flow over smooth and rough walls”. In: *Journal of the Acoustical Society of America* 90.2 (1991), pp. 1041–1047. issn: NA. doi: 10.1121/1.402292.

[66] J. E. Ffowcs Williams. “Hydrodynamic noise”. In: *Annual Review of Fluid Mechanics* 1.1 (1969), pp. 197–222. doi: https://doi.org/10.1146/annurev.fl.01.010169.001213.

[67] A. J. Smits, E. F. Spina, A. E. Alving, R. W. Smith, E. M. Fernando, and J. F. Donovan. “A comparison of the turbulence structure of subsonic and supersonic boundary layers”. In: *Physics of Fluids A* 1.11 (1989), pp. 1865–1875. issn: 08998213. doi: 10.1063/1.857511.

[68] V. Fleury, L. Coste, R. Davy, A. Mignosi, C. Cariou, and J. M. Prosper. “Optimization of microphone array wall mountings in closed-section wind tunnels”. In: *AIAA Journal* 50.11 (2012), pp. 2325–2335. issn: 00011452. doi: 10.2514/1.J051336.

[69] M. Szőke, W. Devenport, A. Borgoltz, C. Roy, and T. Lowe. “Advanced Boundary Simulations of an Aeroacoustic and Aerodynamic Wind Tunnel”. In: (2021), pp. 1–19.

[70] E. Sarradj, C. Fritzsche, T. Geyer, and J. Giesler. “Acoustic and aerodynamic design and characterization of a small-scale aeroacoustic wind tunnel”. In: *Applied Acoustics* 70.8 (Aug. 2009), pp. 1073–1080. issn: 0003682X. doi: 10.1016/j.apacoust.2009.02.009.

[71] A. J. Cooper and N. Peake. “Rotor-stator interaction noise in swirling flow: Stator sweep and lean effects”. In: *AIAA Journal* 44.5 (2006), pp. 981–991. issn: 00011452. doi: 10.2514/1.5857.

[72] J. Biesheuvel, M. Tuinstra, L. D. de Santana, and C. H. Venner. “Effect of turbulent boundary layer induced coherence loss on beamforming measurements in industrial scale wind tunnel tests”. In: *25th AIAA/CEAS Aeroacoustics Conference, 2019*. American Institute of Aeronautics and Astronautics Inc, AIAA, 2019. isbn: 9781624105883. doi: 10.2514/6.2019-2463.

[73] M. K. Okoronkwo, R. Alsaif, R. Haklander, S. Baba, J. M. Eburn, Z. Lu, N. Arafa, O. Stalnov, A. Ekmekci, and P. Lavoie. “Design and characterization of the university of Toronto hybrid anechoic wind tunnel”. In: *Applied Acoustics* 228 (Jan. 2025). issn: 1872910X. doi: 10.1016/j.apacoust.2024.110294.

[74] G. Wickern and N. Lindener. “The Audi Aeroacoustic Wind Tunnel: Final Design and First Operational Experience”. In: *SAE transactions*. 2000, pp. 1387–1402. doi: https://doi.org/10.4271/2000-01-0868.

[75] G. Wickern, W. von Heesen, and S. Wallmann. “Wind tunnel pulsations and their Active Suppression”. In: *SAE transactions*. 2000, pp. 1403–1416.

[76] T. F. Brooks, M. A. Marcolini, and D. S. Pope. “Airfoil trailing edge flow measurements and comparison with theory, incorporating open wind tunnel corrections”. In: *AIAA/NASA 9th Aeroacoustics Conference*. 1984. doi: 10.2514/6.1984-2266.

[77] J. B. Barlow, W. H. Rae, and A. Pope. *Low-speed wind tunnel testing*. John Wiley & Sons, 1999. isbn: 0471557749.

[78] P. Sijtsma. “Executive summary Acoustic beamforming for the ranking of aircraft noise”. In: *National Aerospace Laboratory* NLR-TP-201.March (2012), pp. 12–15.

[79] W. Devenport, C. Bak, K. Brown, A. Borgoltz, J. Osterlund, P. Davidsson, and S. T. O. “Design and Operation of Hybrid Aeroacoustic Wind Tunnels”. In: *Design and Operation of Aeroacoustic Wind Tunnel Tests for Group and Air Transport* STO-EN-AVT.May (2017). doi: 10.14339/STO-EN-AVT-287.

[80] A. Fischer, C. Bak, O. Lylloff, A. S. Olsen, R. F. Mikkelsen, S. B. Ildvedsen, J. S. Beckerlee, A. Borgoltz, M. Kuester, and N. Intaratep. “Cross validation of the aerodynamic and acoustic measurements in two Kevlar-walled wind tunnels”. In: *Journal of Physics: Conference Series*. Vol. 2265. 2. IOP, 2022. doi: 10.1088/1742-6596/2265/2/022103.

[81] J. Serpieri. “Cross-Flow Instability: Flow diagnostics and control of swept wing boundary layers”. PhD thesis. Delft University of Technology, 2018. isbn: 9789055841745. doi: doi.org/10.4233/uuid:3dac1e78-fcc3-437f-9579-048b74439f55.

[82] GRAS Sound & Vibration. *Gras 40ph, CCP Free-field Array Microphone*. Accessed online 2021-10-05. url: https://www.grasacoustics.com/products/special-microphone/array-microphones/product/ss_export/pdf2?product_id=178.

[83] S. Luesutthiviboon, A. Malgoezar, M. Snellen, P. Sijtsma, and D. Simons. “Improving source discrimination performance by using an optimized acoustic array and adaptive high-resolution CLEAN-SC beamforming”. In: *7th Berlin Beamforming Conference*. 2018, pp. 1–26.

[84] S. Luesutthiviboon and D. Ragni. “Characterization of the Acoustically Treated Low-turbulence Tunnel (LTT) of TU Delft”. In: Hybrid Anechoic Wind Tunnel (HAWT) workshop in 26th AIAA/CEAS Aeroacoustics Conference, Online, 2020.

[85] P. L. Bhatnagar, E. P. Gross, and M. Krook. “A Model for Collision Processes in Gases. I. Small Amplitude Processes in Charged and Neutral One-Component Systems”. In: *Physical review* 94.3 (1954), pp. 511–525. doi: https://doi.org/10.1103/PhysRev.94.511.

[86] C. M. Teixeira. “Incorporating turbulence models into the Lattice-boltzmann method”. In: *International Journal of Modern Physics C* 9.8 (1998), pp. 1159–1175. issn: 01291831. doi: 10.1142/s0129183198001060.

[87] V. Yakhot and S. A. Orszag. “Renormalization group analysis of turbulence. I. Basic theory”. In: *Journal of Scientific Computing* 1.1 (1986), pp. 3–51. issn: 08857474. doi: 10.1007/BF01061452.

[88] COMSOL. *Acoustics Module User's Guide*. Tech. rep. 1998. url: www.comsol.com/blogs.

[89] Y. Miki. "Acoustical properties of porous materials - Modifications of Delany-Bazley models". In: *Journal of the Acoustical Society of Japan (E)* 11.1 (1990), pp. 19–24.

[90] R. Merino-Martinez, W. van der Velden, F. Avallone, and D. Ragni. "Acoustic measurements of a DU96-W-180 airfoil with flow-misaligned serrations at a high Reynolds number in a closed-section wind tunnel". In: *7th International Conference on Wind Turbine Noise*. Rotterdam, The Netherlands, 2017.

[91] A. Rubio Carpio, R. Merino Martínez, F. Avallone, D. Ragni, M. Snellen, and S. van der Zwaag. "Experimental characterization of the turbulent boundary layer over a porous trailing edge for noise abatement". In: *Journal of Sound and Vibration* 443 (2019), pp. 537–558. issn: 10958568. doi: 10.1016/j.jsv.2018.12.010.

[92] R. Merino-Martínez, P. Sijtsma, A. R. Carpio, R. Zamponi, S. Luesutthiviboon, A. M. Malgoezar, M. Snellen, C. Schram, and D. G. Simons. "Integration methods for distributed sound sources". In: *International Journal of Aeroacoustics* 18.4-5 (July 2019), pp. 444–469. issn: 20484003. doi: 10.1177/1475472X19852945.

[93] H. F. Mourão Bento, C. P. Vandercreek, F. Avallone, D. Ragni, and M. Snellen. "Lattice Boltzmann very large eddy simulations of a turbulent flow over covered and uncovered cavities". In: *Physics of Fluids* 34.10 (2022), p. 105120. issn: 10897666. doi: 10.1063/5.0100001.

[94] J. Rossiter. *Wind-tunnel experiments on the flow over rectangular cavities at subsonic and transonic speeds*. Tech. rep. Aeronautical Research Council, 1964, p. 32.

[95] P. J. W. Block. *Noise response of cavities of varying dimensions at subsonic speeds*. Tech. rep. December. NASA, 1976, p. 36. url: https://ntrs.nasa.gov/api/citations/19770007874/downloads/19770007874.pdf.

[96] D. Rockwell and E. Naudascher. "Self-Sustained Oscillations of Impinging Free Shear Layers". In: *Annual Review of Fluid Mechanics* 11.1 (Feb. 1979), pp. 67–94. issn: 0066-4189. doi: 10.1146/annurev.fl.11.010179.000435.

[97] H. Yokoyama and C. Kato. "Fluid-acoustic interactions in self-sustained oscillations in turbulent cavity flows. I. Fluid-dynamic oscillations". In: *Physics of Fluids* 21.10 (2009). issn: 10706631. doi: 10.1063/1.3253326.

[98] P. Wang, Y. Deng, and Y. Liu. “Vortex-excited acoustic resonance in channel with coaxial side-branches: Vortex dynamics and aeroacoustic energy transfer”. In: *Physics of Fluids* 30.12 (2018), p. 125104. issn: 10897666. doi: 10.1063/1.5055909.

[99] Y. W. Ho and J. W. Kim. “A wall-resolved large-eddy simulation of deep cavity flow in acoustic resonance”. In: *J. Fluid Mech* 917 (2021), p. 17. doi: 10.1017/jfm.2021.261.

[100] C. W. Rowley, T. Colonius, and A. J. Basu. “On self-sustained oscillations in two-dimensional compressible flow over rectangular cavities”. In: *Journal of Fluid Mechanics* 455 (2002), pp. 315–346. issn: 00221120. doi: 10.1017/S0022112001007534.

[101] L. Larchevêque, P. Sagaut, I. Mary, O. Labbé, and P. Comte. “Large-eddy simulation of a compressible flow past a deep cavity”. In: *Physics of Fluids* 15.1 (2003), pp. 193–210. issn: 10706631. doi: 10.1063/1.1522379.

[102] F. R. Verdugo, A. Guitton, and R. Camussi. “Experimental investigation of a cylindrical cavity in a low Mach number flow”. In: *Journal of Fluids and Structures* 28 (Jan. 2012), pp. 1–19. issn: 08899746. doi: 10.1016/j.jfluidstructs.2011.10.009.

[103] F. Scarano, M. C. Jacob, R. Gojon, X. Carbonneau, and E. R. Gowree. “Modification of a turbulent boundary layer by circular cavities”. In: *Physics of Fluids* 34.6 (2022), p. 065134. issn: 1070-6631. doi: 10.1063/5.0091110.

[104] C. Haigermoser, F. Scarano, and M. Onorato. “Investigation of the flow in a circular cavity using stereo and tomographic particle image velocimetry”. In: *Experiments in Fluids* 46.3 (2009), pp. 517–526. issn: 07234864. doi: 10.1007/s00348-008-0577-2.

[105] S. A. Elder, T. M. Farabee, and F. C. Demetz. “Mechanisms of flow-excited cavity tones at low Mach number”. In: *The Journal of the Acoustical Society of America* 72 (1982), p. 532. doi: 10.1121/1.388034.

[106] A. T. de Jong. “Aeroacoustic Resonance of Slender Cavities: An Experimental and Numerical Investigation”. PhD thesis. Technische Universiteit Delft, 2012, p. 167. isbn: 978-94-6203-047-3. url: https://repository.tudelft.nl/record/uuid:2a3631d9-61a2-4167-b510-efa563f991b0.

[107] B. Ruck and B. Makiola. “Flow Separation over the Inclined Step”. In: *Physics of Separated Flows — Numerical, Experimental, and Theoretical Aspects* (1993), pp. 47–55. doi: 10.1007/978-3-663-13986-7_8.

[108] O. Marsden, C. Bailly, C. Bogey, and E. Jondeau. “Investigation of flow features and acoustic radiation of a round cavity”. In: *Journal of Sound and Vibration* 331.15 (July 2012), pp. 3521–3543. issn: 0022460X. doi: 10.1016/j.jsv.2012.03.017.

[109] M. Hiwada, T. Kawamura, I. Mabuchi, and M. Kumada. “Some Characteristics of Flow Patten and Heat Transfer Past a Circular Cylindrical Cavity”. In: *Bulletin of JSME* 49.438 (1983), pp. 1744–1752. issn: 1881-1426. doi: 10.1299/jsme1958.26.1744.

[110] O. Marsden, C. Bogey, and C. Bailly. “Investigation of flow features around shallow round cavities subject to subsonic grazing flow”. In: *Physics of Fluids* 24.12 (Dec. 2012). issn: 10706631. doi: 10.1063/1.4772194.

[111] P. W. McCarthy and A. Ekmekci. “Flow features of shallow cylindrical cavities subject to grazing flow”. In: *Physics of Fluids* 34.2 (2022), p. 27115. issn: 10897666. doi: 10.1063/5.0072554.

[112] A. Rona. “The Acoustic Resonance of Rectangular and Cylindrical Cavities”. In: *Journal of Algorithms & Computational Technology* 1.3 (Oct. 2007), pp. 329–356. issn: 1748-3018. doi: 10.1260/174830107782424110.

[113] M. Grottadaurea and A. Rona. “Noise sources from a cylindrical cavity”. In: *13th AIAA/CEAS Aeroacoustics Conference (28th AIAA Aeroacoustics Conference)*. Rome, Italy, 2007. isbn: 9781624100031. doi: 10.2514/6.2007-3723.

[114] Y. Yang, D. Rockwell, K. Lai-Fook Cody, and M. Pollack. “Generation of tones due to flow past a deep cavity: Effect of streamwise length”. In: *Journal of Fluids and Structures* 25.2 (Feb. 2009), pp. 364–388. issn: 0889-9746. doi: 10.1016/J.JFLUIDSTRUCTS.2008.05.003.

[115] L. F. East. “Aerodynamically induced resonance in rectangular cavities”. In: *Journal of Sound and Vibration* 3.3 (May 1966), pp. 277–287. issn: 10958568. doi: 10.1016/0022-460X(66)90096-4.

[116] M. L. Pollack. “Flow-induced tones in side-branch pipe resonators”. In: *The Journal of the Acoustical Society of America* 67 (1980), p. 1153. doi: 10.1121/1.384174.

[117] S. Jaeger, W. Horne, and C. Allen. “Effect of surface treatment on array microphone self-noise”. In: *6th AIAA/CEAS Aeroacoustics Conference and Exhibit*. Lahaina, HI, Aug. 2000. doi: 10.2514/6.2000-1937.

[118] C. Teruna, L. Rego, F. Avallone, D. Ragni, and D. Casalino. “Applications of the Multilayer Porous Medium Modeling Approach for Noise Mitigation”. In: *Journal of Aerospace Engineering* 34.6 (2021), p. 04021074. issn: 0893-1321. doi: 10.1061/(asce)as.1943-5525.0001326.

[119] C. Teruna, F. Manegar, F. Avallone, D. Casalino, D. Ragni, A. Rubio-Carpio, and T. Carolus. “Numerical analysis of metal-foam application for trailing edge noise reduction”. In: *25th AIAA/CEAS Aeroacoustics Conference, 2019*. Delft, The Netherlands, 2019. isbn: 9781624105883. doi: 10.2514/6.2019-2650.

[120] G. E. Elsinga and J. Westerweel. “Tomographic-PIV measurement of the flow around a zigzag boundary layer trip”. In: *Experiments in Fluids* 52.4 (Apr. 2012), pp. 865–876. issn: 07234864. doi: 10.1007/s00348-011-1153-8.

[121] G. M. Corcos. “The structure of the turbulent pressure field in boundary-layer flows”. In: *Journal of Fluid Mechanics* 18.3 (Mar. 1964), pp. 353–378. issn: 14697645. doi: 10.1017/S002211206400026X.

[122] S. Luesutthiviboon, D. Ragni, F. Avallone, and M. Snellen. “An alternative permeable topology design space for trailing-edge noise attenuation”. In: *International Journal of Aeroacoustics* 20.3-4 (2021), pp. 221–253. issn: 20484003. doi: 10.1177/1475472X211003295.

[123] X. Gloerfelt and J. Berland. “Turbulent boundary-layer noise: Direct radiation at Mach number 0.5”. In: *Journal of Fluid Mechanics* 723 (2013), pp. 318–351. issn: 00221120. doi: 10.1017/jfm.2013.134.

[124] J. H. M. Ribeiro and W. R. Wolf. “Identification of coherent structures in the flow past a NACA0012 airfoil via proper orthogonal decomposition”. In: *Physics of Fluids* 29.8 (2017), p. 85104. issn: 10897666. doi: 10.1063/1.4997202.

[125] M. A. Mendez, M. Balabane, and J. M. Buchlin. “Multi-scale proper orthogonal decomposition of complex fluid flows”. In: *Journal of Fluid Mechanics* 870 (2019), pp. 988–1036. issn: 14697645. doi: 10.1017/jfm.2019.212.

[126] D. Ninni and M. A. Mendez. “MODULO: A software for Multiscale Proper Orthogonal Decomposition of data”. In: *SoftwareX* 12 (July 2020), p. 100622. issn: 2352-7110. doi: 10.1016/J.SOFTX.2020.100622.

[127] L. Eça and M. Hoekstra. “Discretization Uncertainty Estimation based on a Least Squares version of the Grid Convergence Index”. In: *Proceedings of the Second Workshop on CFD Uncertainty Analysis, Instituto Superior Tecnico, Lisbon, Oct* October (2006), pp. 1–27.

[128] S. Ghaemi and F. Scarano. “Turbulent structure of high-amplitude pressure peaks within the turbulent boundary layer”. In: *Journal of Fluid Mechanics* 735 (2013), pp. 381–426. issn: 14697645. doi: 10.1017/jfm.2013.501.

[129] I. Marusic and G. J. Kunkel. “Streamwise turbulence intensity formulation for flat-plate boundary layers”. In: *Physics of Fluids* 15.8 (2003), pp. 2461–2464. issn: 10706631. doi: 10.1063/1.1589014.

[130] Q. Zhang and D. J. Bodony. “Numerical investigation of a honeycomb liner grazed by laminar and turbulent boundary layers”. In: *Journal of Fluid Mechanics* 792 (2016), pp. 936–980. issn: 14697645. doi: 10.1017/jfm.2016.79.

[131] H. Schlichting and K. Gersten. *Boundary-Layer Theory*. 9th. Springer, 1987. isbn: 9783662529171.

[132] K. Mori, H. Imanishi, Y. Tsuji, T. Hattori, M. Matsubara, S. Mochizuki, M. Inada, and T. Kasiwagi. “Direct total skin-friction measurement of a flat plate in zero-pressure-gradient boundary layers”. In: *Fluid Dynamics Research* 41.2 (2009). issn: 01695983. doi: 10.1088/0169-5983/41/2/021406.

[133] L. T. Lima Pereira, D. Ragni, F. Avallone, and F. Scarano. “Pressure fluctuations from large-scale PIV over a serrated trailing edge”. In: *Experiments in Fluids* 61.3 (2020), pp. 1–17. issn: 14321114. doi: 10.1007/s00348-020-2888-x.

[134] S. Pröbsting, M. Tuinstra, and F. Scarano. “Trailing edge noise estimation by tomographic Particle Image Velocimetry”. In: *Journal of Sound and Vibration* 346.1 (2015), pp. 117–138. issn: 10958568. doi: 10.1016/j.jsv.2015.02.018.

[135] J. Jeong and F. Hussain. “On the identification of a vortex”. In: *Journal of Fluid Mechanics* 285 (1995), pp. 69–94. issn: 14697645. doi: 10.1017/S0022112095000462.

[136] G. P. Scavone. “An Acoustic Analysis of Single-Reed Woodwind Instruments with an Emphasis on Design and Performance Issues and Digital Waveguide Modeling Techniques”. PhD thesis. Stanford University, 1997.

[137] W. K. Blake. “Essentials of Turbulent Wall Pressure Fluctuations”. In: *Mechanics of Flow-Induced Sound and Vibration, Volume 2*. Vol. 2. Elsevier, 2017, pp. 81–177. isbn: 9780128092743. doi: 10.1016/b978-0-12-809274-3.00002-7.

[138] L. Larchevêque, P. Sagaut, T. H. Lê, and P. Comte. “Large-eddy simulation of a compressible flow in a three-dimensional open cavity at high Reynolds number”. In: *Journal of Fluid Mechanics* 516 (2004), pp. 265–301. issn: 00221120. doi: 10.1017/S0022112004000709.

[139] S. W. Rienstra. *Fundamentals of Duct Acoustics*. November. Eindhoven University of Technology, 2015, pp. 1–50. url: https://www.win.tue.nl/~sjoerdr/papers/VKI_Rienstra.pdf%20http://www.win.tue.nl/~sjoerdr/papers/VKI_Rienstra.pdf.

[140] Milton Abramowitz and Irene A. Stegun, eds. *Handbook of Mathematical Functions*. Washington D.C.: National Bureau of Standards, Dec. 1964. url: https://personal.math.ubc.ca/~cbm/aands/abramowitz_and_stegun.pdf.

[141] C. P. VanDercreek, P. Sijtsma, M. Snellen, D. Ragni, F. Avallone, and D. G. Simons. “Deterministic Model of Acoustic Wave Propagation in a Cavity”. In: *25th AIAA/CEAS Aeroacoustics Conference*. Delft, The Netherlands, May 2019. doi: doi:10.2514/6.2019-2425.

[142] H. F. M. Bento, D. Ragni, F. Avallone, D. Simons, and M. Snellen. “Acoustic wall treatments for wind tunnel aeroacoustic measurements”. In: *Applied Acoustics* 199 (2022), p. 108989. issn: 1872910X. doi: 10.1016/j.apacoust.2022.108989.

[143] C. Manes, D. Poggi, and L. Ridolfi. “Turbulent boundary layers over permeable walls: Scaling and near-wall structure”. In: *Journal of Fluid Mechanics* 687 (2011), pp. 141–170. issn: 00221120. doi: 10.1017/jfm.2011.329.

[144] K. Suga, Y. Matsumura, Y. Ashitaka, S. Tominaga, and M. Kaneda. “Effects of wall permeability on turbulence”. In: *International Journal of Heat and Fluid Flow* 31.6 (2010), pp. 974–984. issn: 0142727X. doi: 10.1016/j.ijheatfluidflow.2010.02.023.

[145] S. Guidati, G. Guidati, and S. Wagner. “Beamforming in a reverberating environment with the use of measured steering vectors”. In: *7th AIAA/CEAS Aeroacoustics Conference and Exhibit*. Maastricht, The Netherlands, 2001, p. 2166. doi: 10.2514/6.2001-2166.

[146] B. A. Fenech and K. Takeda. “Towards more accurate beamforming levels in closed-section wind tunnels via de-reverberation”. In: *13th AIAA/CEAS Aeroacoustics Conference (28th AIAA Aeroacoustics Conference)* (2007), pp. 1–12. doi: 10.2514/6.2007-3431.

[147] QSources. *QindW Miniature Sound Source*. 2024. url: https://www.qsources.be/qindw/.

[148] "ISO 25178-2:2012, Geometrical Product Specifications (GPS)—Surface Texture: Areal—Part 2: Terms, Definitions and Surface Texture Parameters". In: *International Standards Organization* (2012).

[149] M. E. Delany and E. N. Bazley. "Acoustical properties of fibrous absorbent materials". In: *Applied Acoustics* 3.2 (1970), pp. 105–116. issn: 0003682X. doi: 10.1016/0003-682X(70)90031-9.

[150] M. Aretz, P. Dietrich, and M. Vorländer. "Application of the mirror source method for low frequency sound prediction in rectangular rooms". In: *Acta Acustica united with Acustica* 100.2 (2014), pp. 306–319. issn: 16101928. doi: 10.3813/AAA.918710.

[151] H. Koruk and G. Genc. *Acoustic and mechanical properties of luffa fiber-reinforced biocomposites*. Elsevier Ltd, 2018, pp. 325–341. isbn: 9780081022924. doi: 10.1016/B978-0-08-102292-4.00017-5.

[152] P. H. Alfredsson and R. Örlü. "The diagnostic plot a litmus test for wall bounded turbulence data". In: *European Journal of Mechanics, B/Fluids* 29.6 (2010), pp. 403–406. issn: 09977546. doi: 10.1016/j.euromechflu.2010.07.006.

[153] J. Jiménez. "Turbulent flows over rough walls". In: *Annual Review of Fluid Mechanics* 36.1991 (2004), pp. 173–196. issn: 00664189. doi: 10.1146/annurev.fluid.36.050802.122103.

[154] M. C. Remillieux, E. D. Crede, H. E. Camargo, R. A. Burdisso, W. J. Devenport, M. Rasnick, P. Van Seeters, and A. Chou. "Calibration and demonstration of the new Virginia Tech anechoic wind tunnel". In: *14th AIAA/CEAS Aeroacoustics Conference (29th AIAA Aeroacoustics Conference)*. May. 2008, pp. 5–7. isbn: 9781563479397. doi: 10.2514/6.2008-2911.

[155] A. S. Hersh and B. Walker. "Acoustic Behavior of Fibrous Bulk Materials." In: *AIAA Paper*. 1980. doi: 10.2514/6.1980-986.

[156] H. F. Mourão Bento, C. P. Vandercreek, F. Avallone, D. Ragni, P. Sijtsma, and M. Snellen. "Wall treatments for aeroacoustic measurements in closed wind tunnel test sections". In: San Diego, CA: AIAA AVIATION Forum, 2023. doi: 10.2514/6.2023-4162.

[157] R. de Vries, N. van Arnhem, T. Sinnige, R. Vos, and L. L. M. Veldhuis. "Aerodynamic interaction between propellers of a distributed-propulsion system in forward flight". In: *Aerospace Science and Technology* 118 (Nov. 2021). issn: 12709638. doi: 10.1016/j.ast.2021.107009.

[158] L. T. Lima Pereira, F. Avallone, D. Ragni, and F. Scarano. “A physics-based description and modelling of the wall-pressure fluctuations on a serrated trailing edge”. In: *Journal of Fluid Mechanics* 938 (2022), A28. issn: 14697645. doi: 10.1017/jfm.2022.173.

[159] P. D. Welch. “The Use of Fast Fourier Transform for the Estimation of Power Spectra: A Method Based on Time Averaging Over Short, Modified Periodograms”. In: *IEEE Transactions on Audio and Electroacoustics* 15.2 (1967), pp. 70–73. issn: 00189278. doi: 10.1109/TAU.1967.1161901.

[160] H. F. Mourão Bento, C. P. VanDercreek, F. Avallone, D. Ragni, P. Sijtsma, and M. Snellen. “Wave propagation modelling approach for improved assessment of the acoustic field in closed test section wind tunnels”. In: *Journal of Sound and Vibration* 600 (Mar. 2025). issn: 10958568. doi: 10.1016/j.jsv.2024.118858.

[161] H. F. Mourão Bento, C. VanDercreek, F. Avallone, D. Ragni, P. Sijtsma, and M. Snellen. “Experimental data, Green’s function correction code and numerical setups used in Wave propagation modelling approach for improved assessment of the acoustic field in closed test section wind tunnels”. In: 4TU.ResearchData. Dataset. Version 1, 2025. doi: https://doi.org/10.4121/e159dc57-9a31-49bc-a12f-6b3de76d9fc4.

[162] Stefan Gombots, Manfred Kaltenbacher, and Barbara Kaltenbacher. “Combined Experimental-Simulation Based Acoustic Source Localization”. In: *Proceedings of DAGA, Aachen, Germany*. 2016.

[163] M. Lehmann, D. Ernst, M. Schneider, C. Spehr, and M. Lummer. “Beamforming for measurements under disturbed propagation conditions using numerically calculated Green’s functions”. In: *Journal of Sound and Vibration* 520 (2022), p. 116638. issn: 10958568. doi: 10.1016/j.jsv.2021.116638.

[164] E. Sarradj. “Three-dimensional acoustic source mapping with different beamforming steering vector formulations”. In: *Advances in Acoustics and Vibration* 2012 (2012), p. 292695. issn: 16876261. doi: 10.1155/2012/292695.

[165] L. T. Lima Pereira, F. Avallone, and D. Ragni. “On the role of coherent turbulent structures on the noise emitted by non-straight trailing edges”. In: *10th Convention of the European Acoustics Association, EAA*. European Acoustics Association, EAA, 2023. isbn: 9788888942674. doi: 10.61782/fa.2023.0665.

[166] A. Fischer, O. Lylloff, E. F. Grande, and C. Bak. “Analytical corrections for acoustic transmission in kevlar-walled wind tunnels”. In: *AIAA Journal* 61.7 (2023), pp. 3119–3133. issn: 1533385X. doi: 10.2514/1.J062313.

[167] H. F. M. Bento, R. de Vries, and L. L. Veldhuis. “Aerodynamic performance and interaction effects of circular and square ducted propellers”. In: *AIAA Scitech 2020 Forum*. 2020, pp. 1–21. isbn: 9781624105951. doi: 10.2514/6.2020-1029.

ACKNOWLEDGEMENTS

Sharing this PhD journey with the people around me has made it very enjoyable and complete. I could never have learned half as much without the discussions with all my colleagues, co-authors and supervisors. I couldn't have stayed as motivated through the research troubles without the support I have received. My time at TU Delft was really fun thanks to everyone around me. I hope this acknowledgements chapter is able to show how much appreciation I keep from my PhD years.

I would like to start by thanking my supervisors, Francesco, Dani and Mirjam. I was lucky to meet Francesco during my Master thesis defence. Thank you for believing at the time, along with Dani and Mirjam, that I would be fit for this PhD. During the PhD, Francesco's close guidance and interest for my research always made me feel that my work was important, keeping me motivated and consistent. Francesco always showed confidence that we would achieve a good modelling of covered cavities or of the sound in the LTT, even before the results were good enough. His ideas and suggestions are a crucial part of this PhD. I am thankful to Dani also for following my research closely, for his enthusiasm and for always pushing me a bit further. The help in the lab, particularly in the first wind tunnel campaign, has made me understand that we would manage to get our campaigns done. Dani's guidance was critical for me to learn how to achieve successful experiments. My meetings with Mirjam have always made me feel positive about the research progress and for the next steps, even in more challenging times. I very much appreciate Mirjam's concerns for her students not to get overstressed when pressure is higher. I am thankful for Mirjam's enthusiasm, especially (but not exclusively) for our signal processing research. I have always looked forward to our discussions, which countless times made me start thinking with a new perspective.

The support I had within the THAMES project was very important for this PhD. I would like to thank the project partners NLR, Deutsche Windguard, Dassault Systémes and NWO. I would like to thank Pieter for the pleasant discussions and for the very interesting insights on beamforming. These insights were extremely helpful for the improvements proposed in this work. I was also lucky to work in the project with Colin. Our experimental and post-processing work together has made the PhD feel more collaborative. Our discussions about cavity flow also made me learn a lot. Besides, I really appreciate the nice times

having a beer outside work.

Being new to aeroacoustics at the start of the PhD, I was lucky to be placed in a research team complete with experts in Aeroacoustics, Lattice-Boltzmann simulations and experiments. I start by highlighting the help from my officemates Christopher, Tércio and Leandro, both in the lab and when learning new topics. This very much contributed to my learning slope, and helped me to start getting results much faster. Fernanda's help in the lab was also very important for my research.

Besides, my experimental research would not have been possible without the contributions of Steve van Herk. Thanks for the great lab setup designs.

In addition to the technical help and conversations, my friends and colleagues from aeroacoustics group and wind energy have made the PhD much more fun and enjoyable. I am thankful for nice times off work having a drink, a barbecue, a bike trip, dinner out, climbing... I would like to thank Christopher, for organising online and (within possible) offline events during Covid, Julia, Edo, Manoel, Gabriel, for reminding everyone to eat well, Jatinder, Dylan, for the great times at Delfts Bleau, Cristina, for being an awesome deskmate with Smints, Yanan, Claudia, Kiran, Federico, Livia, Deepali, Clem, for the fun dinners at Lychee, Flávio, Emanuelle, Kaj, Anastasia and Isaac. Everyone here deserves many PhD of the week awards. For the amazing trip after the San Diego conference, for the beautiful first sight of the Bixby bridge :) and of the National parks, I would like to thank Fernanda, Andrea, Alessia, Tércio, Dani, Hasse and Frits, also for not leaving us at the Death Valley dunes.

Thanks to everyone in Wind Energy department for the nice and supportive atmosphere. Special thanks to Sylvia for always helping everyone, and for being patient when I try to speak in Dutch.

I would like to thank previous colleagues and friends from FPP with whom I have spent a nice time off work, either going out, biking too many km with a NS-bike, going to the gym, playing padel, and climbing. In particular, I would like to thank Nitish, Federica, Alessandro, Francesco Tosto, Rishikesh, Martijn, Biagio, Nando and Reynard. I would like to thank Leo, Georg and all participants of the 'propeller meetings' during the time of my MSc thesis, for everything I have learned about aerodynamics and about research during the discussions.

I also enjoyed the few months spent on the Aircraft Noise and Emissions floor. I would like to thank everyone there, and in particular Lisette, for making me feel welcome. Besides, I would like to thank Roberto, Salil, Yunus and Alejandro for the helpful thoughts and insights.

My friends from outside Aerospace faculty who lived in the Netherlands also made my life in Delft much more enjoyable, and helped me to disconnect from work on the weekends. I would like to thank my friends Domingos, Tiago Nunes, Fatema, Chuck, Raquel, Catarina, Pedro, Parreira, Marina, Ticha, Lenny, for the barbecues, brunches, Secret

Santas', and for convincing me to start climbing. I am also thankful to my former flatmates Iñigo and Jorge. Our ability for doing a barbecue in the worst weather conditions made me feel positive that I could overcome any difficulties of the PhD.

I would like to thank my new colleagues at Airbus for welcoming me and for the discussions on many Aeroacoustics topics. This is an important help for me to stay motivated and to (hopefully) keep my brain sharp for the defence. Also, special thanks to the TU Delft Alumni in Manching for the support with concluding the thesis.

I am also thankful to all my friends who, despite not having lived close to Delft during the time of my PhD, supported me and helped me forget about work whenever needed.

Last but not least, I would like to thank my parents and my entire family for always being there for me. Without them, I would not have managed to arrive here. I would like to thank Serena for always believing in me and for supporting me, even when I spent the weekend typing on Overleaf instead of hiking or exploring new places.

CURRICULUM VITæ

Hugo Filipe Mourão Bento was born in 1994 in Lisbon, Portugal. His curiosity for aerodynamics and aircraft pushed him to follow the Aerospace Engineering Bachelor at the University of Lisbon, at Instituto Superior Técnico. Afterwards, he decided to move to The Netherlands to specialize in Flight Performance and Propulsion, at Delft University of Technology. During this Master's study, Hugo had the opportunity to follow a half year internship at Blackshape Aircraft in Monopoli, Italy. At this aircraft manufacturer company, he expanded his knowledge on aircraft design, as well as his interest.

Hugo performed his Master thesis at TU Delft, on the topic "Aerodynamic interaction effects of circular and square ducted propellers". During the thesis, he learned to perform high fidelity numerical simulations, with the goal of investigating a novel propeller propulsion concept. He graduated from the Masters in 2019. The exciting experience with research during the Master thesis convinced him to start a PhD at TU Delft, in 2019, within the THAMES project. The new research project allowed Hugo to learn about aeroacoustics theory, experimental testing, low fidelity modelling and numerical research. During the PhD, Hugo had the opportunity to help and supervise students, to collaborate with partner companies within the THAMES project, and to participate in international conferences.

Since 2024, Hugo has been working at the Acoustics and Vibration team of Airbus Defence and Space in Manching, Germany. He has been working as Acoustics engineer. In his work, Hugo has the chance to apply the knowledge he previously gained in aeroacoustics, aircraft design and aerodynamics, contributing to European defence projects.

In his free time, Hugo likes to travel and to do sports, sometimes combining the two. Hugo likes to explore the mountains, hiking and skiing. He likes to enjoy the beach, trying out surfing or snorkelling.

Hugo likes experiencing the culture of different countries and trying new food. Hugo enjoys spending time with family and friends, for example going out, doing a barbecue and climbing.

LIST OF PUBLICATIONS

PEER-REVIEWED JOURNAL ARTICLES

3. H. F. Mourão Bento, C. P. VanDercreek, F. Avallone, D. Ragni, P. Sijtsma, and M. Snellen. "Wave propagation modelling approach for improved assessment of the acoustic field in closed test section wind tunnels". In: *Journal of Sound and Vibration* 600 (Mar. 2025). issn: 10958568. doi: 10.1016/j.jsv.2024.118858

2. H. F. Mourão Bento, C. P. Vandercreek, F. Avallone, D. Ragni, and M. Snellen. "Lattice Boltzmann very large eddy simulations of a turbulent flow over covered and uncovered cavities". In: *Physics of Fluids* 34.10 (2022), p. 105120. issn: 10897666. doi: 10.1063/5.0100001

1. H. F. M. Bento, D. Ragni, F. Avallone, D. Simons, and M. Snellen. "Acoustic wall treatments for wind tunnel aeroacoustic measurements". In: *Applied Acoustics* 199 (2022), p. 108989. issn: 1872910X. doi: 10.1016/j.apacoust.2022.108989

CONFERENCE PROCEEDINGS

2. H. F. Mourão Bento, C. P. Vandercreek, F. Avallone, D. Ragni, P. Sijtsma, and M. Snellen. "Wall treatments for aeroacoustic measurements in closed wind tunnel test sections". In: San Diego, CA: AIAA AVIATION Forum, 2023. doi: 10.2514/6.2023-4162

1. H. F. M. Bento, R. de Vries, and L. L. Veldhuis. "Aerodynamic performance and interaction effects of circular and square ducted propellers". In: *AIAA Scitech 2020 Forum*. 2020, pp. 1–21. isbn: 9781624105951. doi: 10.2514/6.2020-1029

DATASETS

1. H. F. Mourão Bento, C. VanDercreek, F. Avallone, D. Ragni, P. Sijtsma, and M. Snellen. "Experimental data, Green's function correction code and numerical setups used in Wave propagation modelling approach for improved assessment of the acoustic field in closed test section wind tunnels". In: 4TU.ResearchData. Dataset. Version 1, 2025. doi: https://doi.org/10.4121/e159dc57-9a31-49bc-a12f-6b3de76d9fc4

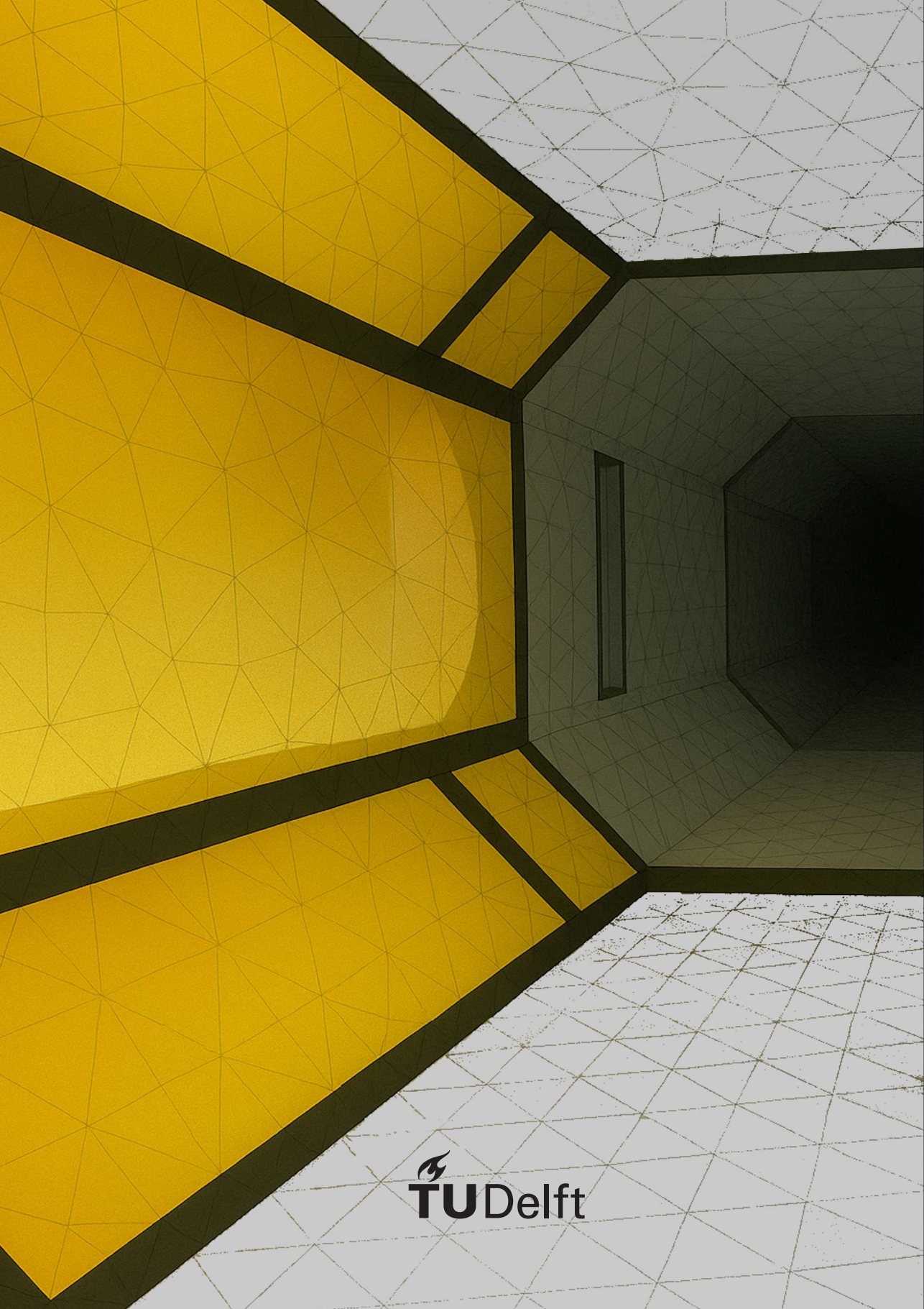
TUDelft